

Simulation of fluid flow and estimation of production from naturally fractured reservoirs

Author:

Fahad, Muhammad

Publication Date:

2013

DOI:

<https://doi.org/10.26190/unsworks/16199>

License:

<https://creativecommons.org/licenses/by-nc-nd/3.0/au/>

Link to license to see what you are allowed to do with this resource.

Downloaded from <http://hdl.handle.net/1959.4/52707> in <https://unsworks.unsw.edu.au> on 2024-05-01

UNIVERSITY OF NEW SOUTH WALES, AUSTRALIA

**SIMULATION OF FLUID FLOW AND ESTIMATION OF
PRODUCTION FROM NATURALLY FRACTURED
RESERVOIRS**

By

Muhammad Fahad

A thesis submitted in fulfilment of the
requirements for the degree of
Doctor of Philosophy
in
Petroleum Engineering

Supervisor: Professor Sheik S. Rahman

Co-Supervisor: Dr. Yildiray Cinar

School of Petroleum Engineering
The University of New South Wales

June 2013

PLEASE TYPE**THE UNIVERSITY OF NEW SOUTH WALES**
Thesis/Dissertation Sheet

Surname or Family name: Fahad

First name: Muhammad

Other name/s:

Abbreviation for degree as given in the University calendar:

PhD

School:

Petroleum Engineering

Faculty: Engineering

Title:

Simulation of Fluid Flow and Estimation of Production from
Naturally Fractured Reservoirs**Abstract 350 words maximum: (PLEASE TYPE)**

In this thesis, fluid flow in naturally fractured reservoirs with arbitrarily oriented fractures is simulated and the flow mechanism in matrix and fracture and their interactions are studied. Three different algorithms are presented to simulate single and two phase fluid flows through naturally fractured reservoirs. These are a grid based effective permeability tensor model, a single phase fluid flow simulator, and a two phase flow simulator. In order to validate the numerical work, series of laboratory experiments are designed and conducted. The grid based effective permeability is a unique tool that allows the use of the actual geometry of the fracture networks in the calculation of block permeabilities. The tensors are obtained by the boundary element method along with periodic boundary conditions. This numerical model includes multi-scale fractures and uses an appropriate methodology for each type of fracture, i.e. short, medium and long fractures. The model incorporates fluid flow in matrix, at the matrix-fracture interface and from fracture to fracture. It also assesses the effect of disconnected fractures on fluid flow. The computational efficiency of the presented model is improved in this thesis.

In the second algorithm, a simulation model based on the grid based effective permeabilities is presented. This is a finite element model that calculates pressures and production rates in naturally fractured reservoirs with arbitrary oriented fractures. To demonstrate an application of this model, a slice of fracture networks from a fractured basement reservoir of the Amadeus Basin is simulated. First, the permeability tensor model is used to obtain the grid based permeabilities. Then the flow simulator is fed by the grid block permeabilities to calculate pressure and velocity profiles throughout the reservoir. In one case, reservoir was depleted (depletion case), while in the second case, a five spot injection production scenario was modelled. Results show the importance of fracture networks in the fluid flow simulation, as flow is highly influenced by the connectivity of the fractures and the orientations.

A new laboratory-based glass bead model is introduced to visualize fluid flow through matrix and fractures as well as to measure absolute and relative permeabilities of homogeneous and fractured porous media. In the experiments, the matrix and fracture are represented by two different sizes of glass beads. Single phase experiments are performed for single and multiple (two) fractures and the absolute permeabilities are measured. These permeabilities are used to validate the permeability tensor model for single and multiple (two) fracture systems. Displacement tests for oil-water systems are conducted for homogeneous and heterogeneous systems. Pressures and productions are recorded for different realizations of fracture networks, and then the history matching technique is employed to obtain final relative permeability curves by using black oil simulator (CMG).

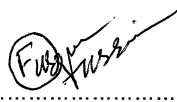
In the third algorithm, a two phase fluid flow (oil-water) model is presented. This model uses the finite difference method and calculates the pressure and saturations for fractured reservoirs. The IMPES method is adopted to solve pressures implicitly and saturations explicitly. The aim of this model is to simulate the laboratory based homogeneous and heterogeneous systems. Finally, laboratory obtained relative permeabilities are fed to the two phase flow model to estimate and compare the pressures and productions for homogeneous and heterogeneous systems. A reasonable agreement between the results is found which ensured the efficiency and accuracy of the numerical model as laboratory experiments provide authentic validations for numerical models.

In the final step, a new methodology is presented to upscale the laboratory-derived two-phase relative permeability relationship for different fracture systems to the reservoir scale. As an application, the proposed upscaling procedure is applied to a multi-fracture region of 1000m×1000m of the Amadeus Basin. Results reveal that the laboratory-based relative permeability based on simplified fracture-matrix geometries can form the benchmark data which can be upscaled for the field applications.

Declaration relating to disposition of project thesis/dissertation

I hereby grant to the University of New South Wales or its agents the right to archive and to make available my thesis or dissertation in whole or in part in the University libraries in all forms of media, now or here after known, subject to the provisions of the Copyright Act 1968. I retain all property rights, such as patent rights. I also retain the right to use in future works (such as articles or books) all or part of this thesis or dissertation.

I also authorise University Microfilms to use the 350 word abstract of my thesis in Dissertation Abstracts International (this is applicable to doctoral theses only).


Signature
Witness12-06-2013
Date

The University recognises that there may be exceptional circumstances requiring restrictions on copying or conditions on use. Requests for restriction for a period of up to 2 years must be made in writing. Requests for a longer period of restriction may be considered in exceptional circumstances and require the approval of the Dean of Graduate Research.

FOR OFFICE USE ONLY

Date of completion of requirements for Award:

THIS SHEET IS TO BE GLUED TO THE INSIDE FRONT COVER OF THE THESIS

COPYRIGHT STATEMENT

'I hereby grant the University of New South Wales or its agents the right to archive and to make available my thesis or dissertation in whole or part in the University libraries in all forms of media, now or here after known, subject to the provisions of the Copyright Act 1968. I retain all proprietary rights, such as patent rights. I also retain the right to use in future works (such as articles or books) all or part of this thesis or dissertation.

I also authorise University Microfilms to use the 350 word abstract of my thesis in Dissertation Abstract International (this is applicable to doctoral theses only).

I have either used no substantial portions of copyright material in my thesis or I have obtained permission to use copyright material; where permission has not been granted I have applied/will apply for a partial restriction of the digital copy of my thesis or dissertation.'

Signed

mhalad.

Date

12-06-2013

AUTHENTICITY STATEMENT

'I certify that the Library deposit digital copy is a direct equivalent of the final officially approved version of my thesis. No emendation of content has occurred and if there are any minor variations in formatting, they are the result of the conversion to digital format.'

Signed

mhalad.

Date

12-06-2013

ORIGINALITY STATEMENT

'I hereby declare that this submission is my own work and to the best of my knowledge it contains no materials previously published or written by another person, or substantial proportions of material which have been accepted for the award of any other degree or diploma at UNSW or any other educational institution, except where due acknowledgement is made in the thesis. Any contribution made to the research by others, with whom I have worked at UNSW or elsewhere, is explicitly acknowledged in the thesis. I also declare that the intellectual content of this thesis is the product of my own work, except to the extent that assistance from others in the project's design and conception or in style, presentation and linguistic expression is acknowledged.'

Signed 

Date 12-06-2013

ACKNOWLEDGEMENTS

Foremost, I am thankful to the most gracious and the beneficent God for his countless blessings on me.

I would like to express my sincere gratitude to Professor Sheik S. Rahman and Dr. Yildiray Cinar from School of Petroleum Engineering, The University of New South Wales, for their continual guidance and supervision.

I owe my deepest gratitude to my parents, for their love, support and appreciation over the period of my studies.

I would also like to thank the staff and research students from the School of Petroleum Engineering, The University of New South Wales. In particular, I am grateful to Nino Zajackowski for providing laboratory technical support and for providing any required software in time. I am also thankful to Mr. Furqan Hussain who made available his support in a number of ways.

I acknowledge University of Engineering and Technology Lahore, Pakistan, for sponsoring my PhD studies at University of New South Wales, Australia.

OUTCOME OF THIS RESEARCH WORK

Following research publications are an outcome of this research work.

- M. Fahad**, S. S. Rahman, Y. Cinar. (2011). "A Numerical and Experimental Procedure to Estimate Grid Based Effective Permeability Tensor for Geothermal Reservoirs." Geothermal Research Council (GRC) 23-26 Oct, 2011 California USA (Published and Presented)
- M. Fahad**, S. S. Rahman, Y. Cinar and T. Tran (2013). "A Laboratory Testing of a Fully Numerical Approach for calculation of Effective Grid Block Permeability for Naturally Fractured Porous Media." Journal of Petroleum Science and Technology: To be submitted.
- M. Fahad**, F. Hussain, S. S. Rahman. Y. Cinar. (2013). "An Innovative Laboratory Method for Evaluating Numerical Procedures for Simulation of Two Phase Flow and Pressure Drawdown of Naturally Fracture Reservoirs: Oil-Water Study." Journal of Petroleum Science and Engineering: To be submitted.

Abstract

In this thesis, fluid flow in naturally fractured reservoirs with arbitrarily oriented fractures is simulated and the flow mechanism in matrix and fracture and their interactions are studied. Three different algorithms are presented to simulate single and two phase fluid flows through naturally fractured reservoirs. These are a grid based effective permeability tensor model, a single phase fluid flow simulator, and a two phase flow simulator. In order to validate the numerical work, series of laboratory experiments are designed and conducted. The grid based effective permeability is a unique tool that allows the use of the actual geometry of the fracture networks in the calculation of block permeabilities. The tensors are obtained by the boundary element method along with periodic boundary conditions. This numerical model includes multi-scale fractures and uses an appropriate methodology for each type of fracture, i.e. short, medium and long fractures. The model incorporates fluid flow in matrix, at the matrix-fracture interface and from fracture to fracture. It also assesses the effect of disconnected fractures on fluid flow. The computational efficiency of the presented model is improved in this thesis.

In the second algorithm, a simulation model based on the grid based effective permeabilities is presented. This is a finite element model that calculates pressures and production rates in naturally fractured reservoirs with arbitrary oriented fractures. To demonstrate an application of this model, a slice of fracture networks from a fractured basement reservoir of the Amadeus Basin is simulated. First, the permeability tensor model is used to obtain the grid based permeabilities. Then the flow simulator is fed by the grid block permeabilities to calculate pressure and velocity profiles throughout the reservoir. In one case, reservoir was depleted (depletion case), while in the second case, a five spot injection production scenario was modelled. Results show the importance of fracture networks in the fluid flow simulation, as flow is highly influenced by the connectivity of the fractures and the orientations.

A new laboratory-based glass bead model is introduced to visualize fluid flow through matrix and fractures as well as to measure absolute and relative permeabilities of homogeneous and fractured porous media. In the experiments, the matrix and fracture are represented by two different sizes of glass beads. Single phase experiments are performed for single and multiple (two) fractures and the absolute permeabilities are measured. These permeabilities are used to validate the permeability tensor model for single and multiple (two) fracture systems. Displacement tests for oil-water systems are conducted for homogeneous and heterogeneous systems. Pressures and productions are recorded for different realizations of fracture networks, and then the history matching technique is employed to obtain final relative permeability curves by using black oil simulator (CMG).

In the third algorithm, a two phase fluid flow (oil-water) model is presented. This model uses the finite difference method and calculates the pressure and saturations for fractured reservoirs. The IMPES method is adopted to solve pressures implicitly and saturations explicitly. The aim of this model is to simulate the laboratory based homogeneous and heterogeneous systems. Finally, laboratory obtained relative permeabilities are fed to the two phase flow model to estimate and compare the pressures and productions for homogeneous and heterogeneous systems. A reasonable agreement between the results is found which ensured the efficiency and accuracy of the numerical model as laboratory experiments provide authentic validations for numerical models.

In the final step, a new methodology is presented to upscale the laboratory-derived two-phase relative permeability relationship for different fracture systems to the reservoir scale. As an application, the proposed upscaling procedure is applied to a multi-fracture region of 1000m×1000m of the Amadeus Basin. Results reveal that the laboratory-based relative permeability based on simplified fracture-matrix geometries can form the benchmark data which can be upscaled for the field applications.

Table of Contents

| | |
|--|------------|
| List of Tables..... | XI |
| List of Figures..... | XII |
| Chapter 1..... | 1 |
| Introduction..... | 1 |
| Chapter 2..... | 6 |
| Laboratory Determination of Absolute and Relative Permeability of Fractured Porous Media..... | 6 |
| 2.1 Literature Review..... | 7 |
| 2.2 Single Phase Flow Visualization Experiments..... | 10 |
| 2.2.1 Experimental Setup..... | 10 |
| 2.2.2 Experimental Procedure..... | 12 |
| 2.2.3 Results and Discussion..... | 13 |
| 2.3 Two Phase Flow Visualisation Experiments..... | 19 |
| 2.3.1 Experimental Setup..... | 19 |
| 2.3.2 Experimental Procedure..... | 20 |
| 2.3.3 Results and Discussion..... | 22 |
| 2.4 Relative Permeability (Oil Water)..... | 33 |
| 2.4.1 Numerical Reservoir Simulation..... | 33 |

| | |
|---|-----------|
| 2.4.2 Comparison between Laboratory and Simulation Results..... | 40 |
| Chapter 3..... | 53 |
| Fluid Flow Simulation in Arbitrarily Oriented Naturally Fractured Reservoirs..... | 53 |
| 3.1 Calculation of Grid based Permeability Tensors for fractured porous media..... | 53 |
| 3.1.1 Literature Review..... | 53 |
| Continuum Approaches..... | 53 |
| Discrete Fracture Approach..... | 59 |
| Models using Effective permeability Tensor..... | 61 |
| 3.1.2 Mathematical Formulation..... | 65 |
| Effective Permeability Tensor..... | 65 |
| Calculation of Effective Permeability..... | 65 |
| Boundary Conditions..... | 70 |
| Boundary Integral Equations..... | 74 |
| Boundary Element Formulation..... | 76 |
| 3.1.3 Results and Discussion..... | 79 |
| Validation of Numerical Results..... | 79 |
| Validation of Numerical Results against Laboratory Results..... | 82 |
| Evaluation of Numerical Results..... | 84 |
| Effect of Short Fractures on Effective Permeability..... | 84 |

| | |
|---|------------|
| Effect of Multiple Fractures on Effective Permeability..... | 85 |
| Effect of Intersecting Fractures on Effective Permeability..... | 88 |
| Potential Application..... | 82 |
| 3.2 Fluid Flow Simulation through Naturally Fractured Reservoirs..... | 94 |
| 3.2.1 Literature Review..... | 94 |
| 3.2.2 Mathematical Formulation of Simulation Model..... | 96 |
| Mapping..... | 98 |
| General Two Dimensional Transformation..... | 99 |
| Four Noded Element Transformation..... | 101 |
| Gaussian Quadrature..... | 102 |
| FEM Formulation for Decoupled Fluid Flow..... | 103 |
| Time-Dependent Analytical Solution for Decoupled Fluid Flow..... | 112 |
| Comparison between Numerical and Analytical Solution..... | 114 |
| 3.2.3 Results and Discussion..... | 117 |
| Chapter 4..... | 126 |
| Multiphase Fluid Flow Simulation in Arbitrarily Oriented Naturally Fractured Porous Media..... | 126 |
| 4.1 Mathematical Formulation..... | 126 |

| | |
|--|-----|
| 4.2 Results and Discussion..... | 132 |
| Chapter 5..... | 146 |
| Up scaling Two Phase Relative Permeability Relationship..... | 146 |
| 5.1 Up scaling Procedure..... | 147 |
| 5.2 Results and Discussion..... | 151 |
| Chapter 6..... | 167 |
| Conclusion and Future work Recommendations..... | 167 |
| 6.1 Conclusions and perspectives..... | 167 |
| 6.2 Recommendations for future studies..... | 169 |
| References..... | 170 |

List of Tables

| | |
|--|-----|
| Table 2-1. Permeability of the heterogeneous systems with respect to the fracture orientation..... | 15 |
| Table 2-2. Permeability of the heterogeneous systems, each containing set of two fractures..... | 17 |
| Table 2-3: Physical properties of oil and water at ambient conditions..... | 22 |
| Table 2-4: Irreducible water saturations for glass bead models at 1 and $2\text{cm}^3 / \text{min}$ | 33 |
| Table3-1. Comparison between numerical and experimental results (single fracture models)..... | 83 |
| Table 3-2. Comparison between numerical and experimental results (multiple fracture models)..... | 83 |
| Table 3-3. Co-ordinates for the fractured system presented in Fig. 3-17 | 86 |
| Table 3-4. Fracture co-ordinates for the upper right grid block in Fig. 3-19 | 90 |
| Table 3-5: Weighing factor and integration points for Gauss quadrature..... | 103 |
| Table 4-1: A comparison for breakthrough times between experimental and numerical results at injection rate of $1\text{cm}^3 / \text{min}$ | 137 |
| Table 4-2: A comparison for pressures at breakthrough between experimental and numerical results at injection rate of $1\text{cm}^3 / \text{min}$ | 137 |
| Table 5-1: Six nominated fractured systems of size $10\text{m} \times 10\text{m}$ from Figure 5-1 | 148 |
| Table 5-2: Pore volume Injected at breakthrough & peak pressures for case 1 to case 6.... | 152 |

List of Figures

| | |
|--|----|
| Figure 2-1: Schematic of glass bead model used for single phase flow experiments..... | 11 |
| Figure 2-2: Schematic of the experimental setup (Single Phase Flow)..... | 12 |
| Figure2-3: Velocity vs. pressure gradient for the single fracture models..... | 15 |
| Figure 2-4: Effect of fracture orientation on permeability..... | 16 |
| Figure 2-5: Effect of the fracture orientation on fluid flow (single fracture models)..... | 16 |
| Figure 2-6: Velocity vs. pressure gradient for multiple fracture models..... | 18 |
| Figure 2-7: Effect of different set of fractures on fluid flow (Multiple fracture models)..... | 19 |
| Figure 2-8: The glass bead model used for two phase flow experiments..... | 20 |
| Figure 2-9: Schematic of the experimental setup (Two Phase Flow)..... | 21 |
| Figure 2-10: Glass bead packs used for two phase flow experiments..... | 23 |
| Figure 2-11: Effect of single and multiple fractures on fluid flow at 0.3 PVI..... | 24 |
| Figure 2-12: PVI at breakthrough for different glass bead packs at $1\text{cm}^3 / \text{min}$ | 26 |
| Figure 2-13: PVI at breakthrough for different glass bead packs at $2\text{cm}^3 / \text{min}$ | 27 |
| Figure 2-14: Differential pressures vs. PVI for the glass bead packs in Fig. 2-12 (at $1\text{cm}^3 / \text{min}$)..... | 29 |
| Figure 2-15: Cumulative produced water vs. injected pore volume for all glass bead packs at $1\text{cm}^3 / \text{min}$ injection rate..... | 30 |

| | |
|--|----|
| Figure 2-16: Differential Pressures vs. Time for glass bead packs in Fig. 2-13 (at $2\text{cm}^3 / \text{min}$)..... | 31 |
| Figure 2-17: Cumulative produced water vs. injected pore volume for all glass bead packs at $2\text{cm}^3 / \text{min}$ injection rate..... | 32 |
| Figure 2-18: Simulator model, designed for the two phase flow study, representing matrix and fracture..... | 34 |
| Figure 2-19: Oil relative permeability for the glass bead models at $1\text{cm}^3 / \text{min}$ | 36 |
| Figure 2-20: Water relative permeability for glass bead models at $1\text{cm}^3 / \text{min}$ | 37 |
| Figure 2-21: Oil relative permeability for glass bead models at $2\text{cm}^3 / \text{min}$ | 38 |
| Figure 2-22: Water relative permeability for glass bead models at $2\text{cm}^3 / \text{min}$ | 39 |
| Figure 2-23: Matches between simulator and laboratory pressure differential results at $1\text{cm}^3 / \text{min}$ | 41 |
| Figure 2-24: Matches between simulator and laboratory production results at $1\text{cm}^3 / \text{min}$... | 42 |
| Figure 2-25: Matches between simulator and laboratory differential pressure results at $2\text{cm}^3 / \text{min}$ | 43 |
| Figure 2-26: Matches between simulator and laboratory production results at $2\text{cm}^3 / \text{min}$.. | 44 |
| Figure 2-27: Fluid flow profiles for homogeneous pack at 0.4PVI..... | 45 |
| Figure 2-28: Fluid flow profiles for 0° fracture system at 0.4PVI..... | 46 |
| Figure 2-29: Fluid flow profiles for 45° fracture system at 0.4PVI..... | 47 |

| | |
|---|----|
| Figure 2-30: Fluid flow profiles for 2 X-Intersecting fractures system..... | 48 |
| Figure 2-31: Fluid flow profiles for 2 Intersecting fracture system at 0.4PVI..... | 49 |
| Figure 2-32: Fluid flow profiles for 2 fractures at 0°, at 0.4PVI | 50 |
| Figure 2-33: Oil relative permeability: a comparison between laboratory and correlation results..... | 52 |
| Figure 3-1: REV in a rock mass (Chen et al. 1999)..... | 54 |
| Figure 3-2: Statistical representation of REV for (a) homogeneous and (b) heterogeneous rocks (Kunkel, Way et al. 1988)..... | 55 |
| Figure 3-3: Size of REV for different rocks (a) Non-Fractured rock (b) high density of fractures (c) low density of fractures (REV is large or non-existent) (Kunkel, Way et al. 1988); (Lee and Farmer 1993)..... | 56 |
| Figure 3-4: Conceptual model of fractured rock (Park and Sung 2000)..... | 57 |
| Figure: 3-5: Dual porosity model description of a naturally fractured reservoir (Warren and Root 1963)..... | 58 |
| Figure 3-6: Conceptual model of fractured rock (DFM) (Park and Sung 2000)..... | 60 |
| Figure 3-7: Discretization of grid block and different fractures present in it in two dimensions..... | 68 |
| Figure 3-8: Periodic boundary conditions over a grid block..... | 72 |
| Figure 3-9: Arbitrary point on domain, Ω | 74 |
| Figure 3-10: Boundary and interior discretization of the domain, Ω | 76 |
| Figure 3-11: Description of aspect ratio representing thickness of Poisson's region..... | 77 |

| | |
|---|-----|
| Figure 3-12: single fracture rotating inside a matrix block..... | 80 |
| Figure 3-13: Comparison of analytically and numerically calculated diagonal elements of permeability tensor..... | 81 |
| Figure 3-14: Comparison of analytically and numerically calculated off-diagonal elements of permeability tensor..... | 82 |
| Figure 3-15: Regularly spaced short fractures..... | 84 |
| Figure 3-16: Equivalent permeability for short fracture's system presented in Fig. 3-15 | 85 |
| Figure 3-17: Medium and long fractures system..... | 87 |
| Figure 3-18: Effective permeability Tensor for fractured system presented in Fig. 3-17 | 87 |
| Figure 3-19: Multiple fracture system with successive addition of a fracture one by one in each grid block..... | 89 |
| Figure 3-20: Elliptical representation of k-tensor for fracture system presented in Fig. 3-19 | 91 |
| Figure 3-21: Elliptical representation of grid based k-tensors for 2-D fracture network of Soultz reservoir..... | 93 |
| Figure 3-22: A general square element with regularly spaced nodes..... | 97 |
| Figure 3-23: four noded square element in local co-ordinates..... | 98 |
| Figure 3-24: Mapping onto the four noded quadrilateral..... | 99 |
| Figure 3-25: Decoupled fluid flow with constant wellbore pressure..... | 112 |

| | |
|---|-----|
| Figure 3-26: Numerical vs. analytical results for unit size region at time step of 10 and 60sec | 115 |
| Figure 3-27: Pore pressure distribution at time step of 10sec (Numerical result)..... | 116 |
| Figure 3-28: Velocity distribution at time step of 10sec (Numerical result)..... | 116 |
| Figure 3-29: Fracture network of a slice from Amadeus Basin..... | 119 |
| Figure 3-30: Permeability map of fracture network in Fig. 3-29 | 120 |
| Figure 3-31: Pressure profile of depletion case at steady state, for $P_{Res} = 4500\text{psi}$, $P_w = 3500\text{psi}$ | 121 |
| Figure 3-32: Velocity profile of depletion case at steady state for $P_{Res} = 4500\text{psi}$, $P_w = 3500\text{psi}$ | 122 |
| Figure 3-33: Pore pressure distribution for five spot pattern at pressure drop of 1000psi..... | 123 |
| Figure 3-34: Velocity profile for five spot pattern at pressure drop of 1000psi..... | 124 |
| Figure 3-35: Pressure losses vs. individual well production rates and total production rates..... | 125 |
| Figure 4-1: Boundary conditions for modelling two phase fluid flow..... | 129 |
| Figure 4-2: Discretization in the x direction..... | 130 |
| Figure 4-3: Differential pressures vs. PVI for the glass bead packs at $1\text{cm}^3 / \text{min}$ (Numerical results)..... | 133 |
| Figure 4-4: Cumulative produced water vs. injected pore volume for the glass bead packs at $1\text{cm}^3 / \text{min}$ injection rate (Numerical results)..... | 134 |

| | |
|--|-----|
| Figure 4-5: Comparison between numerical and experimentally obtained pressure differences for fractured systems at $1\text{cm}^3 / \text{min}$ injection rate..... | 135 |
| Figure 4-6: Comparison between numerical and experimentally obtained cumulative water productions for fractured systems at $1\text{cm}^3 / \text{min}$ injection rate..... | 136 |
| Figure 4-7: Fluid flow profiles for homogeneous system at 0.4PVI..... | 140 |
| Figure 4-8: Fluid flow profiles for 0° fracture system at 0.4PVI..... | 141 |
| Figure 4-9: Fluid flow profiles for 45° fracture system at 0.4PVI..... | 142 |
| Figure 4-10: Fluid flow profiles for 2 X-Intersecting fractures system at 0.4PVI..... | 143 |
| Figure 4-11: Fluid flow profiles for 2 Intersecting fractures system at 0.4PVI..... | 144 |
| Figure 4-12: Fluid flow profiles for system of 2 fractures at 0° at 0.4PVI..... | 145 |
| Figure 5-1: Fracture network used to upscale from laboratory scale..... | 146 |
| Figure 5-2: Grid blocks of $10\text{m}\times 10\text{m}$ size nominated in step 2 from Figure 5-1 | 150 |
| Figure 5-3: Pressure difference across injector and producer for a homogeneous block of size $10\text{m}\times 10\text{m}$ | 156 |
| Figure 5-4: Pore volumes of water produced vs. injected pore volumes of oil for a homogeneous block of size $10\text{m}\times 10\text{m}$ | 156 |
| Figure 5-5: Comparison of pressure difference across injector and producer between single fracture system (fracture oriented at 59°) and upscaled case ($10\text{m}\times 10\text{m}$)..... | 157 |
| Figure 5-6: Comparison for pore volume (PV) of water produced between original single fracture (oriented at 59°) and upscaled case ($10\text{m}\times 10\text{m}$)..... | 157 |

| | |
|---|-----|
| Figure 5-7: Comparison of pressure difference across injector and producer between original single fracture (oriented at 19°) and upscaled case (10m×10m)..... | 158 |
| Figure 5-8: Comparison for pore volume (PV) of water produced between original single fracture (oriented at 19°) and upscaled case (10m×10m)..... | 158 |
| Figure 5-9: Comparison of pressure difference (across injector and producer) between original multi fracture system (one fracture oriented at 30° and other at 32°) and upscaled case (10m×10m)..... | 159 |
| Figure 5-10: Comparison for pore volume (PV) of water produced for multi fracture system (one fracture oriented at 30° and other at 32°) and upscaled case (10m×10m)..... | 159 |
| Figure 5-11: Comparison of pressure difference (across injector and producer) between original multi fracture system (one fracture oriented at 19° and other fracture at 64°) and upscaled case (10m×10m)..... | 160 |
| Figure 5-12: Comparison of pore volume of water produced for original multi fracture system (one fracture oriented at 19° and other fracture at 64°) and upscaled case (10m×10m)..... | 160 |
| Figure 5-13: Comparison of pressure difference (across injector and producer) between original multi fracture system (one fracture oriented at 20° and other fracture at 64°) and upscaled case (10m×10m)..... | 161 |
| Figure 5-14: Comparison of pore volume of water produced for original multi fracture system (one fracture oriented at 20° and other fracture at 64°) and upscaled case (10m×10m)..... | 161 |

| | |
|---|-----|
| Figure 5-15: Comparison of pressure difference across (injector and producer) for original multi fracture reservoir and up-scaled case (1000m×1000m)..... | 162 |
| Figure 5-16: Comparison of pore volume (PV) of water produced for original multi fracture reservoir and up-scaled case (1000m×1000m)..... | 162 |
| Figure 5-17: Up-scaled relative permeability relationship for homogeneous block of size 10m×10m..... | 163 |
| Figure 5-18: Up-scaled relative permeability relationship for single fracture system (oriented at 59°) in a block of size 10m×10m..... | 163 |
| Figure 5-19: Up-scaled relative permeability relationship for single fracture system (oriented at 19° to the direction of flow) in a block of size 10m×10m..... | 164 |
| Figure 5-20: Up-scaled relative permeability relationship for multi fracture system (oriented at 30° and 32°) in a block of size 10m×10m..... | 164 |
| Figure 5-21: Up-scaled relative permeability relationship for multi fracture system (oriented at 64° and 19° non intersecting fracture system) in a block of size 10m×10m..... | 165 |
| Figure 5-22: Up-scaled relative permeability relationship for multi fracture system (oriented at 20° and 64° intersecting fracture system) in a block of size 10m×10m..... | 165 |
| Figure 5-23: Up-scaled relative permeability relationship for multi fracture system (whole reservoir) in a block of size 1000m×1000m..... | 166 |

Chapter 1

Introduction

The fluid flow mechanisms through naturally fractured reservoirs are not well understood. This is mainly because fluid flow process in such reservoirs includes complicated mass transfer between two different media. In addition arbitrary orientations of natural fractures with variable lengths and sizes inside the matrix make it computationally difficult to simulate the flow through fractured media.

The study of flow and transport processes in fractured rock has recently received increased attention because of its importance to underground natural-resource recovery, waste storage, and environmental remediation. Since the 1960s, significant progress has been made towards the understanding and modelling of flow and transport processes in fractured rock (Barenblatt et al. (1960); Warren and Root (1963); Kazemi (1969); Pruess and Narasimhan (1985)). Despite these advances, modelling the coupled processes of multiphase fluid flow, heat transfer, and migration of chemical species in a fractured porous medium remains a conceptual and mathematical challenge. The difficulty stems primarily from (1) the nature of inherent heterogeneity, (2) the uncertainties associated with the characterization of a fracture-matrix system for any field-scale problem, and (3) the difficulties in conceptualizing, understanding, and describing flow and transport processes in such a system. Currently, the approaches to model fluid flow through naturally fractured reservoirs include dual porosity/permeability, discrete fracture approach and hybrid scheme.

In dual porosity/permeability approach, matrix and fractures are considered as two interacting continua where matrix and fracture are two parallel layers with infinite length. Mathematical modelling describing dual porosity/permeability approach involves developing conceptual

models, incorporating the geometrical information of a given fracture-matrix system, and setting up the general mass and energy conservation equations for overlapping fracture matrix domains. The majority of the computational effort is used to solve the governing equations that couple fluid and heat flow either analytically or numerically. The key issue for simulating flow and transport in fractured rock is how fracture and matrix interact under different reservoir conditions. The commonly used mathematical methods for dealing with such interactions include: (1) an explicit discrete-fracture and matrix model (e.g., Snow (1969); Sudicky and McLaren (1992)), (2) the dual-continuum method [including double- and multi-porosity, dual-permeability, or the more general "multiple interacting continua" (MINC) method (e.g., Barenblatt et al. (1960); Warren and Root (1963); Kazemi (1969); Pruess and Narasimhan (Pruess 1985); Wu and Pruess (1988))], and (3) the effective-continuum method (ECM) (e.g., Wu (Wu 2000)). The main drawback with this approach is that it assumes a very simplified geometrical representation of matrix and fracture.

In discrete fracture approach each fracture and matrix is discretized by a mesh system. Equations of fluid flow through matrix and fractures were solved by both exact and approximate methods, e.g. boundary element (Lough et al. (1998)), finite element (Kazemi et al. (1976)), finite volume methods (Niessner(2005)) and mixed finite element method (Hoteit and Firoozabadi 2008). These discrete models require extremely high computational time which limited its application to small blocks within a domain with few fractures. In order to overcome the computational problem associated with discrete fracture approach, hybrid schemes have been developed. In this method a grid based effective permeability tensor concept was developed (Lough et al. (1998), Castaing et al. (2002), Park and Sung (2000), Gupta et al. (2001), Detournay (2004)). Each grid block with fractures is replaced by a homogeneous grid block with an equivalent permeability tensor. Gupta et al. (2001), Castaing(2002) and Detournay(2004) have considered the fluid flow through fractures while

ignoring the contribution of matrix to flow. Lough et al. (1998) and Park and Sung (2000) on the other hand considered flow through both matrix and fracture, however, the authors ignored fluid flow interaction between matrix and fracture. Teimoori et al. [(2003); (2005)] presented a comprehensive grid based effective permeability tensor method in which authors accounted for the fluid flow through matrix, through fracture and matrix-fracture interface. In this study small to large fractures with their individual properties are taken into account. Boundary element technique was used to formulate the integral equations for fluid flow in which quadrature based formula was used to solve the integral equations. This approximation has made the solution unstable for medium to high density fracture system.

Most of previous work to simulate fluid flow in naturally fractured reservoirs is limited to the fluid flow through interconnected fracture networks and the matrix contribution to the flow is ignored. Due to the geometrical complexities associated with the nature of fractured porous media, it is always required to develop a computationally efficient numerical model for flow simulations. Moreover, literature review shows that numerical models are being validated against analytical solutions and an authentic laboratory validation for fluid flow simulation models is still needed.

In an effort to improve the understanding of simulation of fluid flow in naturally fractured reservoirs, this thesis aims to develop an efficient grid-based effective permeability tensor model for fractured reservoirs by using the most recent hybrid schemes while taking into account the actual geometry of fracture networks. To check the reliability of the numerical model, experimentally measured permeability of synthetic fractured networks is used. Next, to evaluate the production potential of a naturally fractured reservoir, the thesis presents a numerical model that can efficiently simulate the pressures and velocities using the grid-based permeability tensor of the fractured reservoirs.

Next, the thesis extends the single-phase simulation to two-phase fluid flow. For this purpose, an innovative laboratory model is designed and constructed. Drainage displacement tests (oil displacing water) allow us to derive the relative phase permeabilities for different synthetic fractured media. Then this oil-water flood is numerically simulated and the results are compared with the aim to assess the capability of the proposed numerical tool.

Furthermore, a new methodology is proposed to upscale two-phase relative permeability of fractured systems from the laboratory (10cm×20cm) to the reservoir scale (1000m×1000m). A commercial black-oil numerical reservoir simulator (CMG IMEX) is used to history match the grid blocks from the lab scale to the reservoir scale. Procedure for upscaling is described and applied to a multi-fracture basement reservoir to show the application of laboratory-derived relative permeabilities for different fracture systems.

This thesis is presented in five chapters according to the objective of the study. To achieve the aims of the study and present it clearly the objective is divided into two major parts; experimental and numerical studies.

In chapter two, experimental determination of permeability for fractured porous media is presented. This chapter contains a detailed literature survey, used experimental setups and adopted experimental procedures for conducting single and two phase fluid flow experiments. Results for single and two phase flow experiments are presented and discussion has been associated in this chapter.

In chapter three, first, theoretical background and mathematical formulation for the calculation of effective permeability tensor model is presented. It contains the process of deriving boundary integral equations and provides details about discretising the problem using boundary element method. Results of the effective permeability tensor model are compared against the analytical solution as well as experimental results. Different numerical experiments

are presented to show the application of the model. Next, permeability tensors are incorporated in fluid flow model to estimate pressure and velocity profile throughout the reservoirs as well as estimation of well productivity.

In chapter four, a numerical model for multiphase (two-phase) fluid flow in a laboratory scale ($10\text{cm}\times 20\text{cm}$) reservoir with single and multiple fractures (both intersected and non-intersected) is formulated. The numerical results are compared against two phase flow laboratory results for validation.

In chapter five, a new methodology to up-scale two phase relative permeability for fractured systems from laboratory scale ($10\text{cm}\times 20\text{cm}$) to reservoir scale ($1000\text{m}\times 1000\text{m}$) is presented. The upscaling procedure is well described and then applied to a multi-fracture $1000\text{m}\times 1000\text{m}$ region of the Amadeus reservoir. History matching results are presented for each step of upscaling and are discussed in detail.

In chapter six, conclusion is drawn for the findings of this study. Also this chapter offers future recommendations in the area of the study.

Chapter 2

Laboratory Determination of Absolute and Relative Permeability of Fractured Porous Media

In this chapter, single and two phase flow visualisation experiments are presented. The objective of visualization study is to understand the flow interaction between matrix and fracture. The motivation behind this work is to investigate the effect of permeability heterogeneity on fluid flow. Numerical models have been commonly used as a tool to estimate permeability of naturally fractured reservoirs. The results of these models are usually compared against analytical solutions and need for an authentic laboratory data for validation purpose is required. One of the objectives of this study is to provide a laboratory validation of numerical models to estimate permeability of fractured porous media.

Another aim of this study is to investigate the interaction of more than one fluid phase on each other in the presence of natural fractures. In fact the effect of natural fractures on immiscible flow has been examined which provided an insight to understand heterogeneity effect on fluid relative phase permeabilities.

To achieve these objectives an innovative laboratory model is designed and built. Experimental set up and procedures for single and two phase flow are discussed throughout in this chapter. Absolute permeabilities have been measured for homogeneous and heterogeneous systems using single phase displacement experiments. Pressure and production data is obtained for two phase flow experiments and this data is tried to be matched using history matching technique. Laboratory based glass bead systems used for two phase flow are constructed using simulator CMG to obtain final relative permeability curves. A review of previous works about fluid flow behaviour in fractured porous media is presented next in this

chapter. Experimental results containing pressure and production profiles and relative permeability curves at two different constant flow rates are further discussed in this chapter.

2.1 Literature Review

Many laboratory based works have been done in the past on heterogeneous reservoirs. Dawe and Grattoni (2008) investigated the effect of heterogeneity on miscible and immiscible fluid flow displacements through 2D glass bead pack. A 2×2 quadrant block geometry was designed and built to observe the effect of permeability as well as wettability heterogeneity. Boundary effects were observed for immiscible flow which was caused by capillary pressure differences created by water saturation changes or wettability contrasts. However, as the resulting flow behaviour has not been much discussed in literature, it was concluded that experimental results can be used as a benchmark to test up-scaling methods as well as verification of simulation models for two phase flow.

Li and Horne (2009) proposed a fractal technique to characterize the capillary pressure curve for Gaysers rock and concluded that values of fractal dimensions can be used to represent the heterogeneity of different rock samples quantitatively. Unlike the Berea sandstone, the capillary pressure curves of The Gaysers rock could not be represented using the frequently used Brooks and Corey model because of the presence of fractures (Li and Horne 2009).

An experimental study of single and two phase flow through fractured granite specimen was performed by Ranjith (2010). Triaxial tests were conducted to find out the flow behaviour within rock fractures; e.g. laminar, turbulent. It was concluded that single and two phase flow through fractures can be characterized as laminar flow provided that the moderate inlet fluid pressures are applied. However an increase in inlet air pressures may cause a turbulent flow for single phase air flows (Ranjith 2010).

Relative permeability is a function of several key parameters that includes; pore scale geometry including porosity and permeability, pore distribution e.g. pore scale heterogeneity, rock fluid interaction e.g. capillarity and wettability, initial fluid saturation distribution and fluid velocity (Goda and Behrenbruch 2004). A new Brooks-Corey type approach was introduced by Goda and Behrenbruch (2004) to study relative permeability data for different rock types for Australian fields with a focus on geology of reservoirs. A number of fields and laboratory data were analysed and new and alternative formulation was applied and compared against Modified Corey Model. It was concluded that the new formulation matches the oil experimental results better than the MBC model results.

Kewen Li (2010) coupled three fluid saturation functions; resistivity index, capillary pressure and relative permeability, and concluded that these functions can be inferred from each other if one of these parameters is known. Abtahi and Torsaeter (1998) presented visual two dimensional model experiments for homogeneous and heterogeneous porous media. The objective was to investigate up-scaling of laboratory relative permeability and capillary pressure curves to a typical reservoir grid block. A three step up-scaling process was introduced to capture the effect of small scale heterogeneity to medium scale and finally to the large grid and results were compared against laboratory results.

A balance between capillary, viscous, and gravitational forces during CO_2 injection into saline aquifers was investigated by Polak et al (2011). Quasi two dimensional glass bead pack experiments were performed to demonstrate the effect of mentioned three forces on the vertical flow of CO_2 . It was concluded that gravitational forces are dominant for the case of low injection rate and high permeability causing less brine displacements. On the other hand higher injection rate caused more fingering but increased total brine displacement.

Relative permeability measurements for two phase flow for unconsolidated sands were carried out by S. Abaci et al. (1992) using steady state technique. The objective of this work was to generate two phase flow data for combination of liquids and gasses that could be used for numerical modelling studies. Effects of rock heterogeneities on the flow functions are demonstrated by one and two dimensional experimental study by Sylte et al. (1998). It was discussed how inaccurate modelling of heterogeneities can cause large errors in estimation of two phase flow functions even for moderate heterogeneity.

A three dimensional , numerical simulator for single and two phase oil and water simulation is presented by Kazemi et al. (1976). The simulator accounts for fluid relative mobilities, gravity effects and imbibition. Also uniformly and non-uniformly distributed fractures can be handled by the simulator. The interaction of two immiscible fluids within a deforming porous medium are studied and modelled by Zienkiewics (1990). Finite element method is used to discretise the governing equations to solve for rock displacement, pressures and wetting phase saturations throughout the reservoir. Linear problems are illustrated in this work and authors recommend further research for highly non linear problems. Maier et al (1998) used lattice Boltzmann method to simulate viscous fluid flow through a column of glass beads. Simulated flow in bead packs are compared against experimental flow.

The main conventional methods to simulate two phase fluid flow through fractured networks are finite difference (FD) method, finite element (FE) method and finite volume (FV) method. All the conventional methods have their inherent limitations such as FD method is restricted to only horizontal and vertical fractures. FE method can not capture the saturation discontinuity at matrix-fracture interface whereas accuracy of FV method depends on size of matrix grids next to fracture, for an acceptable accuracy the matrix grid size next to fracture should be small. Hotiet and Firrozabadi (2008) presented an efficient numerical model for incompressible two phase flow in fractured porous media. An additional feature of this work

is the use of mixed finite element (MFE) method to calculate matrix-fracture and fracture-fracture fluxes. On the other hand, discontinuous Galerkin (DG) method is used to approximate the saturation equations. It was concluded that capillary pressure reduces water velocity in the fracture and therefore improves recovery (Hoteit and Firoozabadi 2008).

A fracture only model is introduced by Unsal et al. (2010) for simulation of multiphase flow through fractured porous media where fracture geometry is modelled explicitly, and fluid movement between matrix and fracture is modelled using empirical transfer functions. This hybrid scheme could capture the advantages of dual porosity as well as discrete fracture/discrete matrix (DFDM) approach. Shad and Gates (2010) derived an analytical theory to obtain relative permeability curves for multiphase flow in fractures. The results of their study showed that change in fluid saturations due to gravity effects can change a co current flow to a counter current one.

2.2 Single Phase Flow Visualization Experiments

2.2.1 Experimental Set-up

A quasi 2-D glass bead model of size $21 \times 21 \text{ cm}^2$ was designed and built for flooding experiments (**Fig. 2-1**). Glass beads were sandwiched between two glass plates which were glued together with a gap of 0.2 cm . A homogeneous model was prepared using glass beads of only one range of bead sizes while the heterogeneous model comprising of fractures and matrix was built using glass beads of two different ranges of bead sizes. The range of larger bead sizes represented the fracture whereas the small sizes range the matrix as shown in **Fig. 2-1**.

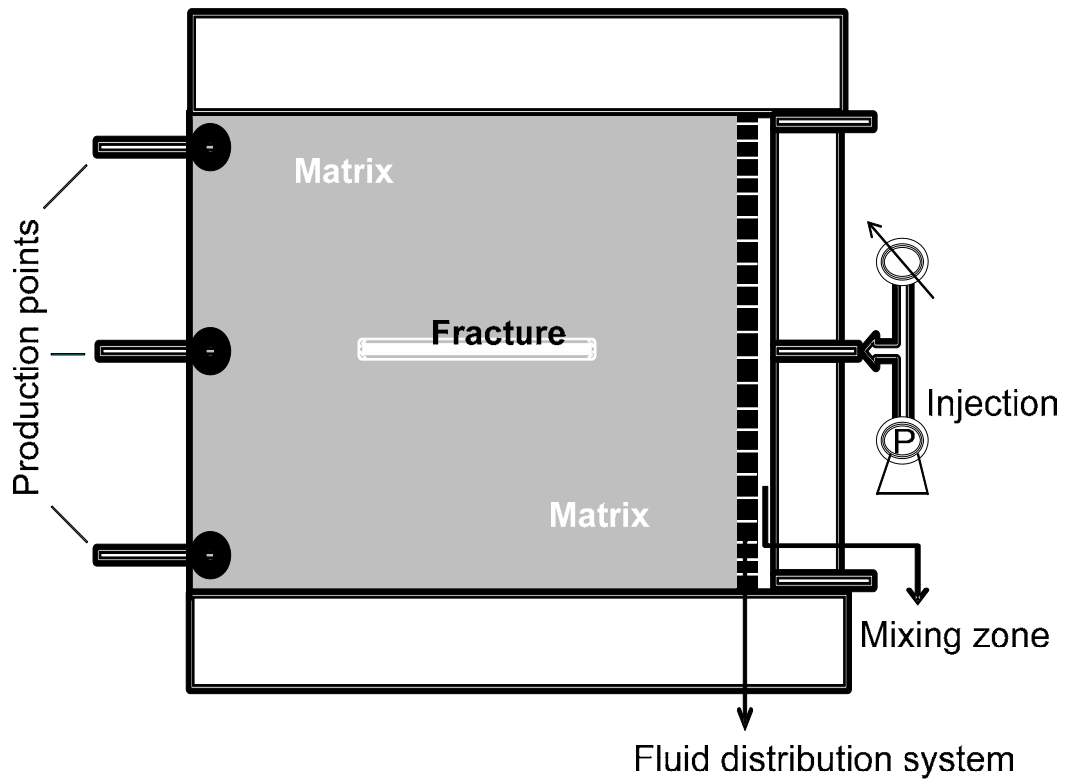


Figure 2-1: Schematic of glass bead model used for single phase flow experiments

The range of mesh size used as matrix glass beads is $-100+140$ while $-30+40$ for fractures, which represent bead sizes of $105-149\mu m$ and $420-590\mu m$ for matrix and fractures, respectively. The model was designed in an efficient way that allowed us to not only to perform experiments with one realisation of fractured system but after that it could be unscrewed, cleaned, dried and made it ready for another experiment with a different realisation of the fractured system. A high accuracy piston pump was used to obtain various constant injection rates and the effluent was collected at the outlet by means of a tubing connected to the production points. A digital camera was used to take pictures of the fluid displacement process during the experiments. A fluorescent light source was placed underneath the model to enhance the picture quality.

2.2.2 Experimental Procedure

A schematic representation of the experimental setup is shown in **Fig. 2-2**. Firstly, the air in the glass bead model was displaced with carbon dioxide to avoid any air entrapment in the pore space. Then distilled water was injected into the model from bottom in a vertical position. The weights of the dry and wet model were taken and the difference in weight was used to estimate the pore volume using density of water at ambient conditions. It should be noted that the dead volume of water (water present in the mixing zone and tubings see **Fig. 2-1**) was subtracted from the obtained volume to calculate original pore volume. Then porosity was calculated using the bulk volume of the model. The pressure drop was recorded for each constant flow rate which ranged from 1 cm³/min to 8 cm³/min with an interval of 1 cm³/min.

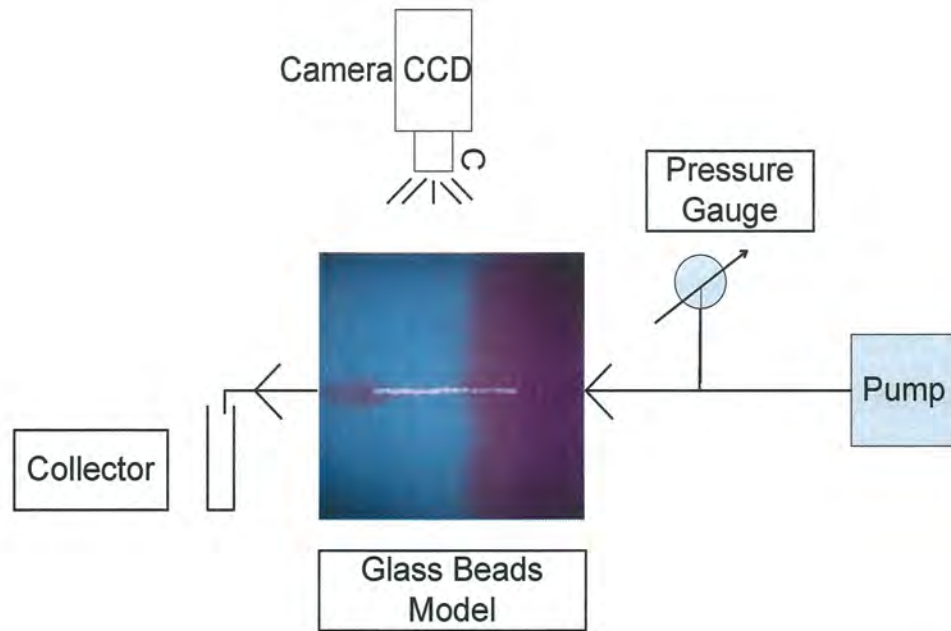


Figure 2-2: Schematic of the experimental setup (Single Phase Flow)

The permeability of the glass bead model was calculated using the Darcy's law by plotting

$\frac{Q}{A}$ (m/sec) against $\frac{\Delta P}{L}$ (Pa/m). Here, Q is the constant flow rate (m³/sec), A is the cross

sectional area (m^2), and ΔP (Pa) is pressure differential applied across the length L (m) of the model. The slope of the plot gives $\frac{k}{\mu}$ (m^2 /Pa-sec) which is multiplied by the viscosity of water μ (Pa-sec) to obtain k (m^2), here k is the permeability. The same procedure was adapted to measure the porosity and permeability of the single and multiple fracture systems with different fracture orientations.

The base case, the homogeneous model was prepared using small range of bead sizes ($105-149\mu m$). The base case has the permeability (matrix permeability) of 3.4D. For the heterogeneous systems, the same size of glass beads was used for the matrix. The fracture permeability was calculated using the Kozeny Carmen Correlation (Carman 1937):

$$k = \frac{D_p^2}{180} \frac{\phi^3}{1-\phi^2} \quad (2-1)$$

where D_p is the diameter of glass beads (meters), ϕ is the porosity of the system (%) for the base model. The calculated permeability (k) is in (m^2). The calculated fracture permeability was $1.058 \times 10^{-10} m^2$ (100 Darcy).

2.2.3 Results and Discussion

For the single fracture model, displacement tests were carried out for three different fracture orientations: 0° , 45° and 90° from the direction of flow. The matrix permeability of the single fracture glass bead model could be achieved as low as 3.37D. The length and aperture of the fracture were set at constant values of 10.5cm and 0.4cm, respectively. In each case, the injection rate was varied from $1cm^3/min$ to $8cm^3/min$. Pressure drops were measured across the length of matrix-fracture system for eight constant flow rates with a stepwise increase of $1cm^3/min$.

Figure 2-3 presents a relation between changes in velocity and pressure gradient for four different systems. Slope of each line leads to the calculation of the permeability using the viscosity of the injected fluid (water) at ambient temperature (0.001 Pa-sec). Results of the calculated permeability for single fracture models are presented in **Table 2-1**. An error of 0.021D was found in permeability measurements. This error was calculated using a general function for error propagation as given below.

$$\delta k = \sqrt{\left(\frac{\partial k}{\partial q} \times \delta q\right)^2 + \left(\frac{\partial k}{\partial \mu} \times \delta \mu\right)^2 + \left(\frac{\partial k}{\partial X} \times \delta X\right)^2 + \left(\frac{\partial k}{\partial A} \times \delta A\right)^2 + \left(\frac{\partial k}{\partial P} \times \delta P\right)^2} \quad 2-2$$

where δ represents error, k is the permeability, q and μ are flow rate and viscosity of the fluid, X is distance between injection and production points, A is cross sectional area of injection and P is the pressure.

The results show that, for a fracture oriented at 90° with respect to the direction of flow, the increase in permeability is negligible 0.05D (only 1.5% greater than the homogeneous model). The percent increase in permeability is calculated using formula given below:

$$\% \text{ increase in } k_{\text{fractured model}} = \frac{(k_{\text{fractured model}} - k_{\text{homogeneous model}})}{k_{\text{homogeneous model}}} \times 100 \quad 2-3$$

A further small increase of 0.21D in permeability can be seen for a fracture oriented at 45° (by 6.2%). When the fracture is oriented at 0° (along the direction of fluid flow) permeability increases considerably by an amount of 0.38D (11.3%). Increase in permeability due to decrease in fracture orientation is plotted in **Fig. 2-4**. A negligible increase in permeability for fracture orientation of 90° is because the fracture contributes hardly any fluid through its aperture (0.4cm) which is 1.9% of the total block length (21cm). An increase in permeability for the cases of 45° and 0° fracture orientations is primarily due to the fact that the fracture

length (full length for 0° orientation and $\sin 45^\circ \times$ fracture length for 45°) takes part in conducting more fluid flow.

Table 2-1. Permeability of the heterogeneous systems with respect to the fracture orientation

| Angle of Fracture | k (D) | Porosity (%) |
|-------------------|------------------|--------------|
| 90° | 3.42 ± 0.021 | 40.0 |
| 45° | 3.58 ± 0.021 | 39.9 |
| 0° | 3.75 ± 0.021 | 40.5 |

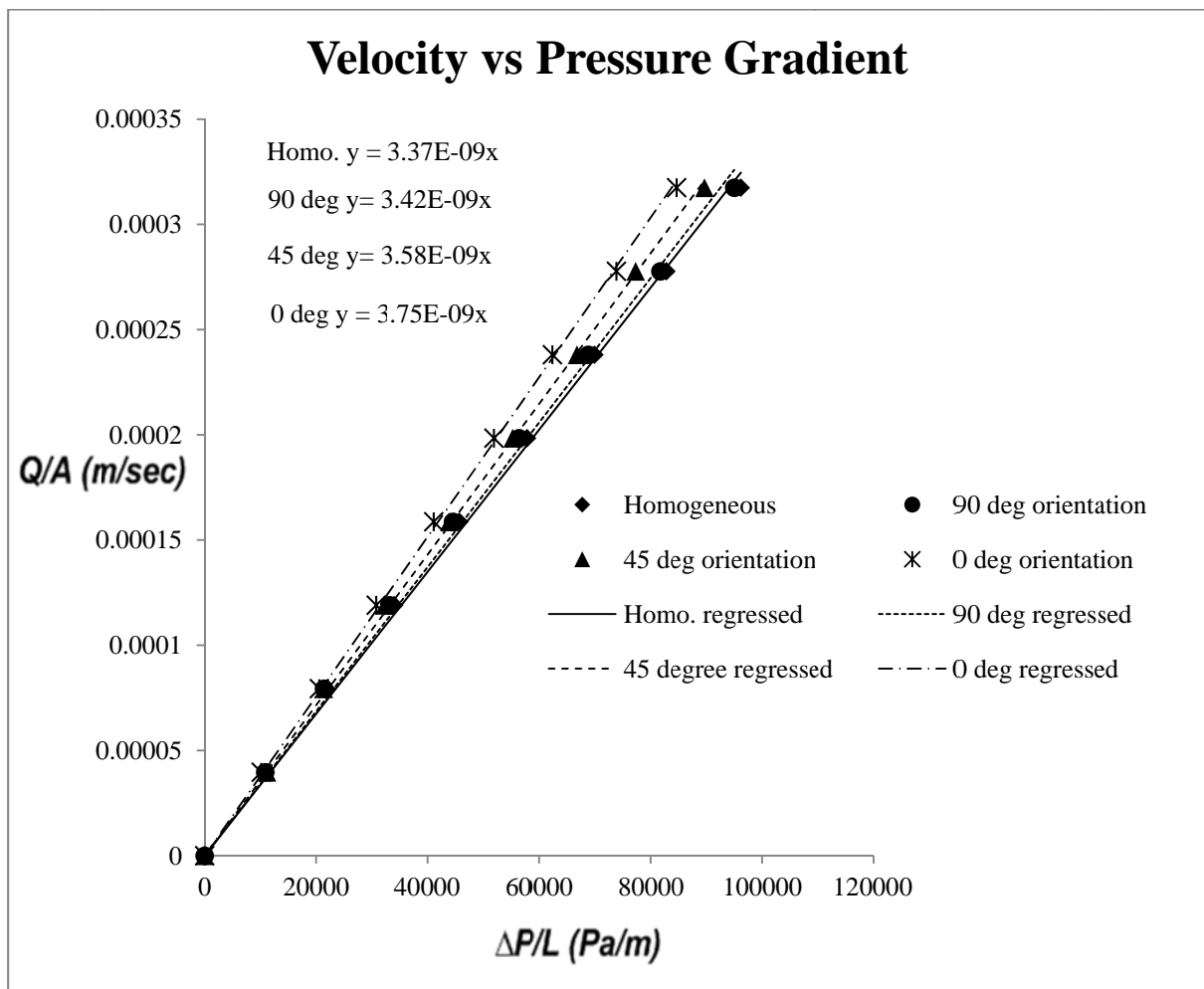


Figure2-3: Velocity vs. pressure gradient for the single fracture models

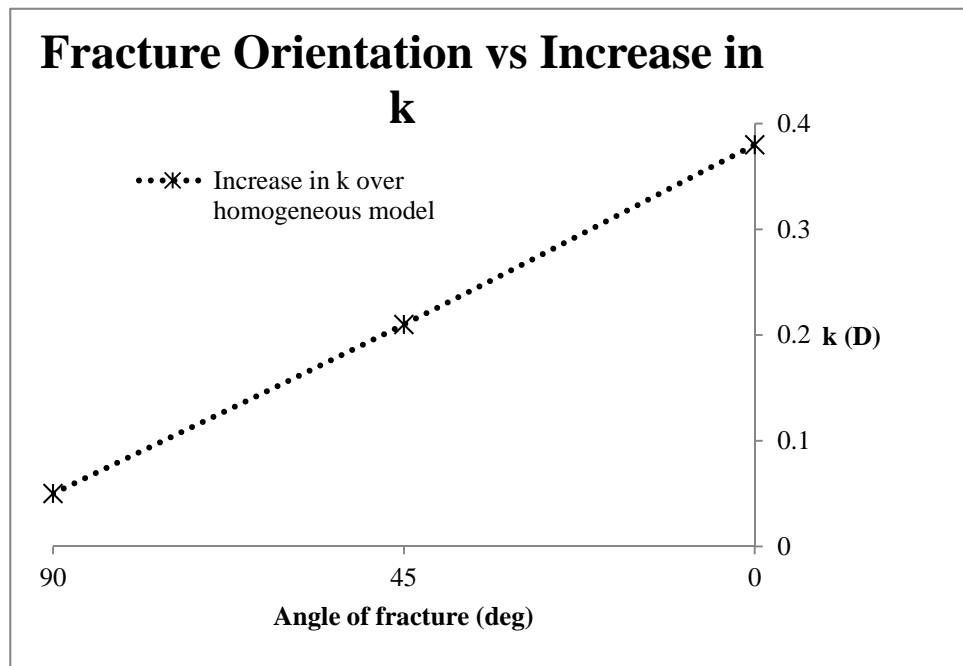


Figure 2-4: Effect of fracture orientation on permeability

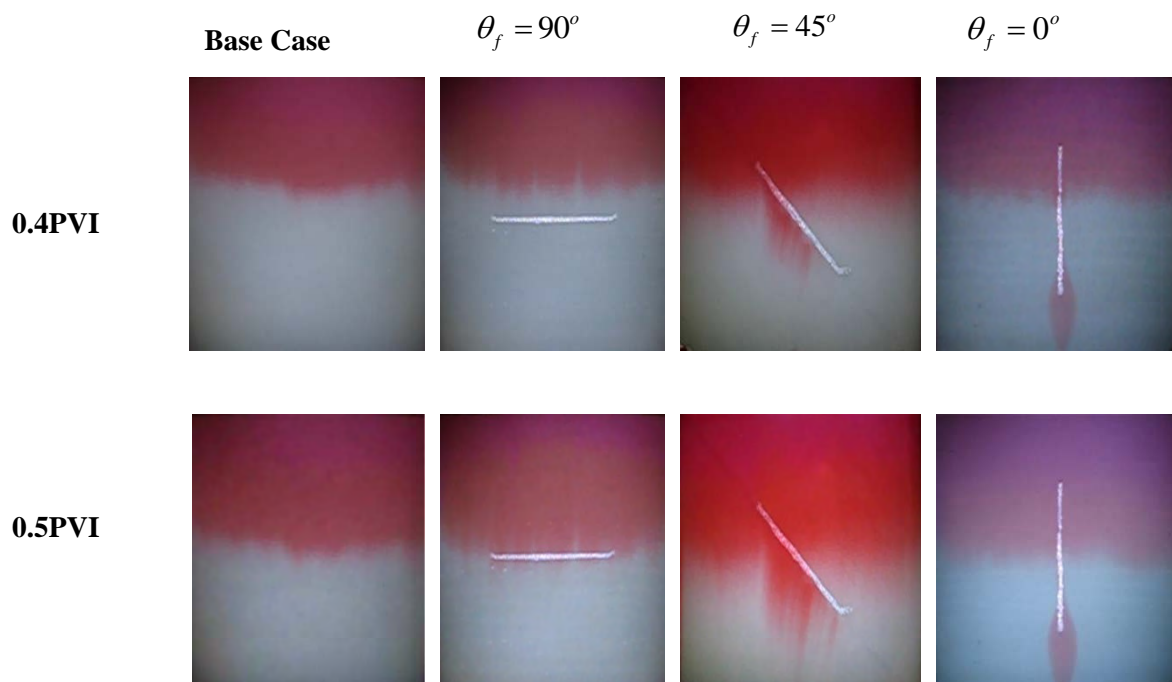


Figure 2-5: Effect of the fracture orientation on fluid flow with respect to pore volume injected “PVI” (single fracture models)

This finding conforms with the camera images taken during the injection of dyed water (see **Fig. 2-5**). The figure shows that the injected dyed water breaks through the fracture, which is oriented at 0° to the flow direction, much quicker than the other two orientations. It is evident from **Fig. 2-5** that for miscible flooding by passing of the injection fluid increases with decrease in orientation of fracture with respect to the flow direction.

Three glass bead models each containing set of two fractures were designed and made. In the first model, fractures were placed parallel to each other and along the flow direction ($\theta = 0^\circ$). In the second model, one fracture was placed along the flow direction and second fracture intersecting the first one at 45° to the direction of fluid flow. Finally in the third model two fractures were placed parallel to each other but oriented at 45° . Similar to the single fracture model displacement tests were carried out and flow patterns were captured as images.

Table 2-2. Permeability of the heterogeneous systems, each containing set of two fractures

| Heterogeneous systems (set of two fractures) | k(D) | Porosity (%) |
|---|------------------|--------------|
| 2 fractures oriented at 45° | 3.78 ± 0.021 | 40.3 |
| 2 intersecting fractures | 3.98 ± 0.021 | 40.0 |
| 2 fractures oriented at 0° | 4.21 ± 0.021 | 40.0 |

Changes in the flow velocity with respect to the pressure gradient for each system are presented in **Fig. 2-6**. In **Table 2-2**, measured permeabilities and porosities for all multiple fracture models are presented. It can be observed that the parallel fracture model with 0° orientation gives the maximum increase in permeability 0.84D (25% increase over the

homogeneous model) while the parallel fracture model with 45° orientation gives the minimum increase of 0.41D (12.2% increase over the homogeneous model) and the intersected fracture model gives the median increase of 0.61D in permeability (18.1% increase over the homogeneous model). Images of the displacement through the three different models shown in **Fig. 2-7** conform the pressure vs. velocity plots presented in **Fig. 2-6**. It is evident from **Fig. 2-7** that lower the effective orientation of multiple fracture models, higher the fluid by passing.

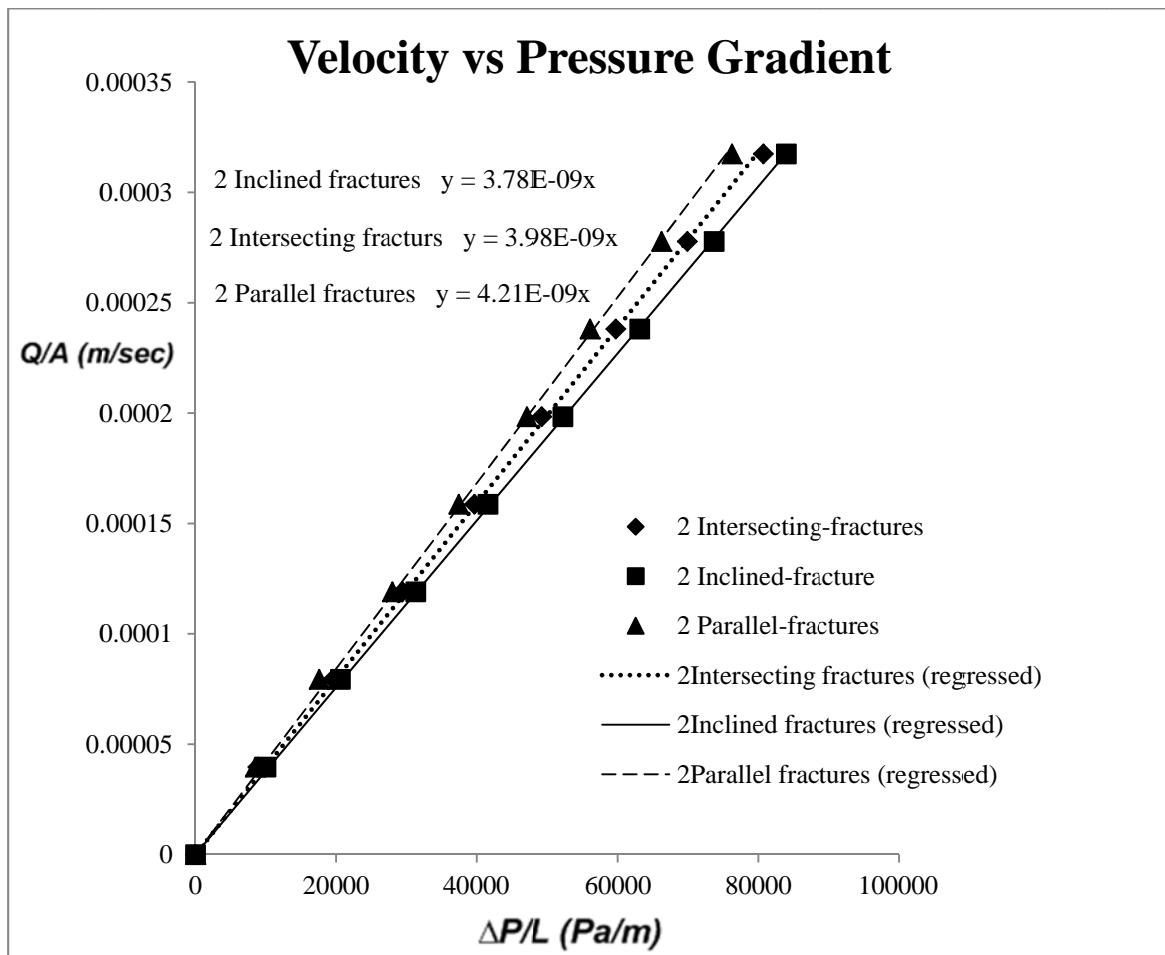


Figure 2-6: Velocity vs. pressure gradient for multiple fracture models

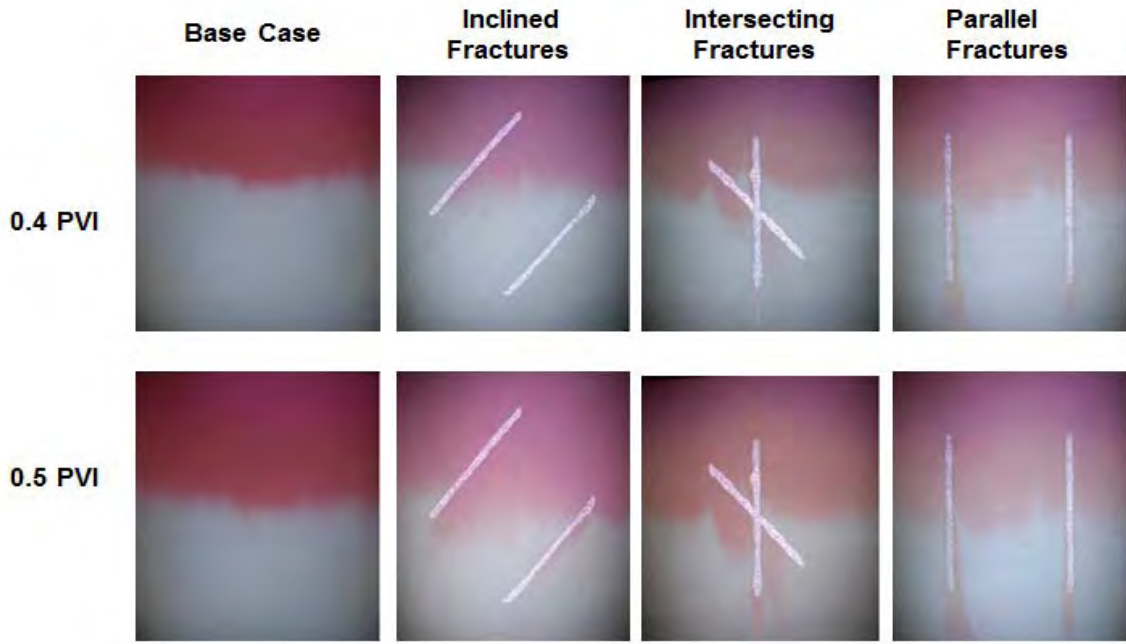


Figure 2-7: Effect of different set of fractures on fluid flow with respect to pore volume injected “PVI” (Multiple fracture models)

2.3 Two Phase Flow Visualisation Experiments

2.3.1 Experimental Setup

A two dimensional glass model of size $12 \times 24 \text{ cm}^2$ was designed and built to observe the two-phase flow behaviour through fractured porous media (see **Fig. 2-8**). It was decided to change the model size for immiscible flow tests to improve displacement. By decreasing the injection cross sectional area capillary effects were minimised and hence oil fingering was controlled. Matrix was represented by glass beads of mesh -100+140 (bead size $105\text{-}149 \mu\text{m}$) whereas the fracture was replaced by an especially designed glass strip of 3mm width which has a groove of 1mm aperture throughout at its centre. The grooved glass strip is used as fracture instead of glass beads to obtain a better matrix to fracture permeability ratio. The strip had cross

grooves of same aperture to allow cross flow between the matrix and fracture. A piston pump was used to obtain various constant injection rates and the effluent was collected at the outlet by means of tubing connected to the production point. A digital camera was used to take pictures of the displacement process during the experiments. A fluorescent light source was placed underneath the model to enhance the picture quality.

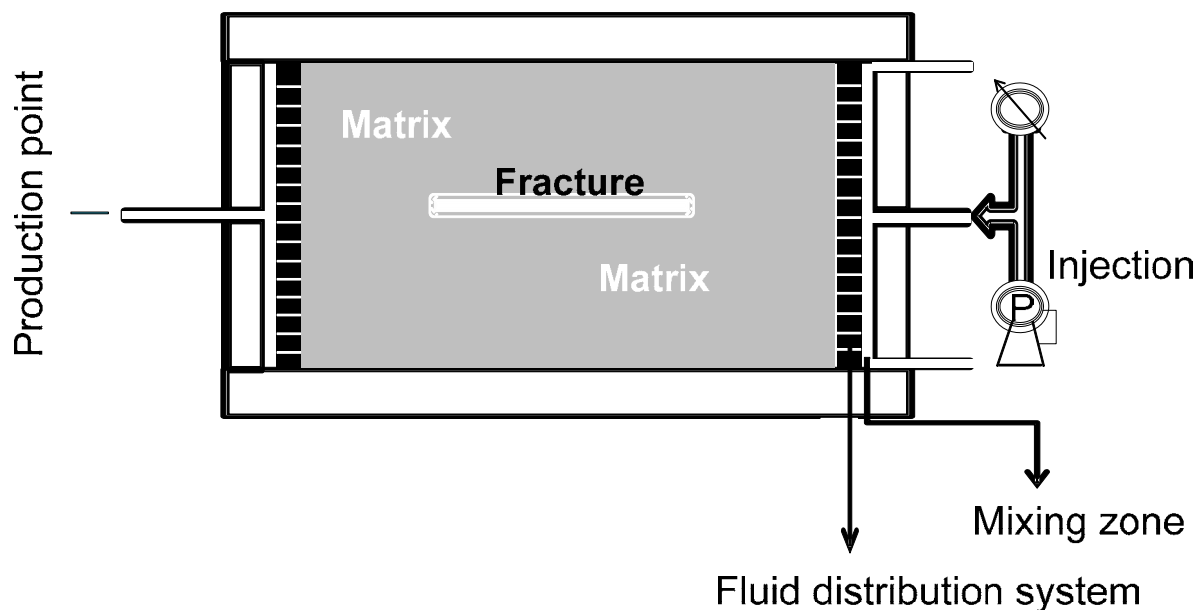


Figure 2-8: The glass bead model used for two phase flow experiments

2.3.2 Experimental Procedure

A schematic of experimental setup used for two phase flow is presented in **Fig. 2-9**. Similar to the single phase experiments, in two phase flow experiments carbon dioxide was injected in the bead pack to displace air, and then the model was saturated with de-aired water by

displacing carbon dioxide while model was kept in the vertical position. Porosity of the system was calculated using pore and bulk volumes of the beads pack in a similar way as mentioned in the experimental procedure of single phase flow.

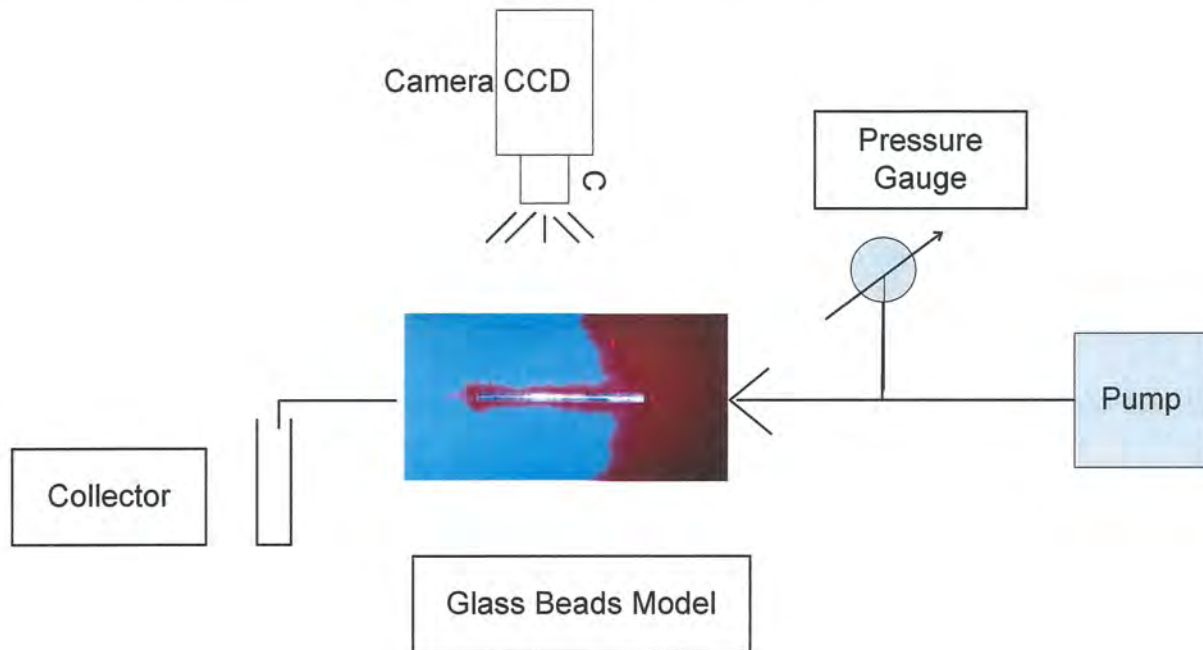


Figure 2-9: Schematic of the experimental setup (Two Phase Flow)

A drainage test was conducted for a homogeneous bead pack of mesh (-100+140) where oil was injected into the water saturated glass bead pack. Soltrol-130 oil (non-wetting phase) was used to displace water (wetting phase). The physical properties of oil and water at ambient conditions are given in **Table 2-3**. Pressure drops between injection and production points were measured for a constant flow rate. Effluents were collected and volumes of both phases were recorded for a constant time interval. Two pore volumes of oil were injected to produce the maximum water from the beads pack. The same procedure was adopted for two constant flow rates, $1\text{cm}^3 / \text{min}$ and $2\text{cm}^3 / \text{min}$. Once the pressure and production data was achieved for the homogeneous glass bead pack (the base case), the same procedure was repeated for

five different realizations of fractured systems including single and multiple fractures (see **Fig. 2-10**). The permeability of fracture is calculated using equation 2-4 where the fracture permeability is obtained from the fracture aperture (Hawkins 1959).

$$k = 54 \times 10^6 W^2 \quad (2-4)$$

where W is the fracture aperture in inches while the calculated fracture permeability k is in Darcy.

Table 2-3: Physical properties of oil and water at ambient conditions

| Liquid | Density gm / cm^3 | Viscosity cp | IFT N/m |
|-------------|------------------------|-----------------|------------|
| Soltrol 130 | 0.75 | 1.4 | 0.037 |
| Water | 0.998 | 1.002 | |

2.3.3 Results and Discussion

Drainage displacement tests were carried out on homogeneous and different heterogeneous glass bead packs as shown in **Fig. 2-10**. This figure presents a homogeneous, two single fracture systems and three multiple fracture systems. Flow tests were carried out keeping the glass model in the horizontal plane to avoid any gravity effects. However in this figure, oil was injected from the top and effluent was collected at the bottom of the model. In this figure, ‘A’ shows a homogenous beads pack while B consisting of a fracture placed at 45° to the direction of flow (top to bottom in **Fig. 2-10**). A fracture at 0° to the direction of flow is presented in **Fig. 2-10C**. Multiple fracture systems are presented in **Figs. 2-10D, 2-10E** and

2-10F. Two fractures parallel to each other and oriented at 0° to the flow direction are presented in **Fig. 2-10D** (referred as “2 Frac’s at 0° ” next in this study). The intersecting fracture system is presented in Figure **2-10E** where one fracture oriented at 45° intersects another oriented at 0° to the direction of flow (referred as “2-Intersecting Frac’s” next in this study). Finally, in **Fig. 2-10F** another intersecting fracture system is shown where both fractures cross each other making shape of a cross (X), one placed at 45° and the other at 135° to the flow direction (referred as “2-X Intersecting Frac’s” next in this study).

The length and aperture of the fracture are set at constant values of 10cm and 0.01cm (groove aperture), respectively.

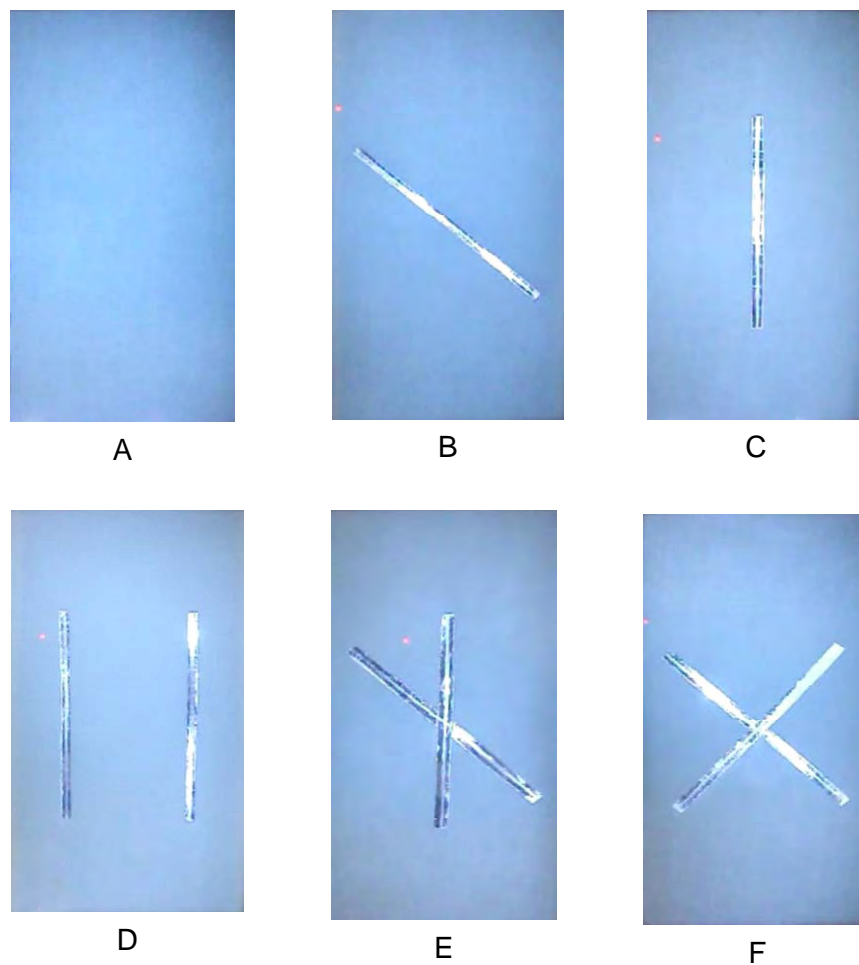


Figure 2-10: Glass bead packs used for two phase flow experiments

Figure 2-11 presents homogeneous and heterogeneous realizations after injection of 0.3 pore volume. This figure illustrates the bearings of fracture inclination as well as the density of fractures on fluid flow for drainage experiments. Red and light blue colours represent oil and water, respectively where oil is the displacing phase and water is the displaced (see **Figure 2-11**). All the experiments in this study were performed keeping the flow of the model in the horizontal direction to avoid the effect of gravity on fluid flow.

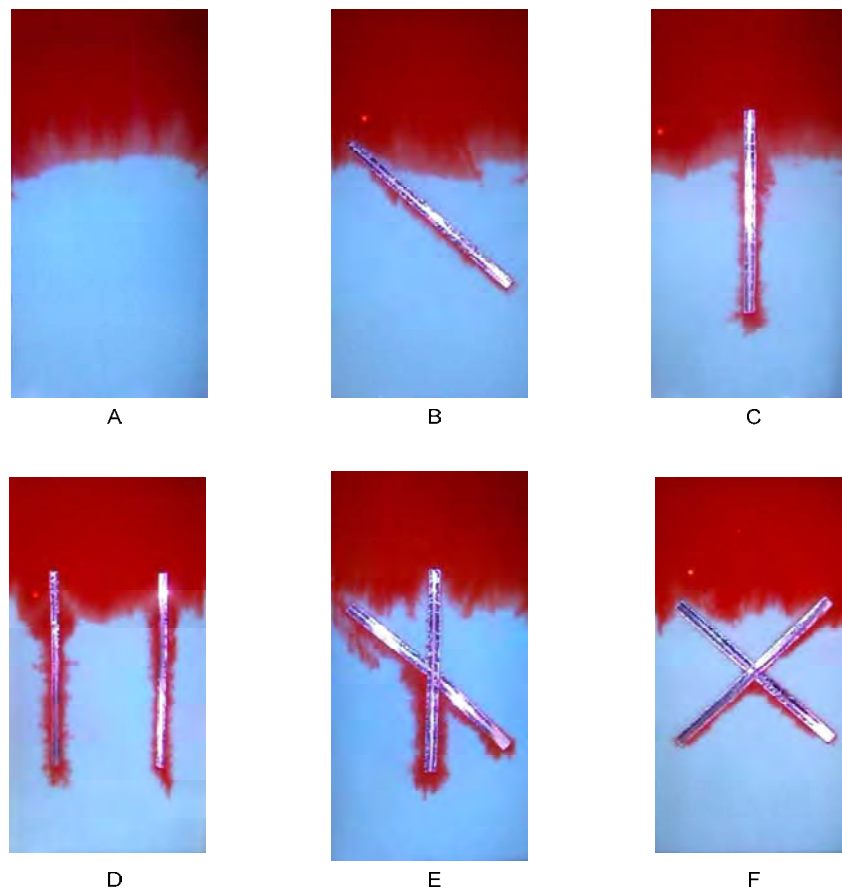


Figure 2-11: Effect of single and multiple fractures on fluid flow at 0.3 PVI

Figures 2-12 and **2-13** present the injected pore volume at which breakthrough happens through all the discussed scenarios for 1 and $2\text{cm}^3/\text{min}$, respectively. Multiple fracture

systems show early breakthrough as compared to single fracture systems (see **Figs. 2-12** and **2-13**). Flow through homogeneous glass beads pack shows a very late breakthrough after injection of 0.74 pore volumes (see **Fig. 2-12 A**). For the flow rate of $1\text{cm}^3 / \text{min}$, an early breakthrough was observed for the case of 2 intersecting fractures; one 0° and other 45° to the direction of fluid flow, where oil could be seen at the production point after the injection of only 0.56 pore volumes (see **Fig. 2-12 E**). After the injection of 0.6 pore volumes, breakthrough was observed for the case the of two fractures parallel to each other and to the direction of flow (see **Fig. 2-12 D**) which was late as compared to the case of intersecting fractures in **Fig. 2-12 E**. A further delay in the breakthrough could be seen for the case of 2-X intersecting fractures where after injection of 0.62 pore volumes the breakthrough was observed (**Fig. 2-12 F**). After injection of 0.67 and 0.71 pore volumes, breakthrough was observed for the cases of single fracture oriented at 0° (**Fig. 2-12 C**) and single fracture placed at 45° to the flow direction (**Fig. 2-12 B**).

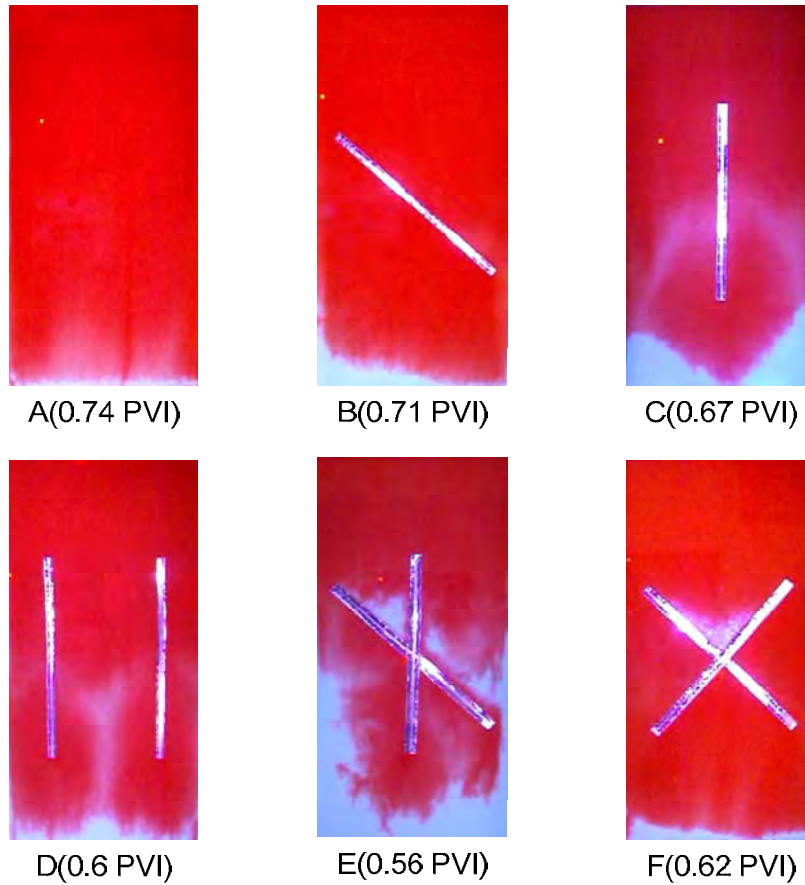


Figure 2-12: PVI at breakthrough for different glass bead packs at $1\text{cm}^3 / \text{min}$

Effect of the fracture orientation as well as the density of fractures on fluid flow is illustrated by **Fig. 2-12**. It is quite clear from this figure that the density of the fractures has strong effects on the behaviour of fluid flow which is evident in the early breakthroughs observed for the bead packs with the multiple fracture systems as compared to the single fracture beads systems. Effect of the fracture orientation on fluid flow could be observed by comparing the single fracture models in **Figs. 2-12 B** and **2-12C**, where early breakthrough was observed for the low orientation of fracture (0°) as compared to the relatively high orientation (45°) to the direction of flow. Oil flowed much faster for the case of 2-intersecting fractures (**Fig. 2-12 E**) which is a combination of low orientation (0°) of fracture with an inclined fracture (45°)

crossing through it. This scenario gave the earliest breakthrough (after 0.56PVI) due to the fracture intersection where both fractures feed each other.

Figure 2-13 shows similar trends of fluid flow for the same scenarios of homogeneous and heterogeneous glass bead packs at a constant injection rate of $2\text{cm}^3/\text{min}$. Low fingering effects and a stable front were observed for the high flow rate injection as can be observed by comparing **Figs. 2-12** and **2-13**.

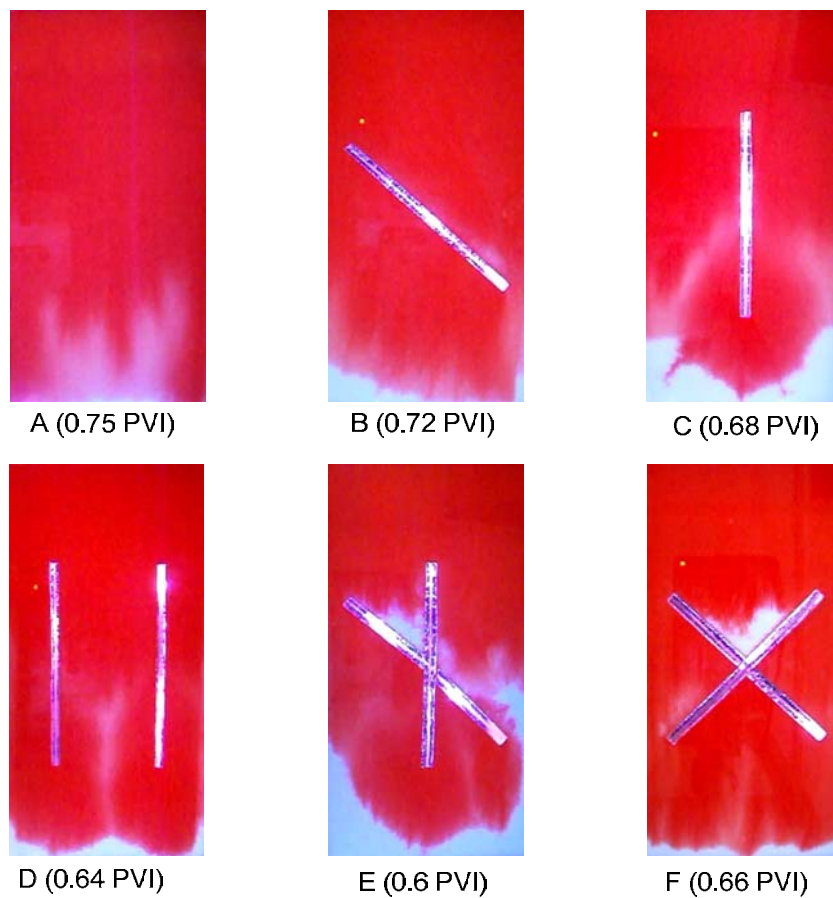


Figure 2-13: PVI at breakthrough for different glass bead packs at $2\text{cm}^3/\text{min}$

Differential pressures between the injection and production points for the discussed homogeneous and heterogeneous systems at a constant injection rate of $1\text{cm}^3/\text{min}$ are plotted in **Fig. 2-14**. As expected the highest pressure difference is obtained for the homogeneous

case as it represents the lowest permeability compared to all the fractured systems (see **Fig. 2-14**). Similarly it can be seen that the lowest pressure difference is obtained for the case of two horizontal fractures (both oriented at 0° to the direction of flow) as this fracture system contains the highest absolute permeability (see **Fig. 2-14**).

The cumulative produced water for the discussed glass bead systems at $1\text{cm}^3 / \text{min}$ are shown in **Fig. 2-15**. It is observed that the maximum water volume was produced for the homogeneous case (12cm^3) as the breakthrough was delayed in this case compared to all fractured glass bead systems. Glass bead systems containing fractures produced lower volumes of water as they show early oil breakthrough and oil at some points by passed the water as can be seen in **Figures 2-12** and **2-13**.

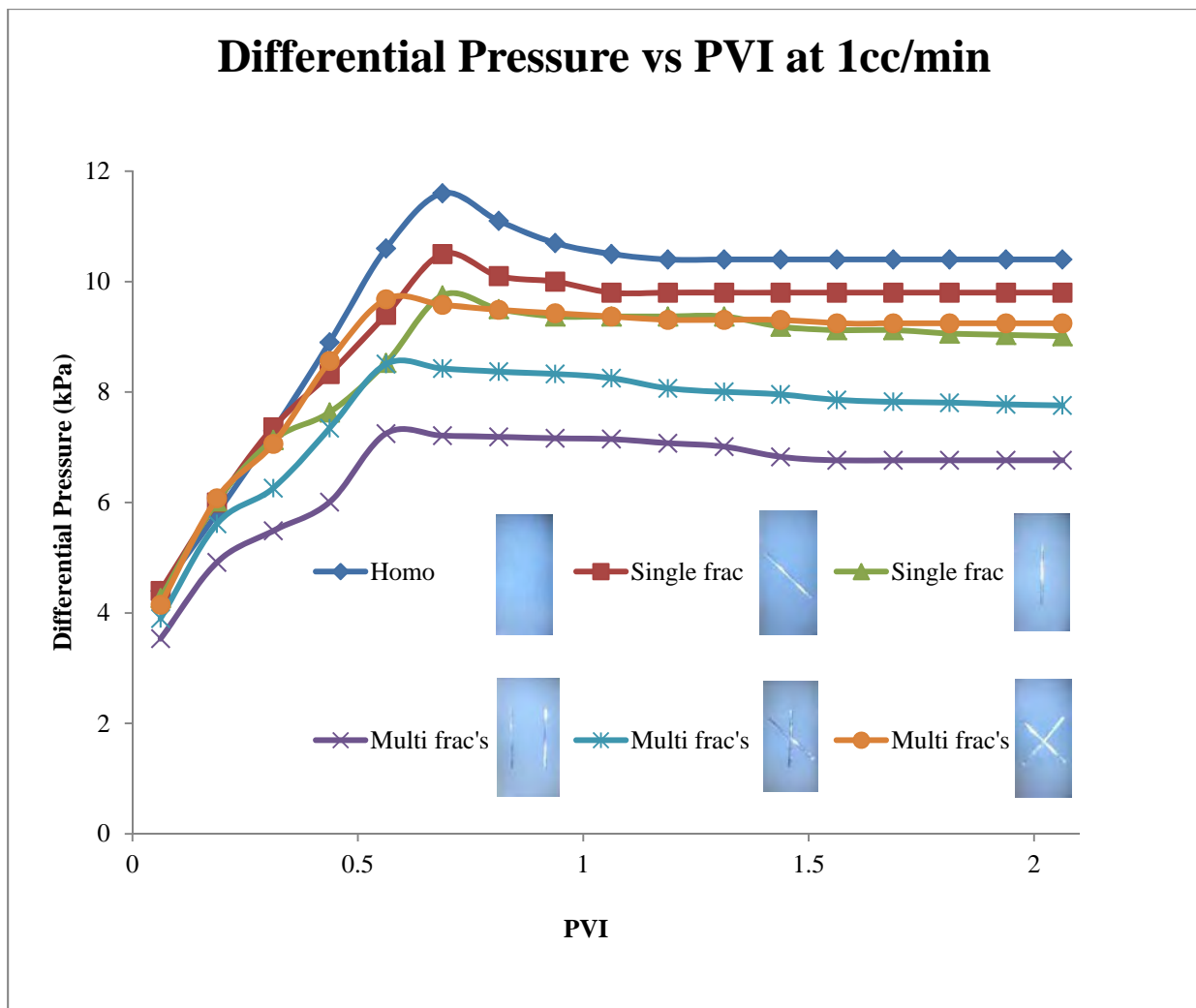


Figure 2-14: Differential pressures vs. PVI for the glass bead packs in **Fig. 2-12** (at $1\text{cm}^3 / \text{min}$)

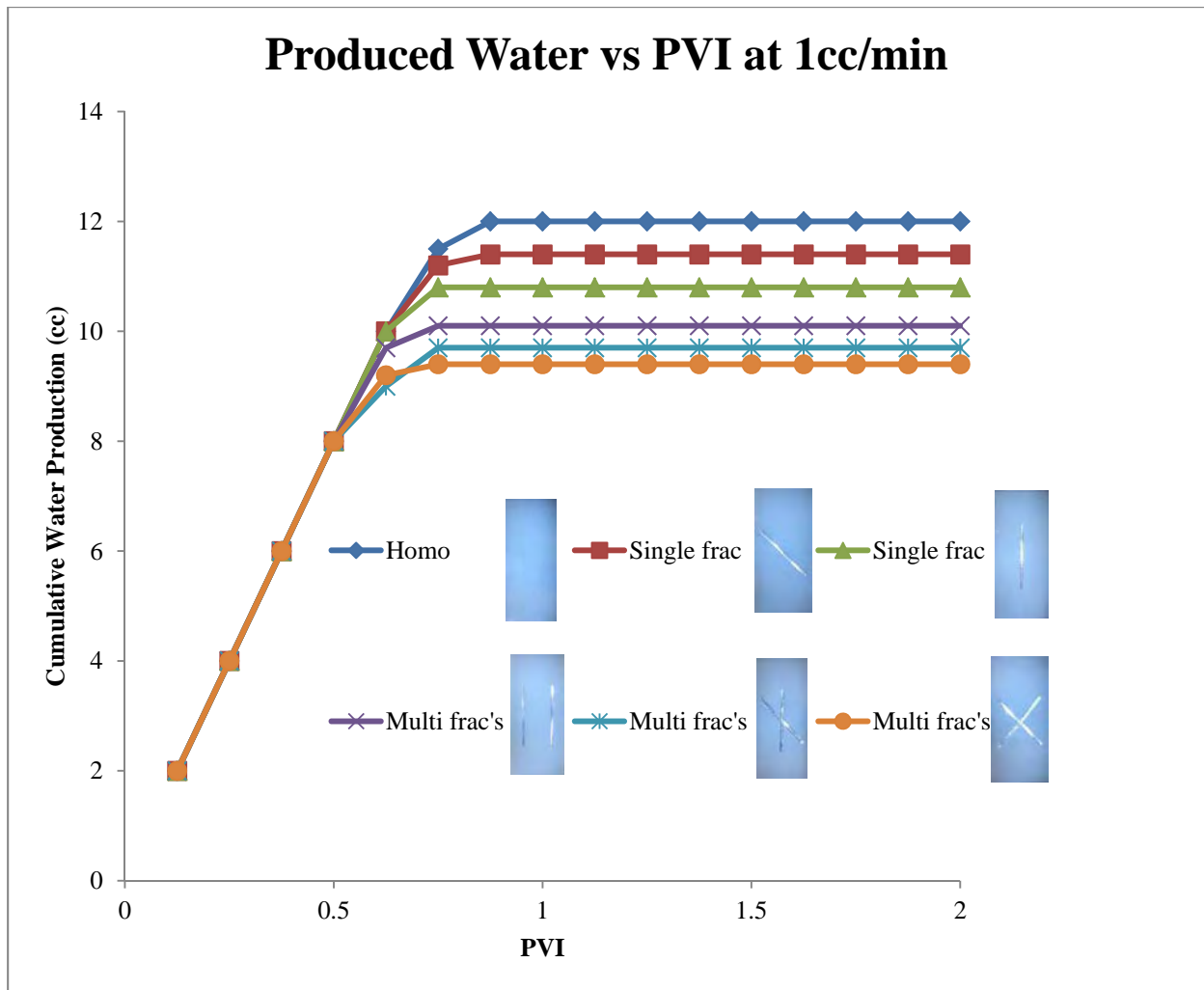


Figure 2-15: Cumulative produced water vs. injected pore volume for all glass bead packs at $1\text{cm}^3 / \text{min}$ injection rate

Similarly, the differential pressures between injection and production points for all glass bead packs at a constant injection rate of $2\text{cm}^3 / \text{min}$ are plotted in **Fig. 2-16**. As expected, all obtained differential pressures are high as compared to the differential pressures at $1\text{cm}^3 / \text{min}$ (**Fig. 2-14**).

The maximum pressure difference (the peak of the curves) for each glass bead pack represents the oil breakthrough (see **Figs. 2-14 & 2-16**). It is observed from **Figs. 2-14** and 2-

16 that earlier breakthrough is achieved for the multiple fracture system as compared to the single fracture systems at both constant injection rates of $1\text{cm}^3/\text{min}$ and $2\text{cm}^3/\text{min}$, respectively. This early breakthrough can also be confirmed by the flow visualizations shown in **Figs. 2-12** and **2-13**.

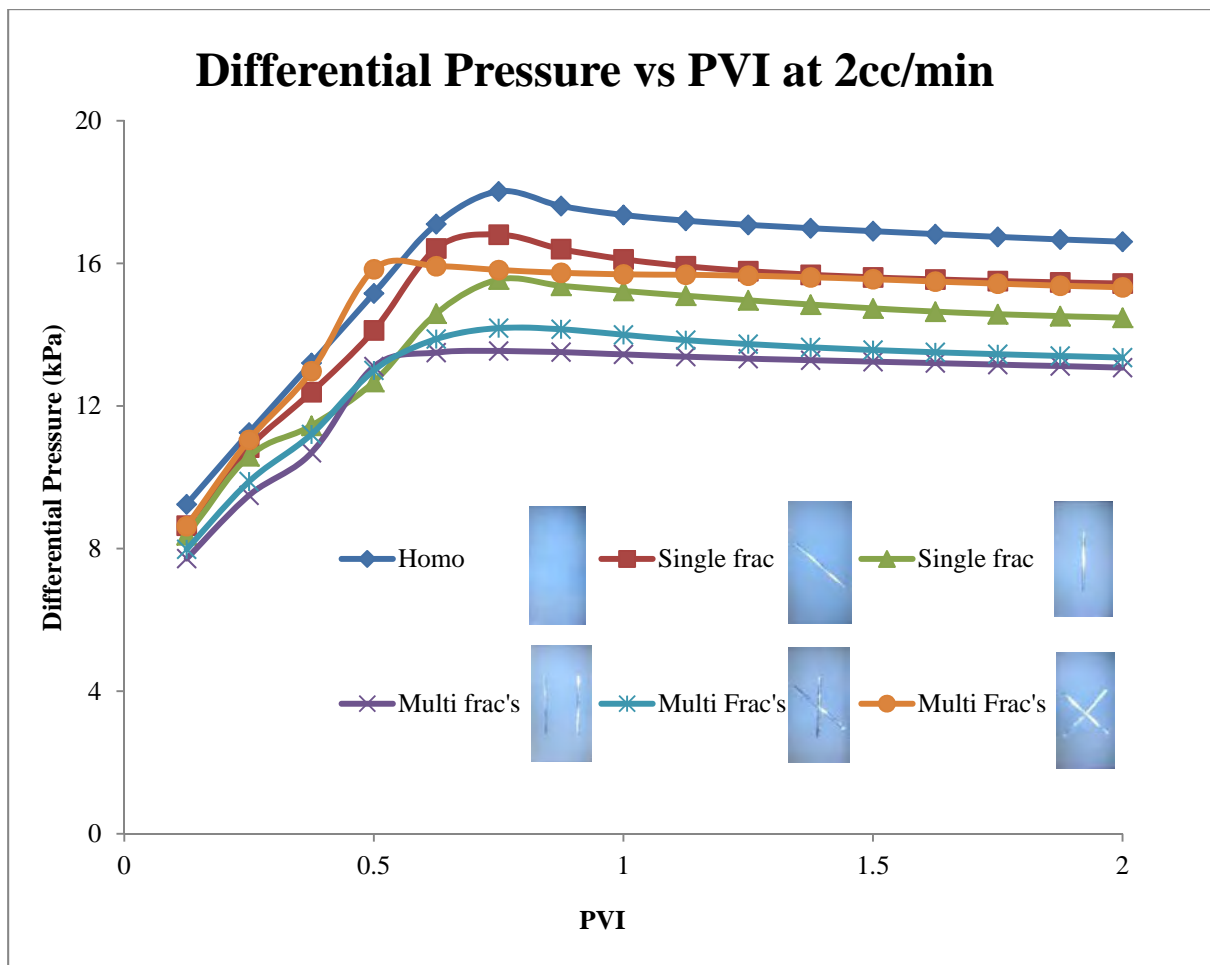


Figure 2-16: Differential Pressures vs. Time for glass bead packs in **Fig. 2-13** (at $2\text{cm}^3/\text{min}$)

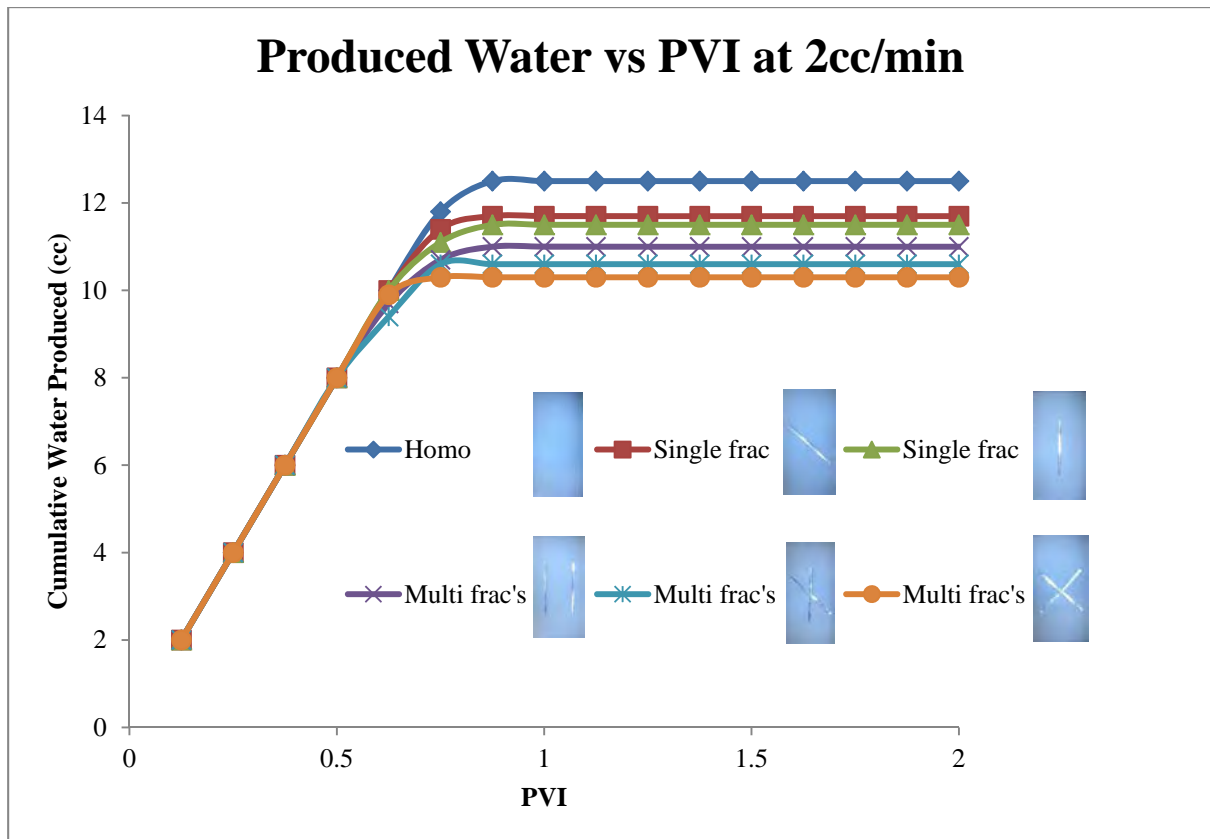


Figure 2-17: Cumulative produced water vs. injected pore volume for all glass bead packs at $2\text{cm}^3 / \text{min}$ injection rate

Figures 2-17 shows the cumulative water production for glass bead systems at $2\text{cm}^3 / \text{min}$. The water volumes produced are close to the water volumes produced at $1\text{cm}^3 / \text{min}$ in Fig. 15. The calculated pore volume of the glass bead system was 16cm^3 . Water production for the case of 2-X Intersecting Frac's is less than single fracture oriented at 45° to the flow direction due to the water volume trapped right before the fracture intersection (see **Figure 2-13F**). Residual water saturations for all cases were calculated based on the cumulative produced water after two pore volumes of injection (see Table 4).

Table 2-4: Irreducible water saturations for glass bead models at 1 and $2\text{cm}^3 / \text{min}$

| Glass Bead Packs | Homo | Single 45° frac | Single 0° frac | 2 Frac's at 0° | 2Intersecting frac's | 2X Intersecting frac's |
|------------------------------------|------|--------------------|-------------------|-------------------|-------------------------|---------------------------|
| Swi($1\text{cm}^3 / \text{min}$) | 0.25 | 0.29 | 0.32 | 0.37 | 0.39 | 0.40 |
| Swi($2\text{cm}^3 / \text{min}$) | 0.22 | 0.27 | 0.28 | 0.31 | 0.34 | 0.35 |

2.4 Relative Permeability (Oil-Water)

2.4.1 Numerical Reservoir Simulation

History matching technique was employed to obtain relative permeabilities for oil and water phases in homogeneous and fractured glass bead models. For this purpose a commercial black oil simulator was used. The laboratory glass bead models were first built using the simulator with same physical dimension of $10\text{cm} \times 20\text{cm} \times 0.2\text{cm}$. The model was then discretised into $50 \times 100 \times 1$ blocks in the x, y, and z directions (**Figure 2-18**), which makes the length of each grid block as 0.2cm in each direction. Matrix block permeabilities were kept constant values of $3.4D$ whereas the fracture permeability as $1 \times 10^4 D$ as calculated using equation 2-4. Permeability for each grid block was kept constant in the x, y, and z directions.

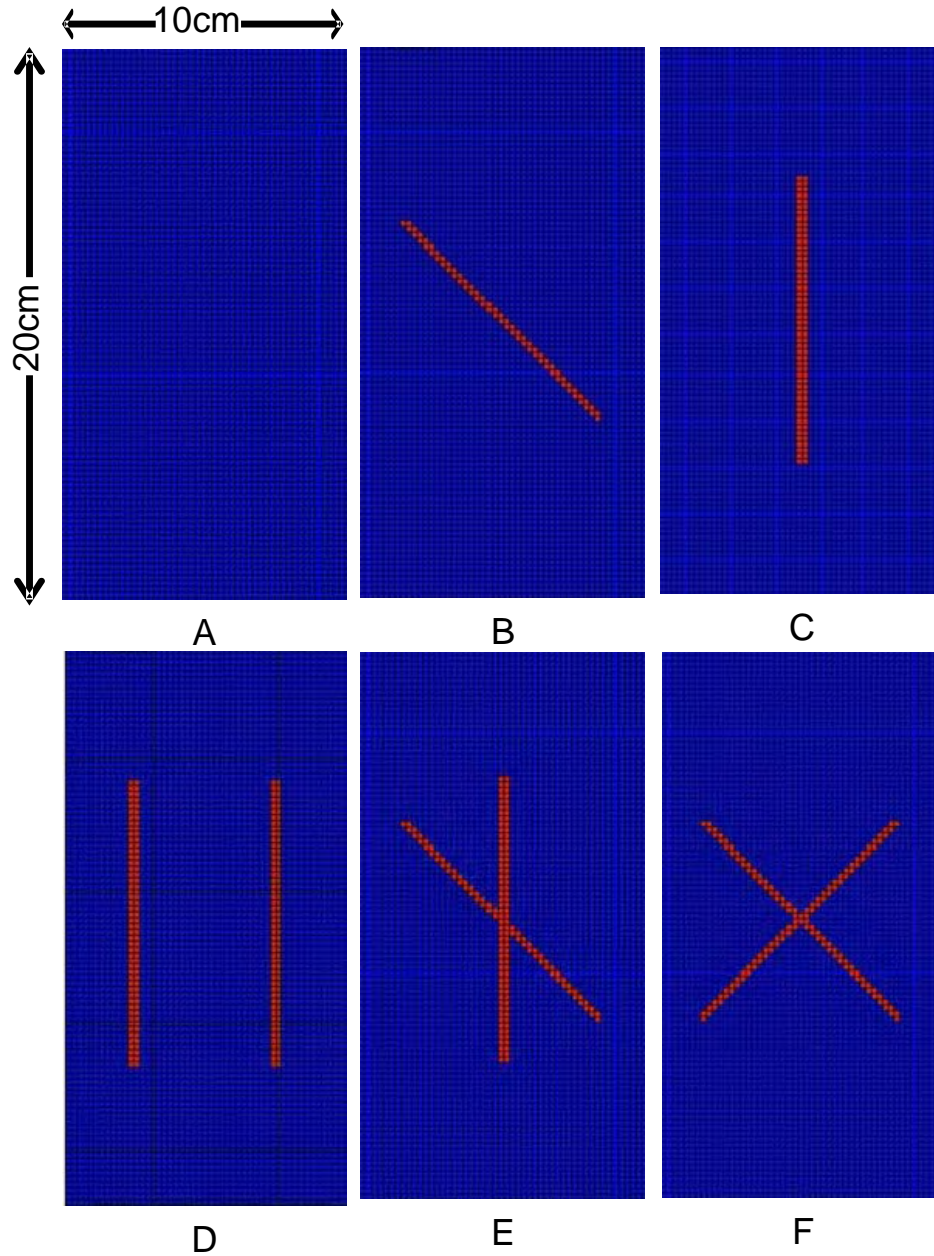


Figure 2-18: Simulator model, designed for the two phase flow study, representing matrix and fracture

Laboratory obtained residual water saturations were used to initiate relative permeability curves which were fed to the simulator in order to match the pressures and productions data obtained in the laboratory. Corey-type power law was used to parameterize relative permeability for different glass bead models as expressed below Corey (1954).

$$k_{rw} = k_{rw-\max} \left(\frac{S_w - S_{ir}}{1 - S_{ir}} \right)^{n_w} \quad (2-5)$$

$$k_{ro} = k_{ro-\max} \left(1 - \frac{S_w - S_{ir}}{1 - S_{ir}} \right)^{n_o} \quad (2-6)$$

where k_{rw} and k_{ro} are the water and oil relative permeabilities, respectively, S_w is water phase saturation, S_{ir} represents the irreducible water saturation, and n_w and n_o are the water and oil Corey exponents, respectively.

The oil and water relative permeability curves for which laboratory based pressure and production data matched for $1\text{cm}^3 / \text{min}$ are shown in **Figs. 2-19** and **2-20**, respectively.

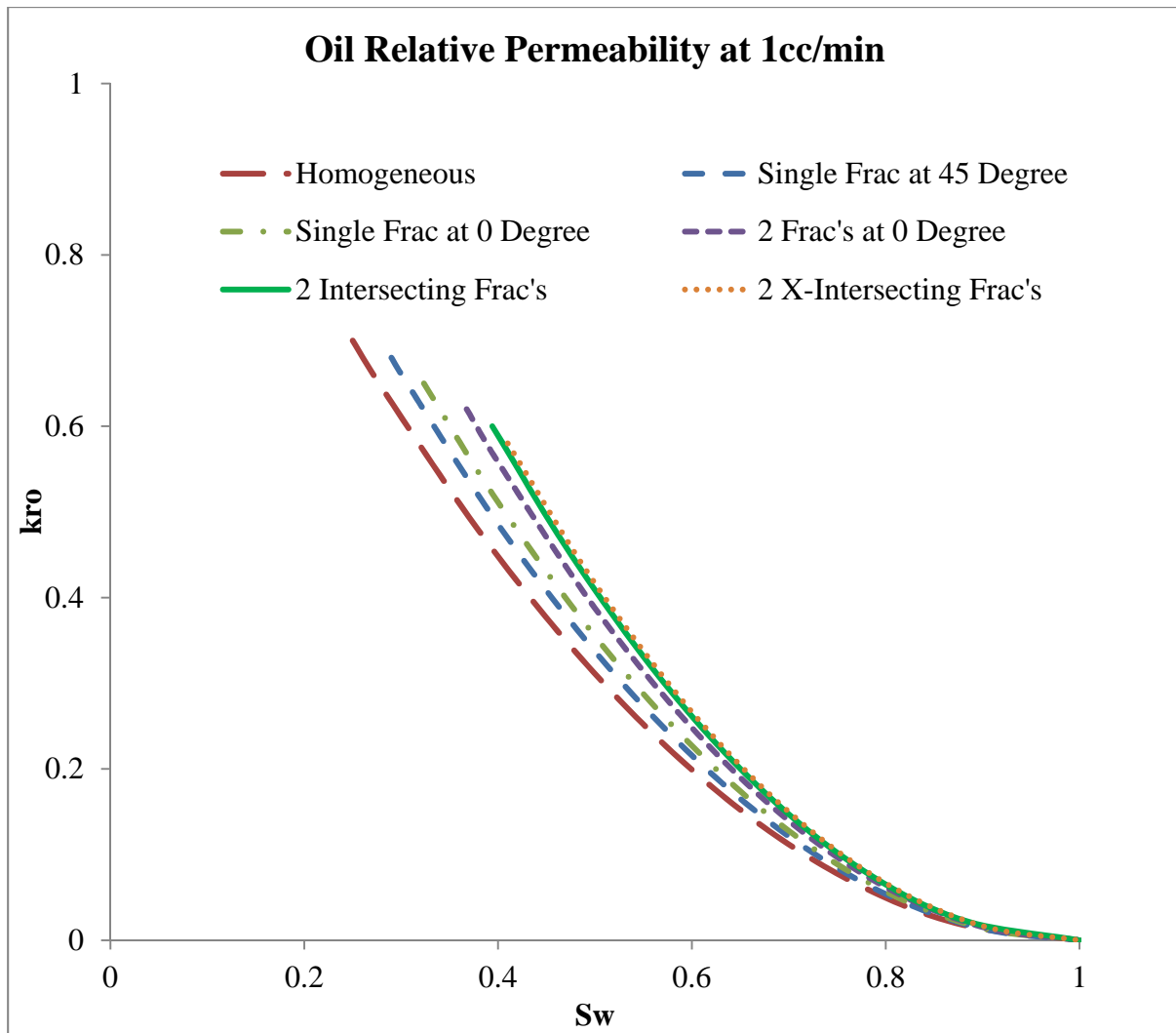


Figure 2-19: Oil relative permeability for the glass bead models at $1\text{cm}^3 / \text{min}$

In **Fig. 2-19**, for a particular value of water saturation, the maximum oil relative permeability is obtained for the intersecting fracture system, which is followed by the system of 2 fractures oriented at 0° to the direction of flow. Single fracture systems show lower oil relative permeabilities for a particular oil or water saturation as compared to multiple fracture systems. Furthermore, the lowest oil relative permeability is obtained by the homogeneous bead pack which is because of the fact that the fractures help the oil phase to pass through the fractured medium much faster as compared to homogeneous bead pack.

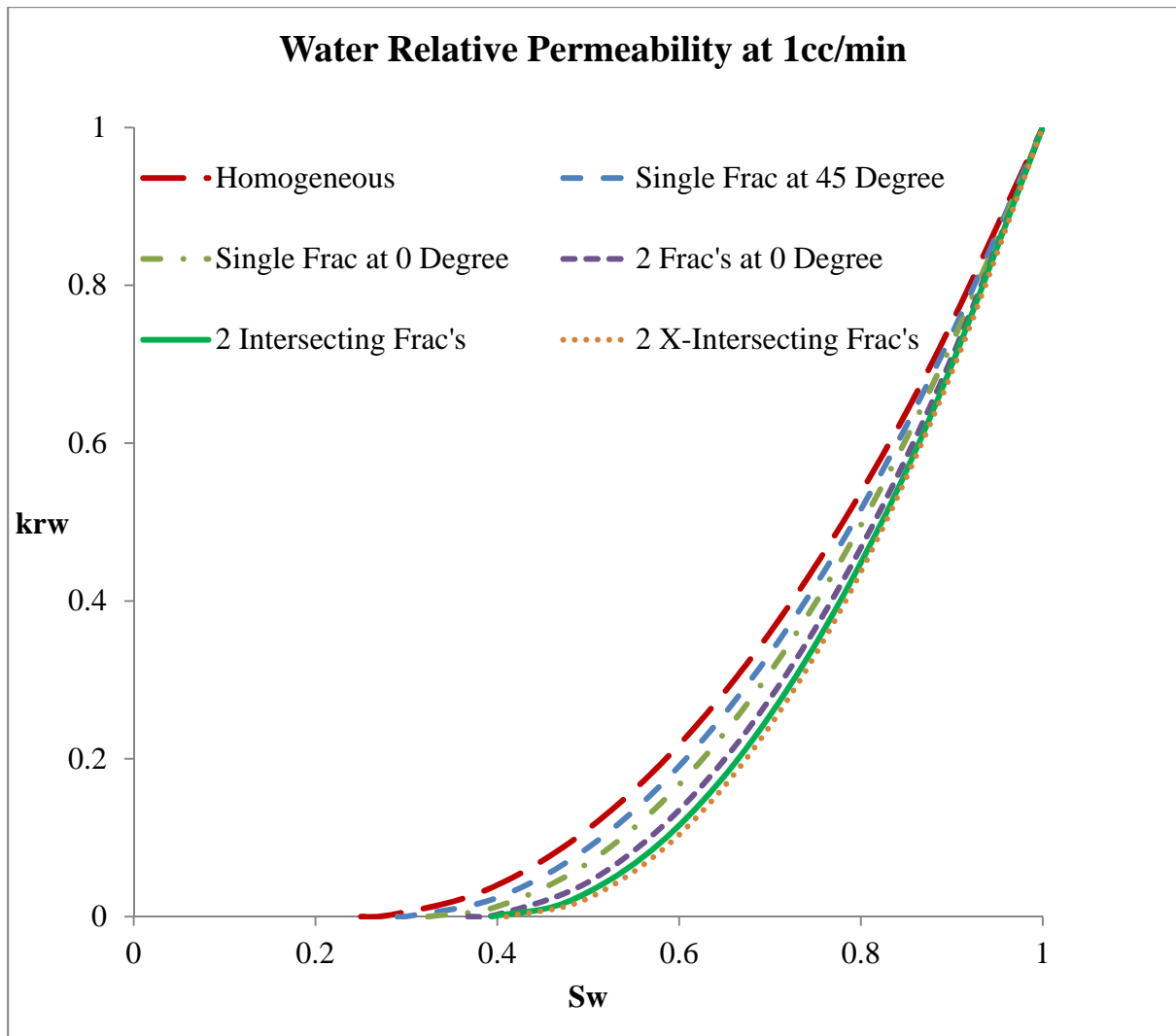


Figure 2-20: Water relative permeability for glass bead models at $1\text{cm}^3 / \text{min}$

For a particular value of water saturation in **Fig. 2-20**, the homogeneous model showed a maximum water relative permeability. Water relative permeabilities for fractured models are lower than homogeneous model which is explained by bypassing of a larger volume of water in the fractured models.

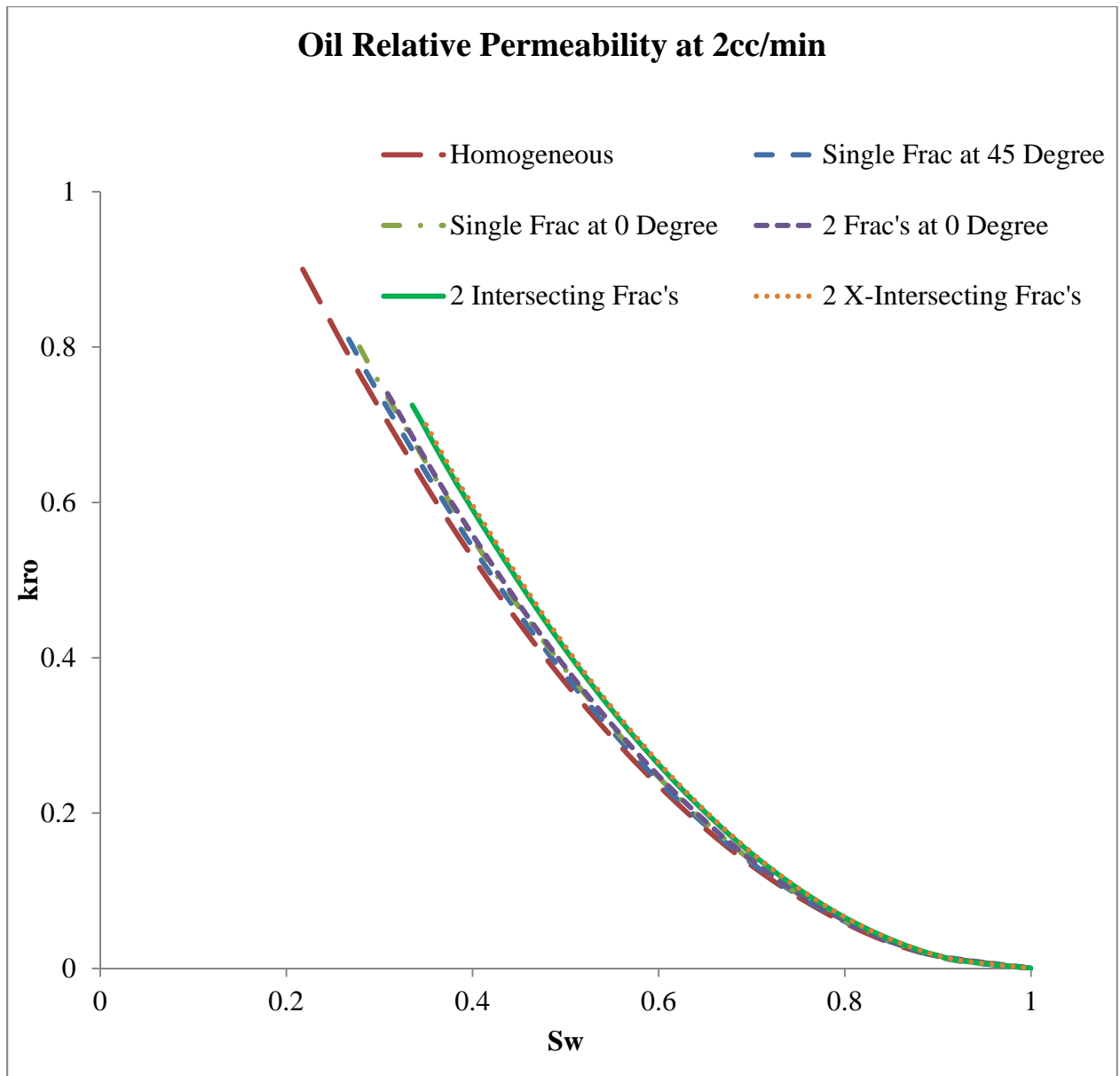


Figure 2-21: Oil relative permeability for glass bead models at $2\text{cm}^3 / \text{min}$

Similarly, oil and water relative permeabilities for the $2\text{cm}^3 / \text{min}$ constant injection rate are presented in **Figs. 2-21** and **2-22**. **Figure 2-21** shows a similar trend of oil relative permeability as at low flow rate in **Fig. 2-19**. It is observed that, at higher flow rate ($2\text{cm}^3 / \text{min}$), oil relative permeabilities are high as compared to the low flow rate ($1\text{cm}^3 / \text{min}$) (see **Figs. 2-19** and **2-21**). It is found that at high flow rate ($2\text{cm}^3 / \text{min}$), relative

permeabilities at a particular water saturation for different bead systems are relatively close to each other as compared to the low flow rate ($1\text{cm}^3 / \text{min}$). This can be explained by the fact that in high rate ($2\text{cm}^3 / \text{min}$) experiments it is hard to differentiate between contribution of different fracture realizations because the flow is rate dominant. **Figure 2-22** showed similar trend of water relative permeabilities for glass bead models as for $1\text{cm}^3 / \text{min}$ in **Fig. 2-20**.

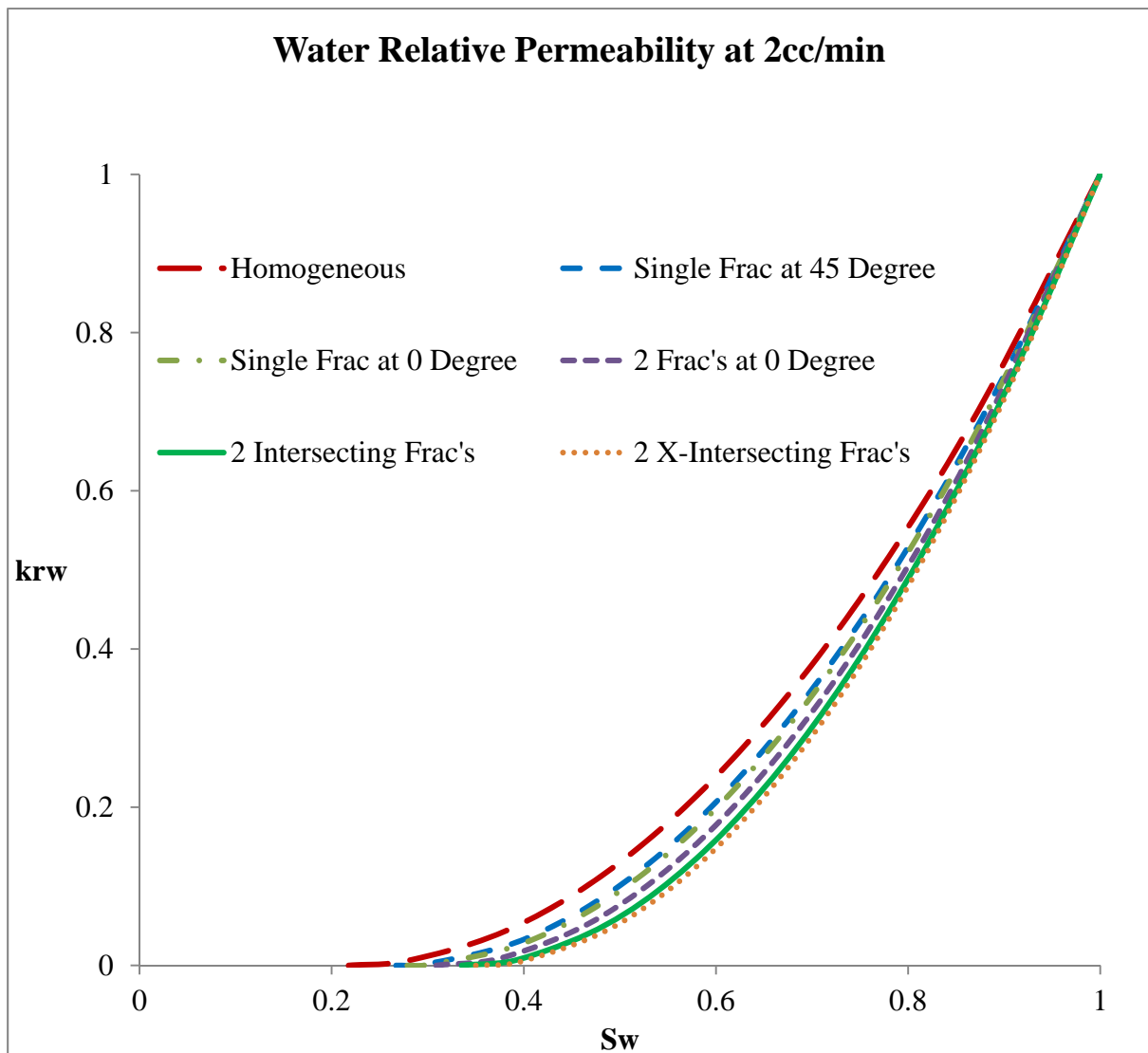


Figure 2-22: Water relative permeability for glass bead models at $2\text{cm}^3 / \text{min}$

2.4.2 Comparison between Laboratory and Simulator Results

Pressure and production matches between laboratory and simulator results are presented in **Figs. 2-23 to 2-26**. Laboratory results are in good agreement with the simulator results for the relative permeability curves shown in **Figs. 2-19 to 2-22**.

Laboratory based displacement profiles after 0.4PVI are compared against the simulator oil saturation profiles and are presented in **Figs. 2-27 to 2-32**. In these figures oil is injected from the top and effluent is collected at the bottom (for figure reference only). Also, for laboratory flow profiles, oil and water are represented by red and light blue colours, respectively. Similarly, for simulator flow profiles, oil is represented by red/orange colour and water by green. Flow profiles for simulator and laboratory observations are in close agreement. Due to capillary effects, small fingering effects can be observed at the oil front in laboratory profiles, whereas it is not the case for simulator profiles where effect of capillary pressure is ignored.

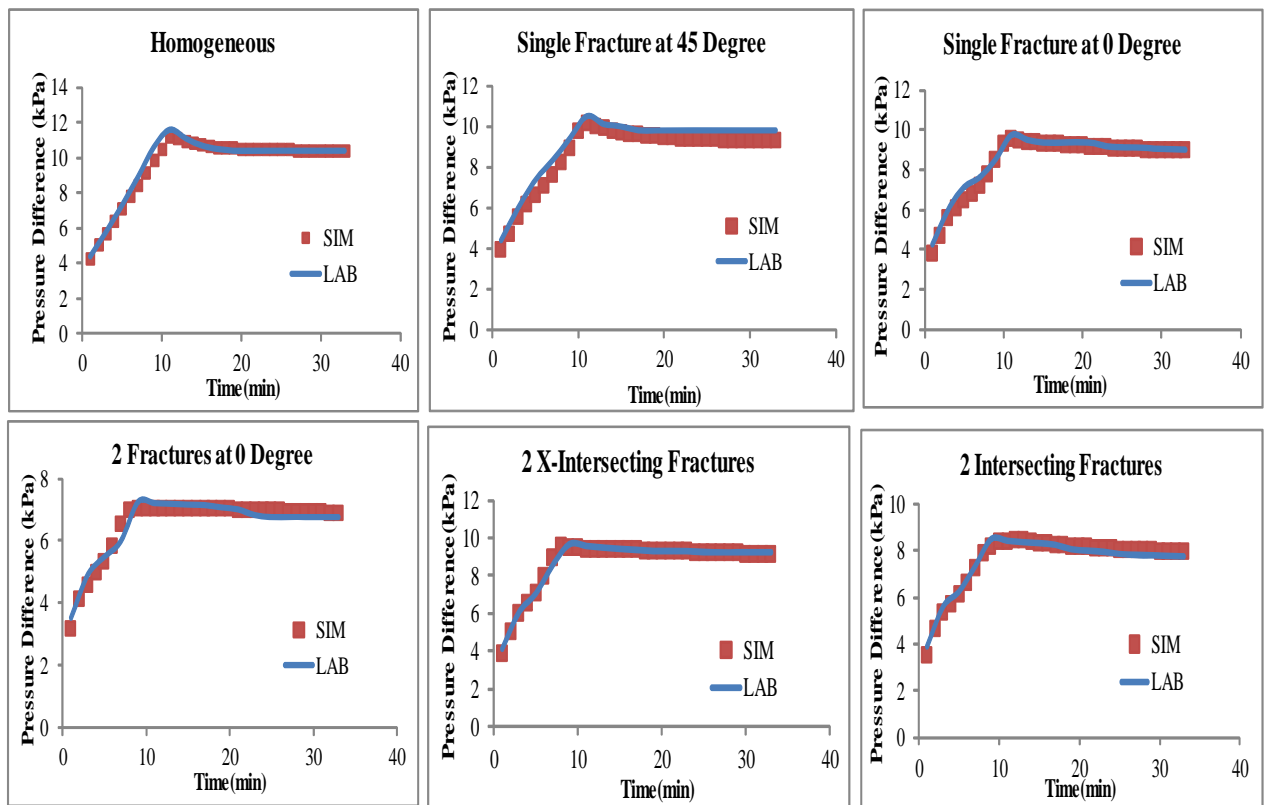


Figure 2-23: Matches between simulator and laboratory differential pressure results at $1\text{cm}^3 / \text{min}$

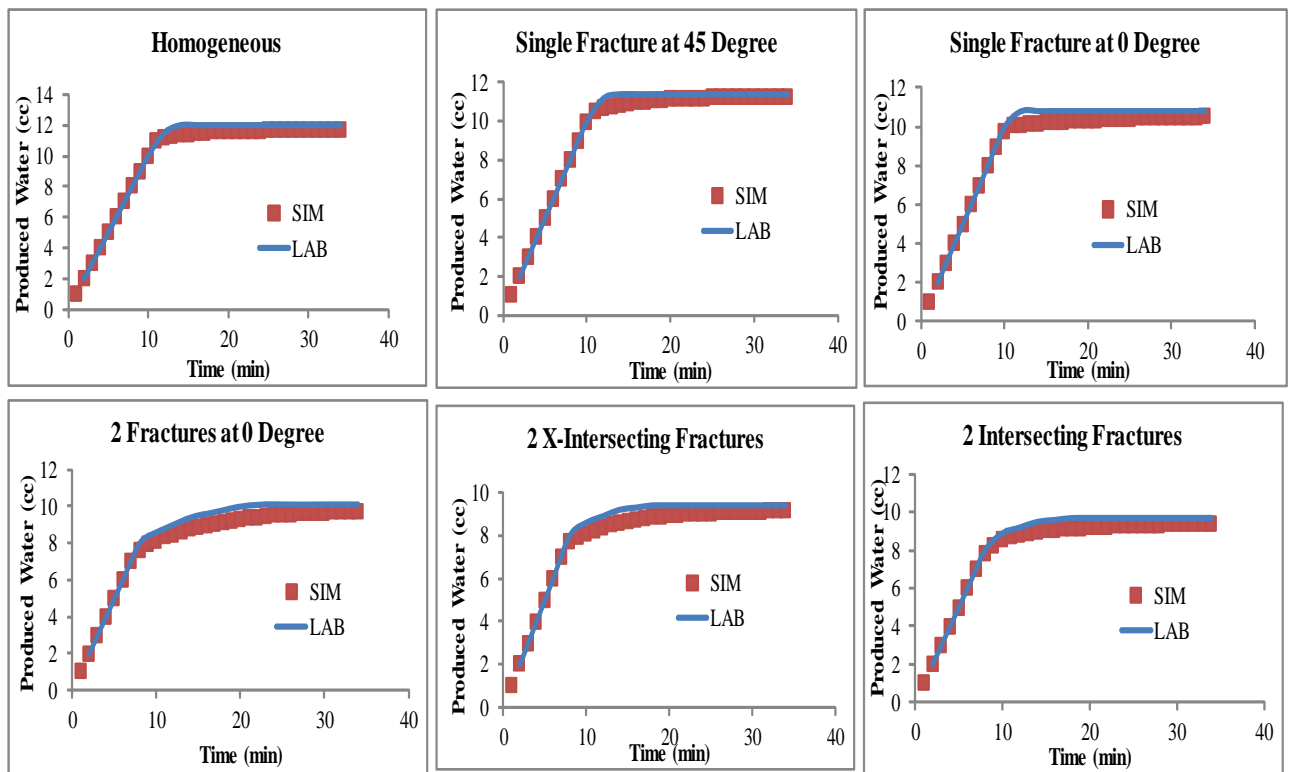


Figure 2-24: Matches between simulator and laboratory production results at $1\text{cm}^3 / \text{min}$

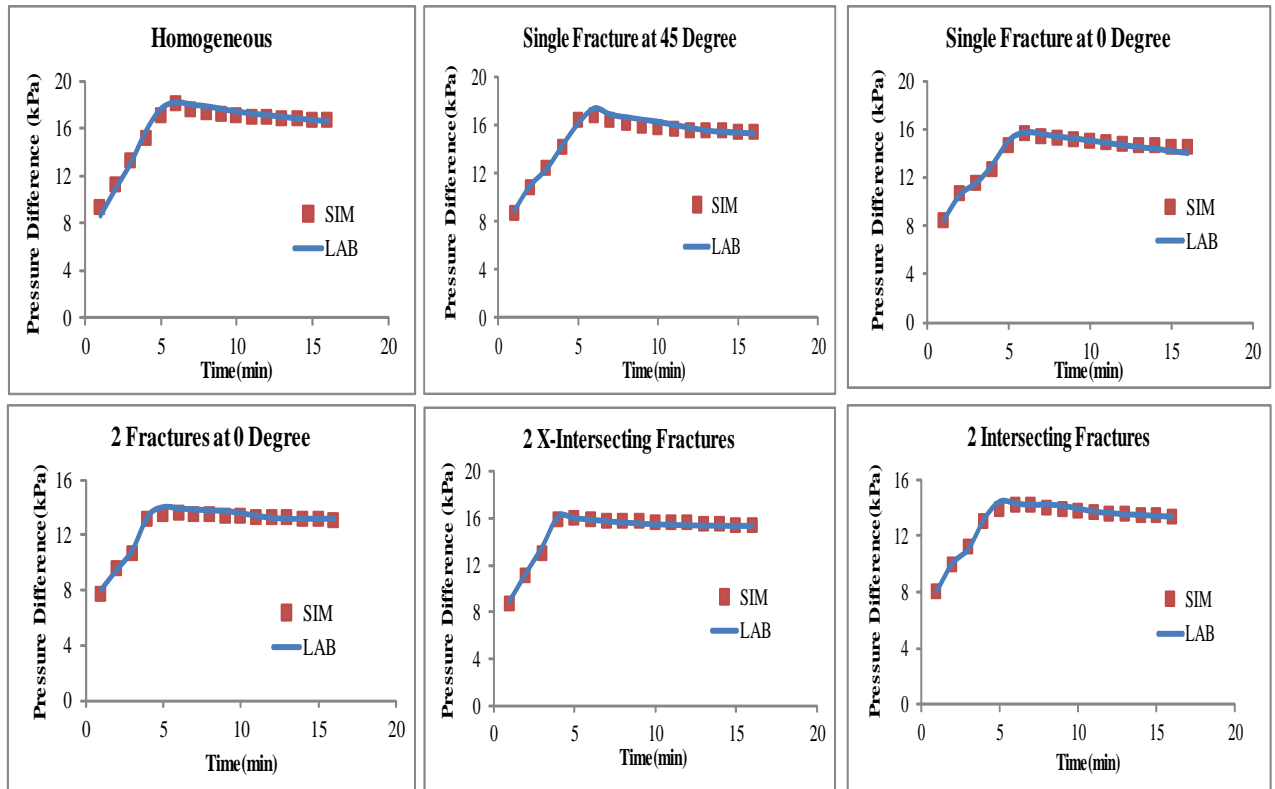


Figure 2-25: Matches between simulator and laboratory differential pressure results at

$2\text{cm}^3 / \text{min}$

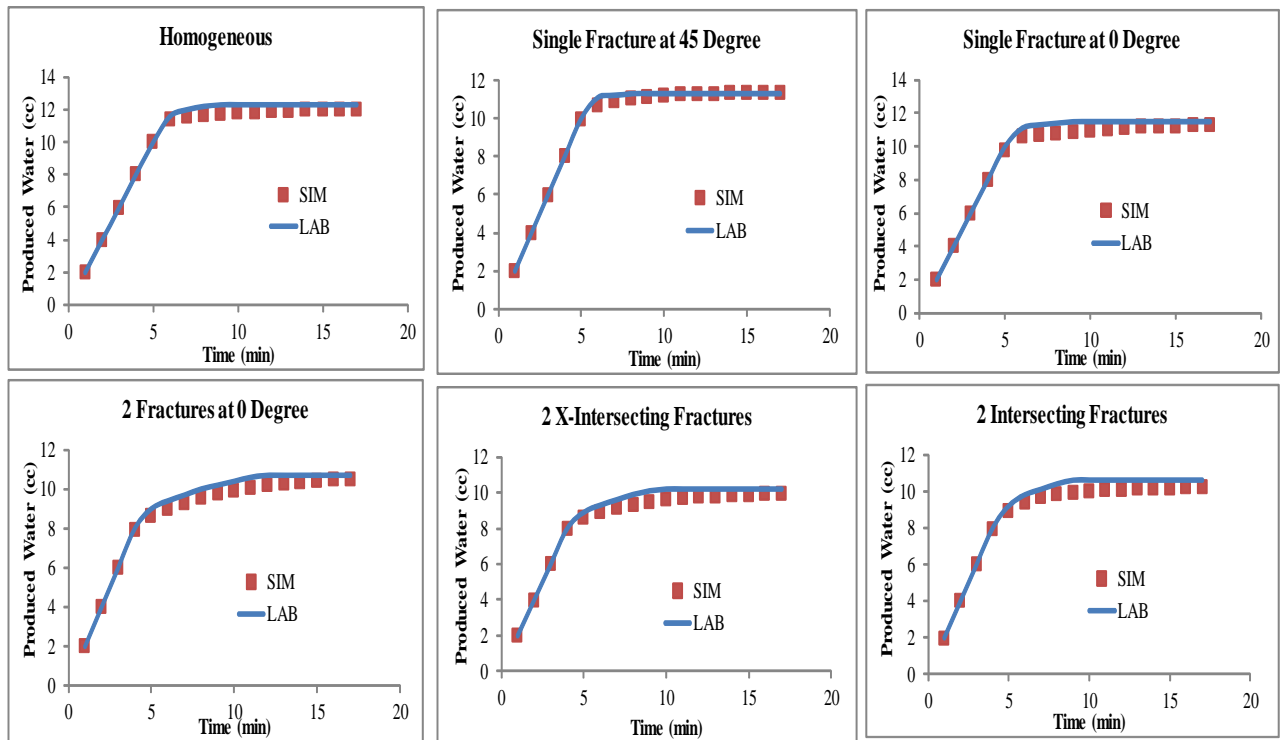


Figure 2-26: Matches between simulator and laboratory production results at $2\text{cm}^3 / \text{min}$

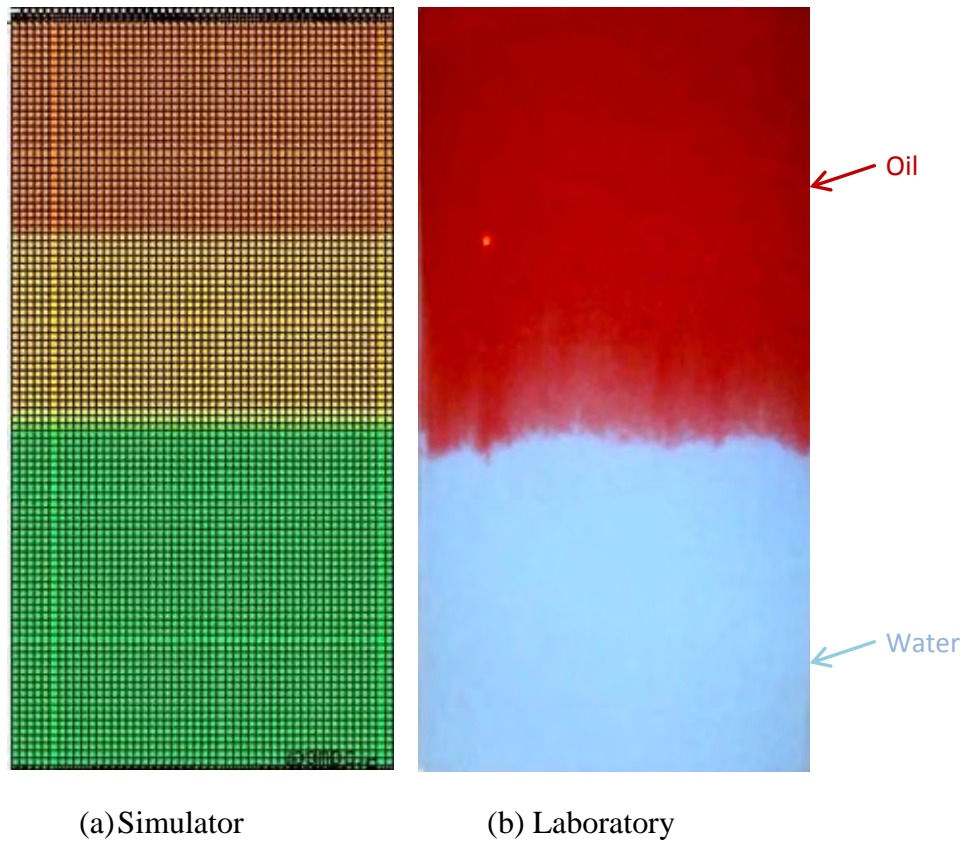


Figure 2-27: Fluid flow profiles for homogeneous pack at 0.4PVI

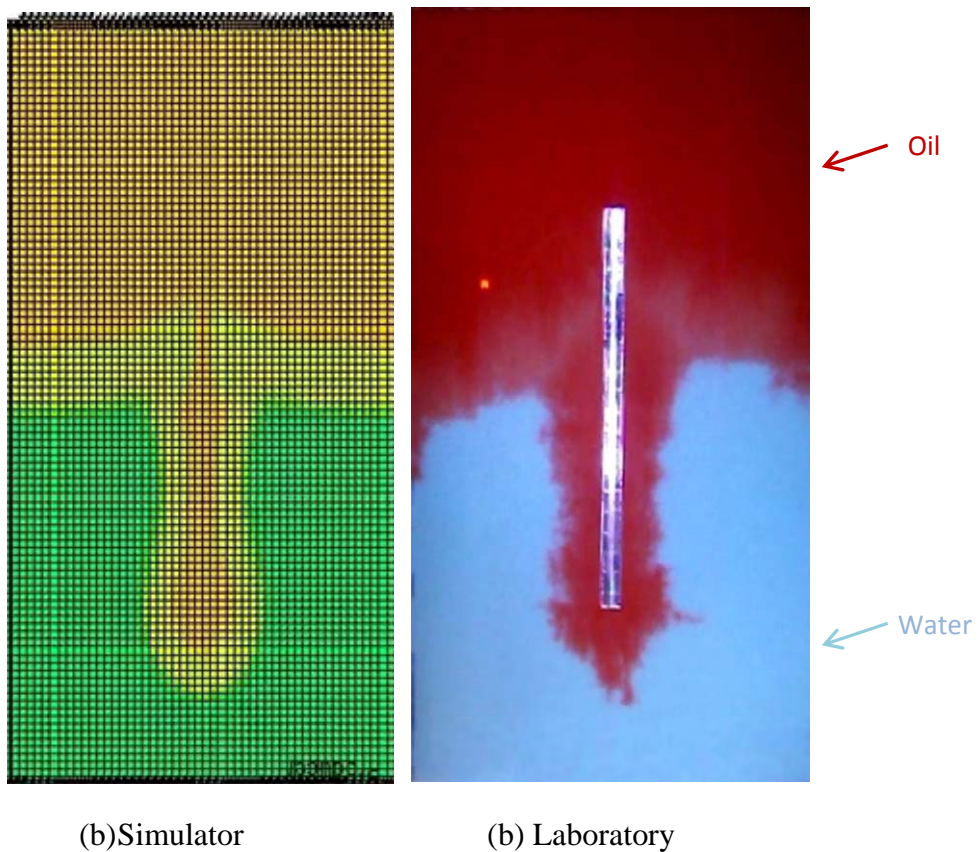


Figure 2-28: Fluid flow profiles for 0° fracture system at 0.4PVI

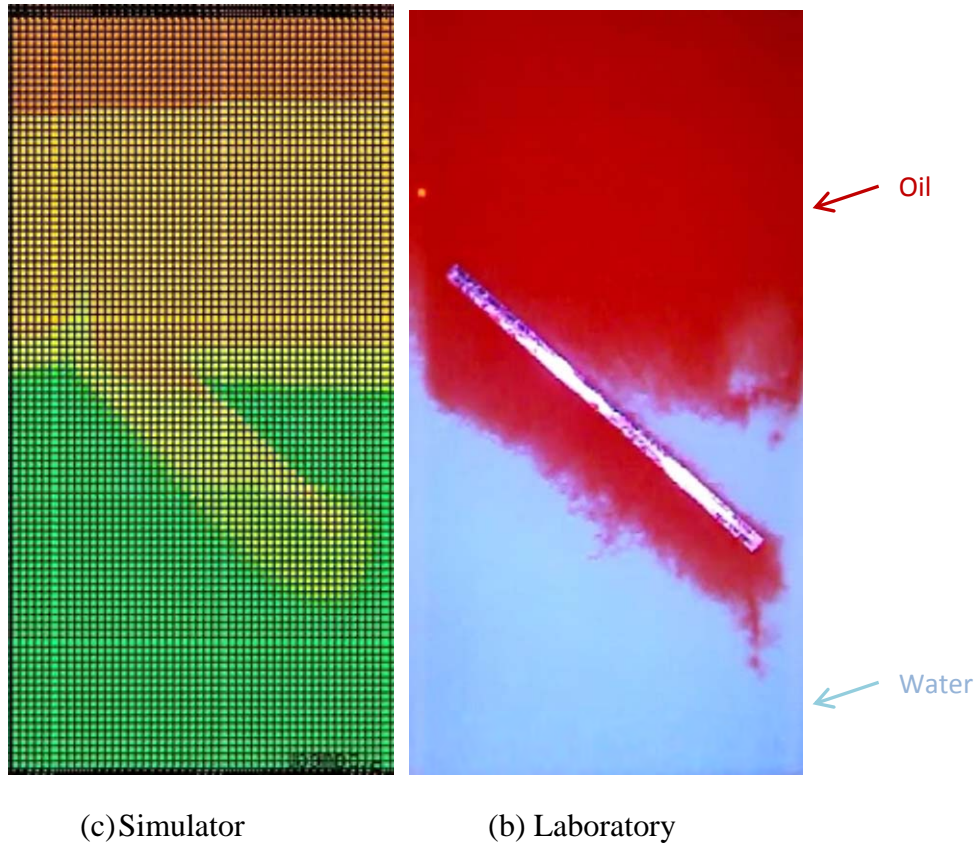
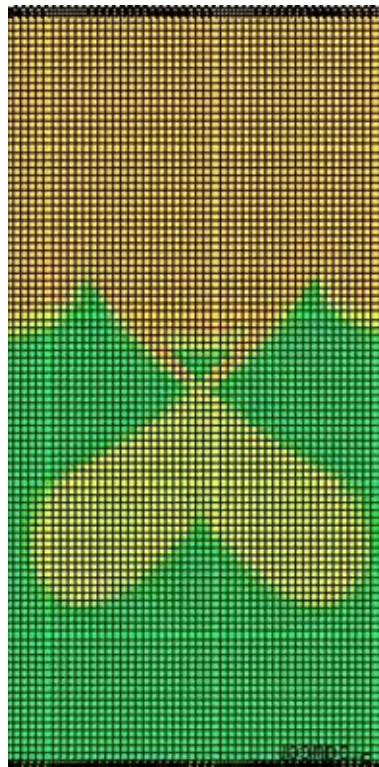
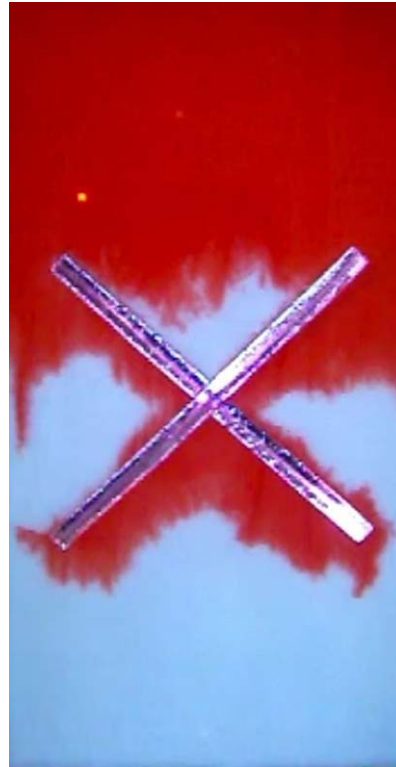


Figure 2-29: Fluid flow profiles for 45° fracture system at 0.4PVI



(d) Simulator



(b) Laboratory

Figure 2-30: Fluid flow profiles for 2 X-Intersecting fractures system

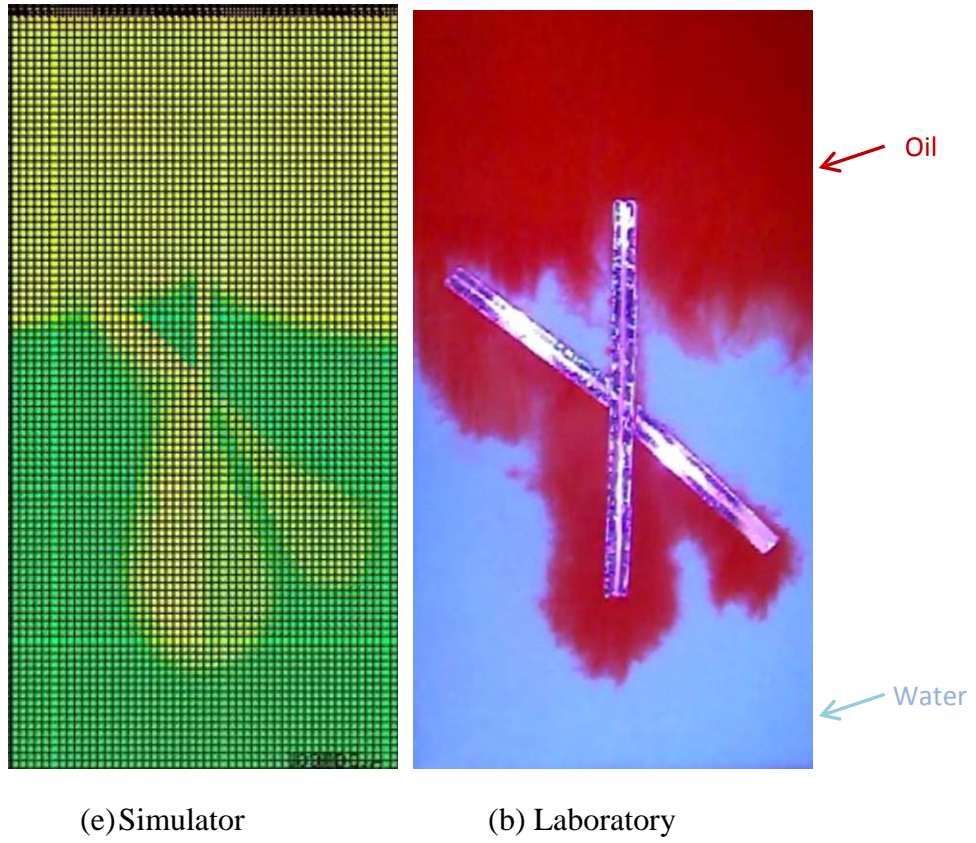
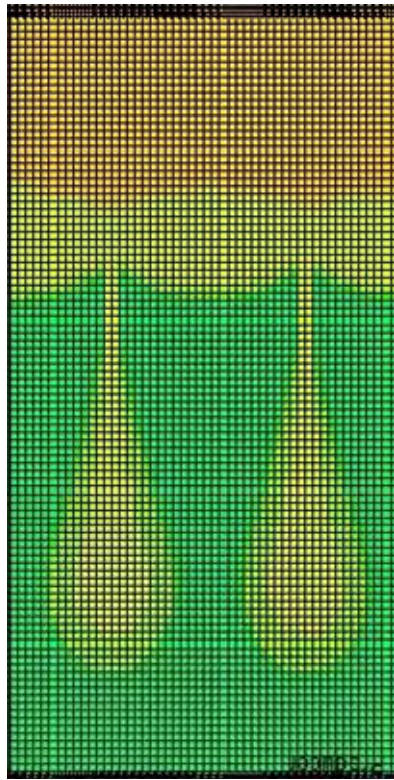
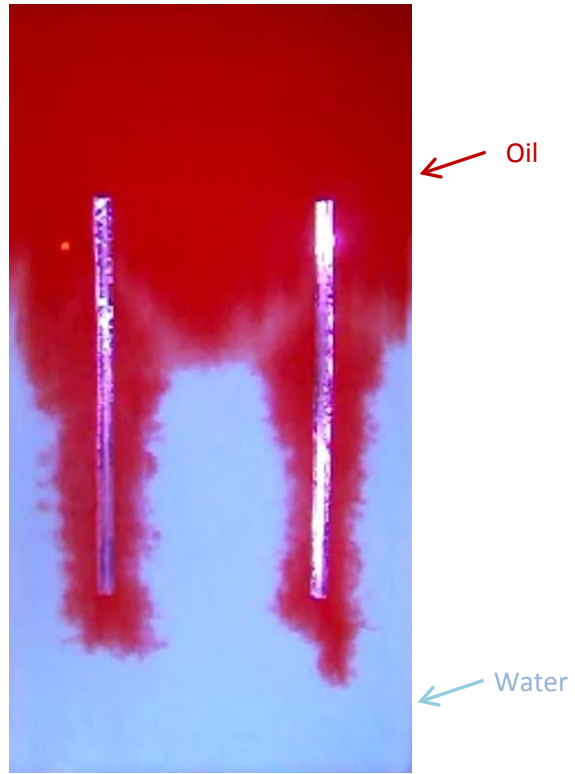


Figure 2-31: Fluid flow profiles for 2 Intersecting fracture system at 0.4PVI



(f) Simulator



(b) Laboratory

Figure 2-32: Fluid flow profiles for 2 fractures at 0°, at 0.4PVI

Results of drainage tests for the homogeneous and heterogeneous systems have been analysed to find a relationship expressing effect of heterogeneity e.g. number of fractures, orientation of fracture, on oil relative permeabilities. Correlation given in equation 2-5 has been found based on the observations of oil relative permeability changes by changing the fracture system. Oil relative permeability for the homogeneous case was taken as the reference for this purpose and relative permeabilities of heterogeneous systems are calculated using the equation below:

$$k_{ro} = \left[1 + (-0.015 \times n_f^2 + 0.155 \times n_f) + \left(0.16 \times e^{-4.01(1 - \sin(\psi))} \right) - 0.085 \times \sin\theta \right] \times k_{ref} \quad (2-7)$$

In this equation k_{ro} is the oil relative permeability, while k_{ref} is the reference oil relative permeability which is k_{ro} of the homogeneous glass bead pack, n_f represents the number of fractures in the system and, ψ is the angle between a fracture with a reference fracture. A fracture close to the top left corner of the system is assumed as the reference fracture and its orientation towards the flow direction is expressed as θ in this equation. It can be seen from this correlation that the number of fractures, orientation of fracture with respect to other fracture as well as with respect to the flow direction, have been successfully incorporated to build this correlation. Results of this correlation have been compared against the laboratory obtained oil relative permeabilities for heterogeneous systems (see **Fig. 2-33**) and an error of 0.03% was found. Though the available information has been intelligently utilised to incorporate the effect of heterogeneity on oil relative permeability, this correlation is limited to the glass bead sizes used in this study (fracture to matrix permeability ratio) and the length of fracture.

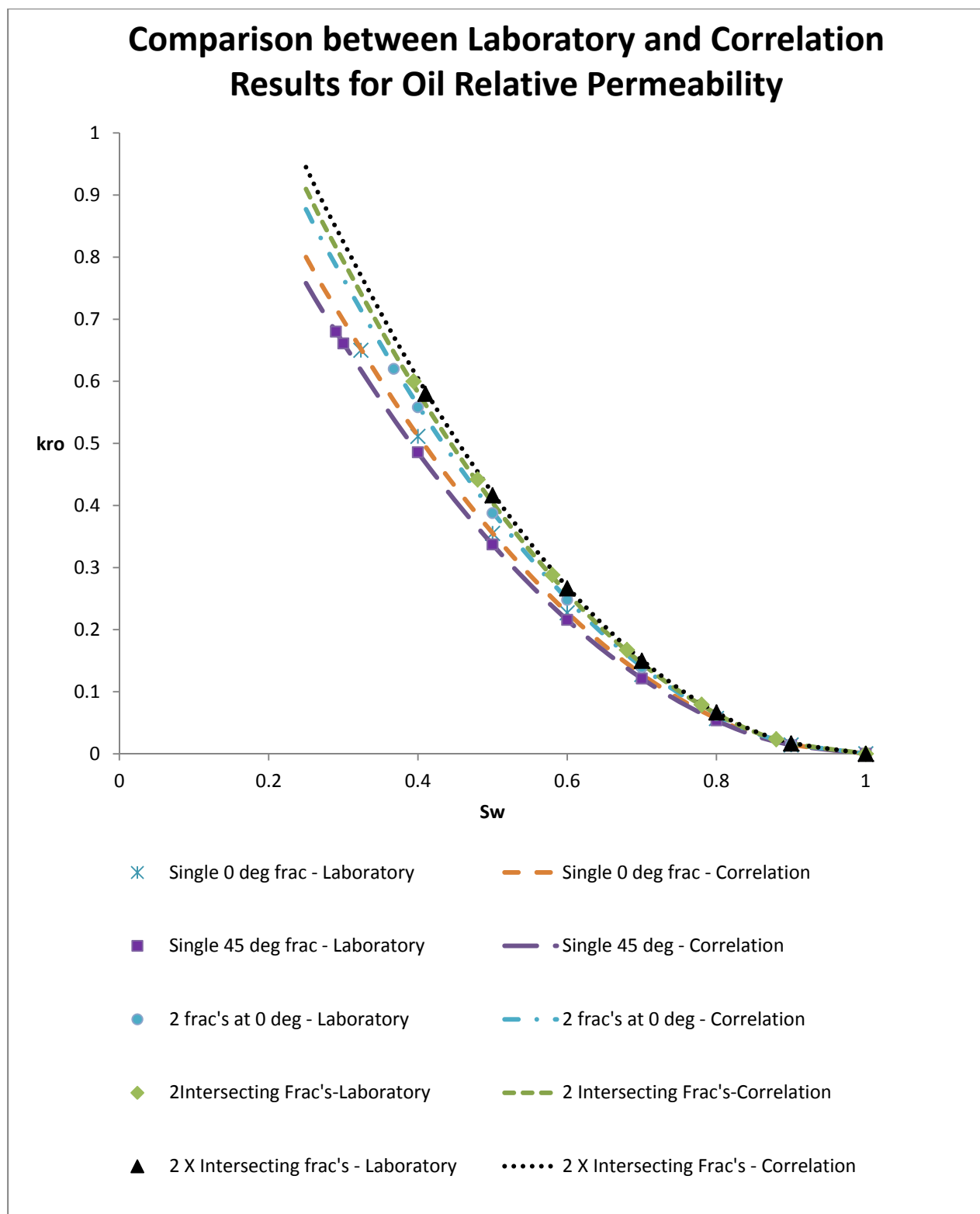


Figure 2-33: Oil relative permeability: a comparison between laboratory and correlation results

Chapter 3

Fluid Flow Simulation in Arbitrarily-Oriented Naturally Fractured Reservoirs

3.1 Calculation of Grid based Permeability Tensors for Fractured Porous Media

3.1.1 Literature Review

Simulation of fluid flow and estimation of pressure and velocity profiles in naturally fractured reservoirs have always been a challenge for reservoir engineers for the past decades. Three different approaches have been used to model fluid flow through naturally fractured reservoirs: Single continuum approach, dual continuum approach and discrete fracture approach.

Continuum Approaches

Continuum approaches are well known for simulating fluid flow through naturally fractured reservoirs over last few decades. These approaches are comprised of single, dual and multiple continuum approaches.

In single continuum approach fractured medium is represented by an equivalent porous medium while the bulk macroscopic properties of fracture are replaced by averaging the point to point variations in petro-physical properties over a representative volume. Defining representative elementary volume (REV) is challenging in this approach (**Fig. 3-1**).

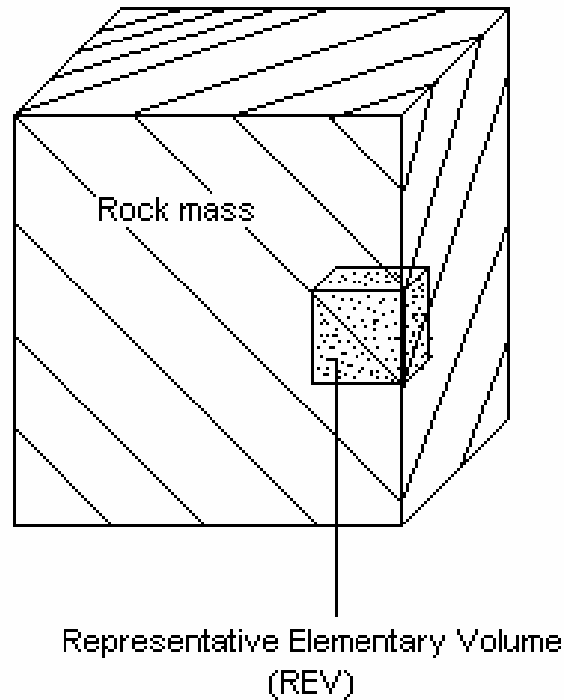


Figure 3-1: REV in a rock mass (Chen et al. 1999)

REV is determined by measuring the permeability of samples with different volumes of a rock achieving statistically a volume for which the permeability is constant and observing that even the sample volume is increased, the permeability remains the same (**Fig. 3-2**). It's easy to achieve REV for homogeneous rocks (**Fig. 3-2(a)**) but for heterogeneous rocks it's hard to achieve a volume of sample (**Figure 3-2(b)**) for which the permeability remains constant because of complex nature of discontinuities present inside the samples.

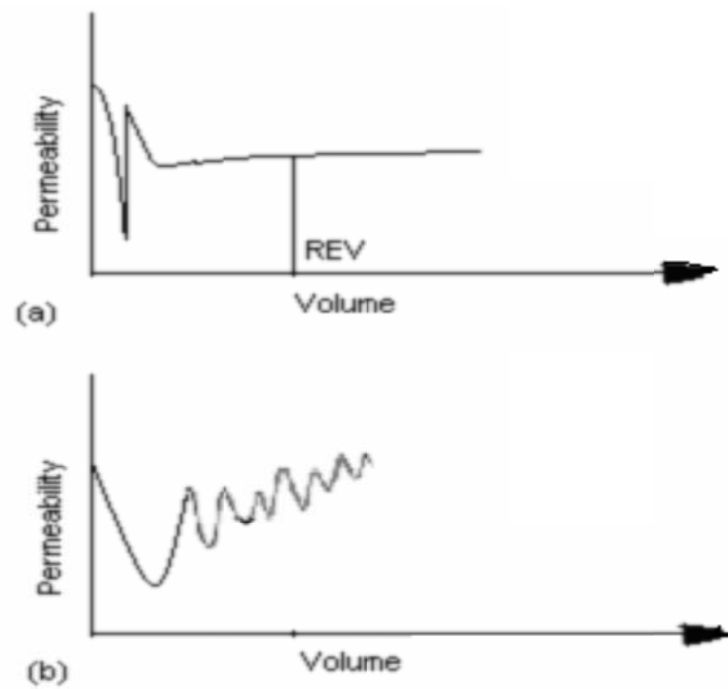


Figure 3-2: Statistical representation of REV for (a) homogeneous and (b) heterogeneous rocks (Kunkel et al. 1988).

Long et al. (1982), Kunkel (1988), Schwarts and Smith (1988), Lee and Farmer (1993), and Therrien and Sudickey (1996) used the concept of single continuum approach for fractured porous media. Kunkel (1988) proved that the higher the discontinuity spacing inside a fractured rock, the larger the size of REV will be. Later it was proved by Lee and Farmer (1993) that REV for fractured rock should be large enough to include sufficient fracture intersections to maintain a constant permeability if a small volume of rock is added or subtracted from REV (**Fig. 3-3**).

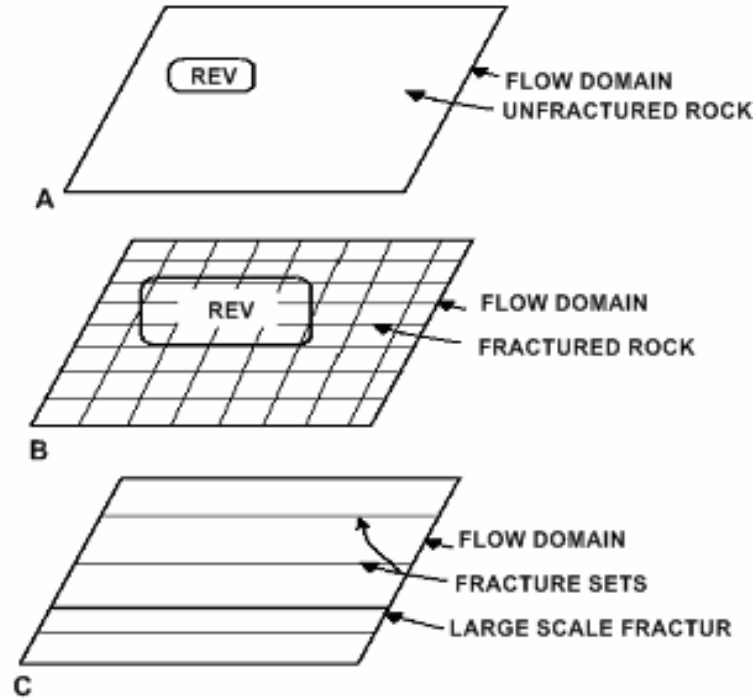


Figure 3-3: Size of REV for different rocks (a) Non-Fractured rock (b) high density of fractures (c) low density of fractures (REV is large or non-existent) (Kunkel et al. 1988); (Lee and Farmer 1993)

The dual-continuum method is conceptually appealing and computationally much less demanding than the discrete-fracture approach. In particular, it is able to handle fracture-matrix interactions more easily than the discrete-fracture model. For these reasons, the dual-continuum approach has currently become the main approach for modelling fluid flow, heat transfer, and chemical transport through fractured reservoirs. Based on the dual continuum approach, a conceptual model of original fractured rock is presented in **Fig. 3-4** where based on the finite element method, a technique was suggested for a heterogeneous porous medium and each fracture element is sandwiched between matrix (Park and Sung 2000).

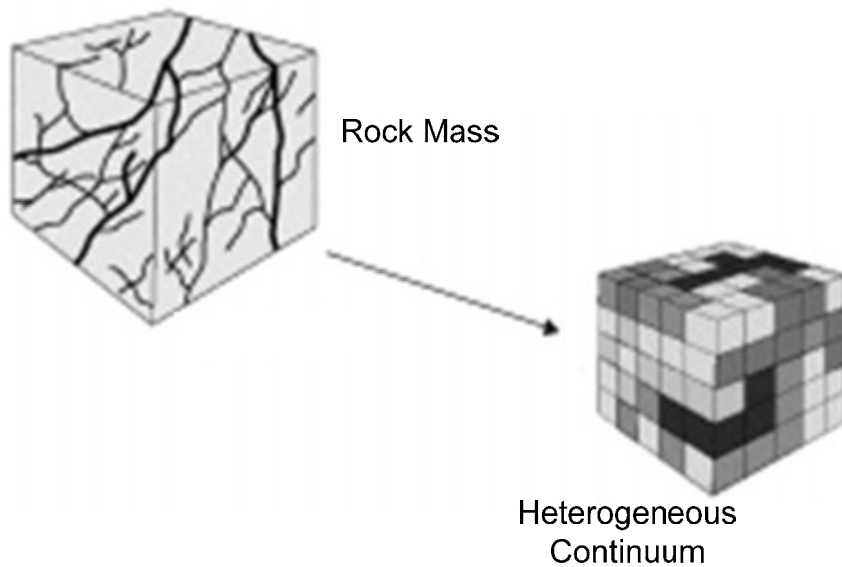


Figure 3-4: Conceptual model of fractured rock (Park and Sung 2000)

The classical dual-porosity model for single phase systems emerged as an initial dual-continuum approach in early 1960s (Barenblatt et al. (1960); Warren and Root (1963)). In this model rectilinear prisms of matrix are separated by an orthorhombic continuum representing fractures (i.e. the sugar-cube-model) as shown in **Fig. 3-5**. Dual porosity approach involves discretisation of a reservoir into two domains, matrix and fracture however, flow occurs through fractures and matrix provide fluid storage. Interconnected fractures provide a flow path between the injection and production wells and are assumed to be completed in the fracture domain. The model treats matrix blocks as spatially distributed sinks or sources to the fracture system without accounting for global matrix-matrix flow. However, the model does account for fracture-matrix interflow, based on a quasi-steady state assumption.

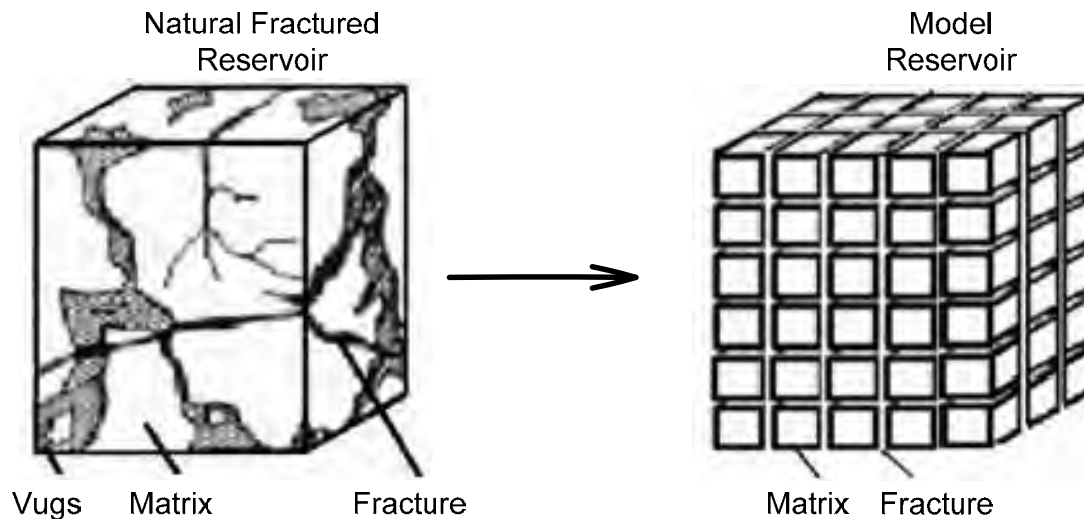


Figure: 3-5: Dual porosity model description of a naturally fractured reservoir (Warren and Root 1963)

In an attempt to incorporate additional matrix-matrix interactions, a dual-permeability model was developed (Pruess 1991). This model considers global flow occurring not only between fractures but also between matrix grid blocks. In this approach, the fractures and matrix are represented by separate grid blocks that are connected to each other. The same quasi-steady state flow assumption as in the dual-porosity model is used to handle the fracture-matrix interflow.

As a generalization to the dual-porosity model, a more rigorous dual-continuum method, the Multiple Interacting Continuum (MINC) concept (Pruess and Narasimhan (1985)), describes gradients of pressures, temperatures, and concentrations between fractures and matrix by further subdividing individual matrix blocks. This approach provides a better approximation for transient fracture-matrix interactions than the quasi-steady state flow assumption used by Warren and Root (1963) for the dual-porosity or dual-permeability model. Fluid and heat flow and transport from the fractures into the matrix blocks can be modelled by means of one- or multidimensional strings of nested grid blocks.

As an alternative method, the Effective Continuum Method (ECM) represents fractures and rock matrix as a single effective continuum. ECM models have long been used for modelling fracture-matrix flow because of their simplicity in data requirements and their computational efficiency. This approach may be applicable to modelling multiphase, no isothermal flow and solute transport in fractured porous media under thermodynamic equilibrium conditions (Wu 2000). When rapid flow and transport processes occur in many subsurface fractured reservoirs, however, thermodynamic equilibrium conditions can not be satisfied in general.

The main drawback of the dual-continuum approach is the concern for fluid flow while ignoring characteristics of individual fractures and their geometry. In fact, majority of the computational effort is used to solve simple mathematical formulations for simulation of fluid flow in fractured reservoirs by assuming matrix and fractures as parallel layers with an infinite length. Based on the geometrical assumptions, the continuum approaches are not considered the best suitable for detailed modelling of naturally fractured reservoirs.

Discrete Fracture Approach

The discrete fracture model (DFM) approach, an alternative to the dual continuum approach, has received considerable interest over last few years in the field of reservoir simulation and hydrology. Outcrop characterization studies have shown that natural fractures vary substantially in height, length, and aperture and fracture networks are complicated due to varying fracture spacing as well as connectivity (Marrett and laubach (1997); Gillespie et al. (1993); Odling (1997); and Odling et al. (1999) This understanding of fracture characterisation emphasizes on the large discrepancy between reality and the assumed inherent uniformity of dual continuum approach. Therefore, the discrete fracture models have been developed to reduce the number of non-physical abstractions inherent in dual continuum models. Most of the DFMs are based on unstructured grids to explicitly represent a fracture

network. A 3D conceptual model representation of DFM approach is shown in **Fig. 3-6**, in which disc-shaped original fracture network with their actual length, orientation, spacing and connectivity are presented (Park and Sung 2000).

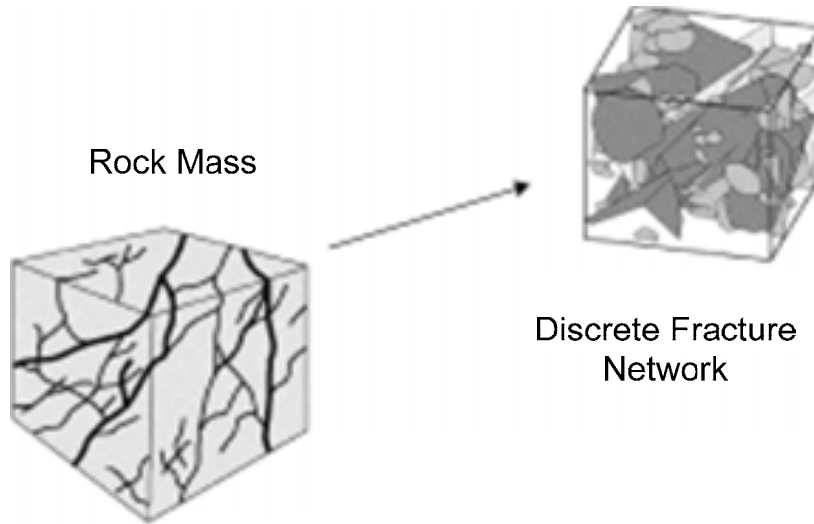


Figure 3-6: Conceptual model of fractured rock (DFM) (Park and Sung 2000)

Depending on the source and availability of information of fracture properties, discrete models are presented in three different forms: deterministic, stochastic and heuristic. Each technique is based on a theoretical, numerical, exact or approximate method.

The deterministic method is based on the geological model of reservoir which is simplified enough to be able to find an exact analytical solution. On the other hand stochastic methods assume an approximate knowledge of the reservoir model and are based on probability to study random functions in the space. Finally the widely used heuristic discrete methods propose rules for calculating reasonable equivalent permeability. The mainly implemented heuristic methods are sampling, averaging means, power average and flexible grid methods.

The discrete fracture model approach offers several advantages as compared to the dual-continuum approach. This approach can simulate the realistic fracture system geometry, and hence accounts explicitly for the effect of individual fracture on fluid flow simulation. Also

this approach is not bound by the grid defined fractured geometry constraints so the fracture network can easily be updated and adapted. And last but not the least advantage of this approach is the simplicity of its implementation for flow interaction between matrix and fracture as it depends directly on fracture geometry. On the other hand, a disadvantage associated with DFMs is complex discrete system of equations which is difficult to solve numerically. Though discrete fracture models account for fracture geometry and the formulations are based on properties of fracture, however, this approach does not account for the effect of matrix permeability and isolated fractures.

An excellent comparison between dual continuum approach and new discrete fracture models is recently provided by Moinfar et al. (2011). To study the behaviour of NFR's they introduced two different and independent DFMs where one model is based on an unstructured gridding with local refinement around fractures while, in the other model, fractures are embedded in a structured matrix grid. They concluded that both DFMs captured the complexity of a typical fractured reservoir better than conventional dual permeability models. They claimed that DFMs can be used as basis for defining the dual permeability model parameters for a very sparse fractured system relative to the grid spacing.

Models using Effective permeability Tensor

Concept of effective permeability tensor was introduced to complete the task of modelling naturally fractured reservoirs which have not been succeeded in the previous works. Continuum models do not take into account the actual geometry of individual fractures, while discrete fracture approaches don't account for matrix permeability and ignore the effect of isolated/disconnected fractures. A complete task of modelling NFRs can be achieved by employing the concept of grid based effective permeability tensor which enables to replace a fractured grid block with a homogeneous block of equivalent permeability. This concept

includes the actual geometry of fracture networks as well as the matrix permeability while ignoring the complexities involved in previously mentioned approaches and hence becomes the best suitable method for modelling NFRs.

Several methods have been proposed to calculate effective permeability tensor. Oda (1985) introduced a method for calculating equivalent permeability tensor of a fractured reservoir using the geometry of fracture network. The method does not require a flow simulator to obtain the permeability tensor; also it does not account for the fracture connectivity; and thus, it is limited to well-connected fracture networks. In other words, it would underestimate equivalent fracture permeability when fracture density is low.

Long and Witherspoon (1985) and Cacas et al. (1990) developed 3D fracture flow models and then Massonnate and Manisse (1994) introduced a 3D fracture flow model which takes into account the matrix permeability. Lough et al. (1998) developed a 2D fracture flow model taking into account the contribution of 3D matrix flows. Odling (1992) introduced a 2D model by considering the matrix permeability. Later, Bourbiaux et al. (1998) proposed a method to calculate the equivalent permeability by applying a pressure drop between the two sides of the parallelepiped network with a specific boundary condition. Using their model, the equivalent permeability for incompressible steady-state flow through the actual 3D fracture network can be calculated.

Fracture connectivity controls many principle properties of fractured reservoirs and the permeability is the most critical one (Berkowitz 1995). For example, Long and Billaux (1987) observed that, due to low fracture connectivity at a field site in France, roughly 0.1% of fractures contribute to the overall fluid flow (i.e., permeability). This parameter, however, is difficult to quantify and embedded in the fracture network permeability correlations. Other parameters including fracture length, density, aperture and orientation also affect the equivalent fracture network permeability.

Semi-quantitative analyses have shown that fracture network characteristics have direct implications on the fracture network permeability. Basically, fracture connectivity, length, density, aperture, and orientation are the crucial parameters of each fracture network controlling the permeability of the network. For instance, Babadagli (Babadagli 2001) speculated that perpendicular fractures to the direction of the flow probably reduce the permeability. Also, as fracture length and density increase, the connectivity of a fracture network will increase (Rossen et al. (2000)); and the hydraulic properties of fractured reservoirs are primarily dependent on the degree of fracture interconnection. A fracture network must have a percolating cluster to be permeable. Hence, the connectivity is of the primary importance in this analysis. Zhang et al (1996) showed that with an increase in fracture aperture and density, permeability of the network also increases.

Min et al. (2004) presented a method to calculate equivalent fracture permeability tensor of fractured rocks using stochastic representative elementary volume (REV) approach. In their method, the equivalent permeability values were calculated using the two-dimensional distinct element code UDEC (Itasca 2000). Nakashima et al. (2000; Nakashima et al. 2001) presented an up-scaling technique by the boundary element method to estimate the effective permeability of naturally fractured reservoirs. Teimoori et al. (2003) used the same method to improve the computation of effective permeability tensor in naturally fractured reservoirs.

It was mentioned that some previous works did not include fluid flow in the matrix as well as flow interaction between matrix and fracture such as snow's model (1969) . On the other hand some methods (Dual porosity / Permeability approach) do not take into account the properties of individual fractures such as orientation, aperture and size of fracture. One of the most efficient method was presented by Lough et al. (1998) where fractures were treated as planar sources inside the matrix. The drawback associated with this method is that it can be applied to only medium sized fractures because it needs discretisation of the whole matrix

block. Also Teimoori et al. (2003) improved the work and presented an extended numerical work including properties of individual fracture as well as computational efficiency. But the solution was unstable because of the use of quadrature based formula to solve integral equations.

In this study, the solution process for integral equations has been significantly improved by employing weighted residual method, e.g. the collocation method. Boundary element technique is applied efficiently as a numerical method to calculate full effective permeability tensor for different fracture systems with variable lengths, size and orientation present in a grid block. In this approach the reservoir is divided into small grid blocks of fixed lengths and widths. Short fractures are considered as part of matrix for each grid block. Laplace equation is used to simulate fluid flow through matrix and periodic boundary conditions are applied across the boundary of the grid block to calculate matrix (local) permeability. Next Poisson's equation is used to simulate fluid flow at matrix fracture interface and cubic law is used to calculate the effective permeability for medium and long fractures. Use of periodic boundary conditions around the boundary of grid block and different boundary conditions for short and medium fractures makes the numerical model efficient in calculating a symmetric, positive-definite permeability tensor.

3.1.2 Mathematical Formulation

Effective Permeability Tensor

Permeability tensor is an equivalent, effective, or homogenised permeability of a fractured grid block. Effective permeability tensor is expressed as the directional permeability for a block containing fractures. For a three dimensional reservoir it is described as:

$$\vec{k} = \begin{bmatrix} k_{xx} & k_{xy} & k_{xz} \\ k_{yx} & k_{yy} & k_{yz} \\ k_{zx} & k_{zy} & k_{zz} \end{bmatrix} \quad (3-1)$$

In this study, effective permeability tensor for two-dimensional fractured reservoir is calculated and presented, which is expressed as:

$$\vec{k} = \begin{bmatrix} k_{xx} & k_{xy} \\ k_{yx} & k_{yy} \end{bmatrix} \quad (3-2)$$

where, k_{xx} and k_{yy} are the diagonal components and k_{xy} & k_{yx} are the off diagonal components of permeability tensor. The effective permeability tensor needs to be symmetric and positive definite to have physical meaning, i.e. $k_{xy} = k_{yx}$ and $k_{xx}k_{yy} \geq k_{xy}^2, k_{xx} > 0$ & $k_{yy} > 0$ (Durlofsky 1991).

Calculation of Effective Permeability

In this approach a grid block containing arbitrarily oriented fractures is replaced by a homogeneous grid block with an equivalent permeability. To achieve this, effective grid block permeability should be computed taking into account the actual geometry of arbitrary

fractured system in the grid block. In this way, the calculated effective grid block permeability will retain the information about the complexity of fractured network that was initially present in the grid block.

It is acknowledged that in reservoir simulation the homogenized matrix-fracture system may lead to imprecise predictions of quantities such as breakthrough times. However, it should be remembered that even if an exact calculation was possible, a precise computation of the breakthrough time would require detailed knowledge of actual fracture system. Such knowledge is seldom, if ever available. Consequently, it is felt that, on average, the homogenized fracture-matrix system will provide meaningful predictions of the important quantities in reservoir simulation (Lough et al. (1998)).

In this section all the equations related to the calculation of effective permeability tensor are presented. Effective permeability tensor for fractured porous media is calculated by solving single phase fluid flow equations where periodic boundary conditions are applied over the boundaries of a grid block. Darcy's law for fluid flow through porous media is expressed as:

$$v = -\frac{\vec{k}}{\mu} \frac{\partial P}{\partial x} \quad (3-3)$$

where v represents the velocity, \vec{k} is the effective permeable tensor, μ is the fluid viscosity and P is the pressure. Assuming unit fluid viscosity ($\mu = 1$) i.e. for water, the equation can be written as:

$$v = -\vec{k} \nabla P \quad (3-4)$$

In fluid dynamics, the continuity equation states that, in any steady state process, the rate at which mass enters a system is equal to the rate at which mass leaves the system. The differential form of the continuity equation is:

$$\frac{\partial \rho}{\partial t} + \nabla \cdot (\rho v) = 0 \quad (3-5)$$

where ρ is the fluid density, t is the time, and v is the flow velocity vector field. If density (ρ) is a constant, as in the case of incompressible flow, the mass continuity equation simplifies to a volumetric continuity equation as follows:

$$\nabla \cdot v = 0 \quad (3-6)$$

This means that the divergence of velocity field is zero everywhere in the field.

If Q represents the flow rate through any source / sink available in the field, then the continuity equation will be written as follows:

$$\nabla \cdot v = Q \quad (3-7)$$

Now the equation representing single phase flow for incompressible fluid can be obtained by combining Darcy's law (3-4) and continuity equation (3-7) as follows:

$$\nabla \cdot \left[\bar{k}(\nabla P) \right] + Q = 0 \quad (3-8)$$

For an isotropic medium this equation can be rewritten in an expanded three dimensional form as:

$$k_x \frac{\partial^2 P}{\partial x^2} + k_y \frac{\partial^2 P}{\partial y^2} + k_z \frac{\partial^2 P}{\partial z^2} + Q = 0 \quad (3-9)$$

Rasmussen et al. (1987) presented a method to calculate the effective permeability for fractured blocks, but matrix and fracture were treated as two separate systems. Then Lough et al. (1998) improved the work in several ways whereby matrix and fracture systems have a common interface. The common interface is made up of those parts of fracture boundaries

that are contained in the matrix (Lough et al. (1998)). Fluid flow and pressure equations for matrix as defined by Lough et al. (1998) are as follows:

$$v_m(x) = -k_m \nabla P_m(x) \quad (3-10)$$

$$\nabla v_m(x) = 0 \quad (3-11)$$

where v_m represents the velocity in matrix, k_m the matrix permeability, and P_m the matrix pressure.

Figure 7 shows a discretization of matrix and fractures present in a block using the boundary element method for a two-dimensional problem.

The final equation for flow through matrix (region 3) can be obtained by combining equation 10 and 11 which is a well-known Laplace's equation:

$$k_m \frac{\partial^2 P_m}{\partial x^2} + k_m \frac{\partial^2 P_m}{\partial y^2} = 0 \quad (3-12)$$

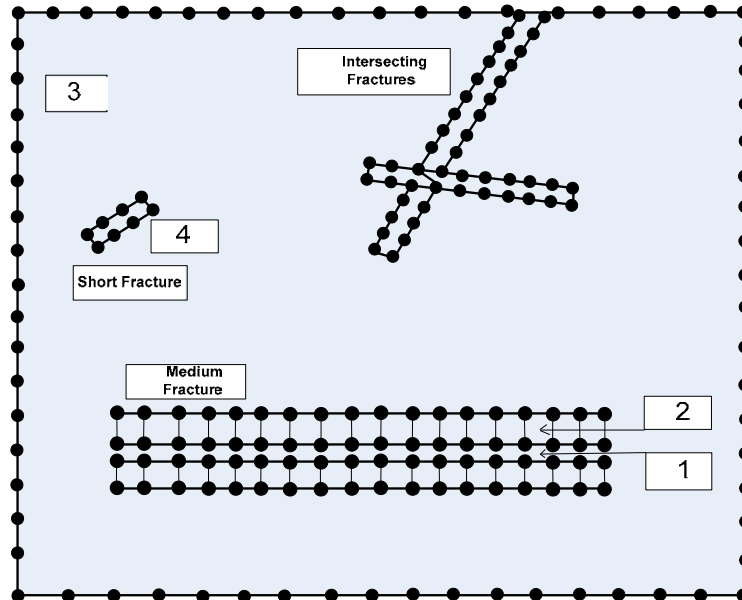


Figure 3-7. Discretization of grid block and different fractures present in it in two dimensions

The interface between matrix and fracture (medium and long fractures), region 2 in **Fig. 3-7** is named as Poisson's region, where fluid flow is modelled separately as flow in this region is affected due to the high conductivity of fracture. Equation 3-11 can be modified for medium fractures by applying source term of Poisson's equation to the matrix porous media around the medium sized fractures (Poisson's region), so equation 3-11 is rewritten as follows (Lough et al.(1998)):

$$\nabla \cdot v_m(x) = \sum_{j=1}^N \int_{F_i} q_j(x(z)) \delta(x_o - z) dA_z \quad (3-13)$$

where q_j is the flow interaction between matrix and fracture in element j of fracture F_i . $\delta(.)$ is the Dirac delta function and A is the area of element j . Equations 8 and 13 can be combined to achieve a final equation for a medium sized fracture (region 2 in **Fig. 3-7**) as given below:

$$k_m \frac{\partial^2 P_m}{\partial x^2} + k_m \frac{\partial^2 P_m}{\partial y^2} + Q(x) = 0 \quad (3-14)$$

where k_m is the matrix permeability while $Q(x) = Q_m$ where Q_m represents the flow from matrix to fracture. Flow through medium and long fractures (region 1 in **Fig. 3-7**) is modelled by a modified equation 3-14 such as fracture permeability and its source strength Q_{f_i} is used as given below (Teimoori et al.(2003)):

$$k_f \frac{\partial^2 P_{f_i}}{\partial L^2} + Q(x) = 0 \quad (3-15)$$

In this equation P_{f_i} represents the pressure for fracture i , k_f is the fracture permeability, L is the length of fracture and $Q(x) = Q_{f_i}$ where Q_m represents the flow from fracture to matrix.

Flow through medium and long fractures is considered similar to the flow between a pair of

parallel plates as fracture aperture is assumed very small. Cubic law defines the permeability of fracture (Binder, 1958). Fracture permeability k_f is defined by Teimoori et al.(2003) & Lee et al. (2001) as;

$$k_f = \frac{h_f^2}{12} \quad (3-15a)$$

where h_f is fracture aperture (m) and k_f is fracture permeability (m^2).

For this fracture if intersected by many different fractures, $Q(x)$ will be equal to $Q_i + q_{ff}$, where q_{ff} represents the flow from intersected fracture to the fracture i . Now equation 3-15 can be rewritten for intersecting fractures as:

$$k_f \frac{\partial^2 P_{f_i}}{\partial L^2} + Q_i + q_{ff} = 0 \quad (3-16)$$

If a medium fracture i is intersected by other fractures for an instance at m_i intersection points on a line of intersection L then q_{ff} is expressed as (Lough et al.(1998)):

$$q_{ff} = \sum_{j=1}^{m_i} \int_{L_i^j} q_i^j(x_o) \delta(x - x_o) dl(x_o) \quad (3-17)$$

where x and x_o represent the position vectors for points on fracture i , $\delta(\cdot)$ represents the Dirac delta function and j is the number of intersections on line L .

Short fractures (see **Fig. 3-7**) are treated as large pores inside matrix and hence source term $Q(x)$ is ignored, and Laplace's equation for short fractures becomes:

$$k_f \frac{\partial^2 P_f}{\partial x^2} + k_f \frac{\partial^2 P_f}{\partial y^2} = 0 \quad (3-18)$$

Boundary Conditions

Interface boundary conditions are applied to the boundaries of short fractures, which are expressed as (Teimoori et al. 2003; Teimoori et al. 2005):

$$P_{m_i} = P_{f_i}$$

$$v_{m_i} = -v_{f_i}$$

where P_{f_i} is the pressure at boundary of fracture i and P_{m_i} the corresponding matrix pressure as matrix and fracture are sharing same node at matrix-fracture interface.

$$v_{m_i} = \vec{v}_m \cdot \vec{n}$$

$$v_{f_i} = \vec{v}_f \cdot \vec{n}$$

where \vec{v}_m and \vec{v}_f are the normal velocity vectors at matrix-fracture interface.

Long fractures are the fractures which have the length exceeding the block length. Following are the boundary conditions for medium and long fractures (Teimoori et al. 2005):

$$P_{fi} = P_{av}$$

$$v_{mi}^+ - v_{mi}^- = Q_i$$

where $v_{mi}^+ = \vec{v}_m^+ \cdot \vec{n}$, $v_{mi}^- = \vec{v}_m^- \cdot \vec{n}$, \vec{v}_m^+ and \vec{v}_m^- are the velocity vectors on the opposite nodes of fracture faces with \vec{v}_{mi}^+ and \vec{v}_{mi}^- as their corresponding normal, respectively. Q_i is the flow interaction between the matrix m and fracture i which depends on the source strength

of the fracture. P_{av} is the average pressure inside the fracture and P_{fi} is the pressure along boundaries of fracture i .

Considering all kind of discontinuities present inside a grid block, we apply periodic boundary conditions along the boundaries of grid block as described by Lough et al. (1998).

Figure 3-8 shows periodic boundary conditions where, Γ_1 and Γ_2 are the two opposite boundaries of grid block in the x_2 direction, while Γ_3 and Γ_4 are the opposite boundaries in the x_1 direction.

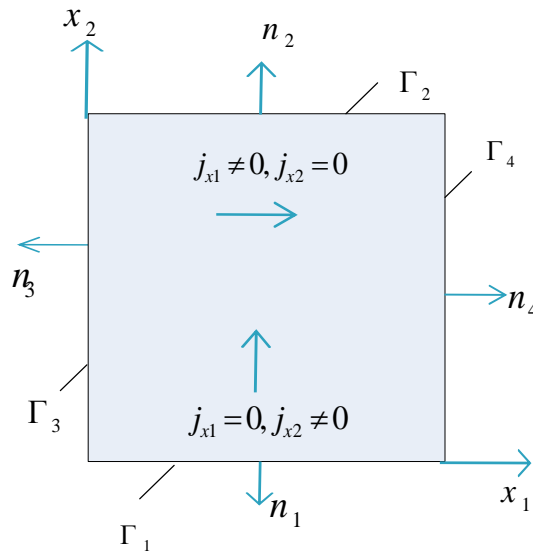


Figure 3-8: Periodic boundary conditions over a grid block

If x_0 is the centre point of grid block, and pressure at this center point is P_0 then pressure at any given point $x = (x_1, x_2)$ inside the grid block is defined as:

$$P(x) = P_0 + J(x - x_0) \quad (3-19)$$

where, J is the local pressure gradient for a unit cell ($\Delta x_1 = 1$ & $\Delta x_2 = 1$) defined in two directions x_1, x_2 as: J_{x_1} the pressure gradient in the x_1 direction, J_{x_2} the pressure gradient in the x_2 direction:

$$J_{x_1} = P(x_1 = 1, x_2) - P(x_1 = 0, x_2) \quad (3-20a) \quad \text{For } \Gamma_3 \text{ and } \Gamma_4$$

$$J_{x_2} = P(x_1, x_2 = 1) - P(x_1, x_2 = 0) \quad (3-20b) \quad \text{For } \Gamma_1 \text{ and } \Gamma_2$$

Also, velocities normal to the grid block boundaries are:

$$v(x_1 = 0, x_2) \cdot \vec{n}_3 = -v(x_1 = 1, x_2) \cdot \vec{n}_4 \quad (3-20c) \quad \text{For } \Gamma_3 \text{ and } \Gamma_4$$

$$v(x_1, x_2 = 0) \cdot \vec{n}_1 = -v(x_1, x_2 = 1) \cdot \vec{n}_2 \quad (3-20d) \quad \text{For } \Gamma_1 \text{ and } \Gamma_2$$

Durlofsky(1991) presented a solution for the calculation of average velocity through a unit cell after applying periodic boundary conditions as mentioned above:

$$\langle v_1 \rangle = - \int_{\Gamma_3} v \cdot \vec{n}_3 dx_2 \quad (3-21)$$

$$\langle v_2 \rangle = - \int_{\Gamma_1} v \cdot \vec{n}_1 dx_1 \quad (3-22)$$

Once v_1 and v_2 are calculated then it becomes easy to calculate permeability tensor using the explicit form of equation 3-4 for pressure gradient in the x_1, x_2 directions:

$$\langle v_1 \rangle = -(k_{xx} J_{x1} + k_{xy} J_{x2}) \quad (3-23)$$

$$\langle v_2 \rangle = -(k_{yx} J_{x1} + k_{yy} J_{x2}) \quad (3-24)$$

Applying periodic boundary conditions $J_{x1} \neq 0, J_{x2} = 0$ in above equations k_{xx}, k_{yx} are calculated. Applying the conditions of $J_{x1} = 0$ and $J_{x2} \neq 0$ gives k_{xy}, k_{yy} .

Boundary Integral Equations

To solve the above two dimensional equations using any numerical technique, it is necessary to solve the related integral equations in an efficient way to achieve reasonable accuracy for a heterogeneous grid block with large number of fractures. Boundary integral equations are solved using Green's second identity for a regular function which is a fundamental solution. A fundamental solution is a function that satisfies a differential equation with zero right hand side at any point of an infinite domain except at points known as source or sink, where the right hand side is infinite (Beer 1992).

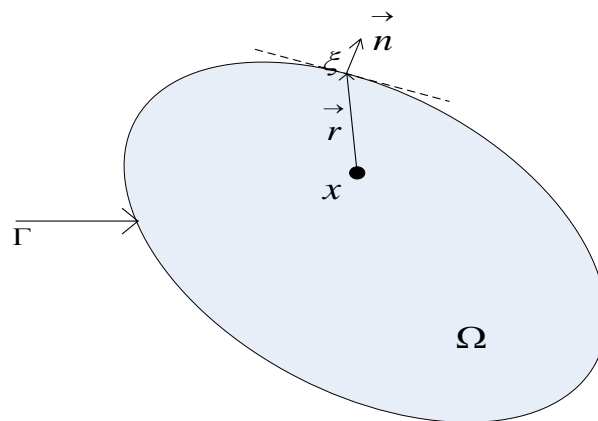


Figure 3-9: Arbitrary point on domain, Ω

In order to explain this further let's consider a domain Ω as shown in **Fig. 3-9** and $\xi(\xi_1, \xi_2)$ is an arbitrary point present on the boundary Γ of domain Ω . Fundamental solution as defined by Gaul et al. (2004) is given by:

$$u^*(\vec{x}, \vec{\xi}) = -\frac{1}{2\pi} \ln \left| \vec{x} - \vec{\xi} \right| \quad (3-25)$$

$$q^*(\vec{x}, \vec{\xi}) = -\frac{1}{2\pi \left| \vec{x} - \vec{\xi} \right|^2} (\vec{x} - \vec{\xi}) \cdot \vec{n} \quad (3-26)$$

The boundary integral equation for the linear Poisson's equation when applying to an arbitrary point $\xi(\xi_1, \xi_2)$ on the boundary Γ of domain Ω is:

$$c(\xi).u(\xi) = -\int_{\Gamma} u(\vec{x}) q^*(\vec{x}, \vec{\xi}) d\Gamma_x + \int_{\Gamma} q(\vec{x}) u^*(\vec{x}, \vec{\xi}) d\Gamma_x + \int_{\Omega} Q(\vec{x}) u^*(\vec{x}, \vec{\xi}) d\Omega_x \quad (3-27)$$

where, $q(\vec{x}) = k \nabla u(\vec{x}) \cdot \vec{n}$, \vec{n} is the exterior normal vector of Γ at ξ and k is the permeability.

$u^*(\vec{x}, \vec{\xi})$ is the fundamental solution mentioned above, $q^*(\vec{x}, \vec{\xi})$ is the flux corresponding to the fundamental solution and is obtained by taking derivative of fundamental solution,

$q^* = k \frac{\partial u^*}{\partial n}$. $Q(\vec{x})$ is equal to the Dirac Delta function $\sigma(\vec{x} - \vec{\xi})$. $c(\xi)$ is a co-efficient which

is a function of the internal angle of the boundary Γ at point ξ , and is defined as (Gaul et al. 2004):

$$c(\xi) = \begin{cases} 1 - \frac{\alpha}{2\pi} & \text{for } \xi \in \Gamma \\ 1 & \text{for } \xi \in \Omega \\ 0 & \text{for } \xi \notin \Gamma, \xi \notin \Omega \end{cases}$$

As short fractures are treated as pores inside matrix porous media boundary integral equation of Laplace equation can be obtained by omitting the last source term in equation 3-27. So this equation can be re-written for short fractures as:

$$c(\xi).u(\xi) = -\int_{\Gamma} u(\vec{x})q^*(\vec{x},\vec{\xi})d\Gamma_{\vec{x}} + \int_{\Gamma} q(\vec{x})u^*(\vec{x},\vec{\xi})d\Gamma_{\vec{x}} \quad (3-28)$$

Boundary Element Formulation

Boundary Element method (BEM) is developed in the shadow of FEM and FDM to provide an efficient approach for solving boundary integral equations numerically (Brebbia and Walker 1978). BEM treats the problem as a boundary value problem, solves for all the integrals present in the equations for each boundary and reduces complexities associated with meshing (Beer 1992). The advantage of using this method is that it reduces the problem to one dimension and requires the solution of integrals only on the boundary of the domain and sub-domains present inside the domain which is simpler than applying the solution for the whole the domain using FEM or FDM. The disadvantage associated with this numerical method is that it requires the fundamental solution of governing partial differential equations to be known (Gaul et al. 2004).

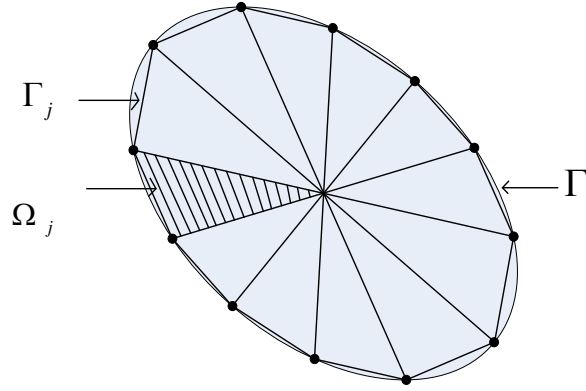


Figure 3-10: Boundary and interior discretization of the domain, Ω

As presented in **Fig. 3-10** domain, Ω has been divided into NT triangular elements, $\Omega_1, \Omega_2, \dots, \Omega_{NT}$ with centers, x_1, x_2, \dots, x_{NT} . Boundary Γ of this domain has been divided into NB intervals, $\Gamma_1, \Gamma_2, \dots, \Gamma_{NB}$. Equation 28 for short fractures will be re-written in discretized form as:

$$c(\xi).u(\xi) + \sum_{j=1}^{j=NB} \int_{\Gamma_j} \vec{u}(\vec{x}) \vec{q}^*(\vec{x}, \vec{\xi}) d\vec{\Gamma}_x = \sum_{j=1}^{j=NB} \int_{\Gamma_j} \vec{q}(\vec{x}) \vec{u}^*(\vec{x}, \vec{\xi}) d\vec{\Gamma}_x \quad (3-29)$$

The Poisson's region around medium to large fractures is well described in **Fig. 3-11** where flow is affected by the fluid flow through fractures. The thickness of this zone 'L2' is assumed to be 1% of the length of element on fracture edge 'L1'. Though it was experimented to change the aspect ratio between 1-4% however, the error in the result never found to be more than 1%.

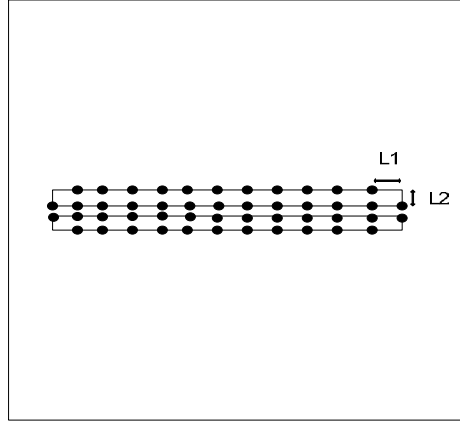


Figure 3-11: Description of aspect ratio representing thickness of Poisson's region

Equation 3-27 for medium to large fractures and region around these fractures (Poisson's Region) can be written in discretised form as:

$$c(\xi).u(\xi) + \sum_{j=1}^{j=NB} \int_{\Gamma_j} u(\vec{x}) q^*(\vec{x}, \vec{\xi}) d\vec{\Gamma}_x = \sum_{j=1}^{j=NB} \int_{\Gamma_j} q(\vec{x}) u^*(\vec{x}, \vec{\xi}) d\vec{\Gamma}_x + \sum_{i=1}^{i=NT} \int_{\Omega_i} Q(\vec{x}) u^*(\vec{x}, \vec{\xi}) d\vec{\Omega}_x \quad (3-30)$$

So far these equations are written for an arbitrary point on the boundary Γ of a domain, Ω .

Now the point is shifted to the middle of each element of Γ_j (see **Fig. 3-10**). Let's suppose

ζ_j is the midpoint of Γ_j and the values of u, q and Q at these midpoints of each element are constant, so $u_i = u(\zeta) = u(\xi) \forall \xi \in \Gamma_j$, $q_i = q(\zeta) = q(\xi) \forall \xi \in \Gamma_j$ and $Q_i = Q(\zeta) = Q(\xi) \forall \xi \in \Omega_j$.

If all the constant values are taken out of integrals, the last equation can be re-written as:

$$c_i . u_i + \sum_{j=1}^{j=NB} u_j \int_{\Gamma_j} q^*(\vec{x}, \vec{\zeta}_i) d\vec{\Gamma}_x = \sum_{j=1}^{j=NB} q_j \int_{\Gamma_j} u^*(\vec{x}, \vec{\zeta}_i) d\vec{\Gamma}_x + \sum_{l=1}^{l=NT} Q_l \int_{\Omega_l} u^*(\vec{x}, \vec{\zeta}_i) d\vec{\Omega}_x \quad (3-31)$$

where, $c_i = \frac{1}{2}$ by substituting interior angle $\alpha = \pi$

$\int_{\Gamma_j} u^*(\vec{x}, \vec{\zeta}_i) d\Gamma_x$ and $\int_{\Gamma_j} q^*(\vec{x}, \vec{\zeta}_i) d\Gamma_x$ represent a relation between node i and element j over

which the integral is going to be calculated. u , q and Q are the pressure, velocity and matrix-fracture flow interaction, respectively, for each element of Γ_j . Equation 21 can be written in a matrix form as:

$$H \vec{u} = G \vec{q} + b \quad (3-32)$$

Solving these equations by applying periodic boundary conditions around grid block boundary in conjunction with boundary conditions along the fracture boundaries, all the unknowns, therefore pressure and normal velocity at grid block boundaries, pressure and velocity at fracture boundaries, flow rate inside fracture and at the line of intersection of fractures can now be calculated.

3.1.3 Results and Discussion

Validation of Numerical Results

First the numerical results are checked for consistency using an analytical formula. Next the results are validated using new laboratory studies (see chapter 2).

The purpose of this section is to analyse comparatively the results of the written numerical algorithm against an analytical formula which is believed to be a useful tool for measuring the consistency of the variation in the effective permeability by varying the angle of fracture (Lough et al. (1998)). The same analytical method has been used by Lough et al. (1998) and Teimoori et al. (2003) and its use in their studies is the same to show the accuracy in numerical results.

As it is known that effective grid block permeability is dependent on the fracture orientation so it is written as:

$$K(\theta) = \begin{bmatrix} K_{xx}(\theta) & K_{xy}(\theta) \\ K_{yx}(\theta) & K_{yy}(\theta) \end{bmatrix} \quad (3-33)$$

However, for a horizontal fracture $\theta = 0$, the effective permeability tensor is written as:

$$K(0) = \begin{bmatrix} K_1 & 0 \\ 0 & K_2 \end{bmatrix} \quad (3-34)$$

Now the components of permeability tensor in equation 33 can be written as follows:

$$K_{xx}(\theta) = K_1 \cos^2 \theta + K_2 \sin^2 \theta \quad (3-35)$$

$$K_{xy}(\theta) = K_{yx}(\theta) = (K_1 - K_2) \sin \theta \cos \theta \quad (3-36)$$

$$K_{yy}(\theta) = K_1 \sin^2 \theta + K_2 \cos^2 \theta \quad (3-37)$$

In order to produce consistent numerically estimated permeabilities for different fracture orientations following analytical equation is used (Lough et al. (1998)):

$$K = \begin{bmatrix} k_{xx} \cos^2 \theta + k_{yy} \sin^2 \theta & (k_{xx} - k_{yy}) \sin \theta \cos \theta \\ (k_{xx} - k_{yy}) \sin \theta \cos \theta & k_{xx} \sin^2 \theta + k_{yy} \cos^2 \theta \end{bmatrix} \quad (3-38)$$

where k_{xx} and k_{yy} are the x and y components of the effective permeability tensor for a horizontal fracture, respectively and θ is the rotation angle (Lough et al.(1998)).

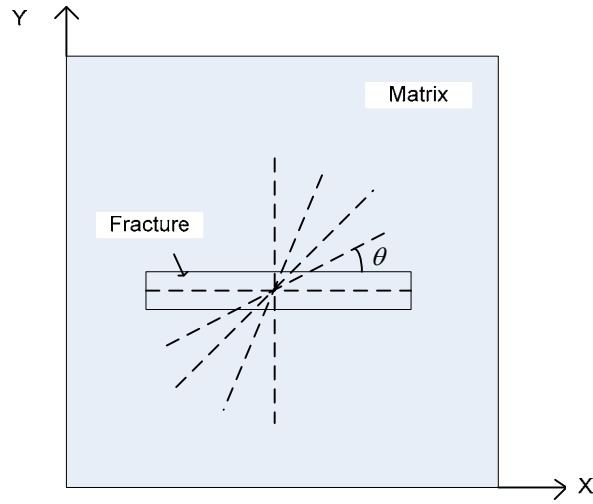


Figure 3-12: single fracture rotating inside a matrix block

The numerical experiments were carried out using a single fracture with a length of 0.6 units and an aperture of 1×10^{-4} units while fluid viscosity is taken 1cp. The orientation of fracture was varied from 0° to 90° . The matrix permeability of the block is set at 1 mD and the fracture permeability 2×10^6 mD. In **Fig. 3-12** fracture geometry and matrix block dimensions are presented. The diagonal and off-diagonal components of effective permeability as a function of orientation angle are presented in **Figs. 3-13** and **3-14** respectively. From these figures it can be seen that the diagonal component, k_{xx} decreases while the diagonal component, k_{yy} increases with the increase in fracture orientation (see **Fig. 3-13**). Similarly the off-diagonal components (k_{xy} and k_{yx}) of effective permeability increase until the fracture orientation reaches 45° and then decrease to 0 when it reaches 90° (see **Fig. 3-14**). This comparative study shows that numerical results agree well with the analytical solution presented in Eq. 3-38.

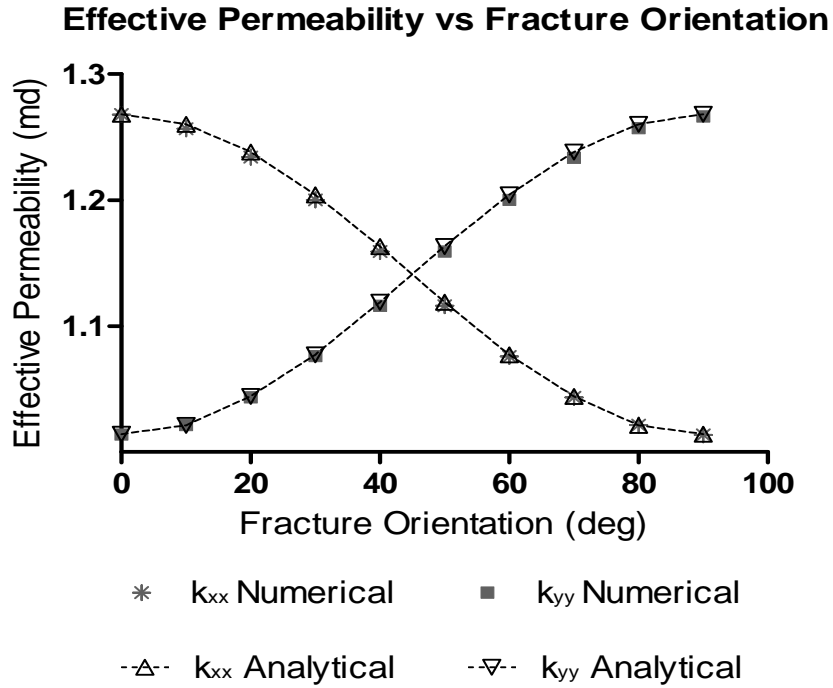


Figure 3-13: Comparison of analytically and numerically calculated diagonal elements of permeability tensor

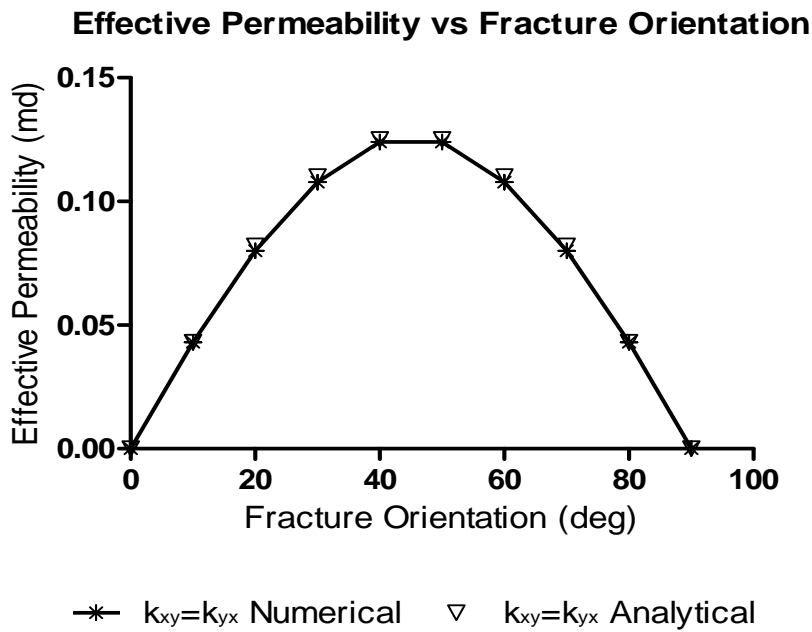


Figure 3-14: Comparison of analytically and numerically calculated off-diagonal elements of permeability tensor

Validation of Numerical Results against Laboratory Results

In the numerical experiments the model parameters block size, fracture length, aperture and orientation as well as matrix and fracture permeabilities were kept the same as those of laboratory experiments. Numerical results are presented in **Table 3-1**. From the results it can be seen that the numerical results are in good agreement with those of the experimental results.

Table3-1. Comparison between numerical and experimental results (single fracture models)

| Angle of Fracture | k (D) Experimental (Error ± 0.021) (see chapter 2) | | k (D) Numerical |
|-------------------|---|------|-----------------|
| 90° | k_{yy} | 3.42 | 3.44 |
| 45° | $k_{xx} = k_{yy}$ | 3.58 | 3.60 |
| 0° | k_{xx} | 3.75 | 3.78 |

Numerical results for multiple-fracture system are presented in **Table 3-2**. From the results it can be seen that the numerical results are in good agreement with the experimental results.

Table 3-2. Comparison between numerical and experimental results (multiple fracture models)

| Heterogeneous systems (set of two fractures) | k(D) Experimental (Error ± 0.021) (see chapter 2) | k (D) Numerical |
|---|--|-----------------|
| 2 fractures oriented at 45° | 3.78 | 3.8 |
| 2 intersecting fractures | 3.98 | 4.0 |
| 2 fractures oriented at 0° | 4.21 | 4.2 |

Evaluation of Numerical Results

Analytically validated permeability tensor model is used to calculate grid based effective permeability of multiple fracture systems. Results of the numerical model are presented in different examples as follows:

Effect of Short Fractures on Effective Permeability

In this example, numerical model is run for short fractures only. Four blocks with different numbers of regularly spaced short fractures in each block are presented in **Fig. 3-15**. Each block is of size $15 \times 15 \text{ ft}^2$. First block (bottom left) contains 15 numbers of fractures, similarly 5, 25 and 15 are the number of fractures in second, third and fourth blocks, respectively. Matrix permeability for this example is set as 0.1 md and fracture permeability as $2 \times 10^6 \text{ md}$ using equation 3-15a. Also length and aperture of fracture are set constant values of 0.5 ft and $1 \times 10^{-4} \text{ ft}$, respectively.

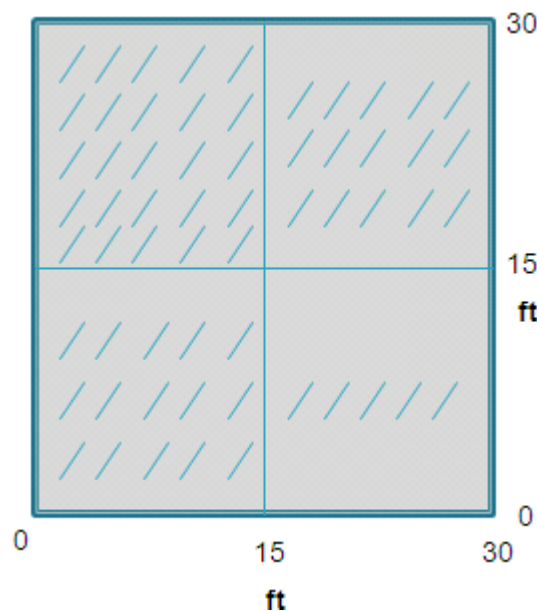


Figure 3-15: Regularly spaced short fractures

Off diagonal components of grid based permeability tensor are ignored for short fractures and grid based permeability enhancement due to presence of short fractures is expressed as:

$$k = \sqrt{\left(\frac{1}{2}\right) \times (k_{xx}^2 + k_{yy}^2)} \quad (3-39)$$

Figure 3-16 represents the permeability enhancement due to the presence of short fractures, which shows that the magnitude of grid based permeability depends on the number of short fractures present in that grid block.



Figure 3-16: Equivalent permeability (equation 3-39) for short fracture's system presented in **Fig. 3-15**

Effect of Multiple Fractures on Effective Permeability

Purpose of this example is to show contribution of medium and long fractures in permeability enhancement of a grid block. **Figure 3-17** shows a fracture network which is divided into 4×4 blocks. Matrix permeability is set as $1md$ while fracture as $2 \times 10^6 md$ using equation 3-15a. Co-ordinates of the fractures presented in **Fig. 3-17** are given in **Table 5**. The resultant grid-based permeability tensors are offered in **Fig. 3-18**.

Table 3-3. Co-ordinates for the fractured system presented in **Fig. 3-17**

| $(x1, y1)$ | $(x2, y2)$ | $(x1, x2)$ | $(x2, y2)$ |
|------------|------------|------------|------------|
| (1,4) | (11,13) | (16,31) | (26,41) |
| (4,18) | (14,22) | (31,10) | (42,22) |
| (1,20) | (14,28.5) | (31,46) | (36,53) |
| (2,31) | (12,38) | (31,43) | (48,58) |
| (2,40) | (22,55) | (33,31) | (44,44) |
| (16,7) | (46,38) | (49,40) | (57,56) |
| (16,22) | (33,33) | (49,31) | (54,37) |
| (46,13) | (55,25) | (49,10) | (58,20) |

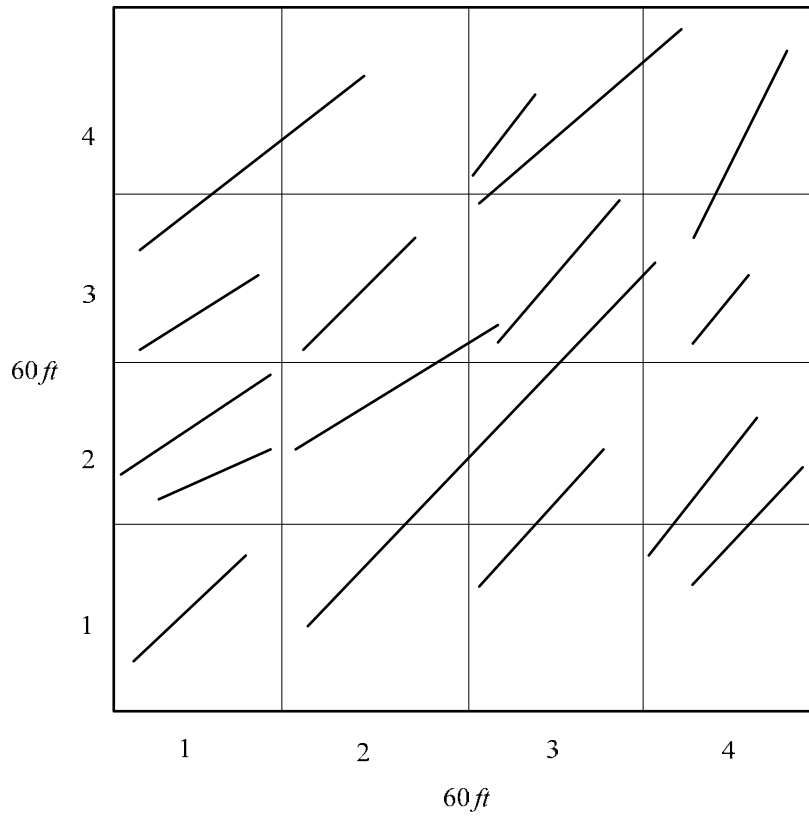


Figure 3-17: Medium and long fractures system

| | | | |
|--|--|--|--|
| $\begin{pmatrix} 1.1 & 0.1 \\ 0.1 & 1.1 \end{pmatrix}$ | $\begin{pmatrix} 1.16 & 0.09 \\ 0.09 & 1.05 \end{pmatrix}$ | $\begin{pmatrix} 2.01 & 0.06 \\ 0.06 & 1.6 \end{pmatrix}$ | $\begin{pmatrix} 1.95 & 0.29 \\ 0.29 & 2.2 \end{pmatrix}$ |
| $\begin{pmatrix} 1.49 & 0.2 \\ 0.2 & 2.34 \end{pmatrix}$ | $\begin{pmatrix} 2.62 & 0.05 \\ 0.05 & 1.61 \end{pmatrix}$ | $\begin{pmatrix} 3.04 & 0.38 \\ 0.38 & 4.11 \end{pmatrix}$ | $\begin{pmatrix} 1.28 & 0.06 \\ 0.06 & 2.22 \end{pmatrix}$ |
| $\begin{pmatrix} 2.42 & 0.34 \\ 0.34 & 1.74 \end{pmatrix}$ | $\begin{pmatrix} 2.1 & 0.12 \\ 0.12 & 2.3 \end{pmatrix}$ | $\begin{pmatrix} 1.81 & 0.1 \\ 0.1 & 2.81 \end{pmatrix}$ | $\begin{pmatrix} 1.54 & 0.16 \\ 0.16 & 1.52 \end{pmatrix}$ |
| $\begin{pmatrix} 1.34 & 0.3 \\ 0.3 & 1.27 \end{pmatrix}$ | $\begin{pmatrix} 1.2 & 0.2 \\ 0.2 & 1.2 \end{pmatrix}$ | $\begin{pmatrix} 1.07 & 0.07 \\ 0.07 & 1.07 \end{pmatrix}$ | $\begin{pmatrix} 1.27 & 0.02 \\ 0.02 & 1.09 \end{pmatrix}$ |

Figure 3-18: Effective permeability Tensor for fractured system presented in **Fig. 3-17**

Figure 3-18 shows the effect of orientation and length of fracture on grid based permeability tensors. It can be seen from block (1, 1) by comparing **Figs. 3-17** and **3-18** that the magnitude of x and y components of permeability tensor depends on the fracture orientation. This block contains only one fracture at 42° from the horizontal axis which makes the resultant x-component of k tensor slightly higher than the y-component as x and y components of k tensor are equal for a fracture oriented at 45° . It is also clear from **Figs. 3-17** and **3-18** that fractures crossing a number of grid blocks have strong bearing on the magnitude of permeability and direction of flow as can be seen for blocks (2,1), (2,2), (3,2) and (3,3).

Effect of Intersecting Fractures on Effective Permeability

In this example, the permeability tensor model is used to calculate grid-based effective permeability of a multiple fracture system as presented in **Fig. 3-19**. This fracture system with 4 grid blocks was generated in a manner that the effect of fracture orientation and intersection on the permeability tensor can be studied. For example, bottom left block incorporates two parallel fractures. Then, in the bottom right, a fracture intersecting two initial fractures is added. Next in top left block another horizontally oriented fracture is added. Finally, in top right block, a fifth vertical fracture intersecting the bottom one is added. Permeability tensors of these blocks are presented in **Fig. 3-20**. The co-ordinates of fractures in top right block are given in **Table 3-4**, whereas the co-ordinates of fractures present in remaining blocks can be obtained by subtracting (0,1), (1,0) or (1,1) from the appropriate co-ordinates in **Table 3-4**. In this study, matrix and fracture permeabilities are set at 1 and $2 \times 10^6 mD$, respectively.

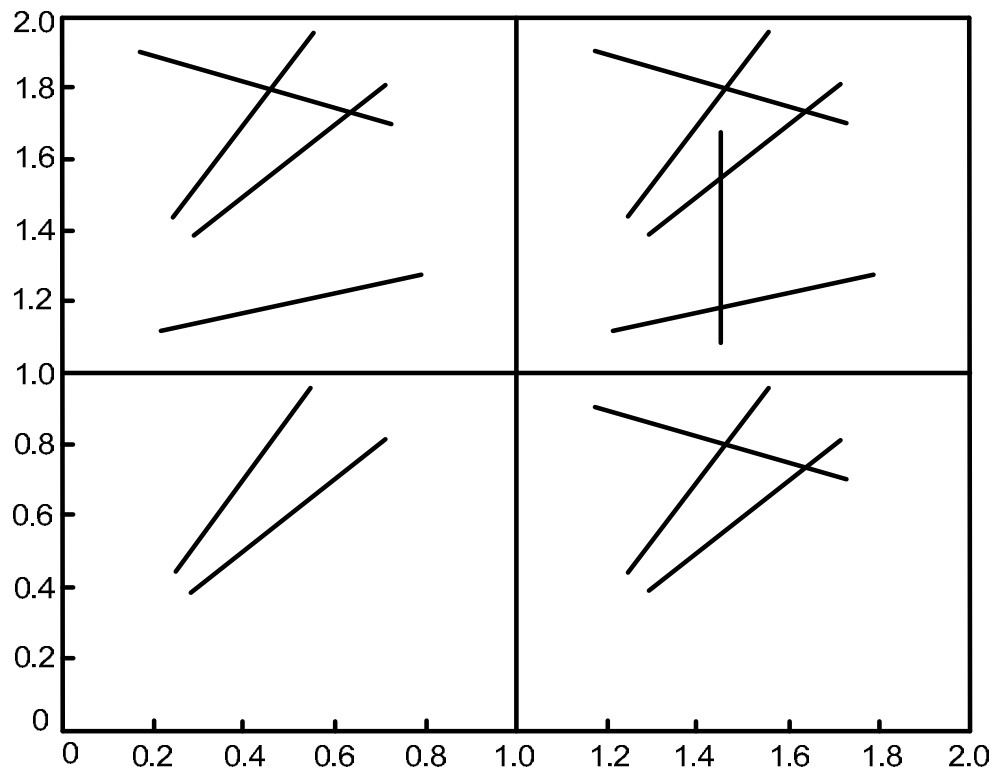


Figure 3-19: Multiple fracture system with successive addition of a fracture one by one in each grid block

Table 3-4. Fracture co-ordinates for the upper right grid block in **Fig. 3-19**

| $x1$ | $y1$ | $x2$ | $y2$ |
|-------|-------|-------|-------|
| 1.25 | 1.44 | 1.55 | 1.96 |
| 1.288 | 1.388 | 1.712 | 1.812 |
| 1.732 | 1.697 | 1.168 | 1.903 |
| 1.21 | 1.122 | 1.79 | 1.278 |
| 1.445 | 1.08 | 1.455 | 1.68 |

Major and minor axes of an ellipse represent the magnitude of dominant component by an arrow and non-dominant component (diagonal permeability) by a fixed line, while the direction of ellipse represents the direction of flow in each grid block. From **Figs. 3-19** and **3-20** it can be observed that the effect of x or y-component of k-tensor and resulting flow direction depends on the fracture intersections and orientations. As fractures are added to individual blocks, the size and orientation of the ellipse change to reflect the changes in permeability tensor and flow direction accordingly.

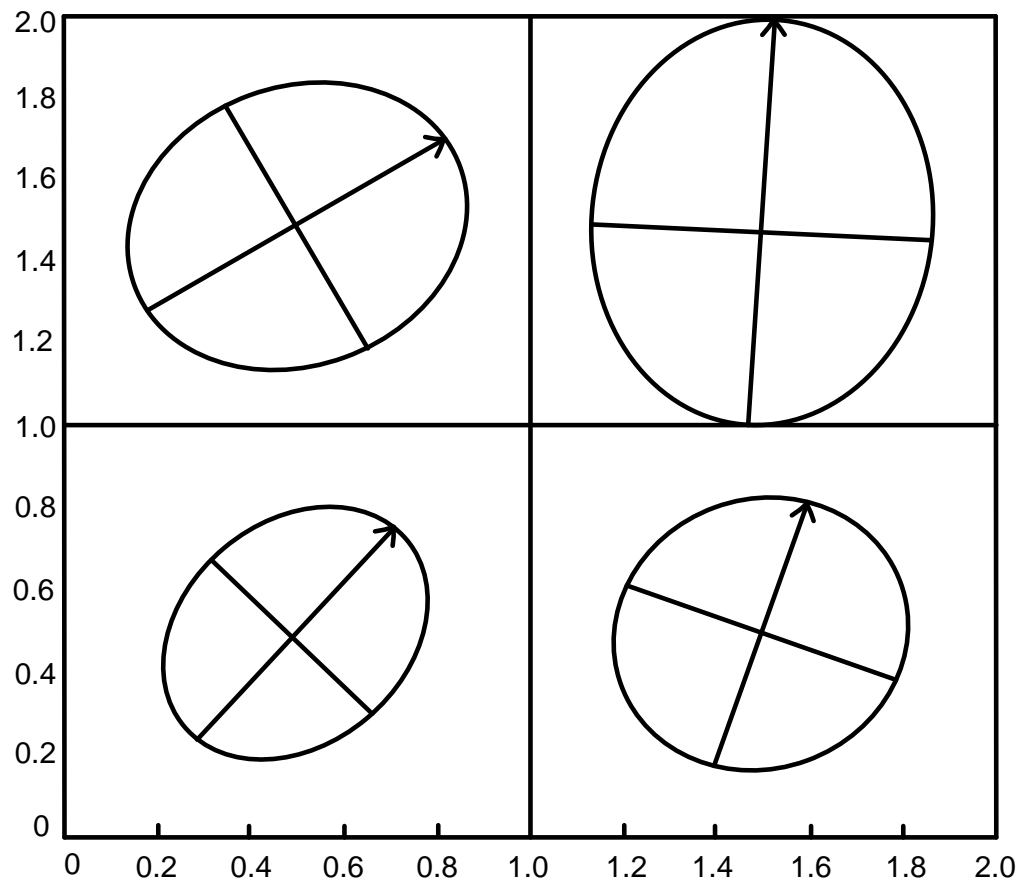


Figure3-20: Elliptical representation of k-tensor for fracture system presented in **Fig. 3-19**

Potential Application

In the final example, the fracture system of Soultz geothermal reservoir in France is considered. **Figure 3-21** represents about 106 fractures at a depth of 4,480m in an areal space of 500m by 1200m of Soultz reservoir. This 2D fracture system is obtained by altering the fractal dimension of 3D realization ((Sausse et al.(2007), Gentier et al. (2010), Joshua Koh et al. (2010)). The entire region is divided into 50m×50m blocks. The matrix permeability for each grid block is 0.01md and fracture aperture 100μm. **Figure 3-21** shows an elliptical representation of effective permeability tensor for each grid block. By comparing the permeabilities in different blocks it becomes clear that effective permeability tensor is a function of many parameters: fracture orientation, length, density and more importantly connectivity. It is also evident from **Fig. 3-21** that fracture length and density have a strong impact on effective permeability (see blocks (5, 13) and (5, 15)) while small and disconnected fractures have limited effect (see blocks (1, 5) and (9, 11)). Furthermore fracture orientations have a significant bearing on flow direction.

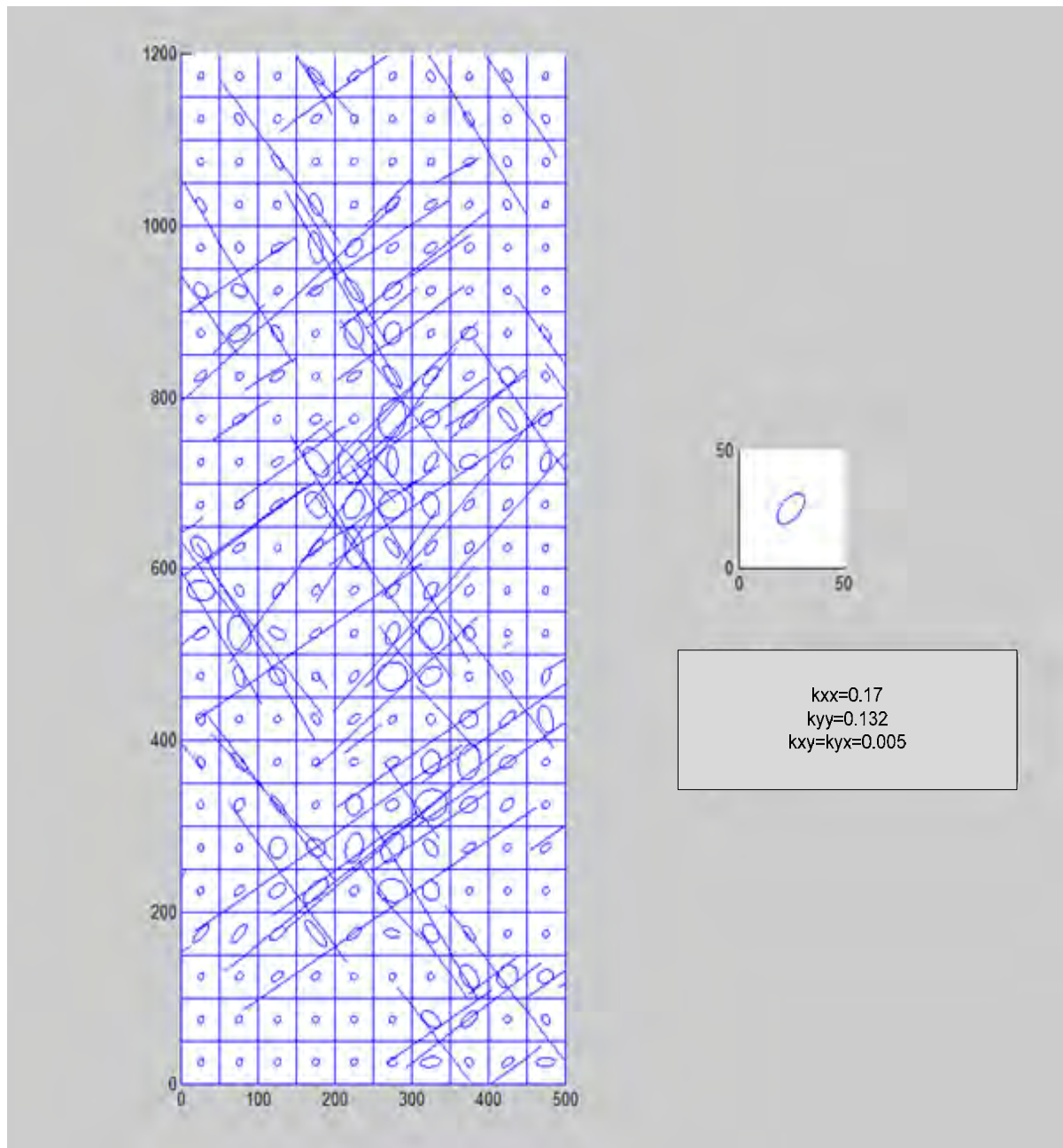


Figure 3-21: Elliptical representation of grid based k-tensors for 2-D fracture network of Soultz reservoir

3.2 Fluid Flow Simulation through Naturally Fractured Reservoirs

3.2.1 Literature Review

Estimating pressure and velocity profiles are the major interest in the simulation of fluid flow for heterogeneous porous media. Continuum approaches as well as discrete fracture approach used for simulations are discussed earlier in this chapter with their advantages and limitations.

A number of theoretical and numerical methods have been developed using the control volume method in the calculation of fluid flow from homogeneous reservoirs. Chou and Kwak (2000) outlined the necessity of these methods in fluid flow simulation and employed them for the calculation of fluid velocity. The control volume approach for the mixed formulation of the linear elliptic problem was first developed by Russell (Russell 1995). This technique has been widely used as discretisation techniques for conservation of mass by Ohlberger (1997); Feistauer et al. (1995); Durlofsky et al. (1992); Weiser and Wheeler (1988); Suli (1991); Cai et al. (1997). Control volume discretisation in finite difference and mixed finite element methods have been used by engineers in the simulation of fluid flow in petroleum reservoirs.

A number of models have been developed using the block-centred finite difference method with continuity of velocity between blocks (Thomas and Trujillo, (1995); Aavatsmark et al., (1998)). Lee et al. [(1997); (2002)] further improved the simulation of naturally fractured reservoirs (NFRs) using the full tensor effective permeability in a flux-continuous finite difference method. Lee et al. [(1997); (1999)] developed a flux-continuous finite difference model in the simulation of production from heterogeneous reservoirs by applying a full tensor effective permeability. One of the advantages of this method is the

applicability of the model to the simulation of fractured reservoirs where the heterogeneity is described by permeability tensor.

Combining the finite difference method with control volume permits the direct calculation of fluid velocity, whereas in the previous methods velocity is calculated by differentiating the pressure which is not very accurate in the simulation of NFRs.

However, the finite difference formulation is valid for uniform grids and creates error in the case of fractured reservoirs with complex geometry. For heterogeneous reservoirs with non-uniform grids, the finite difference formulation is not effective and one needs to use other methods such as the finite element which is capable of handling the complex geometry in the simulation of fluid flow in NFRs.

Furthermore, control volume and mixed finite element techniques are used in modelling of fluid flow in heterogeneous and fractured reservoirs (Edwards and Rogers 1994; Edwards and Rogers 1998) ; Naji and Kazemi (1996); Nakashima et al. (2000); and Cia et al. (1997)). Cia et al. (1997) theoretically formulated this method for heterogeneous reservoirs with irregular geometry and outlined its technical success and applicability. They used a block-centred approach to calculate pressure at the centre and velocity at the middle of the grid block edges. They claimed that their method is more accurate than the methods utilised by Aavatsmark et al. (1998) in which dual velocity grids are associated with the corners of pressure block. The use of control volume mixed finite element method enables us to simulate fluid flow in reservoirs with irregular geometry while maintaining many of the familiar properties of block-centred finite difference methods for rectangular grids.

Chou and Kwak (2000) developed a mathematical control volume model in a same manner as Cia et al. (1997) and proved its first order optimal rate of convergence for the

approximate velocities as well as for the approximate pressures. Arihara et al. (2001) applied Cia et al. (1997) model for the simulation of NFR with two-phase flow and regular fracture pattern. In Cia et al.'s method permeability was assumed to be a scalar term whereas in the simulation of NFRs permeability is usually defined in a tensor form. However, it should be noted that in the mixed methods pressure is not a continuous function and is calculated in the block centres.

For detailed modelling one needs to calculate pressures at as many points as possible inside a heterogeneous reservoir instead of just block centred pressures. Also block centred pressures need to be interpolated to get a pressure profile throughout the reservoir where accuracy is meant to be lost for pressure profile inside the reservoir. Based on this drawback associated with mixed approaches, it was decided to use finite element modelling to obtain pressure and velocity profiles in heterogeneous reservoirs as used for decoupled problem by Hodge (2006) and Aghighi (2007). Finite element method (FEM) enables us to calculate reasonably accurate nodal pressures and velocities for each element inside the reservoir which is advantageous over control volume mixed approaches.

3.2.2 Mathematical Formulation of Simulation Model

Fluid flow equations are solved based on the finite element discretization. Permeability tensors obtained from the tensor model are fed to the simulation model to calculate pressure and velocity distribution throughout the reservoir. Reservoir is discretised into small elements (blocks) and four noded elements are described. Two dimensional discretization of the fluid flow problem using decoupled flow equation is discussed further.

Square Elements

We can divide a square element by placing regularly spaced nodes as shown in **Fig. 3-22**.

Using the Lagrange polynomial we have a shape function for the square element as given by Zienkiewicz (2000).

$$N_{ij} = L_i^n(\xi)L_j^m(\eta) \quad (3-40)$$

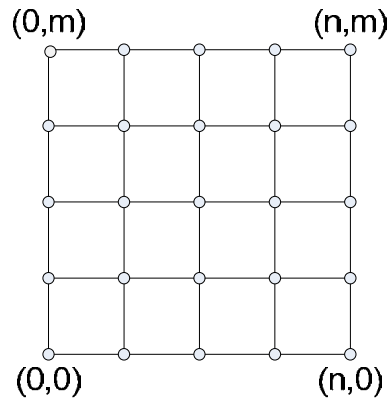


Figure 3-22: A general square element with regularly spaced nodes.

Four Nodded Square Element

Zienkiewicz (2000) uses a term local co-ordinates to position the centre of an element at the origin. The four noded square element as defined by Zienkiewicz (2000) by using local co-ordinates is shown in **Fig. 3-23**:

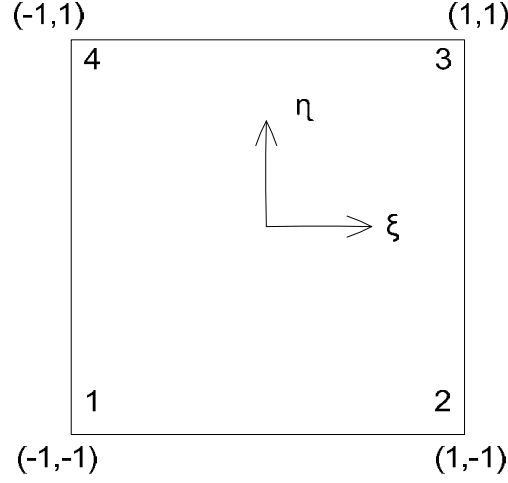


Figure 3-23: four noded square element in local co-ordinates

On this element we have two linear Lagrange equations (Zienkiewicz 2000):

$$L_0^1(\xi) = \frac{1-\xi}{2} \quad \& \quad L_1^1(\xi) = \frac{1+\xi}{2} \quad (3-41)$$

Using equation (3-40) and starting with the bottom left hand corner and working anticlockwise around the element we have four shape functions:

$$N_1 = \frac{(1-\xi)(1-\eta)}{4}, N_2 = \frac{(1+\xi)(1-\eta)}{4}, N_3 = \frac{(1+\xi)(1+\eta)}{4}, N_4 = \frac{(1-\xi)(1+\eta)}{4} \quad (3-42)$$

Mapping

Simple elements such as square elements can be mapped onto elements of any arbitrary shape. **Figure 3-24** represents mapping of a four noded square with local co-ordinates (ξ, η) onto an arbitrary four noded quadrilateral with global co-ordinates (x, y) . Mapping leads to the following relationships for this element:

$$x = N_1x_1 + N_2x_2 + N_3x_3 + N_4x_4 \quad (3-43)$$

$$y = N_1y_1 + N_2y_2 + N_3y_3 + N_4y_4 \quad (3-44)$$

where shape functions N_1 to N_4 are given in equation (3-42)

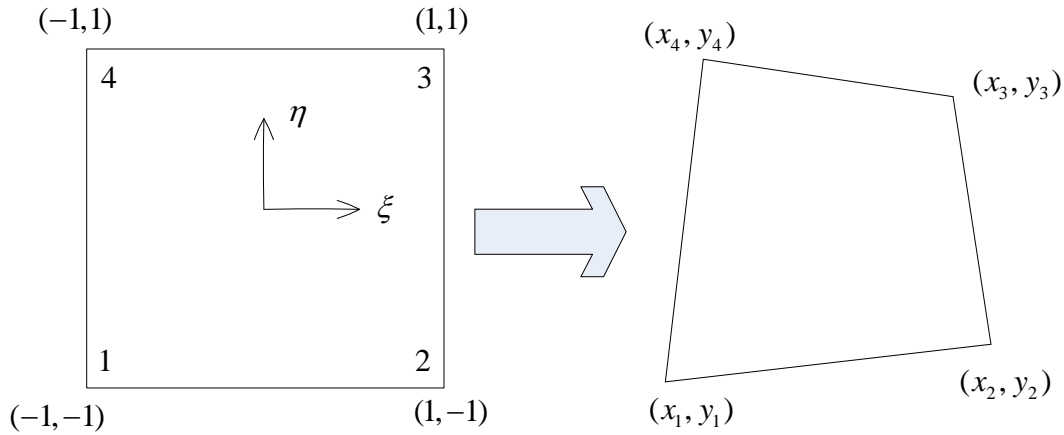


Figure 3-24: Mapping onto the four noded quadrilateral

General Two Dimensional Transformation

We have shape functions in terms of local co-ordinates. In order to operate on derivatives in the global co-ordinates (x, y) , transformations are required. Using the rules of partial differentiation Zienkiewics (2000) wrote transformations of the shape function N_i from local to global co-ordinates:

$$\begin{pmatrix} \frac{\partial N_i}{\partial \xi} \\ \frac{\partial N_i}{\partial \eta} \end{pmatrix} = \vec{J} \begin{pmatrix} \frac{\partial N_i}{\partial x} \\ \frac{\partial N_i}{\partial y} \end{pmatrix} \quad (3-45)$$

where Jacobian \vec{J} is defined as:

$$\vec{J} = \begin{pmatrix} \frac{\partial x}{\partial \xi} & \frac{\partial y}{\partial \xi} \\ \frac{\partial x}{\partial \eta} & \frac{\partial y}{\partial \eta} \end{pmatrix} \quad (3-46)$$

By differentiating the relationships \vec{J} can be found explicitly. To calculate the global co-ordinates we can re-write equation (3-45) as follows:

$$\begin{pmatrix} \frac{\partial N_i}{\partial x} \\ \frac{\partial N_i}{\partial y} \end{pmatrix} = \vec{J}^{-1} \begin{pmatrix} \frac{\partial N_i}{\partial \xi} \\ \frac{\partial N_i}{\partial \eta} \end{pmatrix} \quad (3-47)$$

For area integrals we require a relationship between the area in local co-ordinates ($d\xi d\eta$) and the area in global co-ordinates ($dx dy$). Zienkiewics (2000) presented such a relation for area transformations from local to global co-ordinates:

$$dx dy = \det \begin{vmatrix} \frac{\partial x}{\partial \xi} & \frac{\partial y}{\partial \xi} \\ \frac{\partial x}{\partial \eta} & \frac{\partial y}{\partial \eta} \end{vmatrix} d\xi d\eta = \det \vec{J} d\xi d\eta \quad (3-48)$$

where $\det \vec{J}$ represents the determinant of Jacobian.

For line integrals, in global co-ordinates we have $\vec{n} dS$ where \vec{n} is the unit vector normal to line S . To express this in local co-ordinates Zienkiewics (2000) presented a relationship as follows:

$$\vec{n} dS = \begin{pmatrix} n_x \\ n_y \end{pmatrix} dS = \begin{pmatrix} \frac{\partial y}{\partial \xi} \\ -\frac{\partial x}{\partial \xi} \end{pmatrix} d\xi \quad (3-49)$$

Four Noded Element Transformation

For the four noded element we need to know shape functions N_i , their derivatives with respect to global co-ordinates $\left(\frac{\partial N_i}{\partial x}\right)$ and $\left(\frac{\partial N_i}{\partial y}\right)$, and area $dxdy$ in terms of local co-ordinates ξ, η .

Shape functions are defined in terms of local co-ordinates in equation (3-42). Also equations (3-43) and (3-44) relate global co-ordinates to the local co-ordinates. In order to obtain derivatives of the shape functions with respect to local co-ordinates $\left(\frac{\partial N_i}{\partial \xi}\right)$ and $\frac{\partial N_i}{\partial \eta}$ we can differentiate equation (3-42) as follows:

$$\frac{\partial N_1}{\partial \xi}(\eta) = \frac{\eta-1}{4}, \frac{\partial N_2}{\partial \xi}(\eta) = \frac{1-\eta}{4}, \frac{\partial N_3}{\partial \xi}(\eta) = \frac{1+\eta}{4} \text{ and } \frac{\partial N_4}{\partial \xi}(\eta) = -\frac{1+\eta}{4} \quad (3-50)$$

$$\frac{\partial N_1}{\partial \eta}(\xi) = \frac{\xi-1}{4}, \frac{\partial N_2}{\partial \eta}(\xi) = -\frac{1+\xi}{4}, \frac{\partial N_3}{\partial \eta}(\xi) = \frac{1+\xi}{4} \text{ and } \frac{\partial N_4}{\partial \eta}(\xi) = \frac{1-\xi}{4} \quad (3-51)$$

Derivatives of the x component of global co-ordinates with respect to the local co-ordinates can be obtained by differentiating equation (3-43) and then by combining with equation (3-50) will give us:

$$\frac{\partial x}{\partial \xi}(\eta) = \sum_{i=1}^4 \frac{\partial N_i}{\partial \xi} x_i = \frac{\eta-1}{4} x_1 + \frac{1-\eta}{4} x_2 + \frac{1+\eta}{4} x_3 - \frac{1+\eta}{4} x_4 \quad (3-52)$$

$$\frac{\partial x}{\partial \eta}(\xi) = \sum_{i=1}^4 \frac{\partial N_i}{\partial \eta} x_i = \frac{\xi-1}{4} x_1 - \frac{1+\xi}{4} x_2 + \frac{1+\xi}{4} x_3 + \frac{1-\xi}{4} x_4 \quad (3-53)$$

Similarly derivative of y component of global co-ordinate with respect to local co-ordinates are obtained by differentiating equation (3-44) and then combining with equation (3-51) will give:

$$\frac{\partial y}{\partial \xi}(\eta) = \sum_{i=1}^4 \frac{\partial N_i}{\partial \xi} y_i = \frac{\eta-1}{4} y_1 + \frac{1-\eta}{4} y_2 + \frac{1+\eta}{4} y_3 - \frac{1+\eta}{4} y_4 \quad (3-54)$$

$$\frac{\partial y}{\partial \eta}(\xi) = \sum_{i=1}^4 \frac{\partial N_i}{\partial \eta} y_i = \frac{\xi-1}{4} y_1 - \frac{1+\xi}{4} y_2 + \frac{1+\xi}{4} y_3 + \frac{1-\xi}{4} y_4 \quad (3-55)$$

Using equations (3-52) to (3-55), we can calculate Jacobian \vec{J} as defined in equation (3-46).

Combining Jacobian and equations (3-50) and (3-51) with equation (3-47), shape functions

with respect to global co-ordinates $(\frac{\partial N_i}{\partial x} \text{ and } \frac{\partial N_i}{\partial y})$ can be calculated. Combining Jacobian

with equation (3-48), we have the area integral as a function of local co-ordinates.

Gaussian Quadrature

Gauss quadrature is used to exactly integrate a polynomial using a sum. As given Zienkiewicz (2000), the Gauss quadrature formula is:

$$I = \int_{-1}^1 f(\xi) d\xi = \sum_{i=1}^n H_i f(\xi_i) \quad (3-56)$$

where n is the number of points, H is the weighting factor and is exact for a polynomial of degree $(2n-1)$ or less. This formula can be extended to an area integral by:

$$I = \int_{-1}^1 \int_{-1}^1 f(\xi, \eta) d\xi d\eta = \int_{-1}^1 \sum_{i=1}^n H_i f(\xi_i, \eta) d\eta = \sum_{j=1}^n \sum_{i=1}^n H_i H_j f(\xi_i, \eta_j) \quad (3-57)$$

The integration points for accurate integration are listed below (Zienkiewicz 2000) in **Table**

3-5:

Table 3-5: Weighing factor and integration points for Gauss quadrature

| n | ξ_i | H_i |
|-----|--|--|
| 1 | 0 | 2 |
| 2 | $-\frac{1}{\sqrt{3}}$ and $\frac{1}{\sqrt{3}}$ | 1 and 1 |
| 3 | $-\sqrt{0.6}, 0, \sqrt{0.6}$ | $\frac{5}{9}, \frac{8}{9}$ and $\frac{5}{9}$ |

FEM Formulation for Decoupled Fluid Flow

Decoupled two dimensional balance of fluid momentum equation is given as:

$$\nabla \cdot \left(\frac{\vec{\vec{k}}}{\mu} \nabla P \right) + C_f \nabla P \cdot \left(\frac{\vec{\vec{k}}}{\mu} \nabla P \right) = \phi C_T \frac{dp}{dt} \quad (3-58)$$

where $\vec{\vec{k}}$ is the effective permeability tensor expressed in two dimensions as follows:

$$\vec{\vec{k}} = \begin{pmatrix} k_{xx} & k_{xy} \\ k_{yx} & k_{yy} \end{pmatrix} \quad (3-59)$$

Assuming constant viscosity, equation (3-58) can be rewritten as:

$$\nabla \cdot \left(\vec{\vec{k}} \nabla P \right) + C_f \nabla P \cdot \left(\vec{\vec{k}} \nabla P \right) = \mu \phi C_T \frac{dp}{dt} \quad (3-60)$$

Expanding this equation will give:

$$\left(\frac{\partial k_{xx}}{\partial x} \frac{\partial P}{\partial x} + k_{xx} \frac{\partial^2 P}{\partial x^2} + \frac{\partial k_{xy}}{\partial x} \frac{\partial P}{\partial y} + (k_{xy} + k_{yx}) \frac{\partial^2 P}{\partial x \partial y} + \frac{\partial k_{yx}}{\partial y} \frac{\partial P}{\partial x} + \frac{\partial k_{yy}}{\partial y} \frac{\partial P}{\partial y} + k_{yy} \frac{\partial^2 P}{\partial y^2} \right) +$$

$$C_f \left(k_{xx} \left(\frac{\partial P}{\partial x} \right)^2 + (k_{xy} + k_{yx}) \frac{\partial P}{\partial x} \frac{\partial P}{\partial y} + k_{yy} \left(\frac{\partial P}{\partial y} \right)^2 \right) = \mu \phi C_T \frac{dp}{dt} \quad (3-61)$$

Assuming,

$$C_f \left(\frac{\partial P}{\partial x} \right)^2 \ll \frac{\partial^2 P}{\partial x^2}$$

$$C_f \frac{\partial P}{\partial x} \frac{\partial P}{\partial y} \ll \frac{\partial^2 P}{\partial x \partial y} \quad \text{and}$$

$$C_f \left(\frac{\partial P}{\partial y} \right)^2 \ll \frac{\partial^2 P}{\partial y^2}$$

Now from equations (3-60) and (3-61) we can write:

$$\nabla \cdot \left(\frac{\vec{k}}{\mu} \nabla P \right) = \phi C_T \frac{dp}{dt} \quad (3-62)$$

Expanding this equation using equation (3-59) gives:

$$\frac{\partial}{\partial x} \left(\frac{k_{xx}}{\mu} \frac{\partial P}{\partial x} + \frac{k_{xy}}{\mu} \frac{\partial P}{\partial y} \right) + \frac{\partial}{\partial y} \left(\frac{k_{yx}}{\mu} \frac{\partial P}{\partial x} + \frac{k_{yy}}{\mu} \frac{\partial P}{\partial y} \right) = \phi C_T \frac{dp}{dt} \quad (3-63)$$

Introducing the variational formulation we have:

$$\int_{\Omega} w \left(\frac{\partial}{\partial x} \left(\frac{k_{xx}}{\mu} \frac{\partial P}{\partial x} + \frac{k_{xy}}{\mu} \frac{\partial P}{\partial y} \right) + \frac{\partial}{\partial y} \left(\frac{k_{yx}}{\mu} \frac{\partial P}{\partial x} + \frac{k_{yy}}{\mu} \frac{\partial P}{\partial y} \right) \right) d\Omega = \int_{\Omega} w \phi C_T \frac{dp}{dt} d\Omega \quad (3-64)$$

where $w = w(x, y)$ is a trial function and Ω is a domain.

After applying the integration in equation (3-64) we have,

$$\int_{\Gamma} w \left(\left(\frac{k_{xx}}{\mu} \frac{\partial P}{\partial x} + \frac{k_{xy}}{\mu} \frac{\partial P}{\partial y} \right) n_x + \left(\frac{k_{yx}}{\mu} \frac{\partial P}{\partial x} + \frac{k_{yy}}{\mu} \frac{\partial P}{\partial y} \right) n_y \right) d\Gamma - \int_{\Omega} \frac{\partial w}{\partial x} \left(\frac{k_{xx}}{\mu} \frac{\partial P}{\partial x} + \frac{k_{xy}}{\mu} \frac{\partial P}{\partial y} \right) + \frac{\partial w}{\partial y} \left(\frac{k_{yx}}{\mu} \frac{\partial P}{\partial x} + \frac{k_{yy}}{\mu} \frac{\partial P}{\partial y} \right) d\Omega = \int_{\Omega} w \phi C_T \frac{\partial p}{\partial t} d\Omega \quad (3-65)$$

where Γ is the boundary and n is the normal to the boundary

Setting a constant pressure on some boundaries and no flow on others, the boundary integral can be omitted and after rearranging we will get:

$$\int_{\Omega} \frac{\partial w}{\partial x} \left(\frac{k_{xx}}{\mu} \frac{\partial P}{\partial x} + \frac{k_{xy}}{\mu} \frac{\partial P}{\partial y} \right) + \frac{\partial w}{\partial y} \left(\frac{k_{yx}}{\mu} \frac{\partial P}{\partial x} + \frac{k_{yy}}{\mu} \frac{\partial P}{\partial y} \right) d\Omega + \int_{\Omega} w \phi C_T \frac{\partial p}{\partial t} d\Omega = 0 \quad (3-66)$$

Using the finite difference implicit method to discretise with respect to time and assuming porosity and permeability changes for each time step are negligible we can write:

$$\int_{\Omega} \frac{\partial w}{\partial x} \left(\frac{k_{xx}^{i-1}}{\mu} \frac{\partial P^i}{\partial x} + \frac{k_{xy}^{i-1}}{\mu} \frac{\partial P^i}{\partial y} \right) + \frac{\partial w}{\partial y} \left(\frac{k_{yx}^{i-1}}{\mu} \frac{\partial P^i}{\partial x} + \frac{k_{yy}^{i-1}}{\mu} \frac{\partial P^i}{\partial y} \right) d\Omega + \int_{\Omega} w \phi^{i-1} C_T^{i-1} \frac{P^i - P^{i-1}}{\Delta t^i} d\Omega = 0 \quad (3-67)$$

where subscript i represents the current time step and $i-1$ the previous time step. Pressure and displacement are described at material location for the given time.

Rearranging equation (3-67) we have,

$$\Delta t^i \left[\int_{\Omega} \frac{\partial w}{\partial x} \left(\frac{k_{xx}^{i-1}}{\mu} \frac{\partial P^i}{\partial x} + \frac{k_{xy}^{i-1}}{\mu} \frac{\partial P^i}{\partial y} \right) + \frac{\partial w}{\partial y} \left(\frac{k_{yx}^{i-1}}{\mu} \frac{\partial P^i}{\partial x} + \frac{k_{yy}^{i-1}}{\mu} \frac{\partial P^i}{\partial y} \right) d\Omega \right] + \int_{\Omega} w \phi^{i-1} C_T^{i-1} (P^i - P^{i-1}) d\Omega = 0 \quad (3-68)$$

Using the finite element discretisation with respect to space we can write as:

$$\Delta t^i \left[\int_{\Omega} \frac{\partial \vec{N}}{\partial x} \left(\frac{k_{xx}^{i-1}}{\mu} \frac{\partial \vec{N}}{\partial x} + \frac{k_{xy}^{i-1}}{\mu} \frac{\partial \vec{N}}{\partial y} \right) + \frac{\partial \vec{N}}{\partial y} \left(\frac{k_{yx}^{i-1}}{\mu} \frac{\partial \vec{N}}{\partial x} + \frac{k_{yy}^{i-1}}{\mu} \frac{\partial \vec{N}}{\partial y} \right) d\Omega \right] \vec{P}^i + \left[\int_{\Omega} \vec{N}^T \vec{N} \phi^{i-1} C_T^{i-1} d\Omega \right] (\vec{P}^i - \vec{P}^{i-1}) d\Omega = 0 \quad (3-69)$$

where,

$$\vec{P}^T = (P_1 \quad P_2, \dots, P_n)$$

$$\vec{N} = (N_1 \quad N_2, \dots, N_n)$$

The numbered subscripts represent each nodes, while n is the number of nodes and N is a basis function.

Equation (3-69) can be written as:

$$\overrightarrow{M} \vec{1} (\vec{P}^i - \vec{P}^{i-1}) + \Delta t^i \overrightarrow{M} \vec{2} \vec{P}^i = 0 \quad (3-70)$$

where M is the mass matrix.

Adding and subtracting $\Delta t^i \overrightarrow{M} \vec{2} \vec{P}^{i-1}$

$$\overrightarrow{M} \vec{1} (\vec{P}^i - \vec{P}^{i-1}) + \Delta t^i \overrightarrow{M} \vec{2} \vec{P}^i - \Delta t^i \overrightarrow{M} \vec{2} \vec{P}^{i-1} + \Delta t^i \overrightarrow{M} \vec{2} \vec{P}^{i-1} = 0 \quad (3-71)$$

Re-arranging we can write as:

$$\overrightarrow{M} \vec{1} (\vec{P}^i - \vec{P}^{i-1}) + \Delta t^i \overrightarrow{M} \vec{2} \left(\vec{P}^i - \vec{P}^{i-1} \right) + \Delta t^i \overrightarrow{M} \vec{2} \vec{P}^{i-1} = 0 \quad (3-72)$$

$$\left(\overrightarrow{\overrightarrow{M1}} + \Delta t^i \overrightarrow{\overrightarrow{M2}}\right) \left(\overrightarrow{P}^i - \overrightarrow{P}^{i-1}\right) + \Delta t^i \overrightarrow{\overrightarrow{M2}} \overrightarrow{P}^{i-1} = 0 \quad (3-73)$$

$$\left(\overrightarrow{\overrightarrow{M1}} + \Delta t^i \overrightarrow{\overrightarrow{M2}}\right) \left(\overrightarrow{P}^i - \overrightarrow{P}^{i-1}\right) = -\Delta t^i \overrightarrow{\overrightarrow{M2}} \overrightarrow{P}^{i-1} \quad (3-74)$$

$$\overrightarrow{\overrightarrow{M}} \overrightarrow{\Delta P}^i = \overrightarrow{f} \quad (3-75)$$

where,

$$\overrightarrow{\overrightarrow{M}} = \left(\overrightarrow{\overrightarrow{M1}} + \Delta t^i \overrightarrow{\overrightarrow{M2}}\right)$$

$$\overrightarrow{\Delta P}^i = \left(\overrightarrow{P}^i - \overrightarrow{P}^{i-1}\right)$$

$$\overrightarrow{f} = -\Delta t^i \overrightarrow{\overrightarrow{M2}} \overrightarrow{P}^{i-1}$$

The mass matrix M can be obtained by:

$$\overrightarrow{\overrightarrow{M}} = \sum_e \overrightarrow{\overrightarrow{M}}^e = \sum_e \left(\overrightarrow{\overrightarrow{M1}}^e + \Delta t^i \overrightarrow{\overrightarrow{M2}}^e\right) \quad (3-76)$$

where superscript e represents the element

From equation (3-69) we can write:

$$\overrightarrow{\overrightarrow{M1}}^e = \int_{\Omega^e} \overrightarrow{N}^e{}^T \overrightarrow{N}^e \phi^{i-1} C_T^{i-1} d\Omega \quad (3-77)$$

Where, for a four-nodded element,

$$\vec{N}^e = \begin{pmatrix} N_1 & N_2 & N_3 & N_4 \end{pmatrix} \quad (3-78)$$

Taking compressibility and porosity constant for each element we can write as:

$$\vec{\overline{M1}}^e = \phi^{e^{i-1}} C_T^{e^{i-1}} \int_{\Omega^e} \vec{N}^e{}^T \vec{N}^e d\Omega \quad (3-79)$$

Transforming the global co-ordinates (x,y) into local co-ordinates (ξ,η) and substituting equation (3-48) into this equation:

$$\vec{\overline{M1}}^e = \phi^{e^{i-1}} C_T^{e^{i-1}} \int_{-1}^1 \int_{-1}^1 |J| \vec{N}^e{}^T \vec{N}^e d\xi d\eta \quad (3-80)$$

where $|J|$ represents the determinant of Jacobean while Jacobian J is defined by equation (3-46). Using the Gauss quadrature from equation (3-57), equation (3-80) becomes:

$$\vec{\overline{M1}}^e = \phi^{e^{i-1}} C_T^{e^{i-1}} \sum_i^n \sum_j^n H_i H_j |J_{i,j}| \vec{N}_{i,j}^e{}^T \vec{N}_{i,j}^e \quad (3-81)$$

where n is the number of gauss points and H is the weighting factor. Using equation (3-7) we have:

$$\vec{J}_{i,j} = \begin{pmatrix} \frac{\partial x}{\partial \xi}(\xi_i, \eta_j) & \frac{\partial y}{\partial \xi}(\xi_i, \eta_j) \\ \frac{\partial x}{\partial \eta}(\xi_i, \eta_j) & \frac{\partial y}{\partial \eta}(\xi_i, \eta_j) \end{pmatrix} \quad (3-82)$$

Using equation (3-78), we can write:

$$\vec{N}_{i,j}^e = \begin{pmatrix} N_1(\xi_i, \eta_j) & N_2(\xi_i, \eta_j) & N_3(\xi_i, \eta_j) & N_4(\xi_i, \eta_j) \end{pmatrix} \quad (3-83)$$

For four-noded elements the global derivatives are given in equations (3-52) to (3-55) and shape functions are given in equation (3-42).

Also from equation (3-69), $\overrightarrow{\overrightarrow{M2}}^e$ for an element e is written as:

$$\overrightarrow{\overrightarrow{M2}}^e = \int_{\Omega^e} \frac{\partial \vec{N}^e}{\partial x} \left(\frac{k_{xx}^{i-1^e}}{\mu} \frac{\partial \vec{N}^e}{\partial x} + \frac{k_{xy}^{i-1^e}}{\mu} \frac{\partial \vec{N}^e}{\partial y} \right) + \frac{\partial \vec{N}^e}{\partial y} \left(\frac{k_{yx}^{i-1^e}}{\mu} \frac{\partial \vec{N}^e}{\partial x} + \frac{k_{yy}^{i-1^e}}{\mu} \frac{\partial \vec{N}^e}{\partial y} \right) d\Omega \quad (3-84)$$

Taking permeability and viscosity of the fluid constant it becomes:

$$\begin{aligned} \overrightarrow{\overrightarrow{M2}}^e &= \frac{k_{xx}^{i-1^e}}{\mu} \int_{\Omega^e} \frac{\partial \vec{N}^e}{\partial x} \frac{\partial \vec{N}^e}{\partial x} d\Omega + \frac{k_{xy}^{i-1^e}}{\mu} \int_{\Omega^e} \frac{\partial \vec{N}^e}{\partial x} \frac{\partial \vec{N}^e}{\partial y} d\Omega + \\ &\quad \frac{k_{yx}^{i-1^e}}{\mu} \int_{\Omega^e} \frac{\partial \vec{N}^e}{\partial y} \frac{\partial \vec{N}^e}{\partial x} d\Omega + \frac{k_{yy}^{i-1^e}}{\mu} \int_{\Omega^e} \frac{\partial \vec{N}^e}{\partial y} \frac{\partial \vec{N}^e}{\partial y} d\Omega \end{aligned} \quad (3-85)$$

Transforming the global co-ordinates in this equation into local co-ordinates and combining with equation (3-48) we obtain:

$$\begin{aligned} \overrightarrow{\overrightarrow{M2}}^e &= \frac{k_{xx}^{i-1^e}}{\mu} \int_{-1}^1 \int_{-1}^1 |J| \frac{\partial \vec{N}^e}{\partial x} \frac{\partial \vec{N}^e}{\partial x} d\xi d\eta + \frac{k_{xy}^{i-1^e}}{\mu} \int_{-1}^1 \int_{-1}^1 |J| \frac{\partial \vec{N}^e}{\partial x} \frac{\partial \vec{N}^e}{\partial y} d\xi d\eta + \\ &\quad \frac{k_{yx}^{i-1^e}}{\mu} \int_{-1}^1 \int_{-1}^1 |J| \frac{\partial \vec{N}^e}{\partial y} \frac{\partial \vec{N}^e}{\partial x} d\xi d\eta + \frac{k_{yy}^{i-1^e}}{\mu} \int_{-1}^1 \int_{-1}^1 |J| \frac{\partial \vec{N}^e}{\partial y} \frac{\partial \vec{N}^e}{\partial y} d\xi d\eta \end{aligned} \quad (3-86)$$

Using the Gauss quadrature from equation (3-57), this equation can be written as:

$$\begin{aligned}
\overrightarrow{M2}^e = & \frac{k_{xx}^{i-1^e}}{\mu} \sum_i^n \sum_j^n H_i H_j |J_{i,j}| \frac{\overrightarrow{\partial N_{i,j}^e}}{\partial x} \frac{\overrightarrow{\partial N_{i,j}^e}}{\partial x} + \frac{k_{xy}^{i-1^e}}{\mu} \sum_i^n \sum_j^n H_i H_j |J_{i,j}| \frac{\overrightarrow{\partial N_{i,j}^e}}{\partial x} \frac{\overrightarrow{\partial N_{i,j}^e}}{\partial y} + \\
& \frac{k_{yx}^{i-1^e}}{\mu} \sum_i^n \sum_j^n H_i H_j |J_{i,j}| \frac{\overrightarrow{\partial N_{i,j}^e}}{\partial y} \frac{\overrightarrow{\partial N_{i,j}^e}}{\partial x} + \frac{k_{yy}^{i-1^e}}{\mu} \sum_i^n \sum_j^n H_i H_j |J_{i,j}| \frac{\overrightarrow{\partial N_{i,j}^e}}{\partial y} \frac{\overrightarrow{\partial N_{i,j}^e}}{\partial y}
\end{aligned} \quad (3-87)$$

where n is the number of gauss points while H is the weighting factor.

The derivation with respect to x of the shape functions for a four-nodded element is:

$$\frac{\overrightarrow{\partial N}^e}{\partial x} = \begin{pmatrix} \frac{\partial N_1}{\partial x} & \frac{\partial N_2}{\partial x} & \frac{\partial N_3}{\partial x} & \frac{\partial N_4}{\partial x} \end{pmatrix} \quad (3-88)$$

Expanding based on local co-ordinates this equation will take the form:

$$\frac{\overrightarrow{\partial N}^e}{\partial x} = \begin{pmatrix} \frac{\partial \xi}{\partial x} \frac{\partial N_1}{\partial \xi} + \frac{\partial \eta}{\partial x} \frac{\partial N_1}{\partial \eta} \dots\dots \frac{\partial \xi}{\partial x} \frac{\partial N_4}{\partial \xi} + \frac{\partial \eta}{\partial x} \frac{\partial N_4}{\partial \eta} \end{pmatrix} \quad (3-89)$$

Then we have:

$$\frac{\overrightarrow{\partial N_{i,j}^e}}{\partial x} = \begin{pmatrix} \frac{\partial \xi}{\partial x}(\xi_i, \eta_j) \frac{\partial N_1}{\partial \xi}(\xi_i, \eta_j) \dots\dots + \frac{\partial \eta}{\partial x}(\xi_i, \eta_j) \frac{\partial N_4}{\partial \eta}(\xi_i, \eta_j) \end{pmatrix} \quad (3-90)$$

Similarly, we have the derivative of the shape function with respect to y :

$$\frac{\overrightarrow{\partial N_{i,j}^e}}{\partial y} = \begin{pmatrix} \frac{\partial \xi}{\partial y}(\xi_i, \eta_j) \frac{\partial N_1}{\partial \xi}(\xi_i, \eta_j) \dots\dots + \frac{\partial \eta}{\partial y}(\xi_i, \eta_j) \frac{\partial N_4}{\partial \eta}(\xi_i, \eta_j) \end{pmatrix} \quad (3-91)$$

The derivatives of the local coordinates can be obtained by inverting the Jacobian J . The derivatives of the shape functions for four noded elements are given by equations (3-50) and (3-51).

The load vector f can be obtained by:

$$\vec{f} = \sum_e \vec{f}^e \quad (3-92)$$

where \vec{f}^e is described earlier as:

$$\vec{f}^e = -\Delta t^i \overline{\overline{M}}^e \vec{P}_{i-1}^e \quad (3-93)$$

While pressure for four-noded element is described as:

$$\vec{P}_{i-1}^e = \begin{pmatrix} P_1^{i-1} & P_2^{i-1} & P_3^{i-1} & P_4^{i-1} \end{pmatrix}^T \quad (3-94)$$

Once the nodal pressures for four noded elements have been calculated, nodal velocities can easily be calculated based on the pressures. For this purpose Darcy's law is employed and discretisation of the equation is done as follows:

$$\overline{\overline{M}}^e \vec{v}_{i_{xx}}^e = \overline{\overline{M}}^e \vec{P}_{i-1}^e \quad (3-95)$$

$$\overline{\overline{M}}^e \vec{v}_{i_{yy}}^e = \overline{\overline{M}}^e \vec{P}_{i-1}^e \quad (3-96)$$

where $\overline{\overline{M}}^e$ is the same as described earlier, whereas $\overline{\overline{M}}^e$ is given as:

$$\overline{\overline{M}}^e_{3_{xx}} = \frac{k_{xx}^{i-1^e}}{\mu} \sum_i^n \sum_j^n H_i H_j |J_{i,j}| N_{i,j}^e \frac{\partial N_{i,j}^e}{\partial x} \quad (3-97)$$

$$\overline{\overline{M}}^e_{3_{yy}} = \frac{k_{yy}^{i-1^e}}{\mu} \sum_i^n \sum_j^n H_i H_j |J_{i,j}| N_{i,j}^e \frac{\partial N_{i,j}^e}{\partial y} \quad (3-98)$$

Time-Dependent Analytical Solution for Decoupled Fluid Flow

In the following solution the rock is linear elastic, porous, uniform and has isotropic rock properties, while the fluid is single phase and slightly compressible.

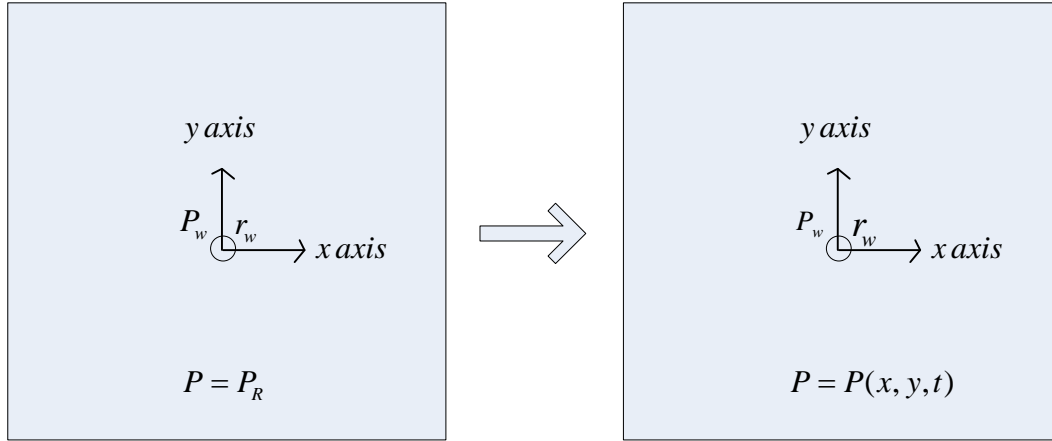


Figure 3-25: Decoupled fluid flow with constant wellbore pressure

Figure 3-25 shows a wellbore in an infinite domain of rock. The borehole radius is r_w and pressure is P_w . The initial pore pressure of the rock is P_R . The solution is given as:

$$P = P_R + (P_w - P_R)g(r, t) \quad (3-99)$$

where,

$$g(r, t) = 1 - \frac{2}{\pi} \int_0^{\infty} e^{-t_D x^2} \frac{J_0(x) Y_0(x r_D) Y_0(x)}{J_0(x)^2 + Y_0(x)^2} \frac{dx}{x} \quad (3-100)$$

where,

J_0 and Y_0 are the zero order Bassel functions of first and second kind, respectively, also:

$$r_D = \frac{r}{r_w} \quad (3-101)$$

$$t_D = \frac{kt}{\mu\phi c_T r_w^2} \quad (3-102)$$

By comparing this with the solution of a similar problem given by Detournay (1988), we have:

$$\tilde{g}(r, s) = \frac{K_0(\xi)}{sK_0(\beta)} \quad (3-103)$$

where, \tilde{g} is the Laplace transformation of g and:

$$\xi = r\sqrt{\frac{s}{c}} \quad (3-104)$$

$$\beta = r_w\sqrt{\frac{s}{c}} \quad (3-105)$$

The Laplace transformation can be inverted using:

$$f(r, t) \approx \frac{\ln 2}{t} \sum_{n=1}^N C_n \tilde{f}\left(r, n \frac{\ln 2}{t}\right) \quad (3-106)$$

where \ln represents the natural logarithm and:

$$C_n = (-1)^{n+\frac{N}{2}} \sum_{k=\lfloor (n+1)/2 \rfloor}^{\min(n, N/2)} \frac{k^{N/2} (2k)!}{(N/2 - k)! k! (k-1)! (n-k)! (2k-n)!} \quad (3-107)$$

where $\lfloor _ \rfloor$ is floor function and $\min(_)$ is the minimum. A good value of use of N is 10. Also the use of equation (3-103) is considered more stable instead of equation (3-100) (Hodge 2006).

Comparison between Numerical and Analytical Solution

A simple example is conducted for a comparison between numerical and analytical solutions. A region of unit length is divided into 10×10 blocks where the size of each block is 0.1×0.1 units. A wellbore at (0,0) co-ordinates is pressurized at unit pressure. Unit permeability and unit viscosity were considered for this case. Radius of investigation 'r' was set as 1 for an analytical solution which is the same as setting unit block parameter in the x and y directions. Total compressibility C_T was set as $1.45 \times 10^{-9} \text{ Pa}^{-1}$.

Nodal pressures are calculated for 10×10 elements and pressure values for the nodes present on *x axis* or *y axis* (the same because of the symmetric problem) are compared with the pressure values obtained from the analytical solution for changing radius from 0.1 unit to 1.

Figure 3-26 shows the comparison between numerical and analytical results for this case.

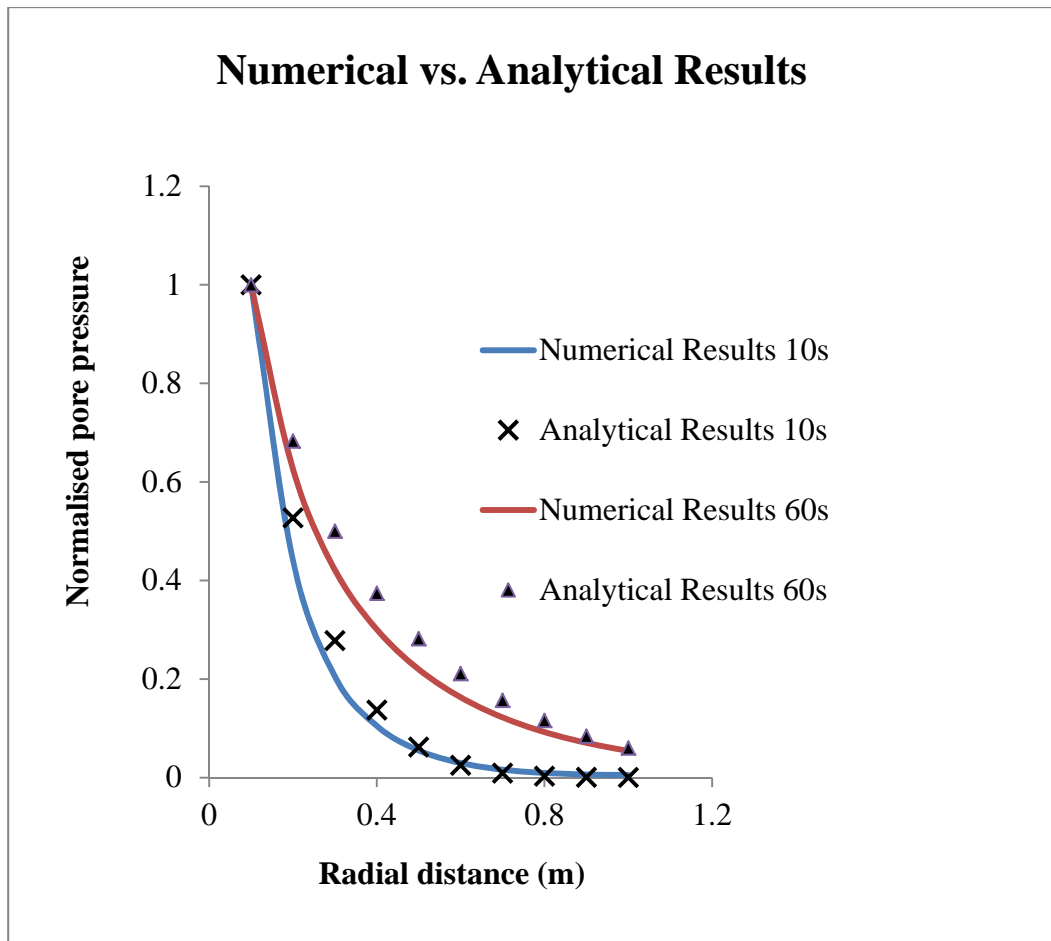


Figure 3-26: Numerical vs. analytical results for unit size region at time step of 10 and 60sec

Numerical results are compared against analytical results for two different time steps 10 seconds and 60 seconds and the plot shows a good match between the two results.

Numerically calculated pressure and velocity profiles for 10seconds time step are presented in **Figs. 3-27** and **3-28**, respectively.

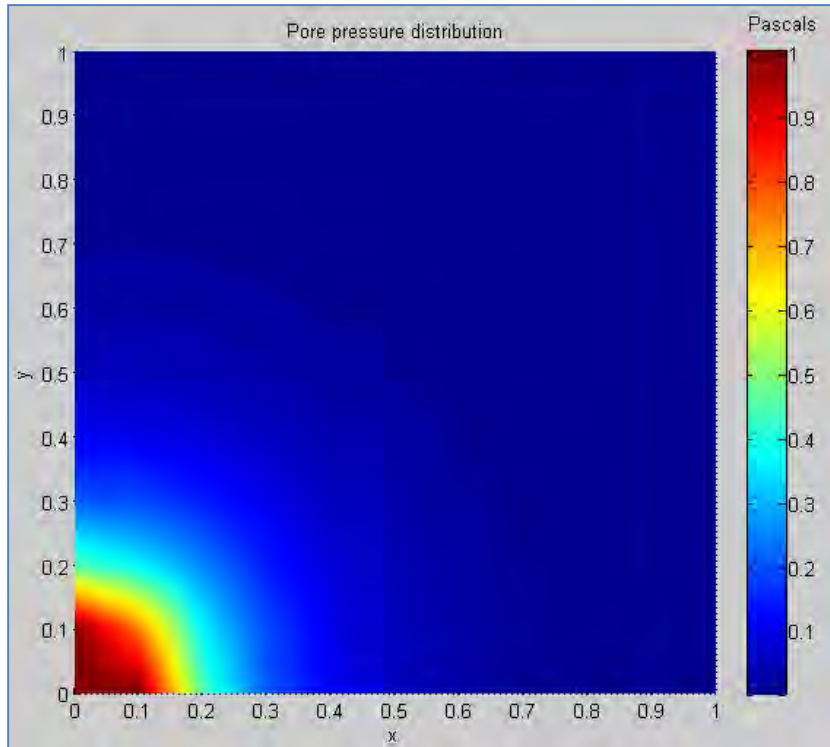


Figure 3-27: Pore pressure distribution at time step of 10sec (Numerical result) for well reference at (0, 0)

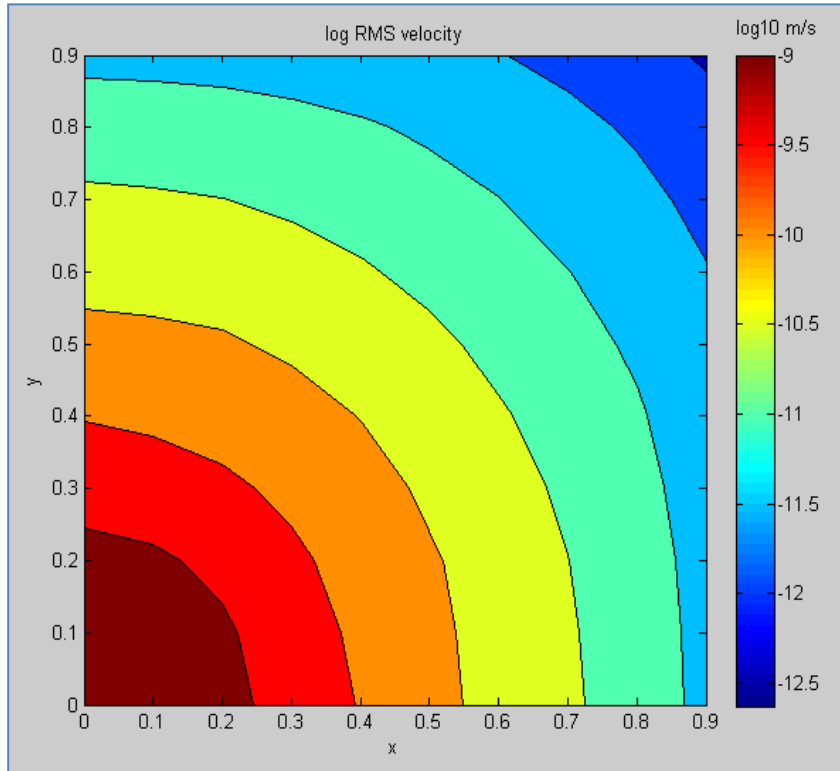


Figure 3-28: Velocity distribution at time step of 10sec (Numerical result) for well reference at (0, 0)

3.2.3 Results and Discussion

A 2D fracture network presented by Gholizadeh and Rahman (2012) is chosen to simulate fluid flow through Amadeus Basin (in Australia) within an area of $1000m \times 1000m$ (see **Fig. 3-29**). The reservoir is discretised into 10,000 grid blocks and the permeability tensor model is run to obtain block permeabilities. In this case, due to the higher number of grid blocks the permeability tensor is presented in a form of permeability map (see **Fig. 3-30**) instead of elliptical representation as mentioned previously (see **Fig. 3-21**). Results of the permeability tensor are fed to decoupled fluid flow model to obtain pressure and velocity profiles throughout the reservoir.

Firstly, depletion flow mechanism is modelled for a well bore at the centre of the reservoir (500m, 500m). Well bottom-hole pressure is set to be 3,500psi whereas the reservoir pressure is 4,500psi. Pressure and velocity distribution profiles over the reservoir are shown in **Figs. 3-31** and **3-32**. Changes in pressure from the boundaries to the centre of the reservoir (wellbore) can be observed from **Fig. 3-31**. In this figure, pressure at boundaries is lower than the given reservoir pressure (4500psi) due to depletion mechanism in a close boundary system to achieve steady state flow. Velocities from the boundaries of the reservoir to the centre point (well bore) indicate the flow path which follows the fracture network (see **Fig. 3-32**).

Next, a five-spot injection production scenario is modelled to evaluate the pressure losses for the reservoir. For this purpose an injection well in the centre of the reservoir (500m, 500m) and four corner production wells are specified. Production wells A, B, C and D are located at (0, 0), (1000, 0), (1000, 1000), and (0, 1000) in meters, see **Fig. 3-29**. First, the injection well pressure is set to be 5,000psi whereas each production well at 4,000psi (pressure drop 1000psi). Pressure and velocity profiles are presented in **Figs. 3-33** and **3-34** where fluid flows through the fracture network path between the injector and producers. Furthermore, simulation for the injection production scenario is rerun for pressure drops of 1,500, 2,000

and 3,000 psi. Individual well production rates and total production rates for each pressure drop are plotted in **Fig. 3-35**. It is observed that well A produces at relatively high flow rates for the applied pressure drops which are followed by production rates of well C (see **Fig. 3-35**). This behaviour can be confirmed by the density and orientation of fractures between the injection and these production wells. Similarly, well B and D show lower production rates for the applied pressure drops (see **Fig. 3-35**) which are expected as there are no fractures oriented towards these wells. It is observed that well A produces at a flow rate 38.7% of the total flow rate, where as well C at 33.9%. Similarly, well B and D produce at 14.2% and 13.2% of the total flow rate (calculated from **Fig. 3-35**), respectively.

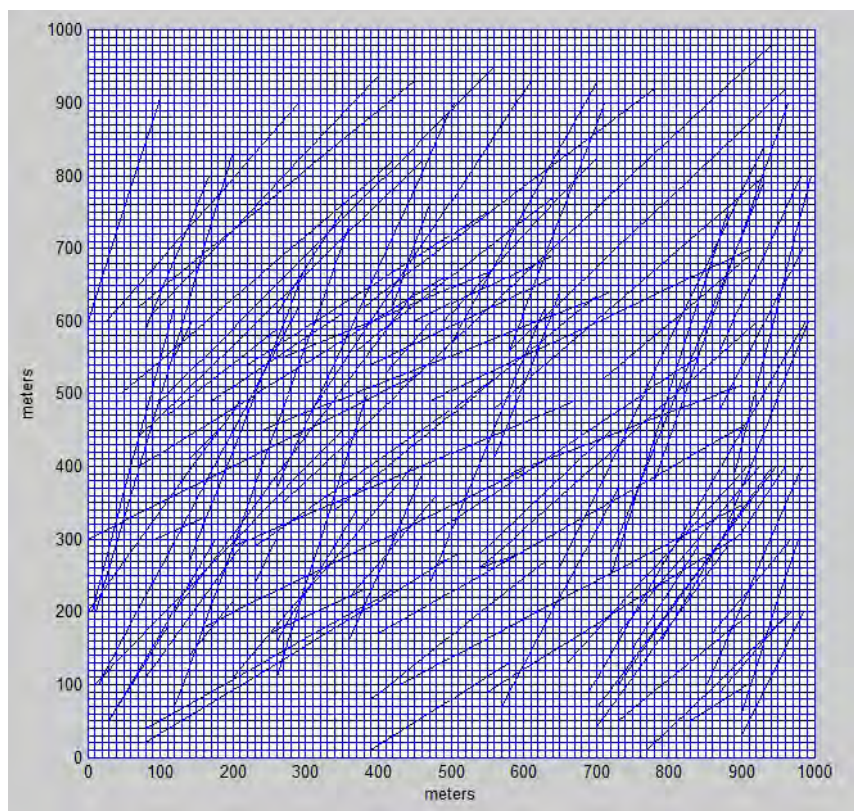


Figure 3-29: Fracture network of a slice from Amadeus Basin

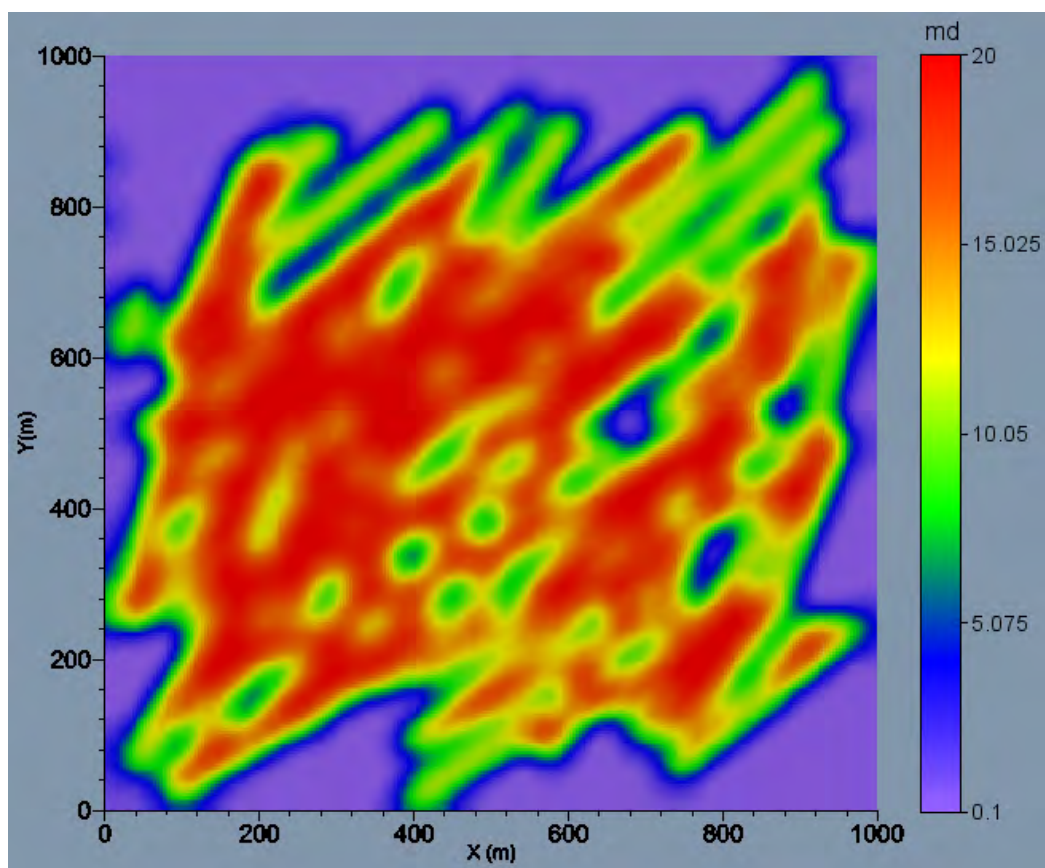


Figure 3-30: Permeability map of fracture network in Fig. 3-29

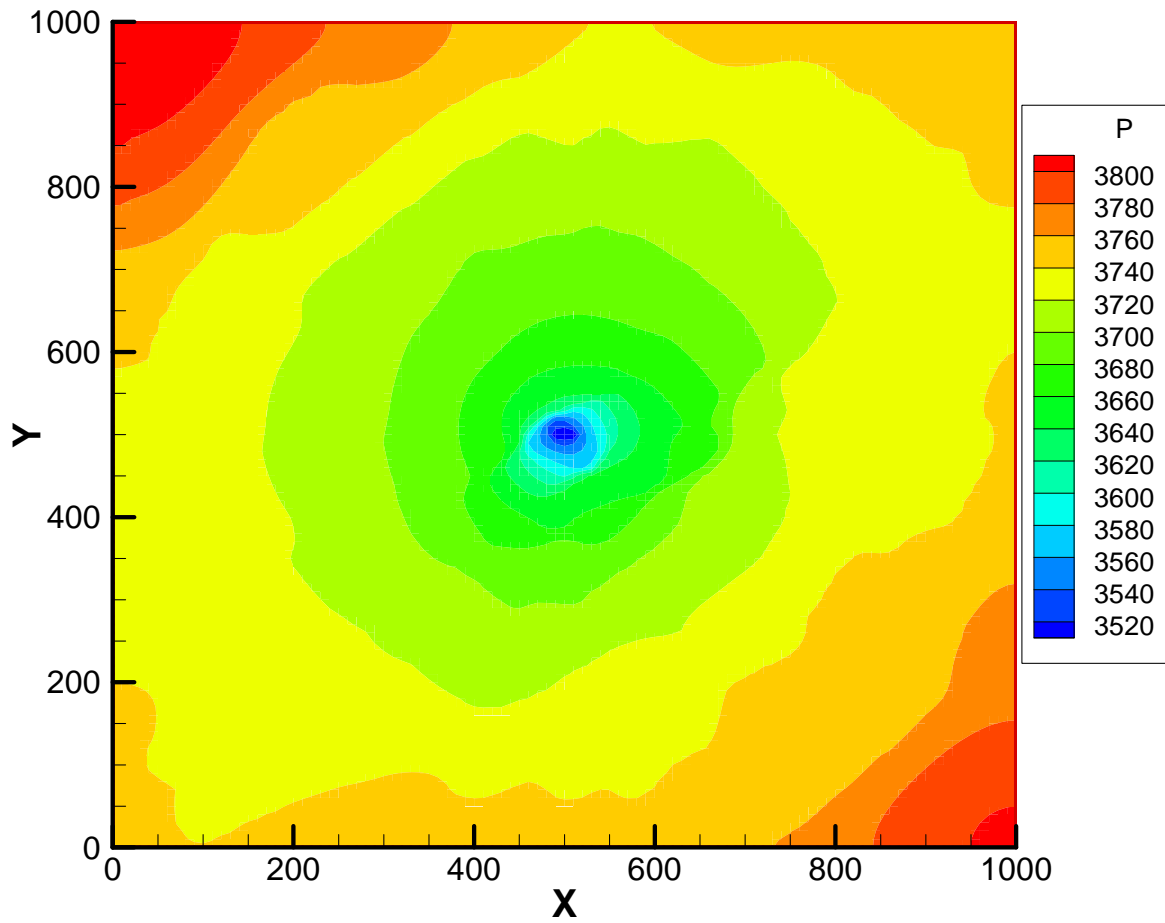


Figure 3-31: Pressure profile (Psi) of depletion case at steady state, for

$$P_{Res} = 4500 \text{ psi} , P_w = 3500 \text{ psi}$$

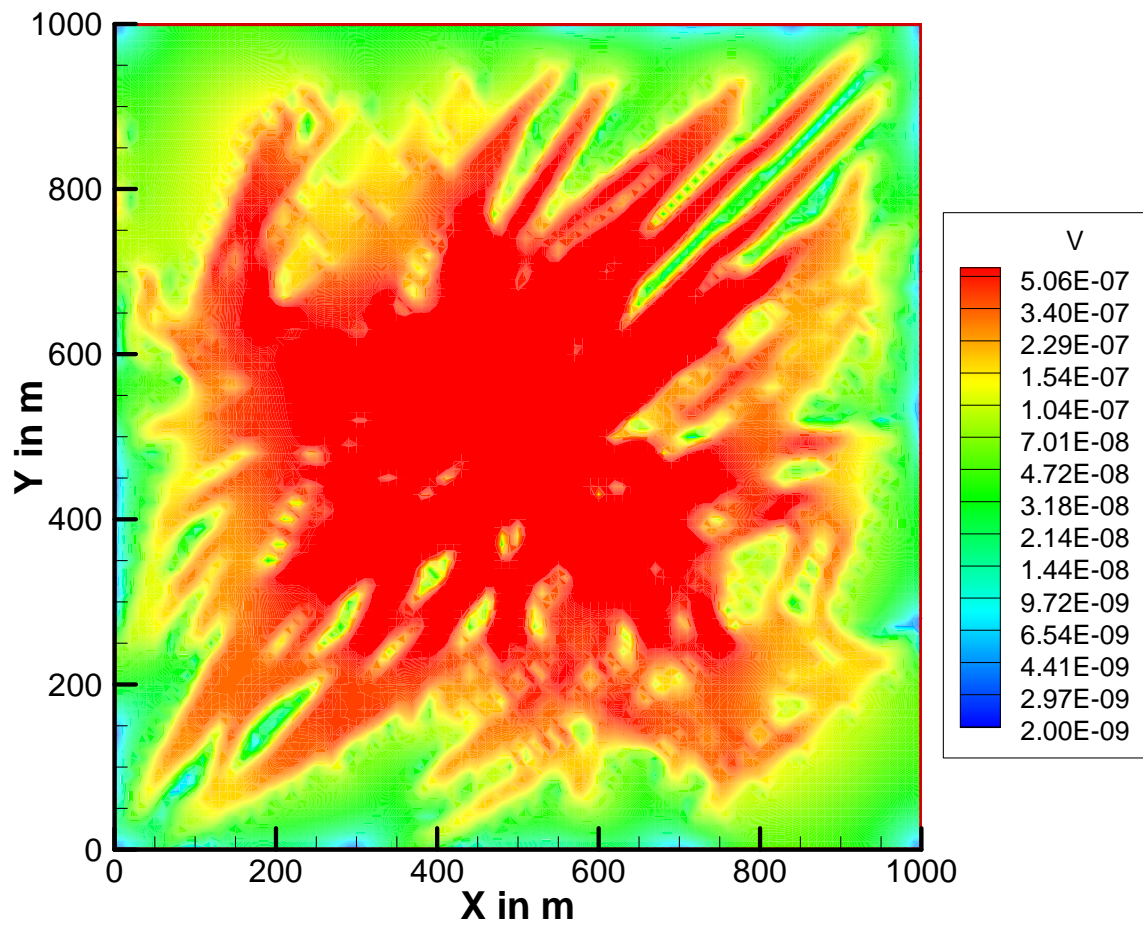


Figure 3-32: Velocity profile (m/sec) of depletion case at steady state for $P_{Res} = 4500\text{ psi}$,

$$P_w = 3500\text{ psi}$$

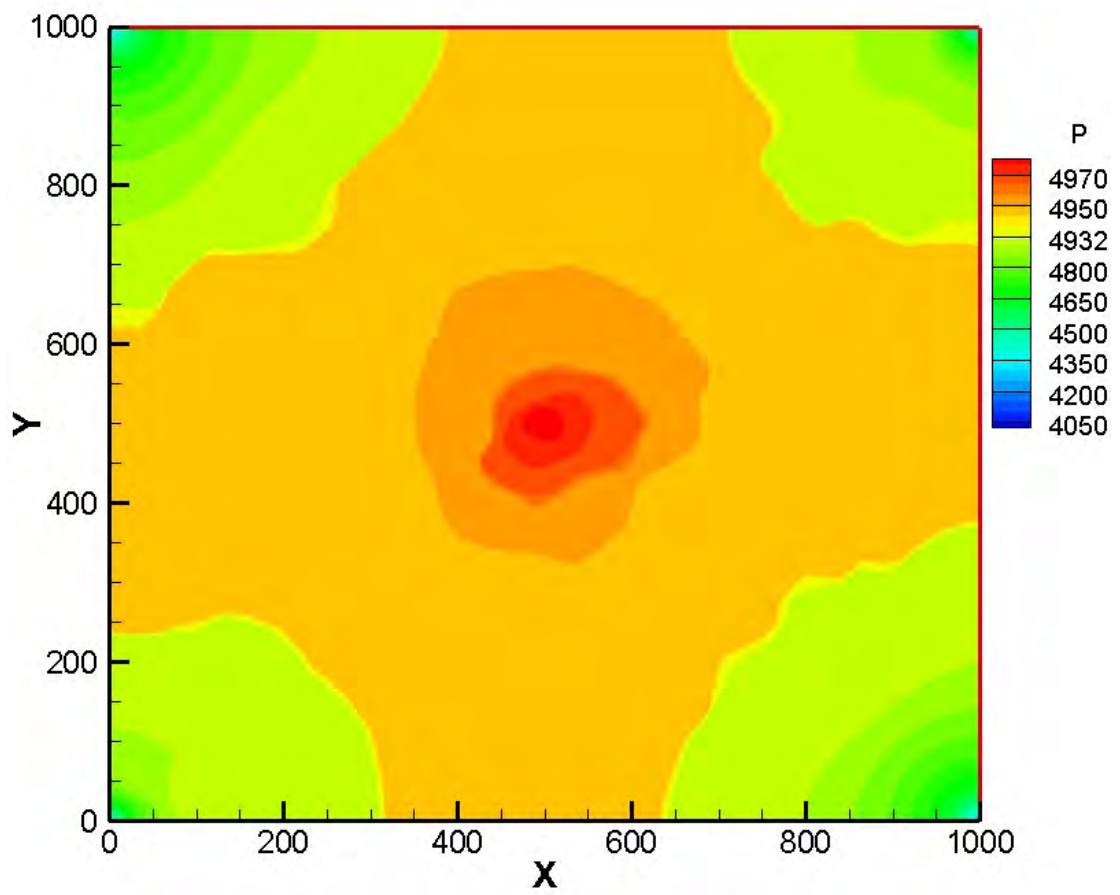


Figure 3-33: Pore pressure (Psi) distribution for five spot pattern at pressure drop of 1000psi

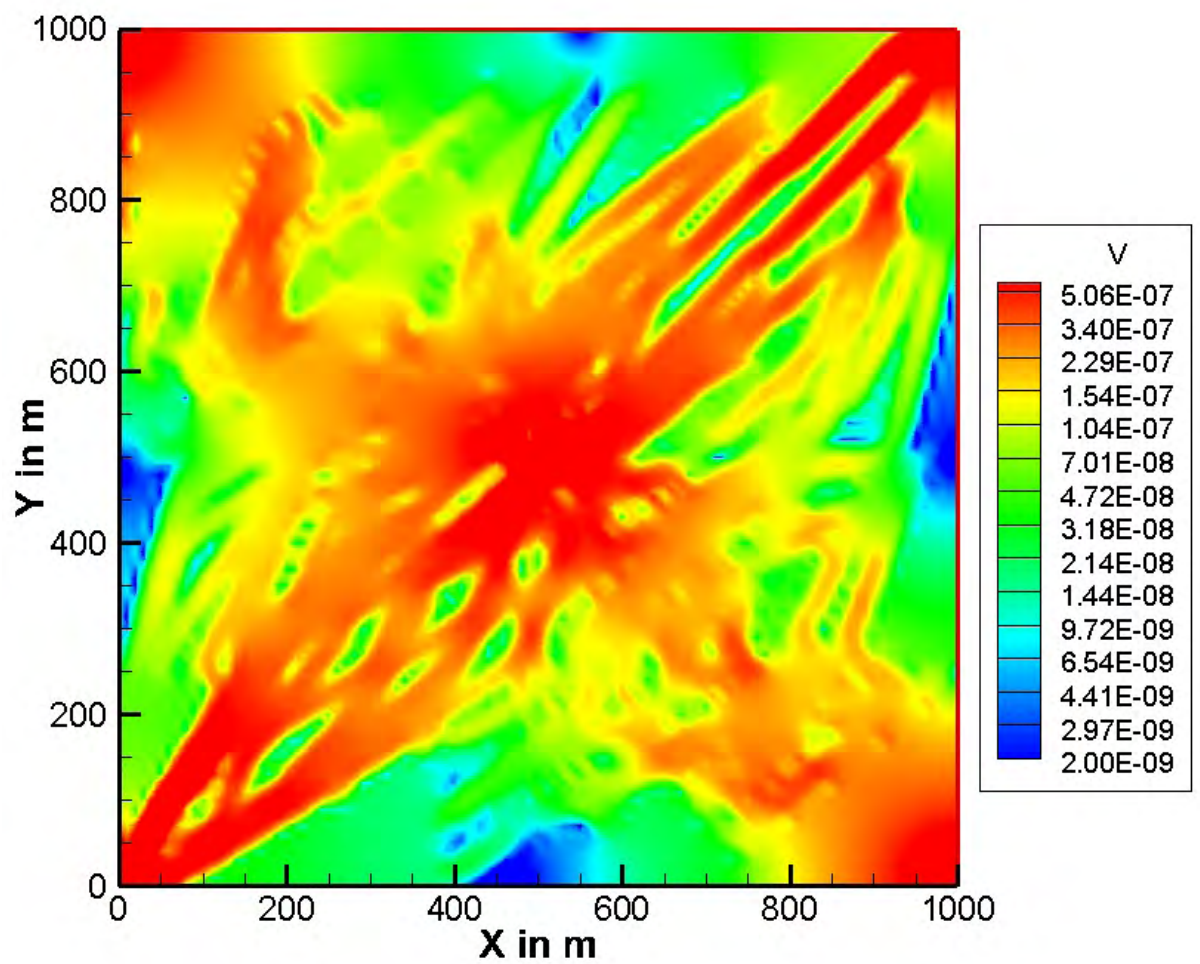


Figure 3-34: Velocity (m/sec) profile for five spot pattern at pressure drop of 1000psi

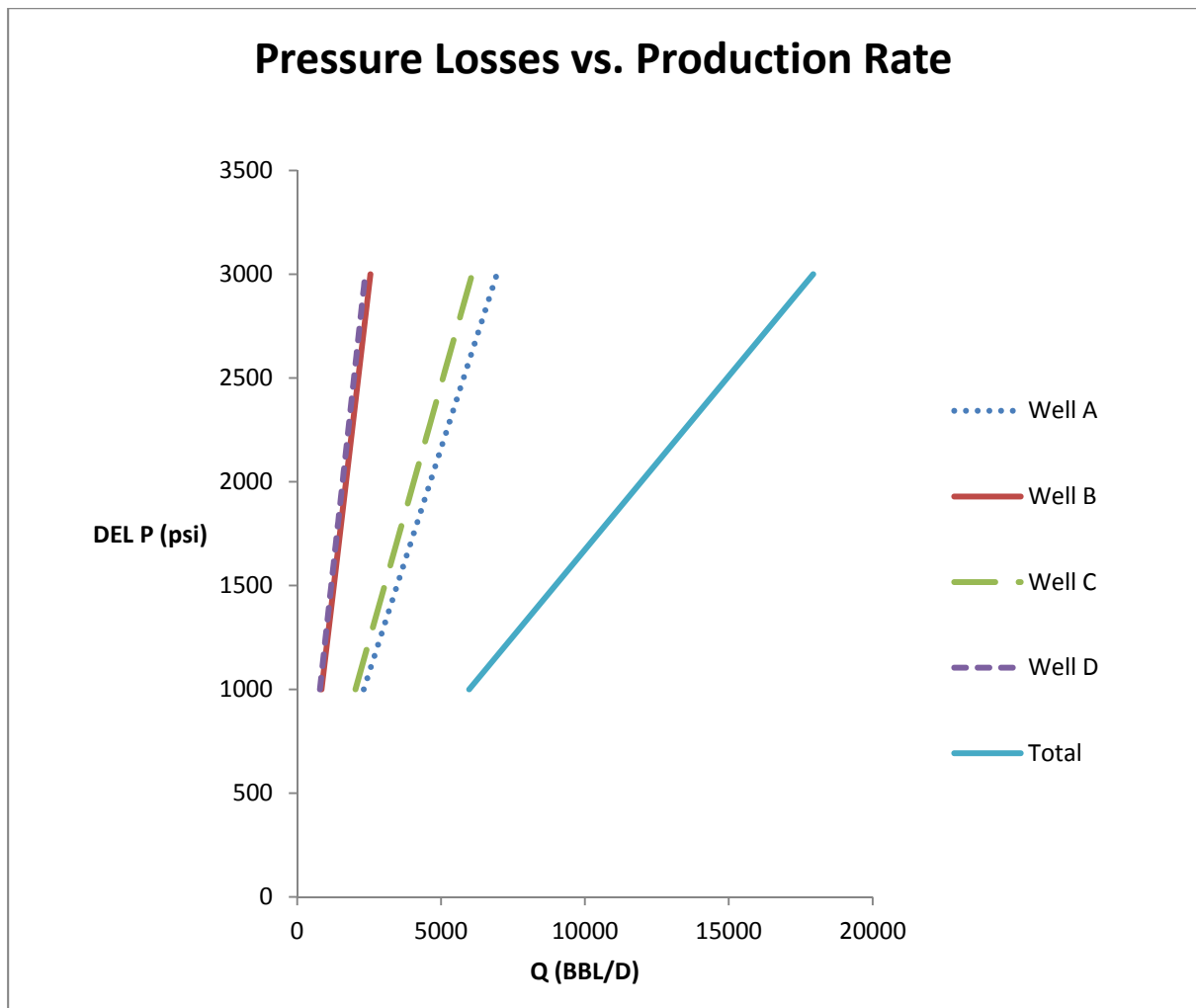


Figure 3-35: Pressure losses vs. individual well production rates and total production rates

Chapter 4

Multiphase Fluid Flow Simulation in Arbitrarily-Oriented Naturally Fractured Porous Media

This chapter aims to present modelling of the behaviour of two phase fluid flow for fractured porous media. A comprehensive literature review on modelling of two phase flow is presented in Chapter 2. Mathematical formulation, boundary and initial conditions as well as discretization of the two phase fluid flow problem are discussed in this chapter. Similar to the laboratory study, several examples are presented to illustrate the performance and capability of the approach. The ultimate objective to model numerically the laboratory two-phase observations has been achieved successfully for a few number of fractures present inside a matrix.

4.1 Mathematical Formulation

A two dimensional, two phase fluid flow numerical simulation model is presented. Finite difference method is used to formulate the oil and water equations. A MATLAB code was written to present the solution process and run efficiently. Two-phase fluid flow modelling includes flow equations for all the fluid phases present in the porous media, as well as additional relationship between fluid phases and initial and boundary conditions. Flow equations used for this modelling are obtained by combining the appropriate forms of the mass-conservation equation, the equation of state and the Darcy's law.

In water oil flow system, it is assumed that there are only two phases which are immiscible; therefore there is no mass transfer between the oil and water phases. In addition it is assumed

that flow is isothermal and fluid phases are in thermodynamic equilibrium. By substituting the Darcy's law for multiphase flow into the mass-conservation equation, following two-dimensional fluid flow equations can be obtained.

$$\frac{\partial}{\partial x} \left[\beta_c k_x A_x \frac{k_{ro}}{\mu_o B_o} \left(\frac{\partial p_o}{\partial x} - \gamma_o \frac{\partial Z}{\partial x} \right) \right] \Delta x + \frac{\partial}{\partial y} \left[\beta_c k_y A_y \frac{k_{ro}}{\mu_o B_o} \left(\frac{\partial p_o}{\partial y} - \gamma_o \frac{\partial Z}{\partial y} \right) \right] \Delta y = \frac{V_b}{a_c} \frac{\partial}{\partial t} \left(\frac{\phi S_o}{B_o} \right) - q_{osc} \quad (4-1)$$

$$\frac{\partial}{\partial x} \left[\beta_c k_x A_x \frac{k_{rw}}{\mu_w B_w} \left(\frac{\partial p_w}{\partial x} - \gamma_w \frac{\partial Z}{\partial x} \right) \right] \Delta x + \frac{\partial}{\partial y} \left[\beta_c k_y A_y \frac{k_{rw}}{\mu_w B_w} \left(\frac{\partial p_w}{\partial y} - \gamma_w \frac{\partial Z}{\partial y} \right) \right] \Delta y = \frac{V_b}{a_c} \frac{\partial}{\partial t} \left(\frac{\phi S_w}{B_w} \right) - q_{wsc} \quad (4-2)$$

where β_c is the transmissibility conversion factor which is constant 1.127 as given by Ertekin et al. (2001), A_x and A_y are the cross sections normal to the x and y directions (ft^2), respectively, k_{ro} and k_{rw} are the oil and water relative permeabilities, respectively, μ_o and μ_w are oil and water viscosities (cp), respectively, B_o and B_w are oil and water formation volume factors (RB/STB), respectively, V_b is the grid block bulk volume (ft^3), a_c is the volume conversion factor and equals to 5.615, ϕ is the porosity, S_o and S_w are the oil and water phase saturations, respectively, and q_{osc} and q_{wsc} are the oil and water production rates at standard conditions (STB/D), respectively. Transmissibilities for oil and water in the x and y directions are by Ertekin et al. (2001).

$$T_{ox} = \beta_c \frac{k_x A_x}{\Delta x} \frac{k_{ro}}{\mu_o B_o} \quad (4-3)$$

$$T_{oy} = \beta_c \frac{k_y A_y}{\Delta y} \frac{k_{ro}}{\mu_o B_o} \quad (4-4)$$

$$T_{wx} = \beta_c \frac{k_x A_x}{\Delta x} \frac{k_{rw}}{\mu_w B_w} \quad (4-5)$$

$$T_{wy} = \beta_c \frac{k_y A_y}{\Delta y} \frac{k_{rw}}{\mu_w B_w} \quad (4-6)$$

The oil and water occupy the whole pore space as expressed by equation 4-7. Capillary pressure effects are neglected as indicated in equation 4-9.

$$S_o + S_w = 1 \quad (4-7)$$

$$P_{cow} = p_o - p_w \quad (4-8)$$

For $P_{cow} = 0$,

$$p_o = p_w \quad (4-9)$$

In equations 4-1 and 4-2 there are four unknowns: p_w , p_o , S_w , and S_o , but using the saturation and pressure relationships in equations 4-7 and 4-9, the number of unknowns can be reduced to two; one saturation and one pressure. Once the saturation and pressure for one phase are calculated, equations 4-7 and 4-9 are used to calculate the second phase saturation and pressure.

Substituting equations 4-7 and 4-9 into equations 4-1 and 4-2 and knowing the initial and boundary conditions for the problem, one may calculate the unknowns S_o and p_o . To solve the two-phase flow problem for laboratory experiments (see chapter 2), the same initial and boundary conditions are assumed. The initial pressure of the laboratory system is set to be 14.7psi and initially the system is saturated fully with water, i.e. the oil saturation is zero.

Similar to the laboratory model two opposite boundaries of the domain are no flow as shown in **Fig. 4-1**. An injection well is specified in each grid block of first layer, and the same flow rate as used in the experimental study is distributed equally to the grid blocks with injection wells. The whole system is discretised into 50×100 grid blocks the in x and y directions.

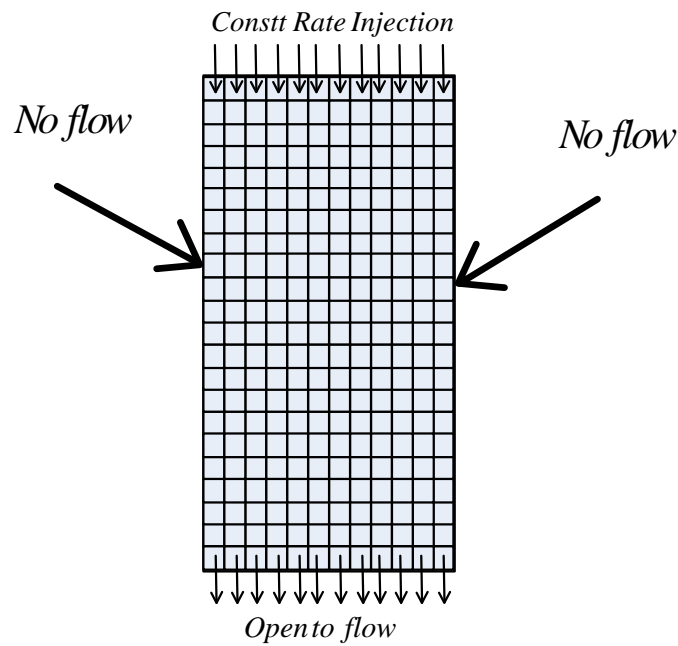


Figure 4-1: Boundary conditions for modelling two phase fluid flow

Block transmissibilities for the current time step are calculated using the oil and water relative permeabilities and oil saturation for the same time step. Then the calculated block transmissibilities are used to obtain pressure and saturations for the next time step.

IMPES method Aziz and Settari (1979) is used to obtain single pressure equations for each grid block in its first step by combining all flow equations to eliminate saturation unknowns. To achieve this, transmissibilities are evaluated explicitly at time level $n+1$. IMPES is used when the saturation changed from one time step to next. Pressure equations for each grid

block are written and resulting set of equations is solved iteratively for the oil phase pressure distribution. In the next step of IMPES method, saturations are explicitly solved by substituting pressures at t^{n+1} into the flow equation. **Figure 4-2** describes grid blocks discretization only in the x direction. Based on this discretization final oil and water fluid flow equations in the x and y directions are expressed below.

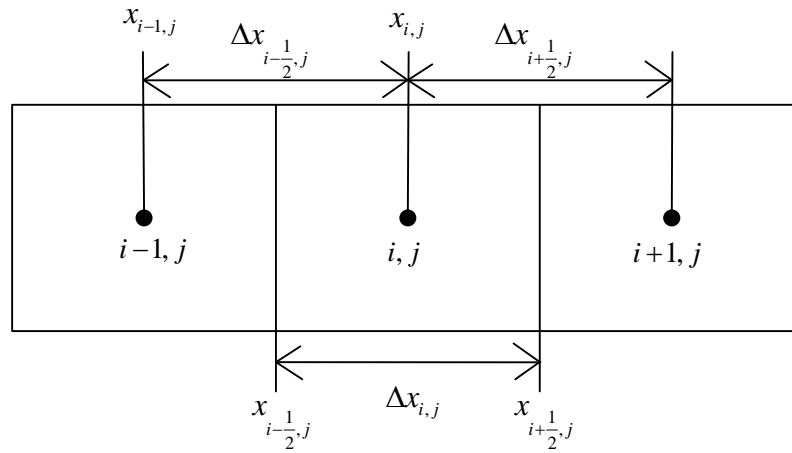


Figure 4-2: Discretization in the x direction

$$\begin{aligned}
 & T_{oy_{i,j-\frac{1}{2}}} p_{o_{i,j-1}} + T_{ox_{i-\frac{1}{2},j}} p_{o_{i-1,j}} - \left(T_{oy_{i,j-\frac{1}{2}}} + T_{ox_{i-\frac{1}{2},j}} + T_{ox_{i+\frac{1}{2},j}} + T_{oy_{i,j+\frac{1}{2}}} \right) p_{o_{i,j}} + T_{ox_{i+\frac{1}{2},j}} p_{o_{i+1,j}} + T_{oy_{i,j+\frac{1}{2}}} p_{o_{i,j+1}} \\
 &= \frac{V_{b_{i,j}}}{a_c \Delta t} \left[\left(\frac{\phi S_o}{B_o} \right)_{i,j}^{n+1} - \left(\frac{\phi S_o}{B_o} \right)_{i,j}^n \right] - q_{osc_{i,j}}
 \end{aligned} \tag{4-10}$$

$$\begin{aligned}
 & T_{wy_{i,j-\frac{1}{2}}} p_{w_{i,j-1}} + T_{wx_{i-\frac{1}{2},j}} p_{w_{i-1,j}} - \left(T_{wy_{i,j-\frac{1}{2}}} + T_{wx_{i-\frac{1}{2},j}} + T_{wx_{i+\frac{1}{2},j}} + T_{wy_{i,j+\frac{1}{2}}} \right) p_{w_{i,j}} + T_{wx_{i+\frac{1}{2},j}} p_{w_{i+1,j}} + T_{wy_{i,j+\frac{1}{2}}} p_{w_{i,j+1}} \\
 &= \frac{V_{b_{i,j}}}{a_c \Delta t} \left[\left(\frac{\phi(1-S_o)}{B_w} \right)_{i,j}^{n+1} - \left(\frac{\phi(1-S_o)}{B_w} \right)_{i,j}^n \right] - q_{wsc_{i,j}}
 \end{aligned} \tag{4-11}$$

In these equations pressures are block-centred whereas transmissibilities are calculated on the boundary of each grid block (see equations 4-10, 4-11 and **Fig. 4-2**). In this model, oil and water relative permeability curves are generated using the Corey type power law as mentioned in chapter 2 (see equations 2-5 and 2-6).

Total and grid block pore volumes of the domain are calculated using the equations below.

$$V_p = \phi \times V_B \quad (4-12)$$

$$V_{p_i} = \phi \times V_{b_i} \quad (4-13)$$

where V_B is total bulk volume of the system and V_{b_i} the bulk volume of grid i . ϕ is 40% , the same as laboratory models (see chapter 2). Cumulative water production is calculated using the equations given below.

$$\text{Cum. water production} = \text{Initial water volume} - \text{Current water volume} \quad (4-14)$$

$$\text{Initial water volume} = \text{Initial water saturation} \times V_p \quad (4-15)$$

$$\text{Current water volume} = \sum_{i=1}^n (1 - S_o) \times V_{p_i} \quad (4-16)$$

Here n is the total number of grid blocks and initial water saturation is 1.

Pore volume injection at any time is calculated based on the cumulative water production.

Before breakthrough, the injected oil volume is equal to the produced water volume so PVI can be calculated as;

$$PVI_{\text{before BT}} = \frac{\text{Cum. water production}}{V_{p_{\text{Total}}}} \quad (4-17)$$

After breakthrough, injected volume is not equal to the produced water volume and following equation is used to calculate PVI.

$$PVI_{afterBT} = \frac{q_{inj}(t - t_b)}{V_{PTotal}} + PVI_{atBT} \quad (4-18)$$

4.2 Results and Discussion:

The two-phase flow simulation is run for experimentally designed homogeneous and heterogeneous glass bead systems of dimension $10cm \times 20cm \times 0.2cm$. All parameters are kept the same as the laboratory study to check the efficiency of the numerical model. Laboratory measured relative permeabilities are input to the numerical model and pressures and productions are calculated. Pressure and production plots are presented in **Figs. 4-3** and **4-4**. Similar to the laboratory study, it is found that single fracture models show relatively late breakthrough as compared to two fracture systems. It is very clear observation from numerical results of single-fracture models that a single fracture oriented at 0 degree to the direction of flow shows a quick breakthrough among single fracture models which is followed by single fracture at 45 degree (see Figure 4-3). A comparison between numerically and experimentally obtained pressure and productions are shown in **Figs. 4-5** and **4-6**. The numerical model predicts the experimental observations well.

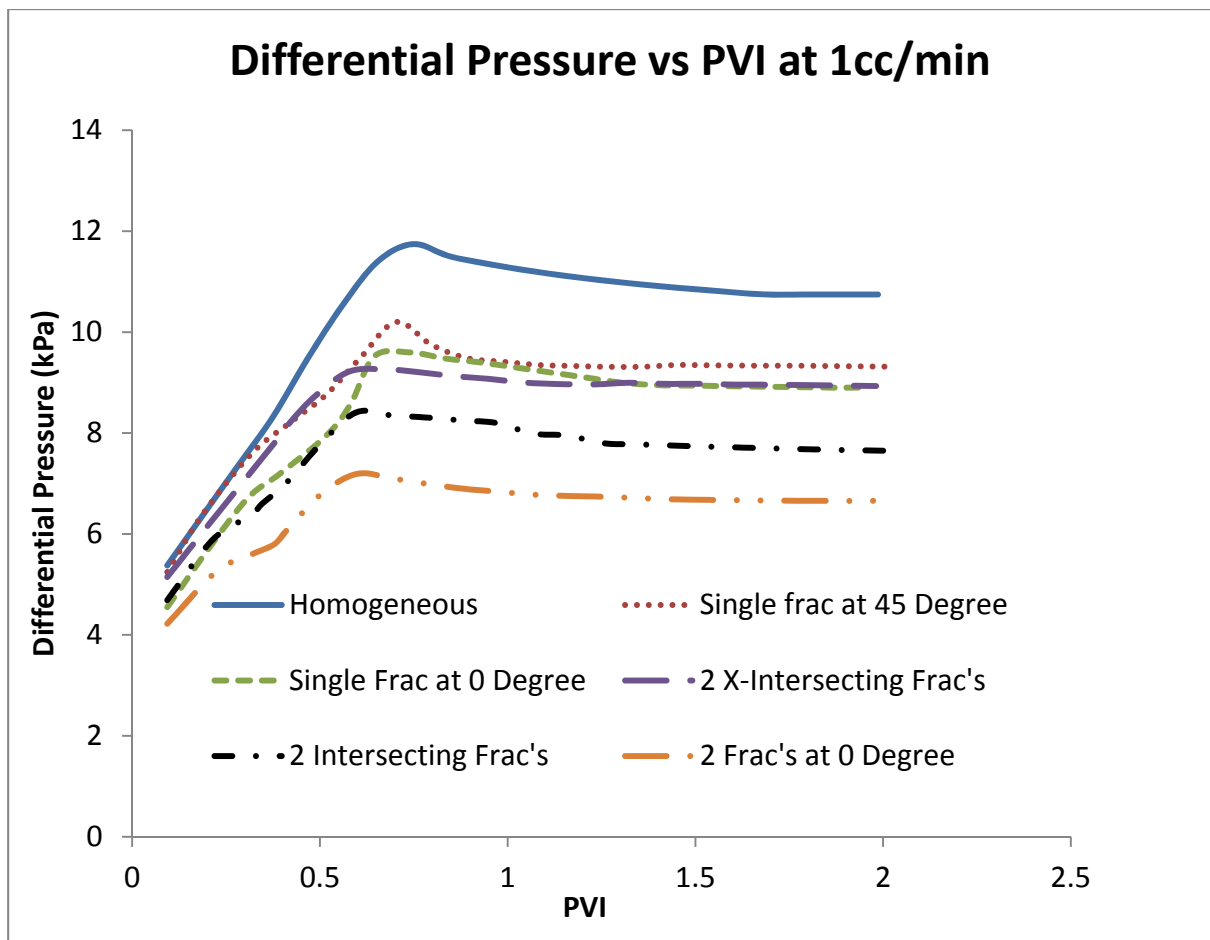


Figure 4-3: Differential pressures vs. PVI for the glass bead packs at $1\text{cm}^3 / \text{min}$ (Numerical results)

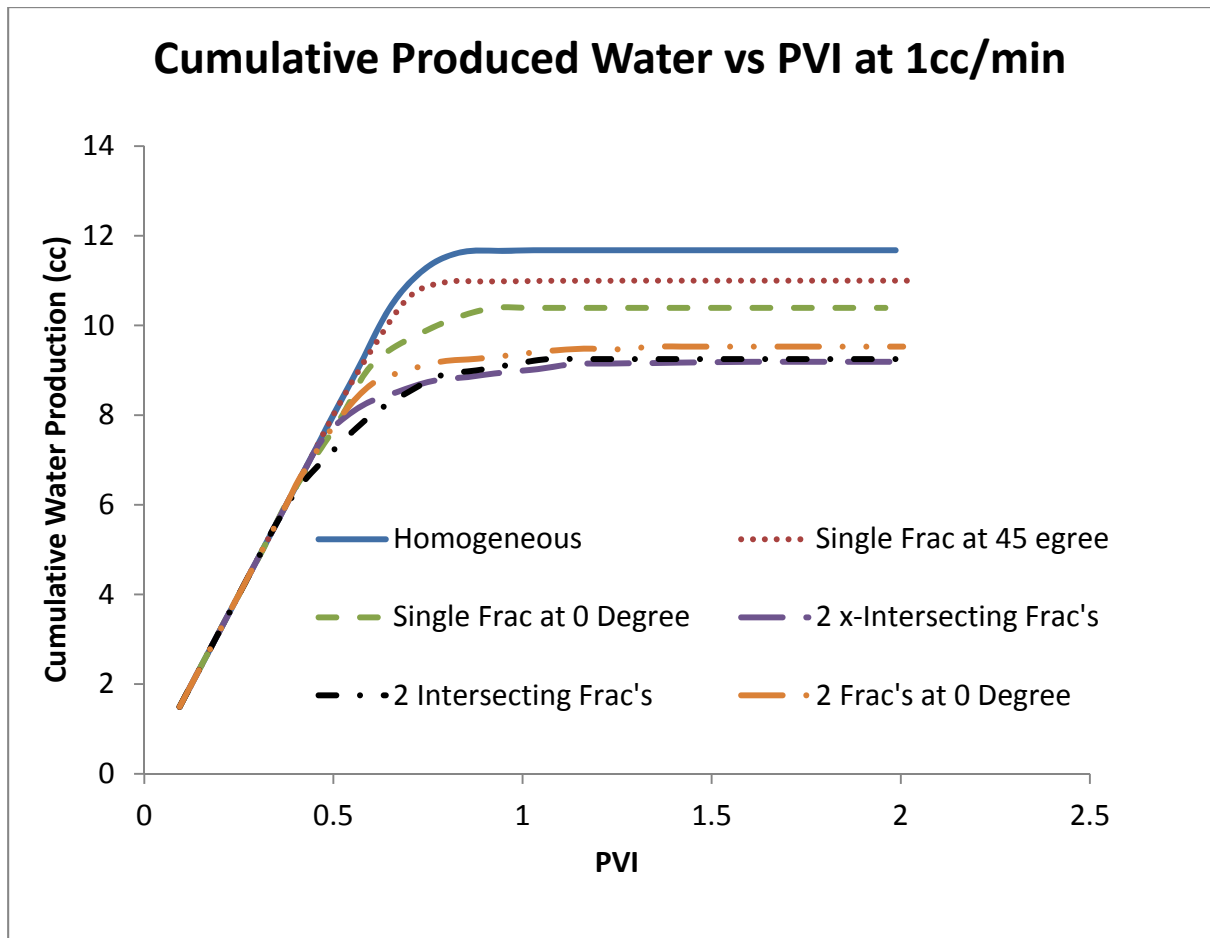


Figure4-4: Cumulative produced water vs. injected pore volume for the glass bead packs at $1\text{cm}^3 / \text{min}$ injection rate (Numerical results)

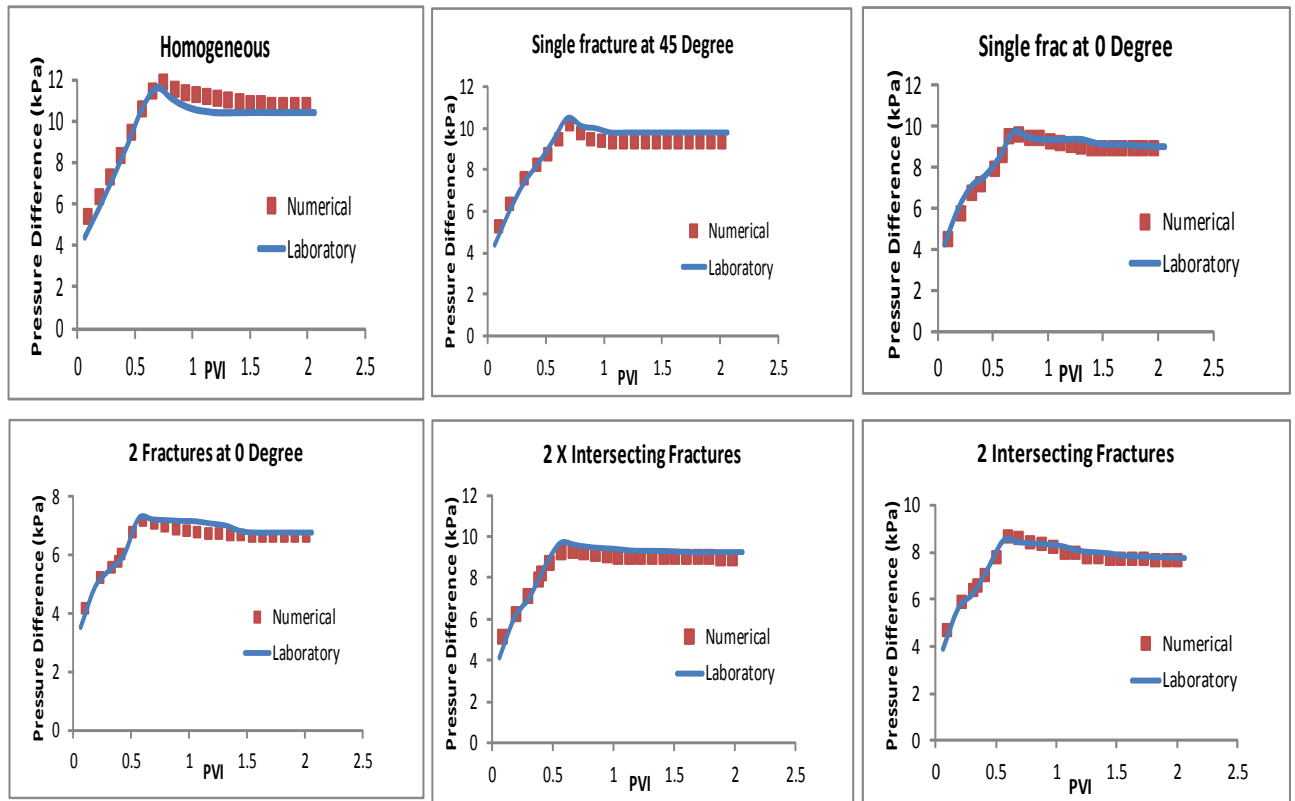


Figure 4-5: Comparison between numerical and experimentally obtained pressure differences for fractured systems at $1\text{cm}^3 / \text{min}$ injection rate

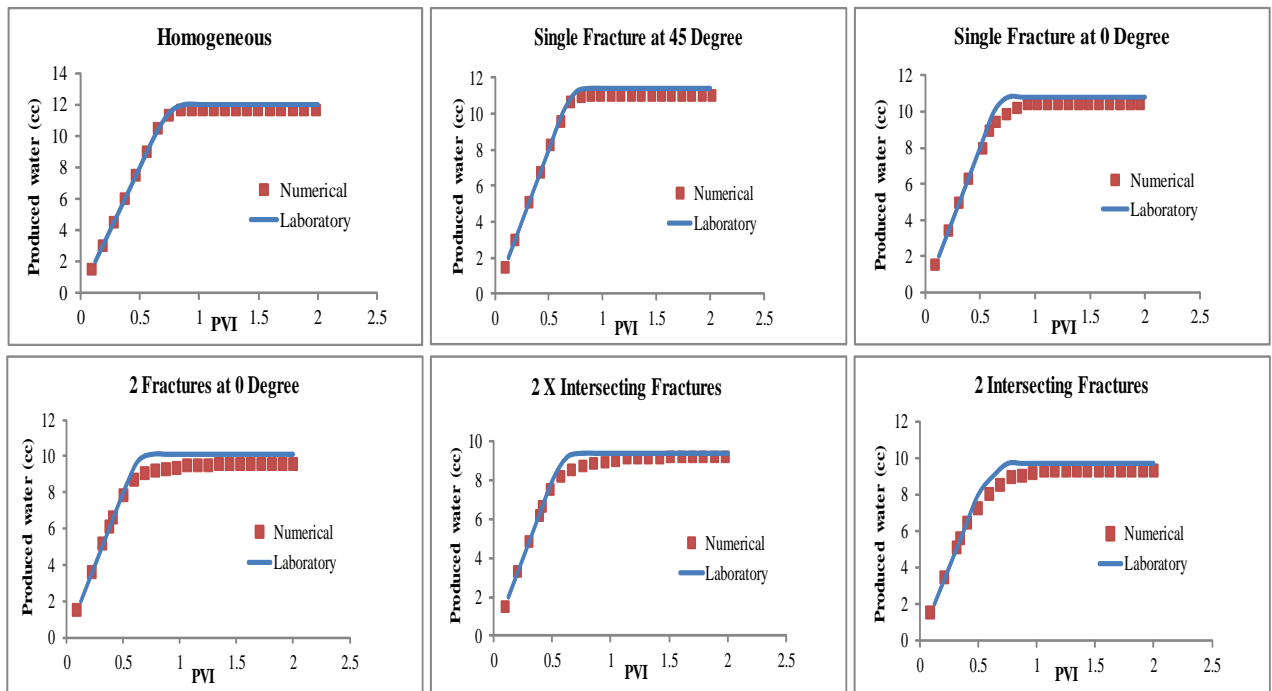


Figure 4-6: Comparison between numerical and experimentally obtained cumulative water productions for fractured systems at $1\text{cm}^3 / \text{min}$ injection rate

Table 4-1: A comparison for breakthrough times between experimental and numerical results at injection rate of $1\text{cm}^3 / \text{min}$

| Homogeneous/ Heterogeneous systems | Breakthrough Time (min) | |
|---------------------------------------|-------------------------|-----------------|
| | Experimental Model | Numerical Model |
| Homogeneous | 11.84 | 11.96 |
| Single fracture at 45° | 11.36 | 11.20 |
| Single fracture at 0° | 10.72 | 10.32 |
| 2 X-Intersecting fractures | 9.92 | 9.40 |
| 2 Intersecting fractures | 8.96 | 8.70 |
| 2 fractures at 0° | 9.60 | 9.20 |

Table 4-2: A comparison for pressures at breakthrough between experimental and numerical results at injection rate of $1\text{cm}^3 / \text{min}$

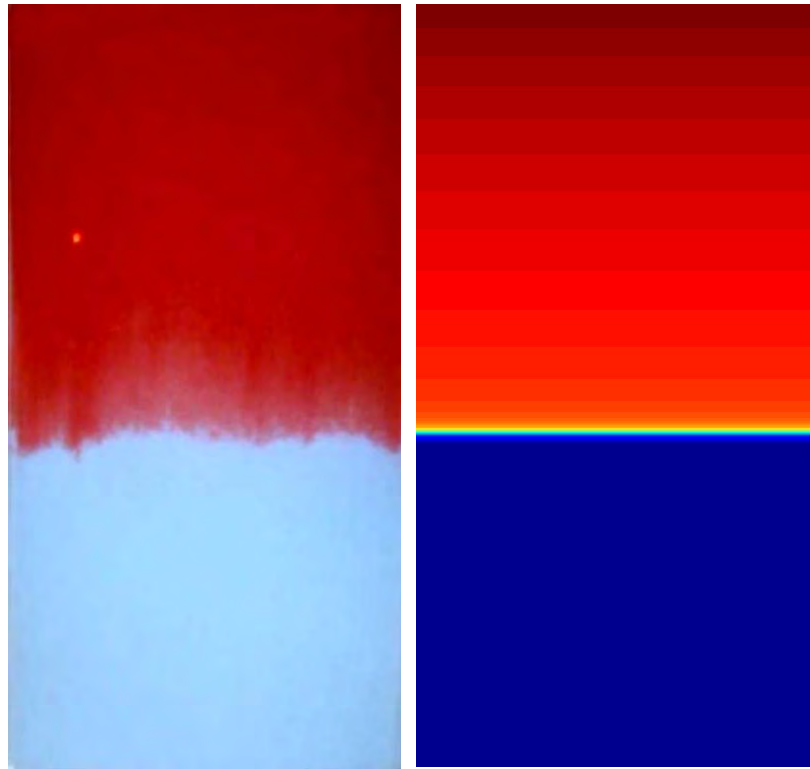
| Homogeneous/ Heterogeneous systems | Pressure difference at breakthrough (kPa) | |
|---------------------------------------|---|-----------------|
| | Experimental Model | Numerical Model |
| Homogeneous | 11.6 | 11.70 |
| Single fracture at 45° | 10.5 | 10.20 |
| Single fracture at 0° | 9.75 | 9.52 |
| 2 X-Intersecting fractures | 9.68 | 9.20 |
| 2 Intersecting fractures | 8.50 | 8.38 |
| 2 fractures at 0° | 7.25 | 7.19 |

Table 4-1 shows a comparison of breakthrough times between experimental and numerical observations for all discussed homogeneous and heterogeneous systems. It is observed that breakthrough times for homogeneous case in experimental and numerical study are quite close (see table 4-1). On the other hand, numerical experiments for all heterogeneous systems show a slightly early breakthrough as compared to experimental breakthrough times. This difference in breakthrough times is probably because of the use of equation 2-4 for calculation of fracture permeability, which seems to be a higher than actual fracture permeability in laboratory experiments, causing an early breakthrough for numerical experiments.

Furthermore, a comparison of pressures at breakthrough times for all discussed glass bead systems are presented in table 4-2. It can be observed that for all the fractured systems, pressure difference between injection and production points for numerical estimation is slightly lower than the experimental measurement. This is a confirmation of use of slightly high fracture permeability in numerical experiments which is causing low pressure drops between injection and production points for only fractured systems (not for homogeneous case).

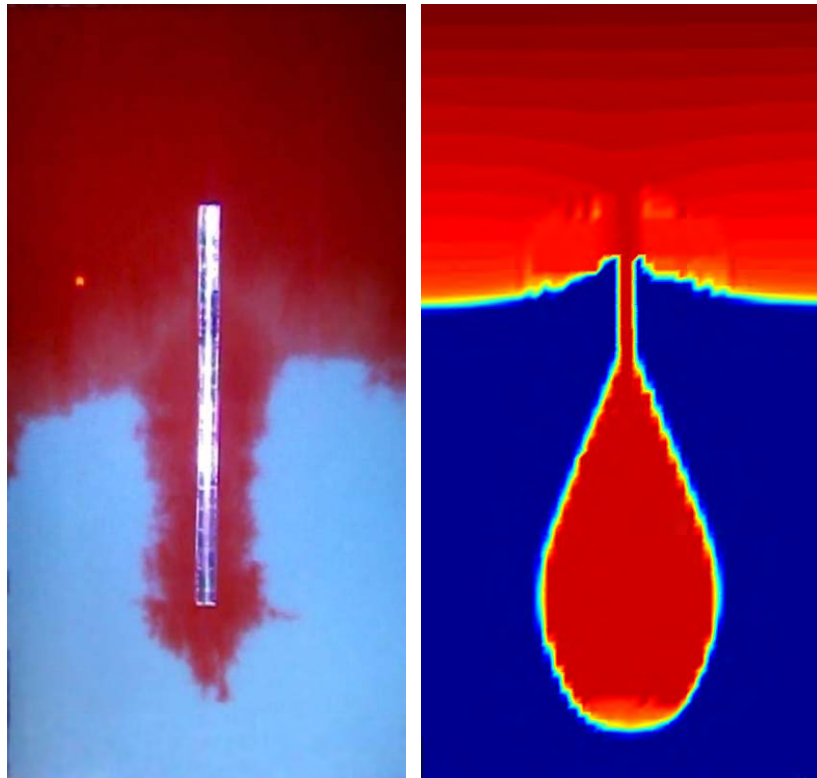
Fluid flow profiles obtained from the numerical model and laboratory experiments are compared at the same pore volumes of oil injection. Figure 4-7 to 4-12 show fluid flow profiles for the discussed glass bead systems in chapter 2 and numerically obtained flow profiles at constant injection of 0.4 pore volumes. Similar to chapter 2, oil is injected from top and produced at the bottom (reference for figures only). In these figures red colour represents oil. The water phase for experimental profiles is shown by light blue colour whereas in numerically obtained profiles it is in dark blue. Flow profiles for numerical and experimental model of homogeneous case (Fig. 4-7) are in good agreement which is expected from table 4-1 and 4-2. From **Fig. 4-8**, in numerical experiment for single fracture oriented at

0° to the direction of flow, high oil saturation is visualized at the production end of fracture as compared to the laboratory experiment. This difference is probably expected because of the high fracture permeability used in numerical study. Similar observations are found in **Fig. 4-11** and **4-12** where at least one fracture along the direction of flow is placed. The flow profile comparisons provided in **Figs. 4-9** and **4-10** are in reasonable agreement where single and two fractures are oriented at 45° to the direction of flow, respectively. By comparing **Fig. 4-9** and **4-11**, it is observed that a fracture placed at 45° contributes differently in different situations. In fact, in **Fig. 4-11** because of the presence of second fracture oriented at 0° to the direction of flow, 45° degree fracture contributes flow to the 0° fracture, resulting in relatively less oil saturation in this fracture as compared to the 45° fracture in **Fig. 4-9**. This feeding of flow from one fracture to another intersected fracture is the reason of early breakthrough for intersected fracture and hence shows high oil relative permeability.



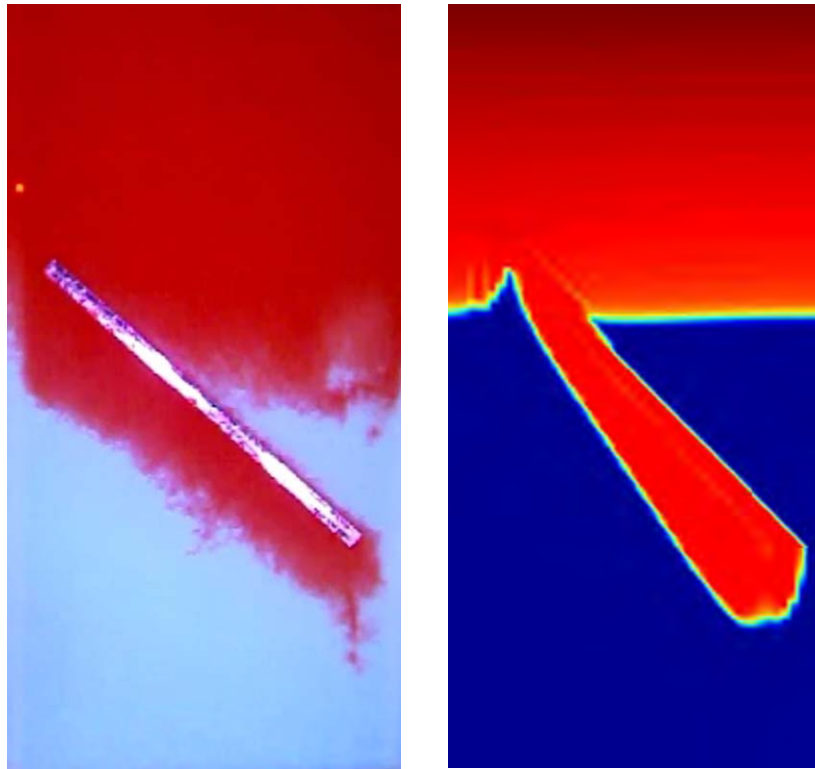
(a) Experimental Oil Water (b) Numerical Oil Water

Figure 4-7: Oil-water drainage profiles for homogeneous system at 0.4PVI



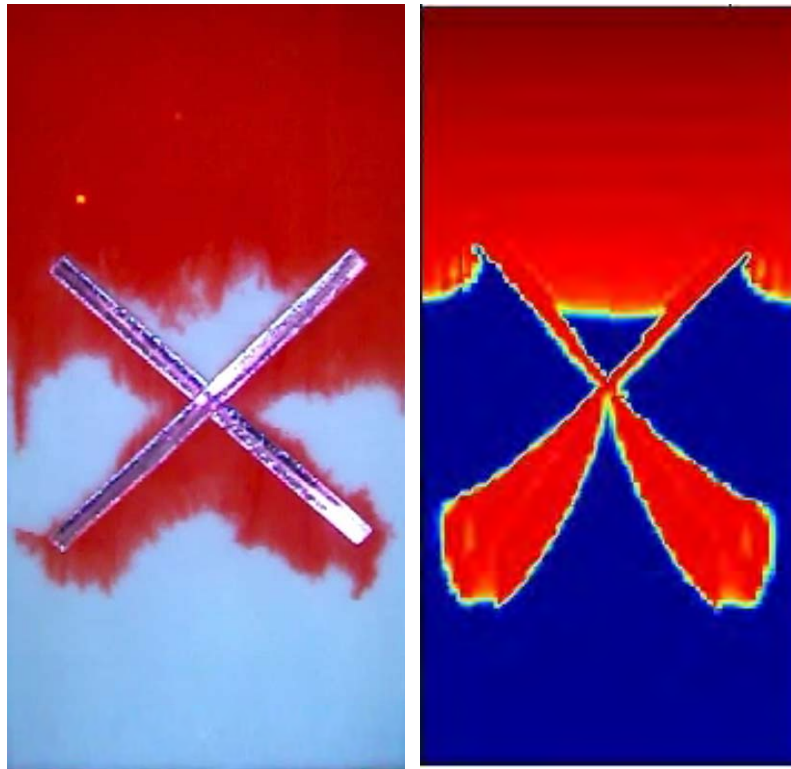
(a) Experimental Oil Water (b) Numerical Oil Water

Figure 4-8: Oil-water drainage profiles for 0° fracture system at 0.4PVI



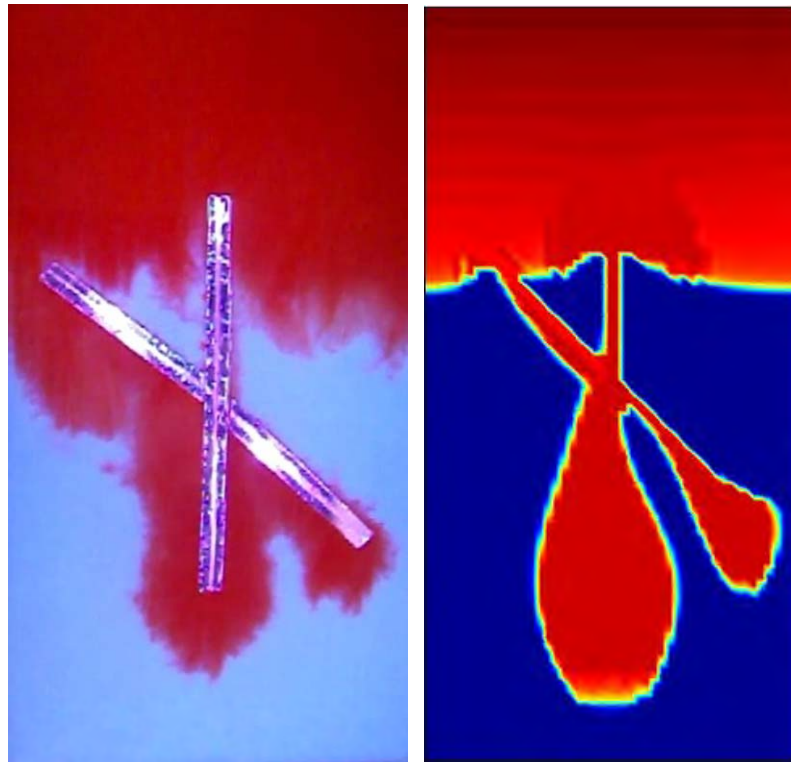
(a) Experimental Oil Water (b) Numerical Oil Water

Figure 4-9: Oil-water drainage profiles for 45° fracture system at 0.4PVI



(a) Experimental Oil Water (b) Numerical Oil Water

Figure 4-10: Oil-water drainage profiles for 2 X-Intersecting fractures system at 0.4PVI



(a) Experimental

Oil

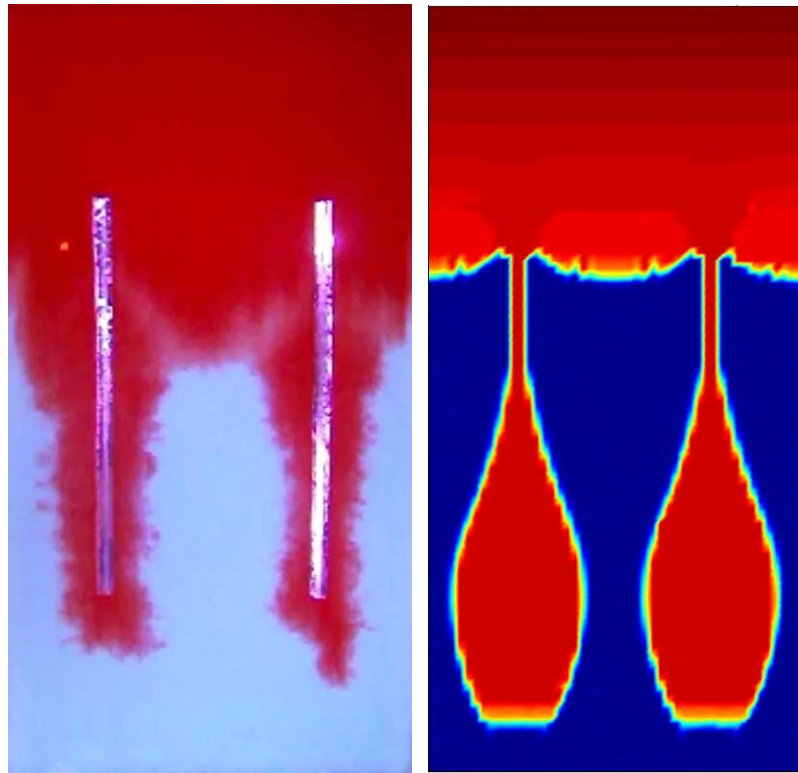
Water

(b) Numerical

Oil

Water

Figure 4-11: Oil-water drainage profiles for 2 Intersecting fractures system at 0.4PVI



(a) Experimental Oil Water (b) Numerical Oil Water

Figure 4-12: Oil-water drainage profiles for system of 2 fractures at 0° at 0.4PVI

Chapter 5

Upscaling Two-Phase Relative Permeability Relationship

In this chapter, a procedure is given to upscale relative permeabilities of different fracture networks from the laboratory scale (10cm×20cm) to the reservoir scale (1000m×1000m). In order to achieve this, a two-dimensional slice of 1000m×1000m region from the Amadeus Basin is considered as an example as shown in **Figure 5-1**. A commercial black oil simulator (CMG IMEX) is used to perform upscaling of two-phase relative permeabilities.

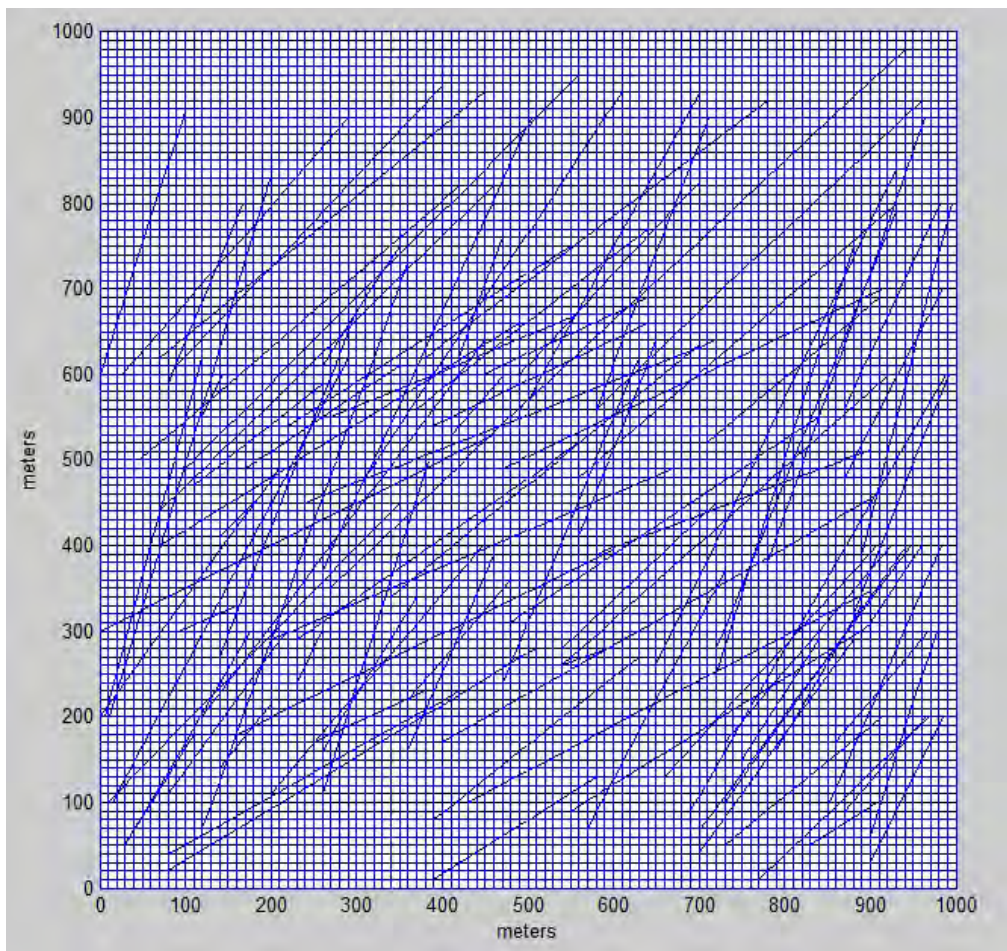


Figure 5-1: Fracture network used to upscale from laboratory scale.

5.1 Upscaling Procedure

Steps involved in the upscaling procedure are described below:

Step 1: Divide the whole reservoir (1000m×1000m) into 100×100 grid blocks of 10m×10m size of each grid block acquiring the knowledge of fracture network co-ordinates in each block of size 10m×10m.

Step 2: Nominate five different blocks of random fracture orientation from 10m×10m blocks obtained in Step 1. These blocks can be nominated based on the fracture system present in an individual block that appears most commonly in the whole reservoir to avoid any repetition of history matching for the same orientation of fracture or fracture system present in other grid blocks. The nominated grid blocks of size 10m×10m from **Figure 5-1** are described in six cases below. In this study, the angle of fracture is presented with respect to the direction of flow whereas the direction of flow is along the y-axis of each grid block.

Case-1: Homogeneous grid block (with no fracture present in the block) or a single fracture present at greater than 70° to the direction of flow (see **Figure 5-2a**).

Case-2: A most commonly appeared single fracture in a grid block at an orientation ranging 20°-70° to the direction of flow e.g. 59° in the reservoir under study (see **Figure 5-2b**)

Case-3: A most commonly appeared single fracture of orientation ranging 0° - 20° to the direction of flow e.g. 19° in the reservoir under study (see **Figure 5-2c**)

Case-4: A most commonly appeared multi-fracture system at inclination close to each other and not intersecting, i.e. two-fracture system, where one fracture oriented at 30° and other at 32° to the direction of the flow in the reservoir under study (see **Figure 5-2d**).

Case-5: A most commonly appeared multi-fracture system where one fracture is oriented between 20° - 70° to the direction of flow and other fracture is oriented at an angle between 0° - 20° whereas fractures do not intersect each other. For example, a fracture oriented at 64° and the other fracture oriented at 19° to the flow direction (see **Figure 5-2e**).

Case-6: A most commonly appeared intersecting multi-fracture system where one fracture oriented at an angle between 20° - 70° intersects another fracture oriented at an angle between 0° - 20° to the direction of flow. For example, in this study, a fracture at 20° intersects another fracture which is oriented at 64° to the direction of flow (see **Figure 5-2f**).

A description of six nominated cases is summarised in **Table 5-1**.

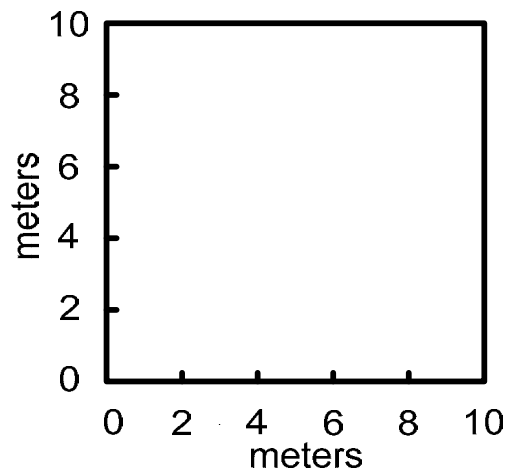
Table 5-1: Six nominated fractured systems of size $10\text{m} \times 10\text{m}$ from **Figure 5-1**

| Single-Fracture System | Case 1 | Case 2 | Case 3 |
|---|--|---|---|
| Angle of Fracture θ w.r.t. the flow direction | Homogeneous or $\theta > 70^{\circ}$ | $70^{\circ} \geq \theta > 20^{\circ}$ | $20^{\circ} \geq \theta > 0^{\circ}$ |
| Multi-Fracture System | Case 4 | Case 5 | Case 6 |
| Angle of Fracture θ w.r.t. the flow direction | $70^{\circ} \geq \theta_1 > 20^{\circ}$ $70^{\circ} \geq \theta_2 > 20^{\circ}$ | $70^{\circ} \geq \theta_1 > 20^{\circ}$ $20^{\circ} \geq \theta_2 > 0^{\circ}$ | $70^{\circ} \geq \theta_1 > 20^{\circ}$ $20^{\circ} \geq \theta_2 > 0^{\circ}$ |

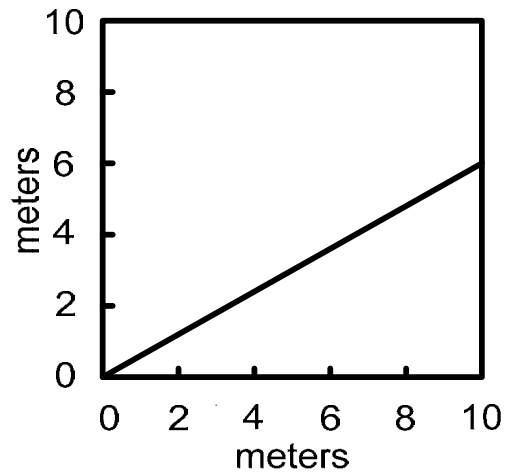
Step 3: Divide each nominated $10\text{m} \times 10\text{m}$ grid block into 100×50 blocks each of $0.1\text{m} \times 0.2\text{m}$ size, equivalent to the laboratory scale ($10\text{cm} \times 20\text{cm}$).

Step 4: In order to obtain an up-scaled absolute permeability of the fracture system, single phase simulation of the model was run. This involved estimating pressure drop across the model with the fracture system present in the grid block of $10\text{m} \times 10\text{m}$ size. Next, single phase

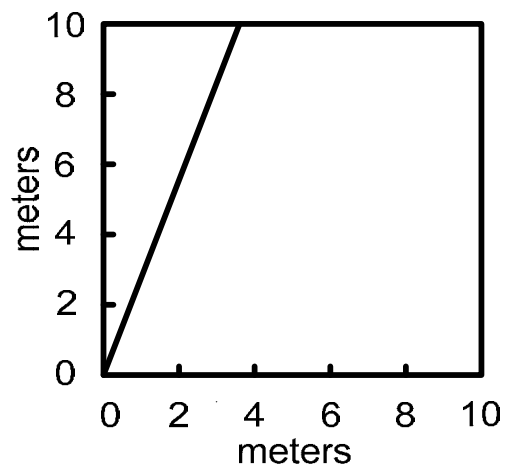
flow simulation was performed for a homogeneous block of same size and the permeability of homogenous block was changed to match the pressure drop. The absolute permeability of the homogeneous block, for which pressure drop of a fractured system matched, was taken as an up-scaled absolute permeability of the fractured grid block.



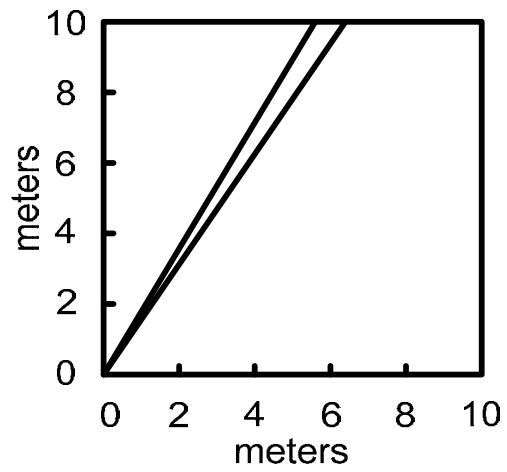
a - Case 1



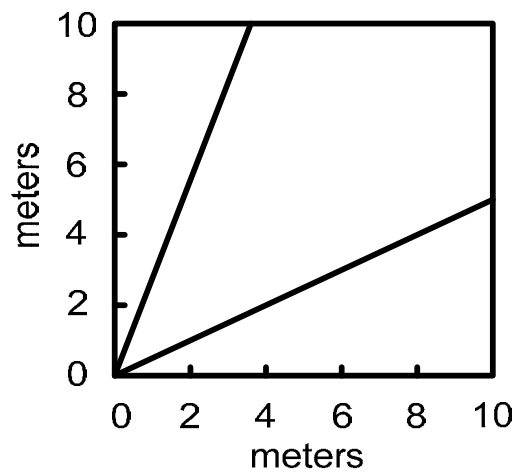
b - Case 2



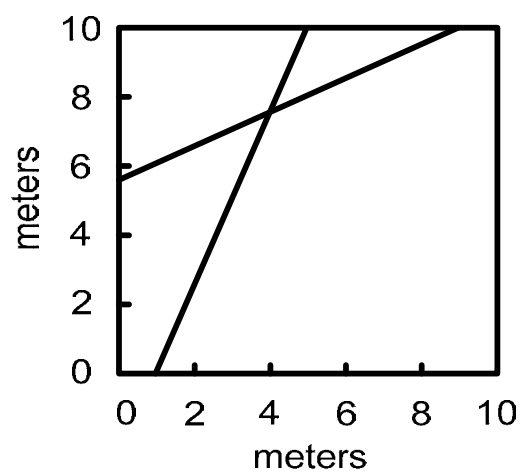
c - Case 3



d - Case 4



e - Case 5



f - Case 6

Figure 5-2: Grid blocks of 10m×10m size nominated in step 2 from Figure 5-1

Step 5: History match each 10m×10m grid block nominated in Step 2 (see Figure 5-2) in order to achieve an up-scaled two-phase relative permeability relationship for each fracture system. This involved obtaining pressure drops across the model as well as pore volume of water produced for a drainage test. Then re-run the simulation for the same model without any fracture system (homogeneous block) to match pressure drops and pore volume of water produced. The relative permeability for which the history of a fractured system matched was taken as an upscaled relative permeability of the block. Mathematical functions presented by Hussain et al. (2010; 2012) are used to obtain reliable history matches. In this process up-scaled absolute permeability obtained in Step4 was used and injector and producer wells were placed along bottom x-axis and top x-axis of each grid block, respectively given in **Figure 5-2**.

Step 6: After achieving up-scaled relative permeability relationship for all nominated grid blocks (see step 2), distribution of these blocks in whole reservoir (100×100 blocks) was found and up-scaled absolute and relative permeabilities were assigned to the blocks with similar fracture realizations.

Step7: History match the whole reservoir 1000m×1000m (100×100 blocks) to obtain two phase relative permeability relationship as described in step 5.

5.2 Results and Discussion

The procedure described in section 5.1 is applied to two dimensional fracture network in an area of 1000m×1000m taken from Amadeus Basin (see **Figure 5-1**). The nominated fracture systems of 10m×10m size are shown in **Figure 5-2**. The results of history matching for six nominated cases are presented in **Figures 5-3 to 5-14**.

Pore volume injected at breakthrough, peak pressure drop and pore volume injected at peak pressure drop for all nominated cases are compared in **Table 5-2**. As expected, a very late oil breakthrough (0.665 PVI) was seen in case 1 (see **Table 5-2**) where there is no fracture present in the matrix block to carry the fluid to producer quick enough.

In Case 2 even there is a fracture present in the grid block but the angle of fracture (59° to the direction of flow) is not favourable for fluid flow and hence presence of fracture could not contribute to a very early breakthrough. In this case, oil breakthrough happens after injection of 0.65 pore volumes of oil which is not too different from 0.665 pore volumes of injection for homogeneous block (case 1).

Table 5-2: Pore volume Injected at breakthrough & peak pressures for case 1 to case 6

| Case ID | Case 1 | Case 2 | Case 3 | Case 4 | Case 5 | Case 6 |
|---------------------------|--------|--------|---------|--------|--------|--------|
| PVI at breakthrough | 0.665 | 0.65 | 0.00012 | 0.11 | 0.0028 | 0.0004 |
| Peak Pressure Drop (kpa) | 213.4 | 199.9 | 42.7 | 87.5 | 161.5 | 132 |
| PVI at Peak Pressure Drop | 0.67 | 0.68 | 2.51 | 1.28 | 0.73 | 0.76 |

It can be clearly seen from **Table 5-2** that from case 3 till case 6 each grid block has at least one fracture along the direction of flow which starts from injector well and ends in production well and hence these 4 cases show very quick oil breakthrough (see **Table 5-2**). It was found that among these four cases an earliest oil breakthrough happened for case 3 (after injection of 0.00012 pore volumes) which was due to the angle of fracture (19°) to the direction of flow as almost whole length of fracture contributes to the fluid flow.

After case 3, second earliest breakthrough (after injection of 0.0004 pore volumes), among the four cases, happened for case 6 where angle of fracture increases from 19° (Case2) to 21° (Case 6) to the direction of flow and hence delays the oil breakthrough (see **Table 5-2**).

After case 6, third quickest breakthrough happened for case 5 (after injection of 0.0028 pore volumes) which consists of two fractures that are not intersecting each other (see **Figure 5-2**). By comparing case 3 and case 5 it is found that even case 5 contains two fractures it shows late break through as compared to case 3 because second fracture is also connected to injector and hence part of oil injection flows through second fracture and delays breakthrough.

A very late breakthrough (after injection of 0.11 pore volumes) was found for case 4 among last four cases (case3-case6) which was due to the increase in angle of fracture to 30° and 32° with respect to the direction of flow as compared to low angle of fracture (19°-20°) to the direction of flow for other three cases.

A comparison of maximum pressure drops between injector and producer and pore volume injection at maximum pressure drop for different fracture systems is also presented in **Table 5-2** (see **Figures 5-2 to 5-15** for details). It can be seen in the table that pressure drop is highest (213.4kpa) for a homogeneous grid block. It is found that, for homogeneous block (case 1), pressure drop is peaking at injection of almost same pore volume (0.67 PVI) as oil breakthrough (0.665 PVI). This behaviour is typical as there is no fracture present in the block and hence injection fluid (oil) cannot bypass the initial fluid in place (water).

It can be clearly seen that pressure difference between injector and producer, for a fracture oriented at 59° to the direction of the flow (case 2), is the highest (119.9kpa) among all the cases of fracture systems (case 2 – case 5). The higher pressure drop is due to the fracture inclination of 59° and due to the fact that, unlike other fracture systems in comparison, the fracture does not reach/intersect the production well. This forces the flow through matrix to

reach production well which requires extra pressure drop. As some water stays trapped behind fracture (due to faster injection fluid flow through fracture), this is why it requires injection of few more pore volumes (0.68) to reach peak pressure as compared to 0.65 PVI where oil breakthrough happens. It is found that presence of fracture in the grid block shows an early breakthrough but requires injection of extra pore volumes to achieve maximum pressure drop and hence to stabilize the pressure across the system.

Furthermore, case 3 shows a minimum pressure drop (42.7kpa) as compared to all other cases which is due to the favourable inclination of fracture (19° to the direction of flow). As oil breakthrough happened quickest due to the favourable inclination, it required injection of extra pore volumes (2.51 PVI), the highest required PVI among all six cases, to obtain the peak pressure for the system. It also means that initial fluid in place (water) was seen in production till 2.51 pore volumes of oil injection.

Further increase in pressure drop was observed for case 4 (87.5kpa) as an angle of fracture increased to 30° and 32° to the direction of flow. Also with increase in fracture inclination to the direction of flow, the amount of fluid trapped behind the fracture is less and hence less pore volume injection is required (1.28 PVI) to obtain the peak pressure for the system as compared to case 3 (2.51 PVI).

It was also found, that even though case 5 and case 6 have at least one fracture connecting from injector to the producer, the maximum pressure drop is not less than a single fracture system at an approximate similar inclination (19°) to the direction of flow (case 3). This is due to the presence of second fracture in the grid block at a higher inclination to the direction of flow which forces the oil flow through matrix and hence pressure drop increases. Among the two cases (case 5 and case 6), case 6 shows a lower pressure drop (132kpa) as compared to case 5 (161.5kpa) which is due to fact that both fractures in case 6 are intersecting each

other and hence feed fluid flow to each other unlike case 5. It is clear that as breakthrough happens early in case 6 (0.0004 PVI) than case 5 (0.0011 PVI), it requires injection of extra pore volumes (0.76 PVI) for case 6 as compared to case 5 (0.73PVI) to obtain maximum pressure drop for the system.

It was observed that at injection of infinite pore volumes (11.9PVI) all the grid blocks have very similar produced pore volumes of water between 0.74 and 0.75 except for case 3 where total produced pore volume of water is 0.67 at injection of 11.9 pore volume injection (see **Figures 5-3 to 5-16**). This shows high volume of water trapped in the pores for case 3 due to favourable inclination of fracture for injection fluid flow that leads to an early breakthrough (see **Figures 5-3 to 5-16**).

Relative permeabilities used to history match different realizations of fracture networks (case 1 – case 6) are presented in **Figures 5-17 to 5-22**. These are upscaled relative permeabilities from the lab scale (0.1m×0.2m) to the 10m×10m reservoir scale. These upscaled relative permeabilities were then used to perform upscaling to a next level (1000m×1000m). History match pressure drop across injector and producer for 1000m×1000m region (see **Figure 5-1**) is shown in **Figure 5-15**. The maximum pressure drop is obtained as 2E6kpa after injection of 0.674 pore volumes. Also, pore volume of water produced for the whole reservoir (1000m×1000m) is presented in **Figure 5-16** which shows that a maximum of 0.74 pore volumes of water can be produced after 9 pore volumes of oil injection. The final upscaled relative permeability for which the history match was obtained for a region of 1000m×1000m (see **Figure 5-1**) is presented in **Figure 5-23**. This is an upscaled relative permeability from the lab scale (0.1m×0.2m) to the reservoir scale (1000m×1000m) and can be used to model two-phase fluid flow particularly for this fracture network presented in **Figure 5-1**.

Case1- Homogeneous Block

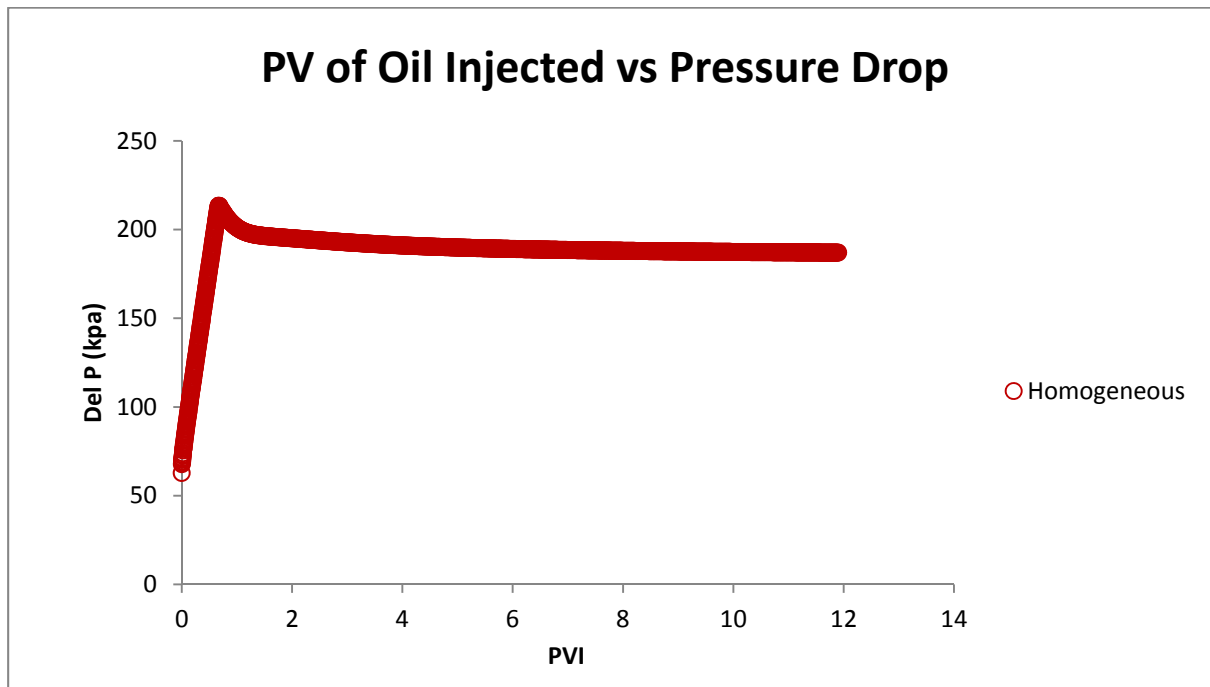


Figure 5-3: Pressure difference across injector and producer for a homogeneous block of size 10m×10m

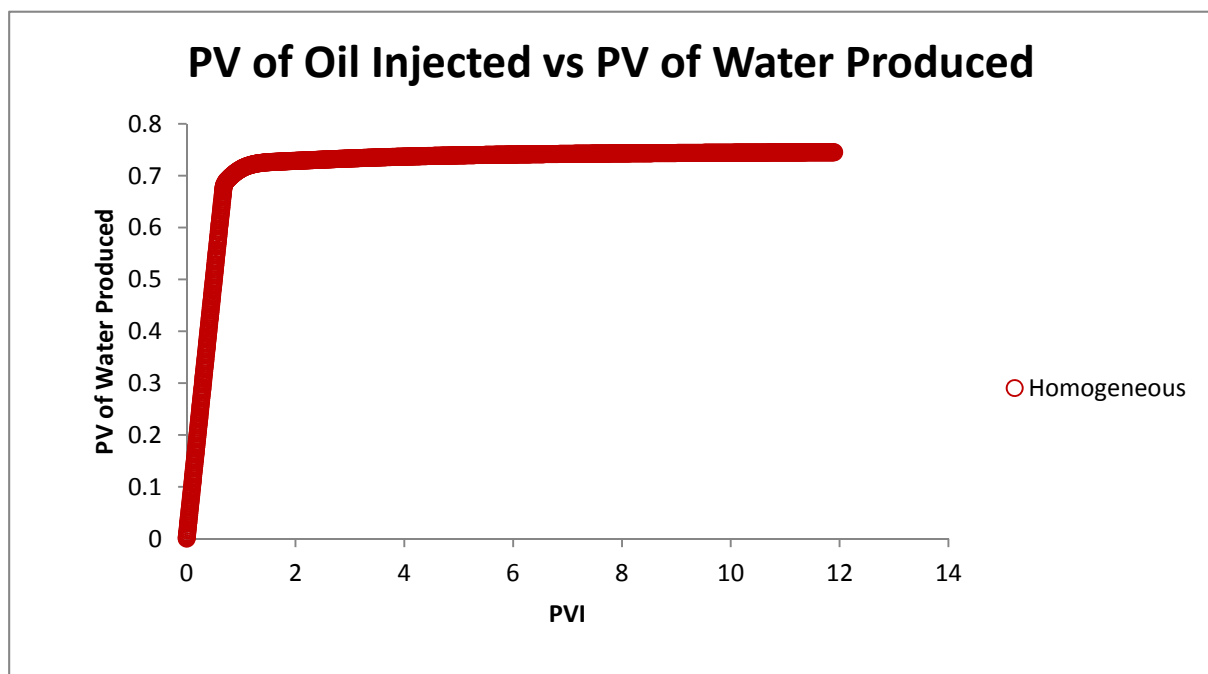


Figure 5-4: Pore volumes of water produced vs. injected pore volumes of oil for a homogeneous block of size 10m×10m

History Matching for Case2

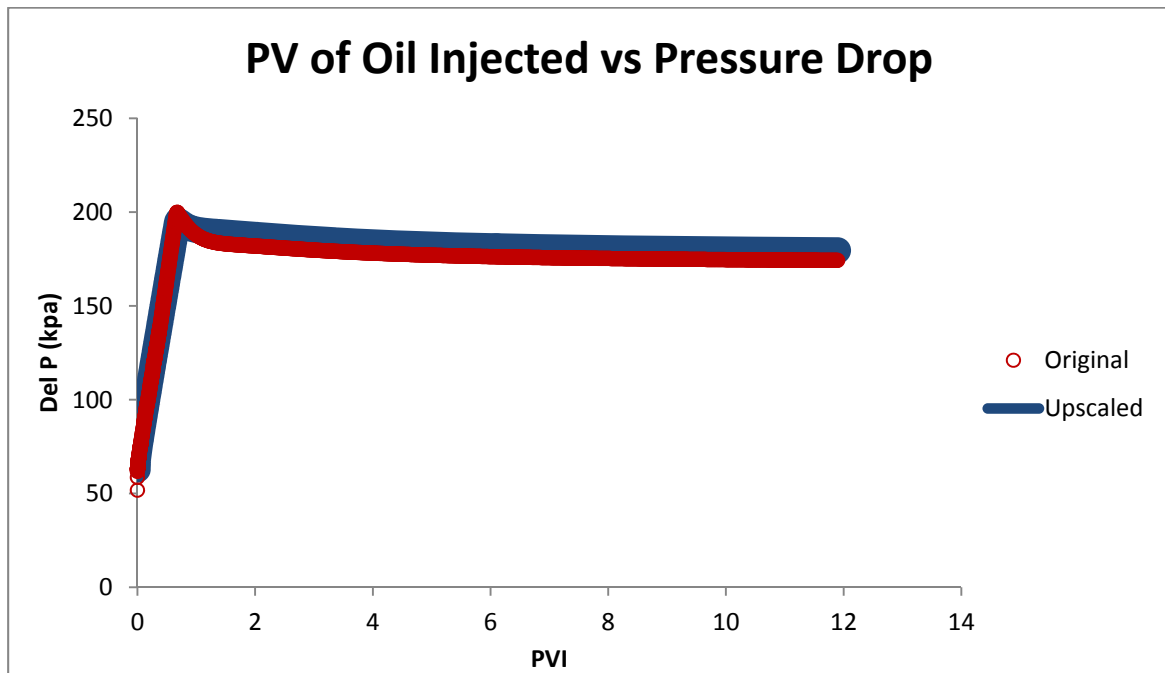


Figure 5-5: Comparison of pressure difference across injector and producer between single fracture system (fracture oriented at 59°) and upscaled case (10m×10m)

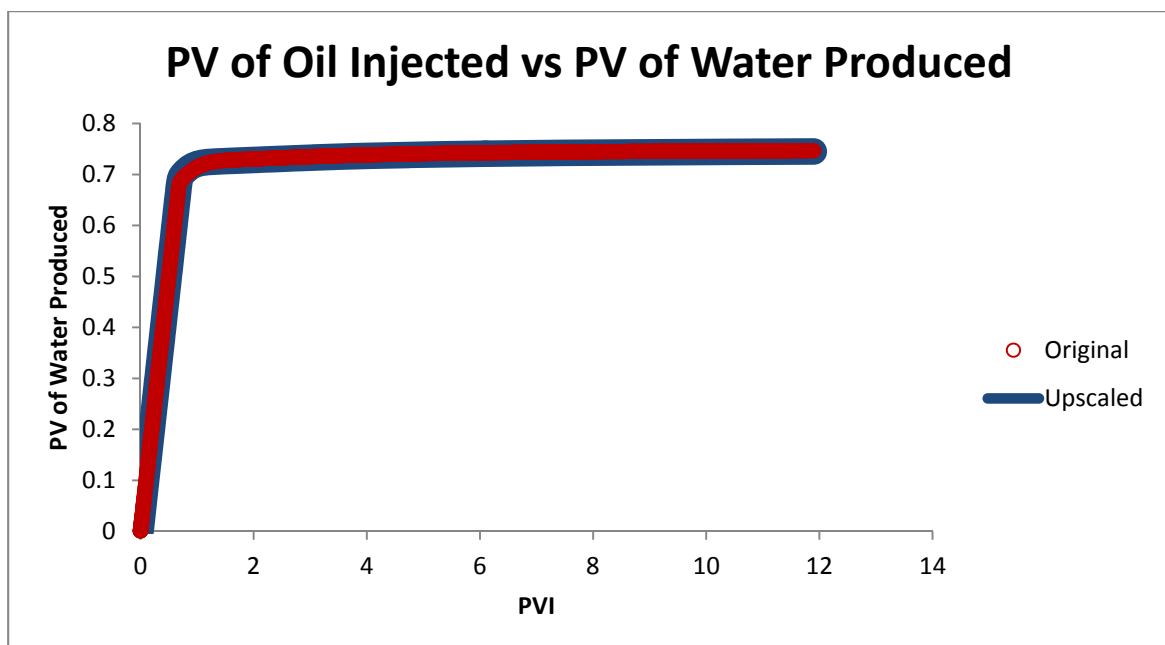


Figure 5-6: Comparison for pore volume (PV) of water produced between original single fracture (oriented at 59°) and upscaled case (10m×10m)

History Matching for Case3

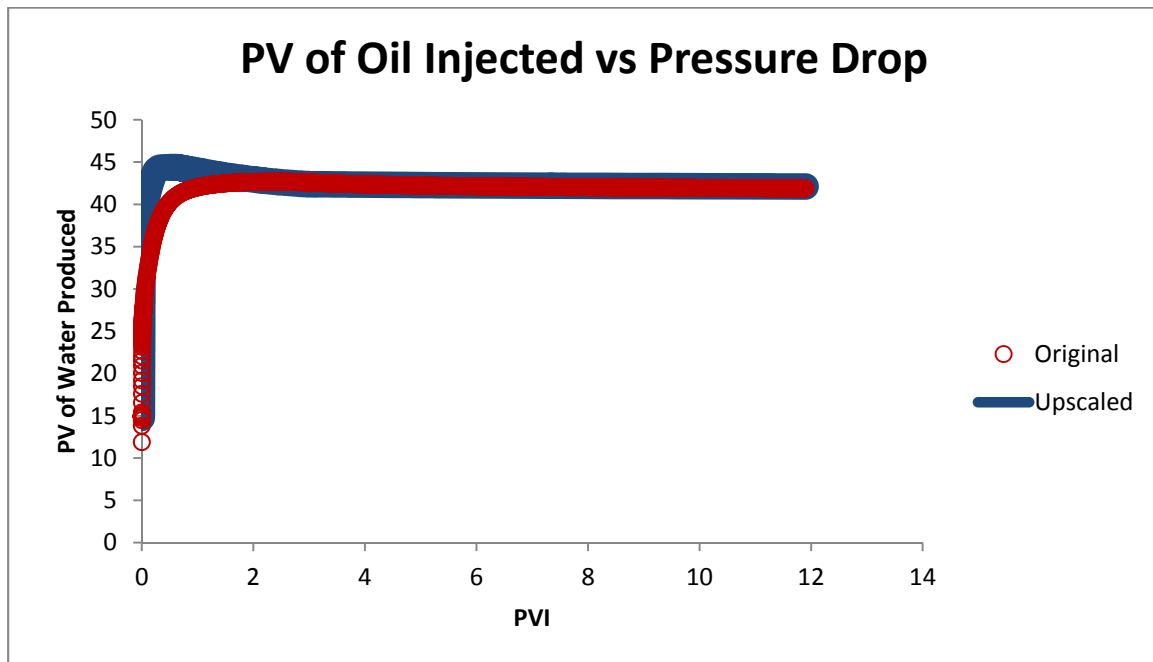


Figure 5-7: Comparison of pressure difference across injector and producer between original single fracture (oriented at 19°) and upscaled case (10m×10m)

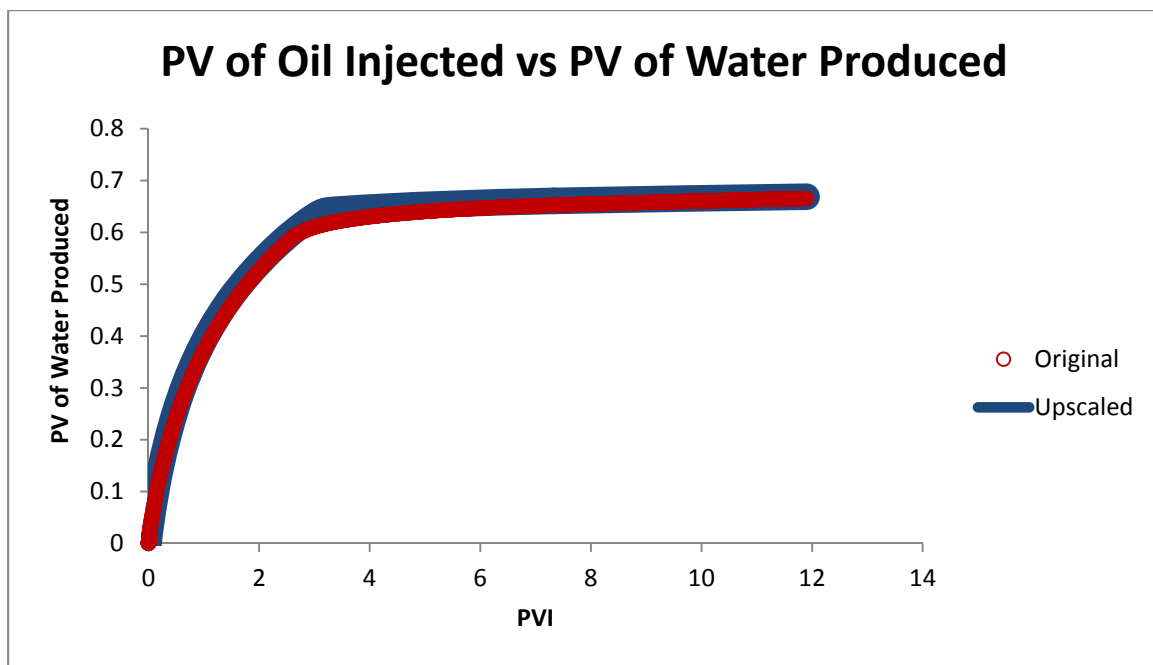


Figure 5-8: Comparison for pore volume (PV) of water produced between original single fracture (oriented at 19°) and upscaled case (10m×10m)

History Matching for Case4

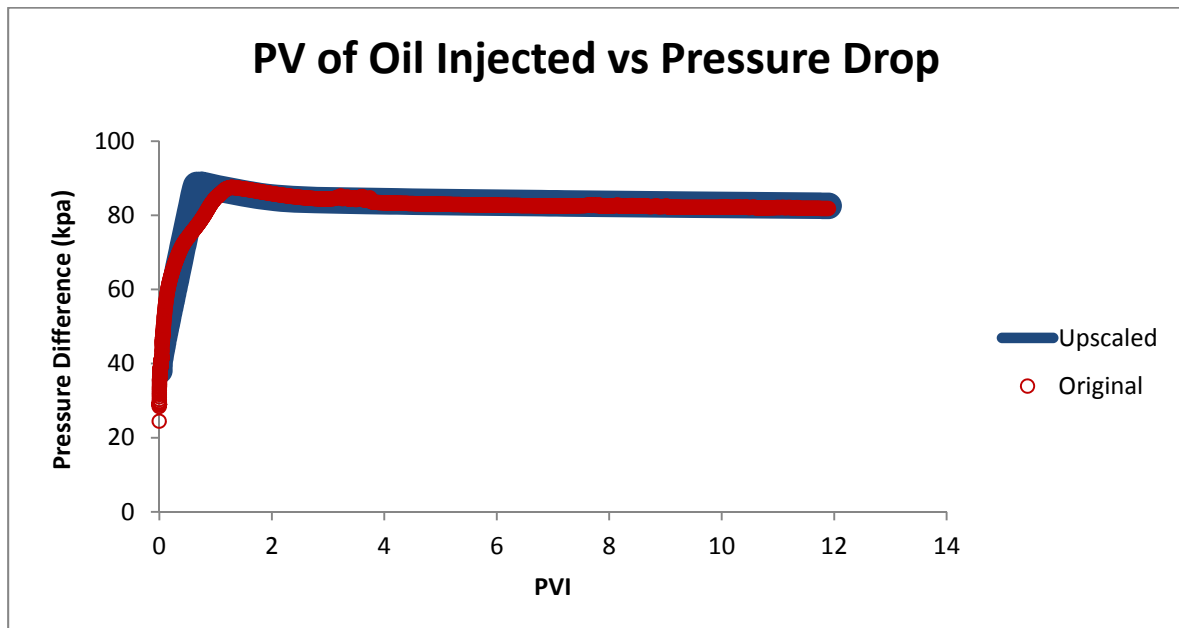


Figure 5-9: Comparison of pressure difference (across injector and producer) between original multi fracture system (one fracture oriented at 30° and other at 32°) and upscaled case (10m×10m)

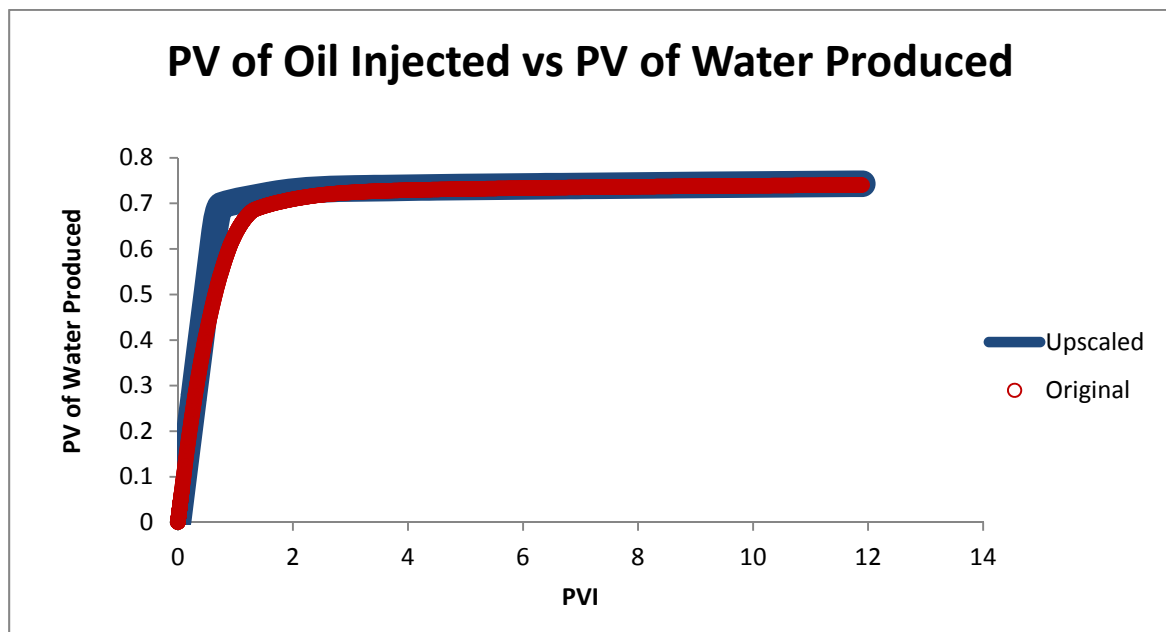


Figure 5-10: Comparison for pore volume (PV) of water produced for multi fracture system (one fracture oriented at 30° and other at 32°) and upscaled case (10m×10m)

History Matching for Case5

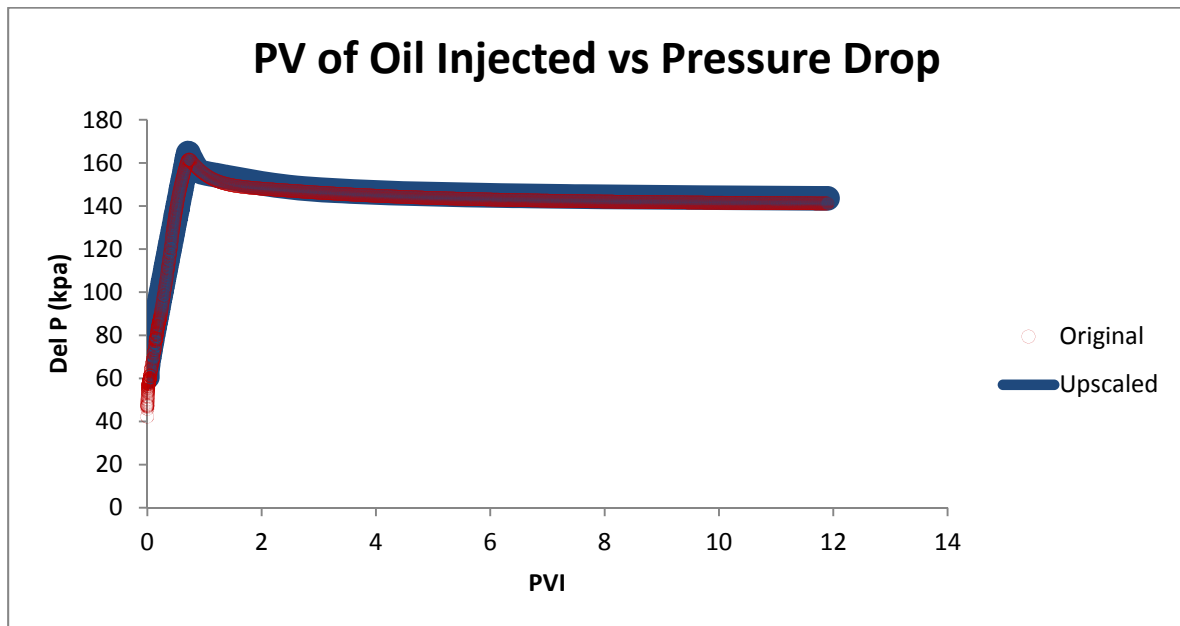


Figure 5-11: Comparison of pressure difference (across injector and producer) between original multi fracture system (one fracture oriented at 19° and other fracture at 64°) and upscaled case (10m×10m)

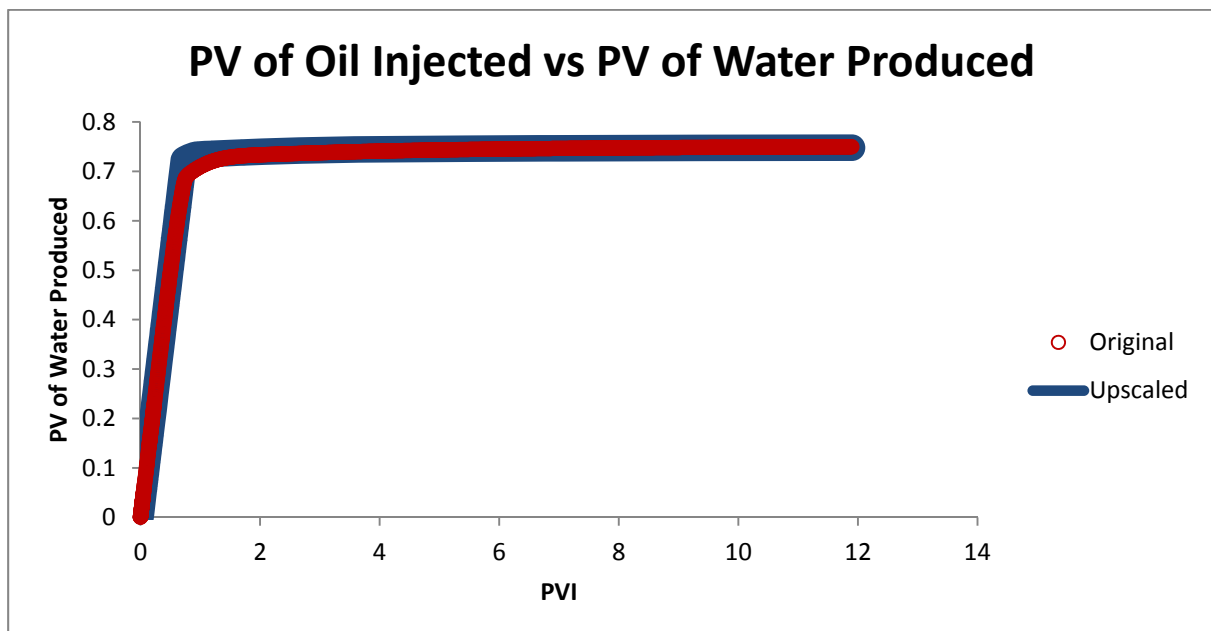


Figure 5-12: Comparison of pore volume of water produced for original multi fracture system (one fracture oriented at 19° and other fracture at 64°) and upscaled case (10m×10m)

History Matching for Case6

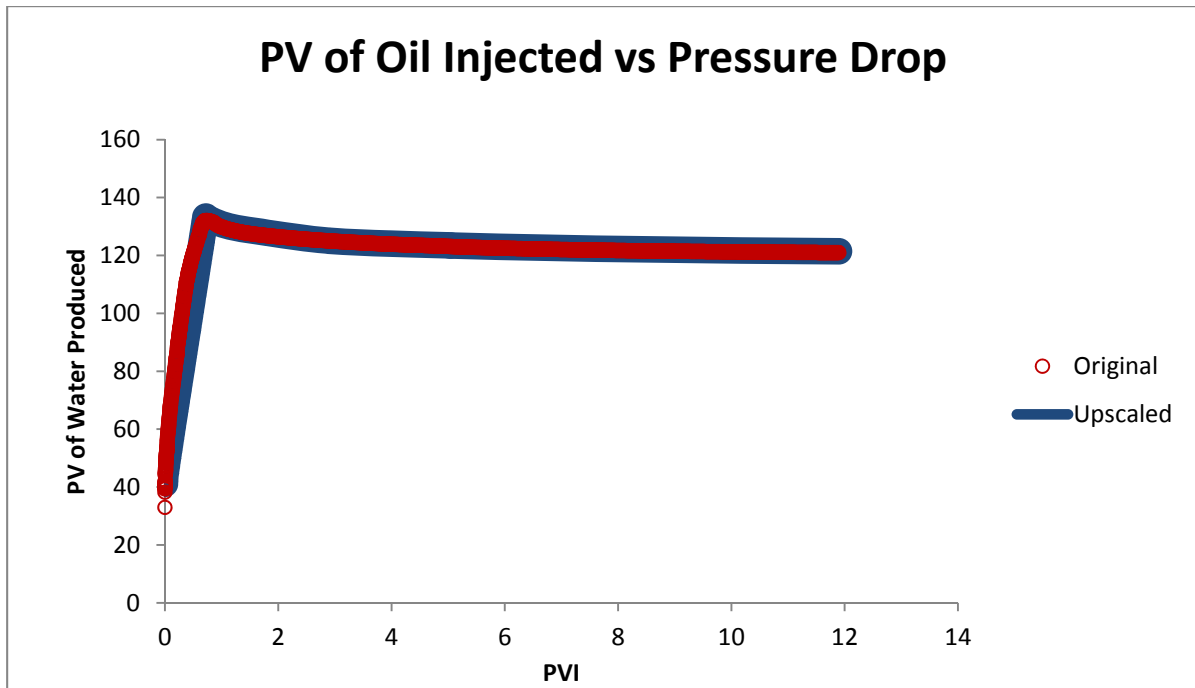


Figure 5-13: Comparison of pressure difference (across injector and producer) between original multi fracture system (one fracture oriented at 20° and other fracture at 64°) and upscaled case (10m×10m)

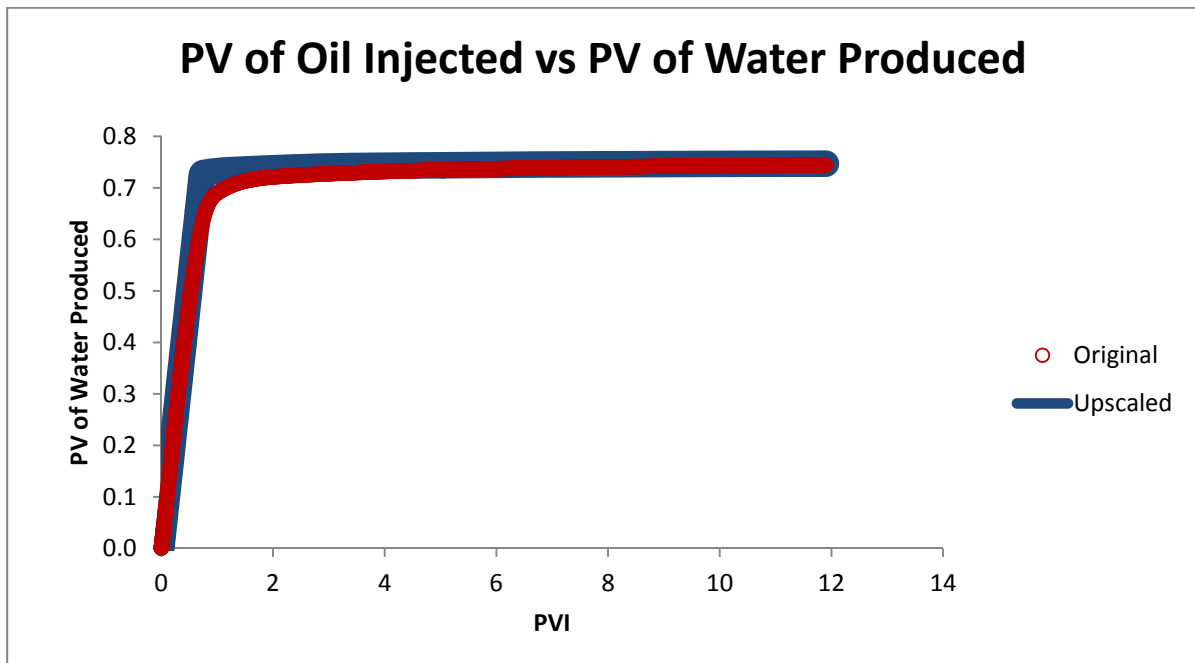


Figure 5-14: Comparison of pore volume of water produced for original multi fracture system (one fracture oriented at 20° and other fracture at 64°) and upscaled case (10m×10m)

History Matching for Whole Reservoir (1000m×1000m)

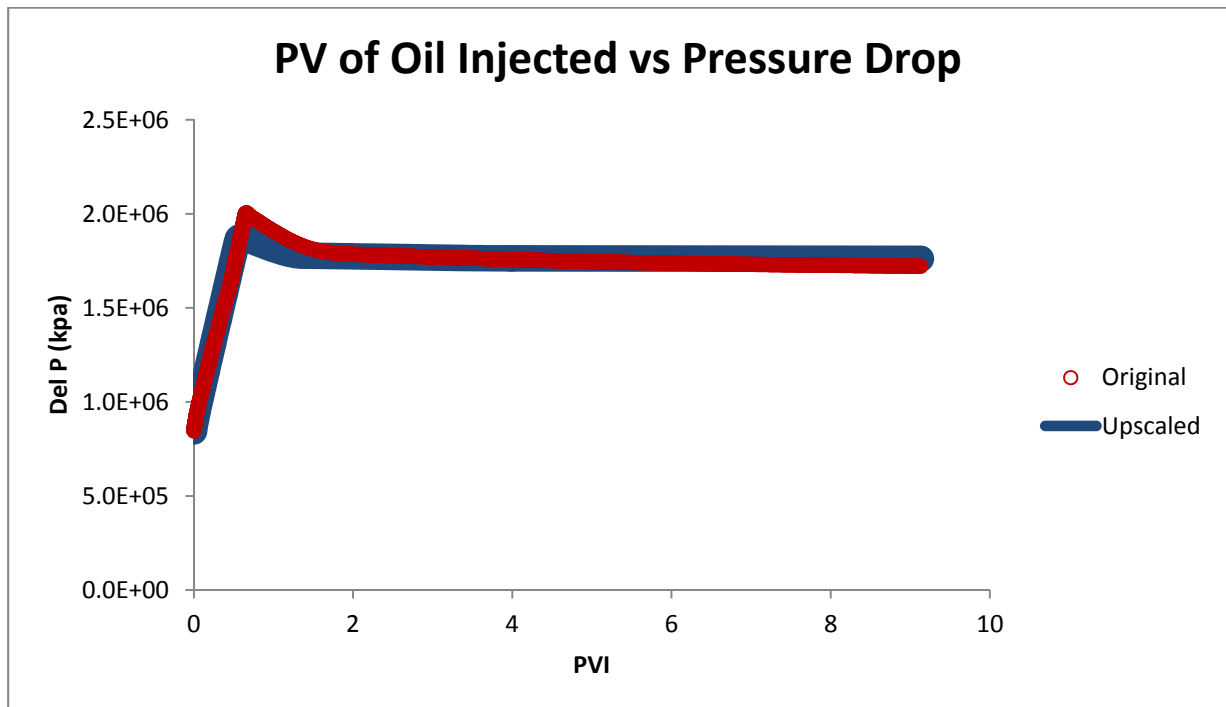


Figure 5-15: Comparison of pressure difference across (injector and producer) for original multi fracture reservoir and up-scaled case (1000m×1000m)

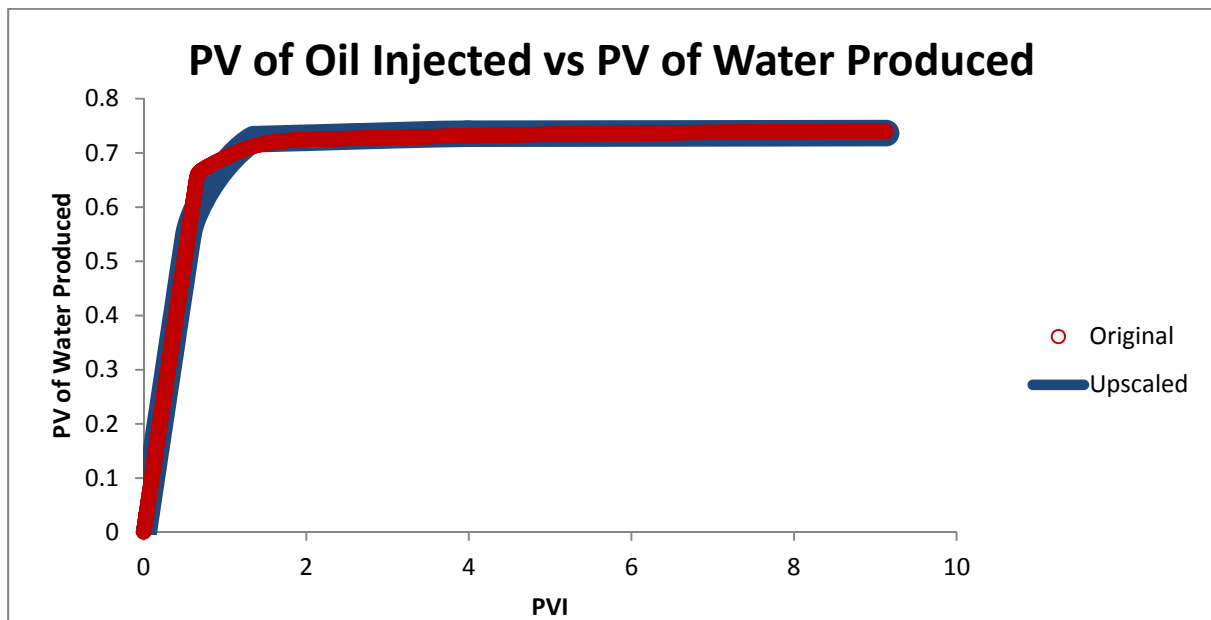


Figure 5-16: Comparison of pore volume (PV) of water produced for original multi fracture reservoir and up-scaled case (1000m×1000m)

Relative Permeability Relationships

Case1:

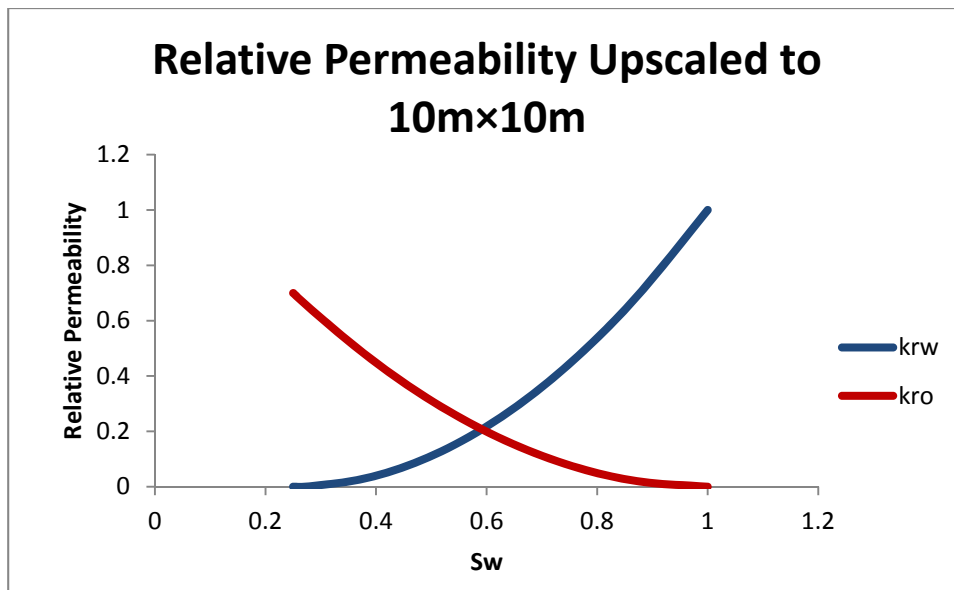


Figure 5-17: Up-scaled relative permeability relationship for homogeneous block of size 10m×10m

Case2:

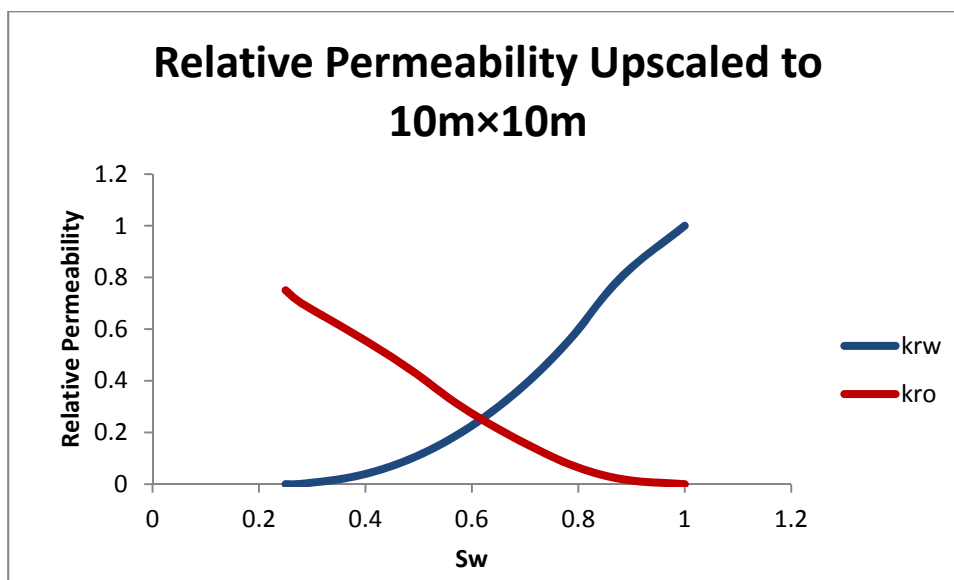


Figure 5-18: Up-scaled relative permeability relationship for single fracture system (oriented at 59°) in a block of size 10m×10m

Case3:

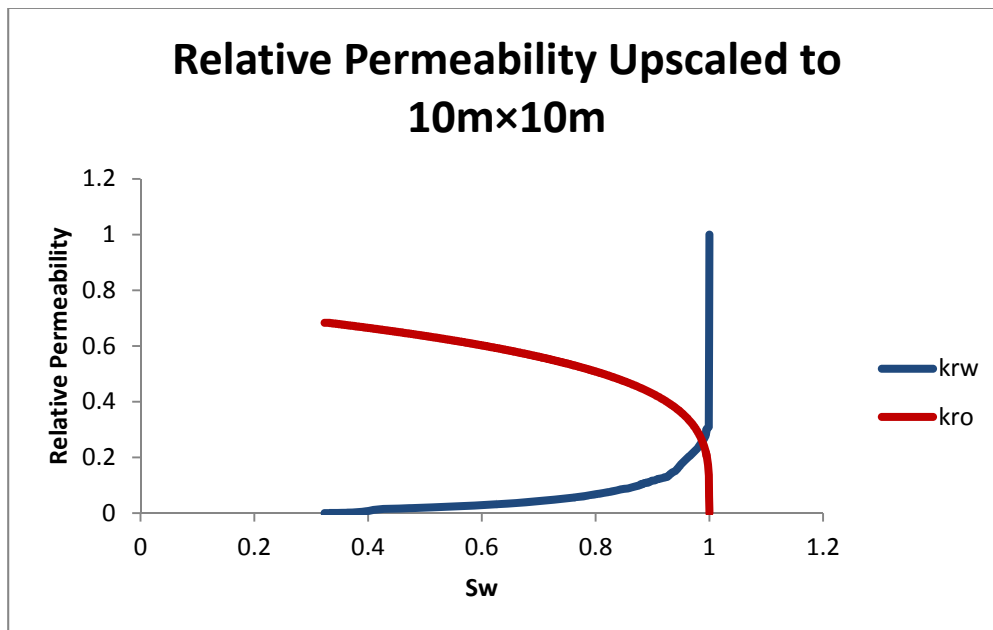


Figure 5-19: Up-scaled relative permeability relationship for single fracture system (oriented at 19° to the direction of flow) in a block of size 10m×10m

Case4:

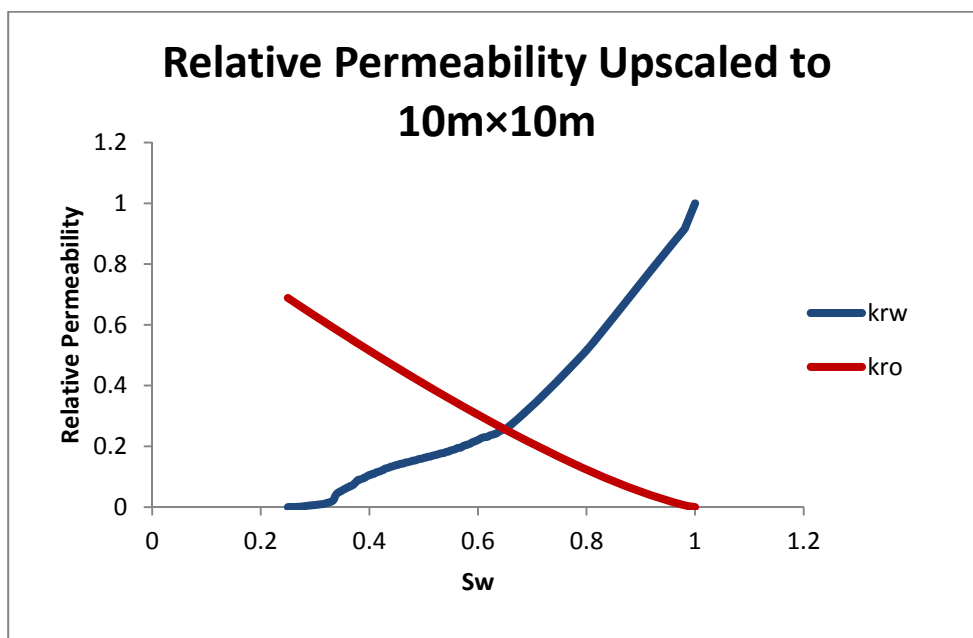


Figure 5-20: Up-scaled relative permeability relationship for multi fracture system (oriented at 30° and 32°) in a block of size 10m×10m

Case5:

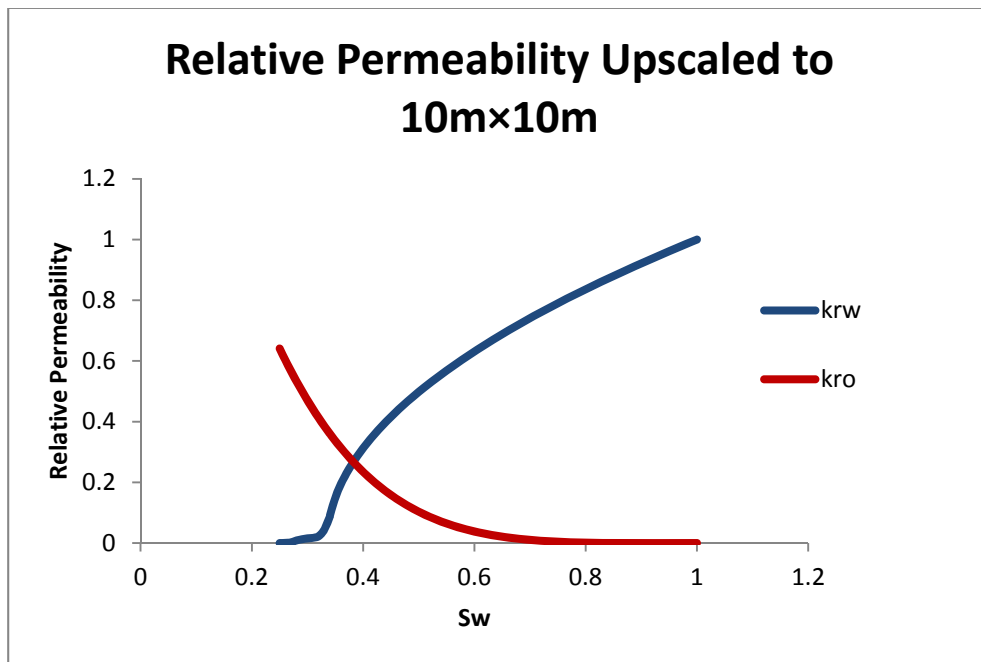


Figure 5-21: Up-scaled relative permeability relationship for multi fracture system (oriented at 64° and 19° non intersecting fracture system) in a block of size 10m×10m

Case6:

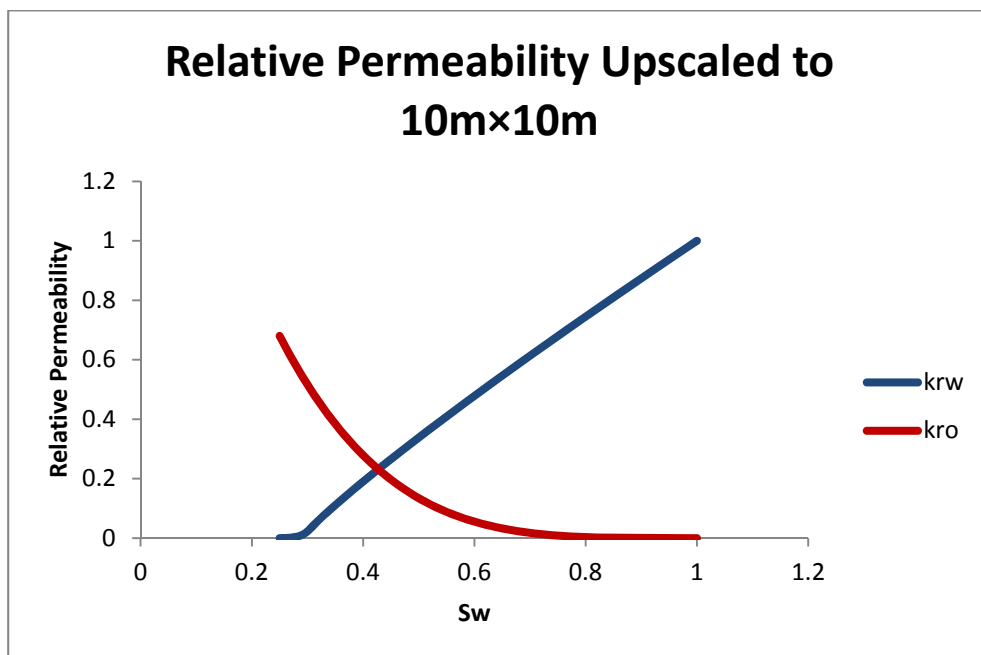


Figure 5-22: Up-scaled relative permeability relationship for multi fracture system (oriented at 20° and 64° intersecting fracture system) in a block of size 10m×10m

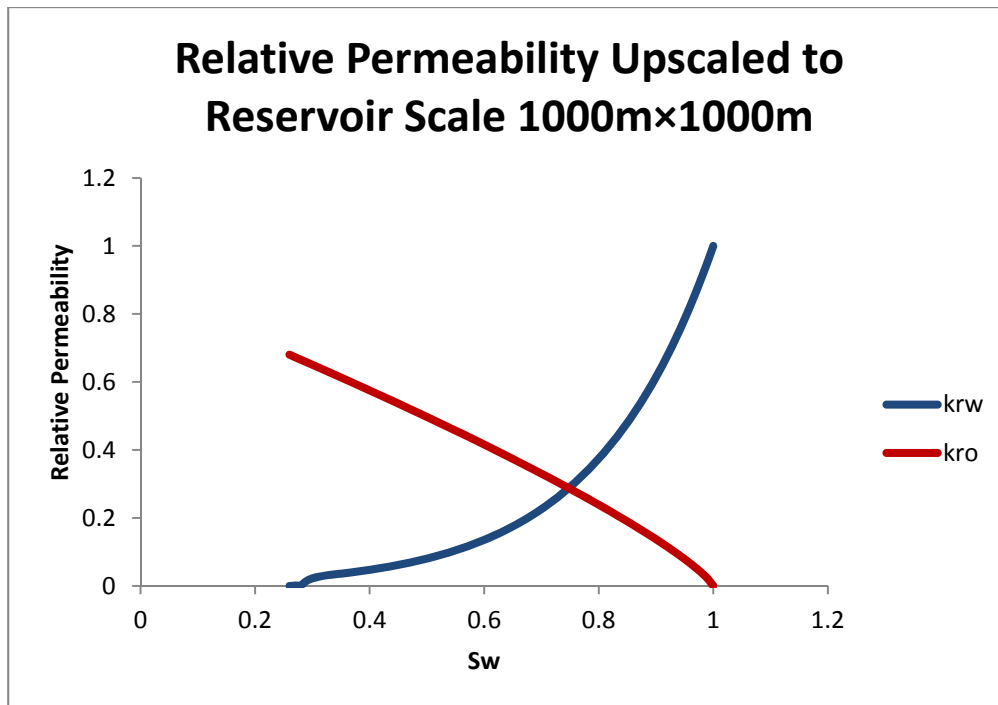


Figure 5-23: Up-scaled relative permeability relationship for multi fracture system (whole reservoir) in a block of size 1000m×1000m

Chapter 6

Conclusion and Future Work Recommendations

6.1 Conclusions and Perspectives

In this thesis, an innovative numerical and laboratory methodology was developed to study the mechanism of fluid flow in arbitrarily-oriented naturally fractured reservoirs. As part of the numerical study a grid-based permeability tensor model was developed and then used to predict pressure and fluid flow velocity profiles throughout the reservoir and well deliverability. As for the laboratory study, single and multiple (two) fractures with different orientations were constructed in $10\text{cm} \times 20\text{cm}$ glass bead model and effective permeability tensor for single phase flow and relative permeability for two phase flow were measured. These data were used to confirm the numerically derived effective permeability tensor and relative permeability. From the results of this study following conclusion can be drawn:

Results of effective permeability tensor are in consistent with the expectation. The effective permeability tensors have been found to be the highest when the fractures (single or multiple) are in line with the flow direction due to the contribution of full length of fracture. As for the two phase flow, the results of oil relative permeability for single fracture systems provided highest when the fracture is along the direction of flow, while for multiple fracture systems the oil relative permeability is highest for intersecting fracture networks. This is expected because the intersecting fractures were feeding the flow to each other causing an early breakthrough. It is also observed that laboratory derived effective permeability tensors and the relative permeabilities are in consistent with the numerically derived data. This consistency provides a mutual validation for the two procedures. A realistic laboratory and

numerical procedure of simulating fluid flow in arbitrary fracture systems have allowed reaching a high level consistency of the results.

Further, the grid based effective permeabilities were used to simulate pressure and velocity profiles throughout the reservoir and to estimate well deliverability. This result again showed quite a good consistency with the expected results. For example, flow is highly influenced by the connectivity of the fractures and the orientations. In an injection production scenario, wells that are placed along the direction of fracture orientations provided the highest production rate at low pressure drawdown. Also in a depletion drive situation it was clear from velocity plots that flow towards the wellbore was taking place through interconnected fractures.

In addition, a new methodology is proposed to upscale two-phase relative permeability (oil-water) from the laboratory to the reservoir scale. It was concluded that laboratory experiments can provide a benchmark for relative permeability which can then be upscaled to the reservoir scale by using the proposed upscaling methodology.

6.2 Recommendations for Future Studies

The major limitation of the permeability tensor model is that the block permeabilities are representing average flow for the block and to capture the fracture contribution effectively, grid block size has to be chosen as small as possible. This brings extra computational load; therefore, it is recommended to improve the technique by using any other appropriate technique that can capture the flow through fractures for any size of grid blocks without losing accuracy and at the same time incorporates flow through matrix.

In the laboratory work, more experiments are recommended with low matrix permeability to generate variety of data that can be used as benchmark. The effect of length of fracture on relative permeability can be studied. Furthermore, the size of the experimental model can be increased to have more flexibility for the geometry of the fractured media, i.e. number of fractures, sizes and orientations of fractures.

References

- Aavatsmark, I., T. Barkve, O. Bøe and T. Mannseth (1998). "Discretization on unstructured grids for inhomogeneous, anisotropic media. Part II: Discussion and numerical results." SIAM Journal on Scientific Computing **19**: 1717.
- Abaci, S., J. Edwards and B. Whittaker (1992). "Relative permeability measurements for two phase flow in unconsolidated sands." Mine water and the environment **11**(2): 11-26.
- Abtahi, M. and O. Torsaeter (1998). Experimental and numerical upscaling of two-phase flow in homogeneous and heterogeneous porous media.
- Aghighi, M. A. (2007). Fully Coupled Fluid Flow and Geomechanics in the Study of Hydraulic Fracturing and Post-Fracture Production. Petroleum Engineering. Sydney, University of New South Wales. **PhD**: 251.
- Arihara, N. and K. Sato (2001). Simulation of Naturally Fractured Reservoirs with Effective Permeability.
- Aziz, K. and A. Settari (1979). Petroleum reservoir simulation, Applied Science Publishers London.
- Babadagli, T. (2001). "Fractal analysis of 2-D fracture networks of geothermal reservoirs in south-western Turkey." Journal of volcanology and geothermal research **112**(1-4): 83-103.
- Barenblatt, G., I. P. Zheltov and I. Kochina (1960). "Basic concepts in the theory of seepage of homogeneous liquids in fissured rocks." J. Appl. Math. Mech **24**(5): 1286-1303.
- Beer, G. (1992). Introduction to finite and boundary element methods for engineers / G. Beer, J.O. Watson. Chichester ;, New York : Wiley.
- Berkowitz, B. (1995). "Analysis of fracture network connectivity using percolation theory." Mathematical Geology **27**(4): 467-483.
- Bourbiaux, B., M. Cacas, S. Sarda and J. Sabathier (1998). "A rapid and efficient methodology to convert fractured reservoir images into a dual-porosity model." REVUE-INSTITUT FRANCAIS DU PETROLE **53**: 785-800.
- Brebbia, C. and S. Walker (1978). The boundary element method for engineers, Pentech Press, London.
- Cacas, M., E. Ledoux, G. De Marsily, B. Tillie, A. Barbreau, E. Durand, B. Feuga and P. Peaudecerf (1990). "Modeling fracture flow with a stochastic discrete fracture network: calibration and validation: 1. The flow model." Water Resources Research **26**(3): 479-489.
- Cai, Z., J. Jones, S. McCormick and T. Russell (1997). "Control-volume mixed finite element methods." Computational Geosciences **1**(3): 289-315.
- Carman, P. (1937). "Fluid flow through granular beds." Transactions-Institution of Chemical Engineers **15**: 150-166.
- Castaigne, C., A. Genter, B. Bourguin, J. Chiles, J. Wendling and P. Siegel (2002). "Taking into account the complexity of natural fracture systems in reservoir single-phase flow modelling." Journal of Hydrology **266**(1-2): 83-98.
- Chou, S. H. and D. Y. Kwak (2000). "Mixed covolume methods on rectangular grids for elliptic problems." SIAM journal on numerical analysis: 758-771.
- Corey, A. T. (1954). "The interrelation between gas and oil relative permeabilities." Producers monthly **19**(1): 38-41.
- Dawe, R. A. and C. A. Grattoni (2008). "Experimental displacement patterns in a 2× 2 quadrant block with permeability and wettability heterogeneities—problems for numerical modelling." Transport in Porous Media **71**(1): 5-22.
- Detournay, E. (2004). "Propagation regimes of fluid-driven fractures in impermeable rocks." International Journal of Geomechanics **4**: 35.
- Durlofsky, L. J. (1991). "Numerical calculation of equivalent grid block permeability tensors for heterogeneous porous media." Water Resour. Res. **27**(5): 699-708.

- Durlofsky, L. J., B. Engquist and S. Osher (1992). "Triangle based adaptive stencils for the solution of hyperbolic conservation laws." Journal of Computational Physics **98**(1): 64-73.
- Edwards, M. and C. Rogers (1994). A flux continuous scheme for the full tensor pressure equation.
- Edwards, M. G. and C. F. Rogers (1998). "Finite volume discretization with imposed flux continuity for the general tensor pressure equation." Computational Geosciences **2**(4): 259-290.
- Ertekin, T., J. H. Abou-Kassem and G. R. King (2001). Basic applied reservoir simulation, Society of Petroleum Engineers.
- Feistauer, M., J. Felcman and M. Lukáčová-Medvid'ová (1995). "Combined finite element-finite volume solution of compressible flow." Journal of computational and applied mathematics **63**(1): 179-199.
- Gaul, L., M. Kogl and M. Wagner (2004). "Boundary Element Methods for Engineers and Scientists: An Introductory Course With Advanced Topics." Applied Mechanics Reviews **57**(6): B31-B31.
- Gentier, S., X. Rachez, T. Ngoc, T. Dung, M. Peter-Borie and C. Souque (2010). 3D Flow Modelling of the Medium-Term Circulation Test Performed in the Deep Geothermal Site of Soultz-Sous-forêts (France). Proceedings World Geothermal Congress 2010, Bali, Indonesia.
- Gholizadeh Doonechaly, N. and S. Rahman (2012). "3D Hybrid Tectono-Stochastic Modeling of Naturally Fractured Reservoir: Application of Finite Element Method and Stochastic Simulation Technique." Tectonophysics.
- Gillespie, P., C. Howard, J. Walsh and J. Watterson (1993). "Measurement and characterisation of spatial distributions of fractures." Tectonophysics **226**(1-4): 113-141.
- Goda, H. and P. Behrenbruch (2004). Using a modified brooks-corey model to study oil-water relative permeability for diverse pore structures.
- Gupta, A., G. Penuela and R. Avila (2001). "An Integrated Approach to the Determination of Permeability Tensors for Naturally Fractured Reservoirs." Journal of Canadian Petroleum Technology (JCPT) **40**(12).
- Hawkins, B. C. C. M. F. (1959). Applied petroleum reservoir engineering, Prentice Hall Inc New Jersey.
- Hodge, M. O. (2006). Avoiding Borehole Failure by Time-Dependent Stability Analysis of Stressed Poroelastic Rocks, The University of New South Wales.
- Hoteit, H. and A. Firoozabadi (2008). "An efficient numerical model for incompressible two-phase flow in fractured media." Advances in water resources **31**(6): 891-905.
- Hussain, F., Y. Cinar and P. Bedrikovetsky (2010). Comparison of methods for drainage relative permeability estimation from displacement tests. SPE Improved Oil Recovery Symposium.
- Hussain, F., Y. Cinar and P. Bedrikovetsky (2012). "A semi-analytical model for two phase immiscible flow in porous media honouring capillary pressure." Transport in Porous Media **92**(1): 187-212.
- Itasca, U. (2000). "User's Guide (Version 3.1)." Itasca Consulting Group Inc., Minneapolis.
- Joshua Koh, N. G.-D., Abdul Ravoof and Sheik S Rahman, Luke Mortimer (2010). Reservoir Characterisation and Numerical Modelling to Reduce Project Risk and Maximise the Chance of Success. an Example of How to Design a Stimulation Program and Assess Fluid Production from the Soultz Geothermal Field, France. Australian Geothermal Energy Conference, Adelaide, Australia.
- Kazemi, H., K. PORTERFIELD and P. Zeman (1976). "Numerical simulation of water-oil flow in naturally fractured reservoirs." Old SPE Journal **16**(6): 317-326.
- Kazemi, H., M. Seth and G. Thomas (1969). "SPE-002156-B-The Interpretation of Interference Tests in Naturally Fractured Reservoirs with Uniform Fracture Distribution." Old SPE Journal **9**(4): 463-472.
- Kunkel, J., S. Way and C. McKee (1988). Comparative evaluation of selected continuum and discrete-fracture models: Emphasis on dispersivity calculations for application to fractured geologic media, creston study area, eastern Washington, Nuclear Regulatory Commission, Washington, DC (USA). Div. of Engineering; In-Situ, Inc., Laramie, WY (USA).
- Lee, C. H. and I. W. Farmer (1993). Fluid flow in discontinuous rocks, Chapman & Hall.

- Lee, S., L. CL Jensen and M. Lough (1999). An efficient finite difference model for flow in a reservoir with multiple length-scale fractures.
- Lee, S., L. Durlofsky, M. Lough and W. Chen (1997). Finite difference simulation of geologically complex reservoirs with tensor permeabilities.
- Lee, S., H. Tchelepi, J. Patrick and L. DeChant (2002). "Implementation of a flux-continuous finite-difference method for stratigraphic, hexahedron grids." SPE Journal **7**(3): 267-277.
- Lee, S. H., M. F. Lough and C. L. Jensen (2001). "Hierarchical modeling of flow in naturally fractured formations with multiple length scales." Water Resour. Res. **37**(3): 443-455.
- Li, K. (2010). "DETERMINATION OF RESISTIVITY INDEX, CAPILLARY PRESSURE, AND RELATIVE PERMEABILITY."
- Li, K. and R. N. Horne (2009). "Experimental Study and Fractal Analysis of Heterogeneity in Naturally Fractured Rocks." Transport in Porous Media **78**(2): 217-231.
- Li, X., O. Zienkiewicz and Y. Xie (1990). "A numerical model for immiscible two-phase fluid flow in a porous medium and its time domain solution." International Journal for Numerical Methods in Engineering **30**(6): 1195-1212.
- Long, J. C. S. and D. M. Billaux (1987). "From field data to fracture network modeling: an example incorporating spatial structure." Water Resources Research **23**(7): 1201-1216.
- Long, J. C. S., J. Remer, C. Wilson and P. Witherspoon (1982). "Porous media equivalents for networks of discontinuous fractures." Water Resources Research **18**(3): 645-658.
- Long, J. C. S. and P. A. Witherspoon (1985). "The relationship of the degree of interconnection to permeability in fracture networks." Journal of Geophysical Research **90**(B4): 3087-3098.
- Lough, M. F., S. H. Lee and J. Kamath (1998). "An efficient boundary integral formulation for flow through fractured porous media." J. Comput. Phys. **143**(2): 462-483.
- Maier, R. S., D. Kroll, Y. Kutsovsky, H. Davis and R. Bernard (1998). "Simulation of flow through bead packs using the lattice Boltzmann method." Physics of Fluids **10**: 60.
- Marrett, R. and S. Laubach (1997). "Diagenetic controls on fracture permeability and sealing." International Journal of Rock Mechanics and Mining Sciences **34**(3): 204. e201-204. e211.
- Massonnat, G. and E. Manisse (1994). "Modélisation des réservoirs fracturés et recherche de paramètres équivalents: étude de l'anisotropie verticale de perméabilité= Fractured reservoir modelling and calculation of equivalent parameters: study of the vertical permeability anisotropy." Bulletin des centres de recherches exploration-production Elf-Aquitaine.
- Min, K. B., L. Jing and O. Stephansson (2004). "Determining the equivalent permeability tensor for fractured rock masses using a stochastic REV approach: Method and application to the field data from Sellafield, UK." Hydrogeology Journal **12**(5): 497-510.
- Moinfar, A., W. Narr, M. H. Hui, B. Mallison and S. Lee (2011). Comparison of Discrete-Fracture and Dual-Permeability Models for Multiphase Flow in Naturally Fractured Reservoirs.
- Naji, H. and K. Hossein (1996). A Fully Implicit, Three-Dimensional, Two-Phase, Control-Volume Finite Element Model for the Simulation of Naturally Fractured Reservoirs.
- Nakashima, T., N. Arihara, Sutopo and K. Sato (2001). Effective Permeability Estimation for Modeling Naturally Fractured Reservoirs. SPE Middle East Oil Show. Bahrain, Copyright 2001, Society of Petroleum Engineers Inc.
- Nakashima, T., K. Sato, N. Arihara and N. Yazawa (2000). Effective permeability estimation for simulation of naturally fractured reservoirs.
- Niessner, J., R. Helmig, H. Jakobs and J. Roberts (2005). "Interface condition and linearization schemes in the newton iterations for two-phase flow in heterogeneous porous media." Advances in water resources **28**(7): 671-687.
- ODA, M. (1985). "Permeability tensor for discontinuous rock masses." Geotechnique **4**: 13.
- Odling, N., P. Gillespie, B. Bourguine, C. Castaing, J. Chiles, N. Christensen, E. Fillion, A. Genter, C. Olsen and L. Thrane (1999). "Variations in fracture system geometry and their implications for fluid flow in fractures hydrocarbon reservoirs." Petroleum Geoscience **5**(4): 373-384.

- Odling, N. E. (1992). "Network properties of a two-dimensional natural fracture pattern." Pure and Applied Geophysics **138**(1): 95-114.
- Odling, N. E. and J. E. Roden (1997). "Contaminant transport in fractured rocks with significant matrix permeability, using natural fracture geometries." Journal of Contaminant Hydrology **27**(3): 263-283.
- Ohlberger, M. (1997). "Convergence of a Mixed Finite Element: Finite Volume Method for the Two Phase Flow in Porous Media." EAST WEST JOURNAL OF NUMERICAL MATHEMATICS **5**: 183-210.
- Park, Y. and W. Sung (2000). Development of FEM Reservoir Model Equipped with Effective Permeability Tensor and Its Application to Naturally Fractured Reservoirs.
- Polak, S., Y. Cinar, T. Holt and O. Torsæter (2011). "An experimental investigation of the balance between capillary, viscous, and gravitational forces during CO₂ injection into saline aquifers." Energy Procedia **4**: 4395-4402.
- Pruess, K. (1985). "A practical method for modeling fluid and heat flow in fractured porous media." Old SPE Journal **25**(1): 14-26.
- Pruess, K. (1991). TOUGH2: A general-purpose numerical simulator for multiphase fluid and heat flow, Lawrence Berkeley Lab., CA (United States).
- Ranjith, P. (2010). "An experimental study of single and two-phase fluid flow through fractured granite specimens." Environmental Earth Sciences **59**(7): 1389-1395.
- Rasmussen, T. C., T.C.Jim-Yeh, D.D. Evan (1987). "Effect of variable fracture permeability/matrix permeability ratio on three dimensional fractured rock hydraulic conductivity." **Preceding of the conference on Geostatistical, sensitivity, and uncertainty methods for ground water flow, San Francisco, California, Bettelle press.**
- Rossen, W., Y. Gu and L. Lake (2000). Connectivity and permeability in fracture networks obeying power-law statistics.
- Russell, T. F. (1995). "Rigorous block-centred discretisation on irregular grids: Improved simulation of complex reservoir systems, Tulsa."
- Sausse, J., C. Dezayes and A. Genter (2007). From geological interpretation and 3D modelling to the characterization of the deep seated EGS reservoir of Soultz (France). Preceedings European Geothermal Congress 2007 Unterhaching, Germany.
- Schwartz, F. W. and L. Smith (1988). "A continuum approach for modeling mass transport in fractured media." Water Resources Research **24**(8): 1360-1372.
- Shad, S. and I. Gates (2010). "Multiphase Flow in Fractures: Co-Current and Counter-Current Flow in a Fracture." Journal of Canadian Petroleum Technology **49**(2): 48-55.
- Snow, D. T. (1969). "Anisotropie Permeability of Fractured Media." Water Resour. Res. **5**(6): 1273-1289.
- Sudicky, E. and R. McLaren (1992). "The Laplace transform Galerkin technique for large-scale simulation of mass transport in discretely fractured porous formations." Water Resources Research **28**(2): 499-514.
- Suli, E. (1991). "Convergence of finite volume schemes for Poisson's equation on nonuniform meshes." SIAM journal on numerical analysis: 1419-1430.
- Sylte, A., T. Mannseth, J. Mykkeltveit and J. Nordtvedt (1998). Relative permeability and capillary pressure: effects of rock heterogeneity.
- Teimoori, A., Z. Chen, S. S. Rahman and T. Tran (2003). Calculation Of Permeability Tensor Using Boundary Element Method Provides A Unique Tool To Simulate Naturally Fractured Reservoirs. SPE Annual Technical Conference and Exhibition. Denver, Colorado, Society of Petroleum Engineers.
- Teimoori, A., Z. Chen, S. S. Rahman and T. Tran (2005). "Effective Permeability Calculation Using Boundary Element Method in Naturally Fractured Reservoirs." Petroleum Science and Technology **23**(5): 693 - 709.

- Therrien, R. and E. Sudicky (1996). "Three-dimensional analysis of variably-saturated flow and solute transport in discretely-fractured porous media." Journal of Contaminant Hydrology **23**(1-2): 1-44.
- Thomas, J. and D. Trujillo (1995). "Analysis of finite volume methods." Mathematical Modelling of Flow Through Porous Media: 318-336.
- Unsal, E., S. K. Matthäi and M. J. Blunt (2010). "Simulation of multiphase flow in fractured reservoirs using a fracture-only model with transfer functions." Computational Geosciences **14**(4): 527-538.
- Warren, J. E. and P. J. Root (1963). "The behavior of naturally fractured reservoirs." Old SPE Journal **3**(3): 245-255.
- Weiser, A. and M. F. Wheeler (1988). "On convergence of block-centered finite differences for elliptic problems." SIAM journal on numerical analysis: 351-375.
- Wu, Y. S. (2000). "On the effective continuum method for modeling multiphase flow, multicomponent transport, and heat transfer in fractured rock." Geophysical monograph **122**: 299-312.
- Wu, Y. S. and K. Pruess (1988). "A multiple-porosity method for simulation of naturally fractured petroleum reservoirs." SPE Reservoir Engineering **3**(1): 327-336.
- Zhang, X., D. Sanderson, R. Harkness and N. Last (1996). Evaluation of the 2-D permeability tensor for fractured rock masses, Elsevier.